Applications of Optical Birefringence With Natural-Materials and Meta-Materials

Tang, Ying

DOI
10.4233/uuid:35115149-ed67-4d73-98d1-ff81022cecae

Publication date
2019

Document Version
Final published version

Citation (APA)
Tang, Y. (2019). *Applications of Optical Birefringence: With Natural-Materials and Meta-Materials*. [Dissertation (TU Delft), Delft University of Technology]. https://doi.org/10.4233/uuid:35115149-ed67-4d73-98d1-ff81022cecae

Applications of Optical Birefringence:

with Natural-Materials and Meta-Materials

Applications of Optical Birefringence:

with Natural-Materials and Meta-Materials

Dissertation

for the purpose of obtaining the degree of doctor
at Delft University of Technology
by the authority of the Rector Magnificus prof.dr.ir. T.H.J.J. van der Hagen
chair of the Board for Doctorates
to be defended publicly on
Wednesday 2 October 2019 at 10:00 o'clock

by

Ying TANG

Master of Engineering in Optical Engineering,
Huazhong University of Science and Technology, China
born in Shaodong, China

This dissertation has been approved by the promoters.

Composition of the doctoral committee:

Rector Magnificus,	chairperson
Prof. dr. H.P. Urbach,	Delft University of Technology, promotor
dr. A.J.L. Adam,	Delft University of Technology, copromotor

Independent members:

Prof. dr. L.K. Kuipers,	Delft University of Technology
Prof. dr. A.F. Koenderink,	AMOLF, the Netherlands
Prof. dr. G. Gerini,	Eindhoven University of Technology, the Netherlands
Prof. dr. S. Zouhdi,	Paris-Sud University, France
Prof. dr. S. Stallinga,	Delft University of Technology, reserve member
dr. M. Xu,	TNO, the Netherlands

The PhD candidate was supported by scholar from
China Scholarship Council (201306160089).
Keywords: meta-materials, birefriengence, waveguide, super-resolution, optical trapping, nanoparticles, imaging

An electronic version of this dissertation is available at
http://repository.tudelft.nl/.

Contents

Summary

Birefringence is the optical property of a material which has refractive index depending on the propagation and the polarization direction of the light. The beauty of this property lies in the fact that it provides an independent control of light over different polarization directions, which leads to many important applications in today's optical systems. This thesis explores the applications of existing naturally-occurring birefringent materials as well as the engineered formed-birefringent meta-materials via nano-fabrication. Since the optical theory of birefringence is highly developed, this thesis will mainly address the applications. The investigation methods include numerical simulation, nano-fabrication and experimental validation. The thesis is structured in six distinct chapters.

Chapter 1 is the introduction. In this chapter, the formed optical birefringence with meta-materials is first introduced. The effective medium theory is used for deriving the permittivity of the meta-materials and the corresponding isofrequency surface is presented. Next, the basic concepts of the applications of birefringence in this thesis are addressed, including Maxwell's stress tensor (MST) in optical trapping, optical waveguide theory in optical communication and scalar diffraction theory in imaging.

In **Chapter 2**, the application of single-crystal rutile TiO_2 in optical trapping is discussed. Optical trapping of (sub)micron-sized particles is broadly employed in nanoscience and engineering. The materials commonly employed, however, have physical properties that limit the transfer of linear or angular momentum (or both). Here, we overcome these limitations through the use of single-crystal rutile TiO_2, which has an exceptionally large optical birefringence, high index of refraction as well as good chemical stability. We show that rutile TiO_2 nanocylinders form powerful joint force and torque transducers in aqueous environments. By using only moderate laser powers, $nN \cdot nm$ torques at kHz rotational frequencies can be applied to tightly trapped TiO_2 particles.

In **Chapter 3**, we further expand the application in optical trapping by employing dielectric multilayer meta-materials as probe materials, which can possess high birefringence and moderate refractive index at the same time. The MM probes are etched and released from a sputtered multilayer film. The results in the optical torque wrench (OTW) show that our MM probes can achieve high angular momentum transfer efficiency. Moreover, the MM probe comes with tunability in its optical properties through changing the composite material filling ratio.

In **Chapter 4**, the application of anisotropic meta-materials with hyperbolic dispersion in waveguide mode engineering is discussed. By using a type II hyperbolic meta-material (HMM) as cladding material, a waveguide which only supports higher order modes can be achieved, while the lower order modes become leaky and are absorbed in the HMM cladding.

In **Chapter 5**, the application of hyperbolic meta-materials in image application is discussed. A hyperlens is made of hyperbolic materials and is capable of achieving super-resolution imaging. Nevertheless, the current hyperbolic materials and hyperbolic meta-materials have intrinsic absorption, which influences the resolution performance of the hyperlens. In this chapter, a theoretical study on lossy hyperbolic media is presented. The results show that the absorption in the medium plays an essential role in the refraction property and the design of the hyperlens.

Finally, **Chapter 6** summarize the discovery of this thesis, and other potential application, such as nano-particle detection and imaging of extended object.

Samenvatting

Dubbele breking is de optische eigenschap van een materiaal dat een brekingsindex heeft afhankelijk van de voortplanting en de polarisatierichting van het licht. Het mooie van deze eigenschap ligt in het feit dat het een onafhankelijke controle over het licht over verschillende polarisatierichtingen biedt, wat leidt tot veel belangrijke toepassingen in hedendaagse optische systemen. Dit proefschrift onderzoekt de toepassingen van dubbelbrekende materialen die in de natuur voorkomen, evenals de kunstmatig ontwikkelde dubbelbrekende meta-materialen die met nanofabricage gemaakt worden. Omdat de optische theorie van dubbele breking al ver ontwikkeld is, zal dit proefschrift voornamelijk de toepassingen behandelen. De onderzoeksmethoden omvatten numerieke simulaties, nanofabricage en experimentele validatie. Het proefschrift is gestructureerd in zes verschillende hoofdstuken.

Hoofdstuk 1 is de inleiding. In dit hoofdstuk wordt eerst de gevormde optische dubbele breking met metamaterialen geïntroduceerd. De effectieve mediumtheorie wordt gebruikt voor het afleiden van de permittiviteit van de metamaterialen en het bijbehorende isofrequentieoppervlak wordt gepresenteerd. Vervolgens worden de basisconcepten van de toepassingen van dubbele breking in dit proefschrift behandeld, waaronder Maxwell's stress tensor (MST) in optische trapping, optische golfgeleidertheorie in optische communicatie en scalaire diffractietheorie in beeldvorming.

In **hoofdstuk 2** wordt de toepassing van monokristallijn rutiel TiO_2 in optische trapping besproken. Optische pincetten worden breed toegepast in nanowetenschap en engineering voor het vangen van deeltjes van (sub) micron-grootte. De gewoonlijk gebruikte materialen hebben echter fysische eigenschappen die de overdracht van impuls of impulsmoment (of beide) beperken. Hier lossen we dit probleem op door het gebruik van monokristallijn rutiel TiO_2, dat een uitzonderlijk grote optische dubbele breking, hoge brekingsindex en goede chemische stabiliteit heeft. We laten zien dat nanocylinders van rutiel TiO_2 krachtige gezamenlijke kracht- en koppelomvormers vormen in waterige omgevingen. Door slechts matige laserkrachten te gebruiken, kunnen koppels van nNnm ordegrootte bij kHz-rotatiefrequenties worden toegepast op strak gevangen TiO_2-deeltjes.

In **hoofdstuk 3** breiden we de toepassing in optische trapping verder uit door gebruik te maken van diëlektrische meerlagige metamaterialen als sondematerialen, die tegelijkertijd een hoge dubbele breking en matige brekingsindex kunnen hebben. De MM-sondes worden geëtst en vrijgegeven uit een gesputterde meerlagige film. De resultaten in de optical torque wrench (OTW) laten zien dat onze MM-sondes een hoge efficiëntie van de impulsoverdracht kunnen bereiken. Bovendien is de MM-sonde voorzien van afstembaarheid in zijn optische eigenschappen door het veranderen van de vulverhouding van composietmateriaal.

In **hoofdstuk 4** wordt de toepassing van anisotrope metamaterialen met hyperbolische dispersie in waveguide mode engineering besproken. Door een type II hyperbolisch metamateriaal (HMM) als bekledingsmateriaal te gebruiken, kan een golfgeleider worden bereikt die alleen modi van hogere orde ondersteunt, terwijl de modi van lagere orde lek worden en worden geabsorbeerd in de HMM-bekleding.

In **hoofdstuk 5** wordt de toepassing van hyperbolische metamaterialen in beeldtoepassing besproken. Een hyperlens is gemaakt van hyperbolische materialen en is in staat om beeldvorming met superresolutie te bereiken. Desondanks hebben de huidige hyperbolische materialen en hyperbolische metamaterialen intrinsieke absorptie, die de resolutieprestaties van de hyperlenzen beïnvloedt. In dit hoofdstuk wordt een theoretische studie over hyperbolische media met verlies gepresenteerd. De resultaten tonen aan dat de absorptie in het medium een essentiële rol speelt in de brekingseigenschap en het ontwerp van de hyperlenzen.

Ten slotte wordt in **hoofdstuk 6** de ontdekking van dit proefschrift samengevat en worden andere mogelijke toepassingen, zoals nanodeeltjesdetectie, en beeldvorming van uitgebreid objecten besproken.

1

Introduction

1

The understanding of light and matter interaction plays an important role in today's optical physics. It is known that modern optical theory is based on two fundamental foundations: the Maxwell's equations [1] and the constitutive relations [2]. The former provides a mathematical model for all optical phenomenons and the later describes the electrical response of materials to an electromagnetic field. It is very clear that the true power of optical theory lies in the constitutive relations, which give raise to many new optical application [3]. In general, the optical response of materials is complex, and not even linear in frequncy or intensity, which dramatically increases the complexity of the light-matter interaction process. Fortunately, in most of the cases, some useful approximations can be applied and can still give us a relatively accurate model compared to the real world. For instance, most materials are non-magnetic at optical frequencies, where the relative permeability is commonly considered to be unity in order to neglect the magnetic effects [4]; the nonlinear effect is often neglected for low field strength [5]; material dispersion is also unimportant for visible light with frequency limited to a narrow bandwidth [6]. In this thesis, we consider only the uniaxial anisotropic material, where there exists a single direction governing the anisotropicity, while all other directions perpendicular to it are optically equivalent [7]. Therefore, in this situation the polarization response to an external electric field $\mathbf{E}$ can be written by

$$\mathbf{D} = \underline{\underline{\epsilon}}\mathbf{E}, \tag{1.1}$$

where $\underline{\underline{\epsilon}}$ is the three-by-three optical permittivity tensor. When the main axis of the uniaxial anisotropic material is aligned with one of the three axes in Cartesian coordinate, it is given by

$$\underline{\underline{\epsilon}} = \begin{bmatrix} \epsilon_x & 0 & 0 \\ 0 & \epsilon_y & 0 \\ 0 & 0 & \epsilon_z \end{bmatrix}. \tag{1.2}$$

If the optical axis is along the z-axis, then we have $\epsilon_x = \epsilon_y \neq \epsilon_z$.

In nature, many crystalline materials are uniaxial anisotropic, such as ice H_2O, calcite $CaCO_3$, quartz SiO_2, sapphire Al_2O_3, rutile TiO_2. The anisotropic materials are widely used in many of today's optical devices, such as polarizing prisms [8], wave-plates [9], color filters [10], optical axis gratings [11], and light modulators [12]. In this thesis we demonstrate one application in optical trapping by using naturally-single-crystalline rutile nanocylinders.

Nevertheless, as the choices of naturally occurring optical birefringent materials are limited, it is necessary to expand the library of optical birefringent materials in order to boost our ability for manipulating light. The search for new materials naturally leds to the development of meta-materials, where the building block of materials is artificially engineered by will [13]. The development in the nanofabrication has enable us to fabricate this type of nano-structure [14].

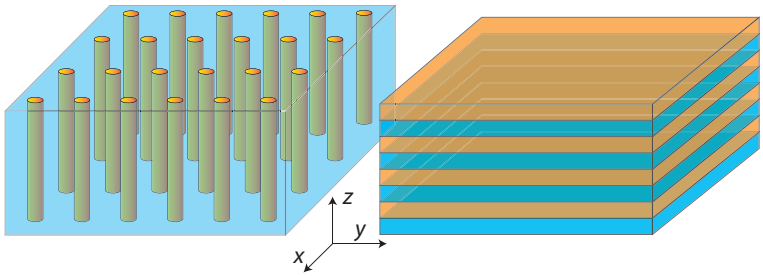

Figure 1.1: The schematics of two common types of 3D meta-material structures. On the left is the nano-wire array structure and on the right is the multilayer structure.

1.1. Effective medium theory for meta-materials

In nano-fabrication, the two most common types of three-dimensional (3D) meta-materials are nano-wire (NW) array and multilayer (ML) structure, as shown in Fig. 1.1. The NW meta-materials consist of a lattice of nano-wire array embedded in a bulk matrix of another material. The ML meta-materials consist of two or more different materials stacking on each other layer by layer. Because the feature sizes of these discontinuous structures are much smaller compared to the wavelength of the electromagnetic wave, the optical response of each individual medium is no longer important. In fact the average collective effect should be considered, which is described by the effective medium theory (EMT). It is trivial to understand that the transversal components of the permittivity tensor remains constant as both structure are equivalent periodicity along either x or y direction. And the unique component of the permittivity tensor can be only along the z-direction. For the NW meta-materials, the permittivity tensor is determined by [15]

$$\epsilon_x = \epsilon_y = \frac{[(1+f)\epsilon_w + (1-f)\epsilon_h]\epsilon_h}{(1-f)\epsilon_w + (1+f)\epsilon_h}, \tag{1.3}$$

$$\epsilon_z = f\epsilon_w + (1-f)\epsilon_h, \tag{1.4}$$

where f denotes the filling ratio of the area occupied by the nano-wire medium in the $x-y$ plane, ϵ_w and ϵ_h are the permittivities of the wire medium and the host medium, respectively.

For the ML meta-materials, the permittivity tensor is given by [15]

$$\epsilon_x = \epsilon_y = f\epsilon_1 + (1-f)\epsilon_2, \tag{1.5}$$

$$\epsilon_z = \left(\frac{f}{\epsilon_1} + \frac{1-f}{\epsilon_2}\right)^{-1}, \tag{1.6}$$

where f denotes the filling ratio of the thickness of the medium 1 in a layer-pair along the z-direction, ϵ_1 and ϵ_2 are the permittivities of the two composed materials.

In both type of meta-materials, the composed material can be either dielectric or metallic. In the case that both materials are dielectric, a formed uniaxial birefringent material can be achieved, in which no extra loss is introduced. In Fig. 1.2, the

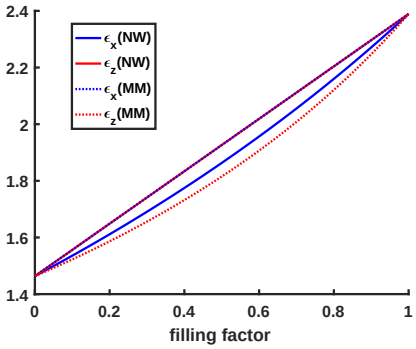

Figure 1.2: The effective permittivities versus filling factor for nano-wire (NW) type and multilayer(ML) type of meta-materials with SiO_2 and TiO_2 composing materials at the wavelength of 633 nm.

effective permittivity for both NW and ML type of meta-materials at the wavelength of 633 nm are shown, where in both cases SiO_2 [16] and TiO_2 [17] are used as composed materials and in the case NW meta-material, SiO_2 is the host medium. As can be seen from the figure, for the NW type meta-material the unique permittivity component ϵ_z is larger than the transversal permittivity ϵ_x (ϵ_y), forming a positive uniaxial birefringence, and for the ML type meta-material, negative uniaxial birefringence is formed with ϵ_x (ϵ_y) $> \epsilon_z$. Moreover, by tuning the filling ratio of the two materials, the birefringence can be tuned accordingly. This means that we can customize the material properties by will according to the specific application.

When one of the composed material is a metal, the situation becomes interesting. In Fig. 1.3, the effective permittivities of the meta-materials composing of SiO_2 and Ag at the wavelength of 633 nm are plotted. In Fig. 1.3a, for the NW meta-material, the longitudinal permittivity component ϵ_z becomes negative while the transversal component ϵ_x still remains positive for the majority of the filling ratio range. The permittivities only become purely positive (or negative) for very small (or large) filling ratio. Fig. 1.3b shows an almost reversed result for the ML meta-material, where the transversal component ϵ_x becomes negative while the longitudinal permittivity component ϵ_z remains positive for a large range of filling ratio. Due to the introducing of Ag with complex permittivity, the effective permittivity tensor also becomes complex, with the imaginary part representing dissipative losses in the material. It can be seen that the imaginary part of the positive component has a peak when this real part jumps for positive to negative, this indicates that the losses in the medium can play a key role in the optical response of the meta-materials. In the next section we will discuss the optical response of this type of meta-material which consists of both dielectric and metal.

1.2. Hyperbolic dispersion property

In order to describe the wave propagation property of light, the dispersion relation of wave is normally used for conceptual understanding. Without derivation, the dis-

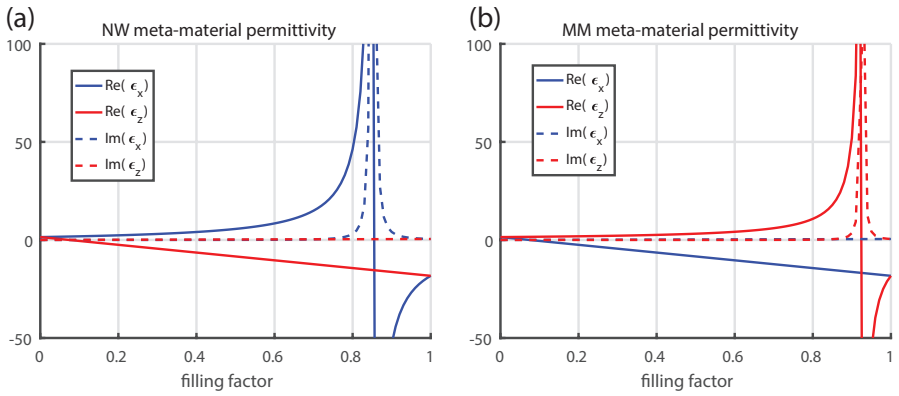

Figure 1.3: The effective permittivities versus filling ratio for nano-wire (NW) type (a) and multilayer(ML) type (b) of meta-materials with SiO_2 and Ag composing materials at the wavelength of 633 nm.

persion relation of transverse magnetic (TM) polarized wave in uniaxial birefringent materials is given by [18]

$$\frac{k_x^2 + k_y^2}{\epsilon_z} + \frac{k_z^2}{\epsilon_x} = k_0^2, \tag{1.7}$$

where $k_0 = \omega/c$ denotes the wavenumber in vacuum. When the permittivities are all real, the equation can be represented by a three-dimensional surface named isofrequency surface [19].

In Fig. 1.4, the isofrequency surface is shown for both NW meta-materials and ML meta-materials consisting of Ag and SiO_2, where their effective permittivities are shown in Fig. 1.3. For simplicity, the imaginary part of the permittivity is ignored. It can be seen when the filling ratio is zero (means purely SiO_2), the isofrequency surface is represented by a sphere with a radius of n_{SiO_2}. The energy flow (Poynting vector **S**) is perpendicular to the surface. Hence in this case the wavevectors in this medium (from coordinate center to the surface) have a constant norm (wavenumber) and they are parallel to the Poynting vector **S**. The spherical shape of the isofrequency surface also indicates that there is an upper limit for the wavevector k_x and k_y, beyond which only imaginary k_z is found, indicating the evanescent wave solution of Eq. 1.7. Therefore, in this medium, the optical resolution is limited. When the filling ratio becomes 0.1, both ϵ_x and ϵ_z are changed but remain positive, and the isofrequency surface becomes a ellipsoid for the NW meta-material and a flat disk for the ML meta-material. For the NW meta-material, the isofrequency surface indicates that the transversal wavevector k_x, k_y is limited to a small value and hence the electromagnetic waves are mostly evanescent modes. For the ML meta-material, for all propagating electromagnetic waves with limited k_x and k_y, the longitudinal wavevector k_z is similar and hence the relative phase of the field of different transversal wavevector during propagation remains the same. On the other hand, the Poynting vector (normal of the surface) is almost always pointing towards the z-direction, indicating a unidirectional emitting property of light in this

medium [20].

When the filling ratio further increases, a region is reached in which both positive and negative permittivities exist. In Fig. 1.4, we can see that when filling ratio reaches 0.5, the isofrequency surface becomes a hyperboloid with two sheets and one sheet for the NW meta-material and the ML meta-material, respectively. In this situation, for the NW meta-material, there is no upper limit for the transversal wavevector k_x and k_y, where there is always a corresponding real k_z can be found, suggesting that there is always a propagating mode existing in the medium. This type of material is defined as type I hyperbolic material [21], where the name 'hyperbolic' originates from its hyperbolic shape of isofrequency surface. For the ML meta-material, the imaginary solution of k_z is found only for very small transversal wavevector k_x and k_y, indicating a band-gap type of structure. This type of material is defined as type II hyperbolic material [21]. Moreover, the energy flow direction of the medium is mainly pointing within a cone solid angle, meaning that the emission of light is also anisotropic. As the filling ratio of Ag is further increased to $f = 0.75$, it can be seen in Fig. 1.4 that the distance between the two sheets gets larger for the NW meta-material and the band-gap also gets larger for the ML meta-material. This indicates that the hyperbolic dispersion property of the material can be adjusted by simply changing the filling ratio.

This type material of hyperbolic dispersion has drawn tremendous attention in the past decades [15, 22–24]. It is mainly because it can support propagating modes of very large transversal wavevector [15], where the detail information is carried by the high-spatial frequency waves which is normally exponentially decayed during propagation, this makes it very difficult to detect or measure. However with the hyperbolic type of dispersion, the high-spatial frequency information remains propagating mode and hence can still be detected in the far-field. Therefore, a lot of research on super-resolution of hyperbolic materials has been done [25–28]. Also, the photonic density of states (PDOS) of the hyperbolic medium is very large due to its infinite large isofrequency surface [29]. Therefore, research on PDOS engineering has been done in many publications [30–33]. It is also noticeable that so far we have neglect the absorption effect, however in most of the hyperbolic materials, the absorption plays a key role in its optical property [34]. Researcher also demonstrated that lossy hyperbolic material can also be used as broadband absorber [35].

1.3. Electromechanics theory: Maxwell's stress tensor

It was discovered in the 19th century that light carries momentum and hence exert 'light pressure' on an illuminated object [36]. This important study was later further developed by Ashkin's group, showing that a focused light can trap an object in the focus center [37, 38]. This discovery was then leads to the invention of optical tweezers [39].

Ideally, if the object is very large or very small, ray-optics analysis or dipole approximation can be used for calculating the force applied on the object [40, 41].

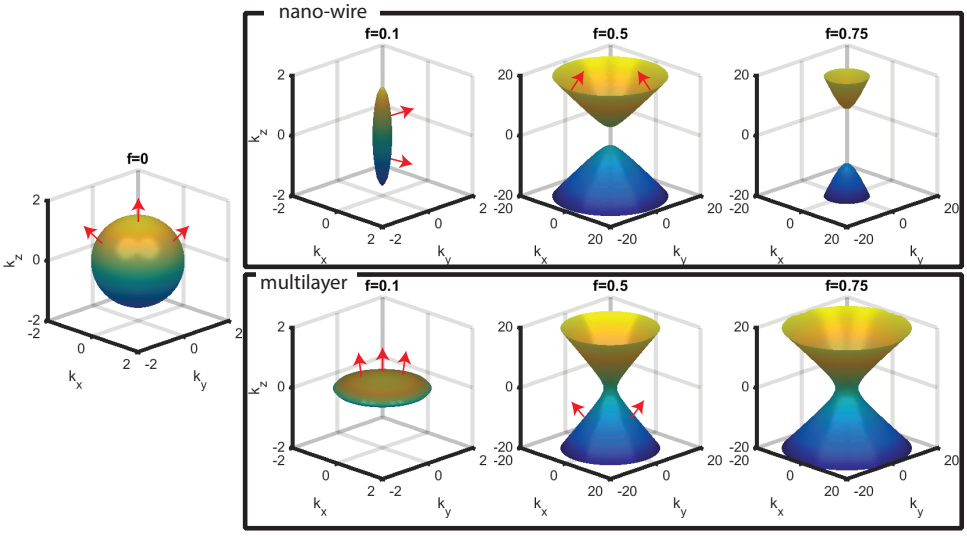

Figure 1.4: The isofrequency surfaces for both NW meta-material and ML meta-material, in which the composed materials are SiO_2 and Ag at the wavelength of 633 nm. The filling ratio showed are (from left to right) f =0, f =0.1, f =0.5 and f =0.75.

However, when the size of the object is comparable to the wavelength, a more rigorous wave analysis is required [42]. The most commonly used tool is Maxwell stress tensor [43–45].

Supposed an arbitrary incident beam $\mathbf{E}_{in}$ is applied on an arbitrary object B and being scattered, as shown in Fig. 1.5. The total field is found to be $\mathbf{E}_{tot} = \mathbf{E}_{in} + \mathbf{E}_s$, where $\mathbf{E}_s$ is the scattered field. Assuming that the object is rigid, the time averaged net mechanical force $\langle \mathbf{F} \rangle$ applied on the object is entirely determined by the field on an arbitrary enclosing surface S, which is linked by the Maxwell stress tensor [43, 46]

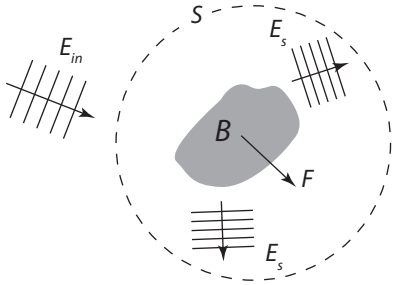

Figure 1.5: Schematic of the mechanical force F act on an object B. The total force is entirely determined by the total electric and magnetic field at an arbitrary surface S enclosing the object B. E_{in} is the incident electric field and E_s is the scattered electric field.

1

$$\langle \mathbf{F} \rangle = \oint_S \langle \overleftrightarrow{\mathbf{T}} \rangle \cdot \mathbf{n}(\mathbf{r}) ds, \tag{1.8}$$

with $\langle \cdots \rangle$ denoting the time average. Here $\overleftrightarrow{T}$ is the Maxwell stress tensor, and it is given by

$$\overleftrightarrow{\mathbf{T}} = \left[\epsilon_0 \epsilon \mathbf{E}_{tot} \mathbf{E}_{tot} + \mu_0 \mu \mathbf{H}_{tot} \mathbf{H}_{tot} - \frac{1}{2} (\epsilon_0 \epsilon E_{tot}^2 + \mu_0 \mu H_{tot}^2) \overleftrightarrow{\mathbf{I}} \right]. \tag{1.9}$$

The notation $\mathbf{E}_{tot}\mathbf{E}_{tot}$ denotes the outer product, $E_{tot}^2 = E_x^2 + E_y^2 + E_z^2$ is the electric field strength, and $\overleftrightarrow{I}$ denotes the unit tensor. The expression for H_{tot} is similar.

Similarly, using the Maxwell stress tensor we are able to calculate the net torque applied on the enclosing object [43, 46]

$$\langle \mathbf{N} \rangle = -\oint_S \langle \overleftrightarrow{\mathbf{T}} \times \mathbf{r} \rangle \cdot \mathbf{n}(\mathbf{r}) ds. \tag{1.10}$$

This method is elegant and convenient as no material property of the scattering object is contained in the expression, and the evaluation can be done in the homogeneous surrounding medium. However the electromagnetic scattered field still needs to be solved numerically before hand [44].

1.4. Waveguide mode theory

A waveguide is any structure that directs the propagation of electromagnetic fields along a pre-defined path [47]. The optical waveguides have been predominantly used in today's Internet network infrastructure [48]. To understand the principle of waveguide, one can start from the simplest waveguide structure, which is the planar dielectric waveguide [49]. The mode of the waveguide can be understood by introducing a plane wave which bounces off at the interfaces between the core and the cladding with difference angle, as shown in Fig. 1.6a. If the incident angle is larger than the critical angle, the plane wave will experience total internal reflection, and hence the field is confined in the core area and being propagated along the z-axis. The field in the core can be regarded as the superposition of two complimentary plane waves that propagate upwards and downwards, respectively, as demonstrated in Fig. 1.6c.

For a planar dielectric waveguide, the eigenmodes can be separated in two distinct sets: the TE (transverse electric) modes with single electric field component E_y, and TM (transverse magnetic) modes with single magnetic field component H_y. Without derivation, the TE eigenmodes are given by [47]

$$\text{even modes} : \tan(k_x d) = \frac{\gamma}{k_x}, \tag{1.11}$$

$$\text{odd modes} : \cot(k_x d) = -\frac{\gamma}{k_x}, \tag{1.12}$$

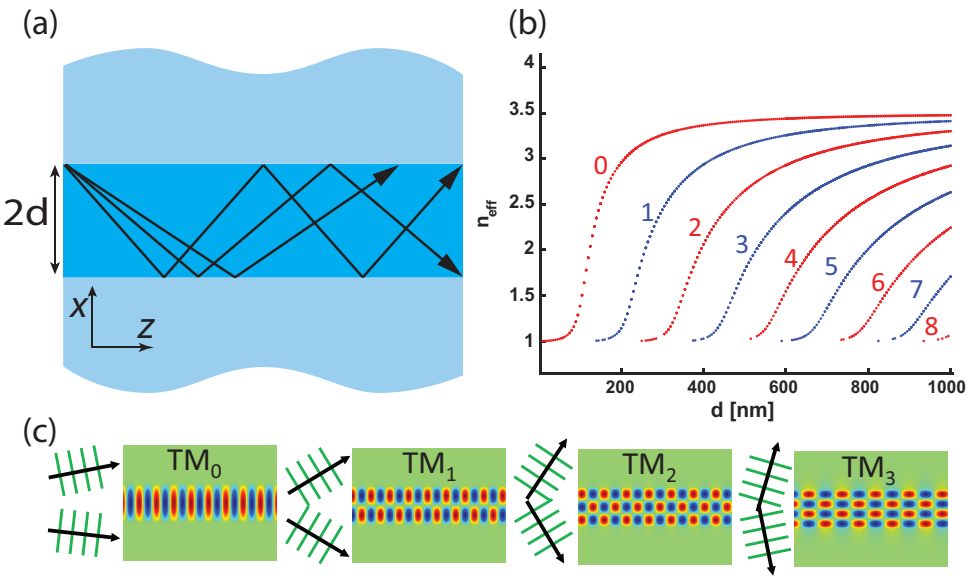

Figure 1.6: (a) Schematics of a planar dielectric waveguide, where the light are confined in the core area by total internal reflection. (b) The calculated effective index of the modes in the waveguide versus half core thickness d. (c) Field distribution the first four TM modes of the waveguide, which can be regarded as the superposition of two complimentary plane waves illustrated on the left.

where d is the half thickness of the core, γ is the decay of the field in the cladding area, and k_x is the wavenumber along x. γ and k_x are defined as:

$$\gamma^2 = \beta^2 - n_{clad}^2 k_0^2, \tag{1.13}$$

$$k_x^2 = n_{core}^2 k_0^2 - \beta^2, \tag{1.14}$$

where β is the propagation constant of the mode, and n_{core} and n_{clad} are the refractive indices of the core and the cladding, respectively.

Similarly the TM eigenmodes are given by [47]

$$\text{even modes} : \tan(k_x d) = \frac{n_1^2 \gamma}{n_2^2 k_x}, \tag{1.15}$$

$$\text{odd modes} : \cot(k_x d) = -\frac{n_1^2 \gamma}{n_2^2 k_x}. \tag{1.16}$$

In Fig. 1.6b, the effective index ($n_{eff} = \beta/k_0$) of the TM mode is plotted as a function of the core thickness at the wavelength of 1550 nm. The materials of the core and the cladding are silicon (Si) and air, respectively. It can be seen that as the thickness of the core increases, the number of modes increases as well. Nevertheless, the fundamental TM mode TM_0 exists for all core thickness, and it is nontrivial to remove this mode from a conventional waveguide structure.

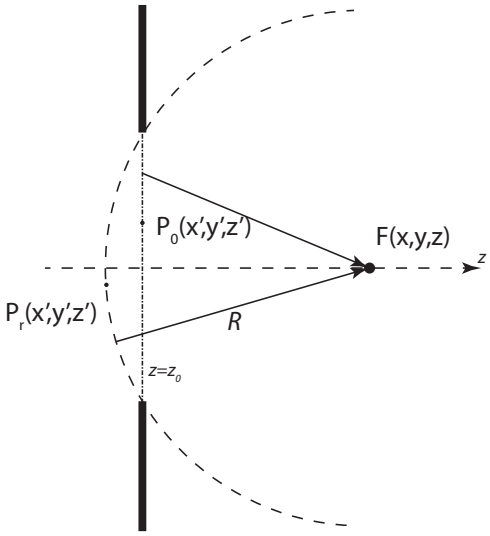

Figure 1.7: Schematic of diffraction integral. The field distribution near point F can be calculated by integrating the field at a arbitrary surface covering the aperture. For example, the integral can be performed by evaluating the field over a surface of $z = z_0$, but can be also performed by evaluating the field over a surface with a constant distance R away from the point F.

1.5. Scalar diffraction integral

The diffraction of light is an important topic for studying electromagnetic wave, such as focusing of light [46]. When light is incidented on an aperture or an opaque screen, the light experiences diffraction. If the aperture is much larger compared to the wavelength of the light, scalar diffraction theory is commonly used for calculating the field after the diffraction interface [50]. Among all diffraction theories, Rayleigh diffraction integral is considered to be the most accurate method within the framework of scalar diffraction theory [51].

Considering the light is scattered by an aperture at $z = z_0$, as shown in Fig. 1.7. The field near a point F which is at a distance much larger than the wavelength of the light is given by

$$U(x,y,z) = \int_S U(x',y',z') \frac{\partial}{\partial \mathbf{n}} \left(\frac{\exp^{ikr}}{r} \right) ds \tag{1.17}$$

where S is an arbitrary surface covering the aperture, $\mathbf{n}$ is the normal vector of the surface, and r is the Euclidean distance from a point $P(x',y'z')$ on the surface S to the position where the field is evaluated. The surface S over which the integral is evaluated is not unique. For example, the integral can be performed by evaluating the field over a surface at $z = z_0$, but can be also performed by evaluating the field over a spherical surface plane with a constant distance R away from the point F.

1.6. Outline of the thesis

As briefly explained before, the main focus of this thesis is to explore the application of uniaxial birefringent optical materials. The composition of the materials can be both natural and artificial. Our investigation methods includes numerical simulation, nano-fabrication and experimental validation. In **Chapter 2**, we demonstrate the application of rutile (TiO_2) nanocylinders for optical tweezers. Rutile has one of the highest birefringence among all naturally occurring crystals in the world. We show that rutile TiO_2 nanocylinders form powerful joint force and torque transducers in aqueous environments. By using only moderate laser powers, $nN \cdot nm$ torques at kHz rotational frequencies can be applied to tightly trapped particles. Moreover, it also demonstrates stable chemical property, making it superior than other birefringent materials like Calcite. The theoretical calculation is then validated by optical experiments. In **Chapter 3**, we demonstrate the application of meta-material birefringent probe for optical tweezer using SiO_2 and Nb_2O_5 multilayer structure. The simulation results show that the proposed structure can achieve a high torque transfer efficiency at only moderate refractive index, indicating its outstanding performance over existing naturally-birefringent probes. Moreover, the ML meta-materials comes with tunability by changing the filling ratio of its composite materials. In **Chapter 4**, we demonstrate the application of hyperbolic birefringent meta-materials in optical waveguide engineering. By using type II hyperbolic material as waveguide cladding, a waveguide which only supports the higher order modes can be achieved. This discovery has a very high potential application in the new Spatial-Division Multiplexing (SDM) optical communication network [52]. In **Chapter 5**, we present a general study of imaging application using hyperbolic meta-materials. The optical lens made of hyperbolic materials are called hyperlens [26], which brings the possibility of super-resolution imaging. However, for simplicity the optical absorption in hyperbolic materials is commonly ignored. Our theoretical results show that the optical loss plays an important role in the optical performance of the hyperlens. Also, we use Rayleigh diffraction integral to evaluate the focusing property of the lens and show a focusing deterioration as the size of the lens increases. Finally **Chapter 6** summarize the main finding of this thesis and future further development of this research is discussed.

References

[1] J. C. Maxwell, *Viii. a dynamical theory of the electromagnetic field,* Philosophical transactions of the Royal Society of London , 459 (1865).

[2] J. D. Jackson, *Classical electrodynamics* (John Wiley & Sons, 1999).

[3] G. I. Stegeman and R. A. Stegeman, *Nonlinear optics: phenomena, materials and devices*, Vol. 78 (John Wiley & Sons, 2012).

[4] G. T. Papadakis, P. Yeh, and H. A. Atwater, *Retrieval of material parameters for uniaxial metamaterials,* Physical Review B **91**, 155406 (2015).

[5] Y. Nakayama, P. J. Pauzauskie, A. Radenovic, R. M. Onorato, R. J. Saykally,

J. Liphardt, and P. Yang, *Tunable nanowire nonlinear optical probe,* Nature **447**, 1098 (2007).

[6] H. C. Hulst and H. C. van de Hulst, *Light scattering by small particles* (Courier Corporation, 1981).

[7] L. Mandel and E. Wolf, *Optical coherence and quantum optics* (Cambridge university press, 1995).

[8] C. C. Montarou and T. K. Gaylord, *Analysis and design of modified wollaston prisms,* Applied optics **38**, 6604 (1999).

[9] S. Ando, T. Sawada, and Y. Inoue, *Thin, flexible waveplate of fluorinated polyimide,* Electronics Letters **29**, 2143 (1993).

[10] K. Hanaoka, H. Yoshida, K. Nakamura, H. Tsuda, and H. Chida, *Color liquid crystal display device using birefringence,* (1996), uS Patent 5,570,211.

[11] S. Nersisyan, N. Tabiryan, D. Steeves, and B. Kimball, *Optical axis gratings in liquid crystals and their use for polarization insensitive optical switching,* Journal of Nonlinear Optical Physics & Materials **18**, 1 (2009).

[12] J. Amako and T. Sonehara, *Kinoform using an electrically controlled birefringent liquid-crystal spatial light modulator,* Applied optics **30**, 4622 (1991).

[13] W. Cai and V. M. Shalaev, *Optical metamaterials*, Vol. 10 (Springer, 2010).

[14] N. I. Zheludev and Y. S. Kivshar, *From metamaterials to metadevices,* Nature materials **11**, 917 (2012).

[15] A. Poddubny, I. Iorsh, P. Belov, and Y. Kivshar, *Hyperbolic metamaterials,* Nature photonics **7**, 948 (2013).

[16] L. Gao, F. Lemarchand, and M. Lequime, *Exploitation of multiple incidences spectrometric measurements for thin film reverse engineering,* Optics express **20**, 15734 (2012).

[17] T. Siefke, S. Kroker, K. Pfeiffer, O. Puffky, K. Dietrich, D. Franta, I. Ohlídal, A. Szeghalmi, E.-B. Kley, and A. Tünnermann, *Materials pushing the application limits of wire grid polarizers further into the deep ultraviolet spectral range,* Advanced Optical Materials **4**, 1780 (2016).

[18] V. M. Agranovich and V. Ginzburg, *Crystal optics with spatial dispersion, and excitons*, Vol. 42 (Springer Science & Business Media, 2013).

[19] Y. Guo, W. Newman, C. L. Cortes, and Z. Jacob, *Applications of hyperbolic metamaterial substrates,* Advances in OptoElectronics **2012** (2012).

[20] S. Jahani and Z. Jacob, *All-dielectric metamaterials,* Nature nanotechnology **11**, 23 (2016).

[21] L. Shen, H. Wang, R. Li, Z. Xu, and H. Chen, *Hyperbolic-polaritons-enabled dark-field lens for sensitive detection,* Scientific reports **7**, 6995 (2017).

[22] S. S. Kruk, Z. J. Wong, E. Pshenay-Severin, K. O'brien, D. N. Neshev, Y. S. Kivshar, and X. Zhang, *Magnetic hyperbolic optical metamaterials,* Nature communications **7**, 11329 (2016).

[23] V. P. Drachev, V. A. Podolskiy, and A. V. Kildishev, *Hyperbolic metamaterials: new physics behind a classical problem,* Optics express **21**, 15048 (2013).

[24] K. V. Sreekanth, Y. Alapan, M. ElKabbash, E. Ilker, M. Hinczewski, U. A. Gurkan, A. De Luca, and G. Strangi, *Extreme sensitivity biosensing platform based on hyperbolic metamaterials,* Nature materials **15**, 621 (2016).

[25] Z. Liu, H. Lee, Y. Xiong, C. Sun, and X. Zhang, *Far-field optical hyperlens magnifying sub-diffraction-limited objects,* science **315**, 1686 (2007).

[26] D. Lu and Z. Liu, *Hyperlenses and metalenses for far-field super-resolution imaging,* Nature communications **3**, 1205 (2012).

[27] Z. Jacob, L. V. Alekseyev, and E. Narimanov, *Optical hyperlens: far-field imaging beyond the diffraction limit,* Optics express **14**, 8247 (2006).

[28] J. Sun, M. I. Shalaev, and N. M. Litchinitser, *Experimental demonstration of a non-resonant hyperlens in the visible spectral range,* Nature communications **6**, 7201 (2015).

[29] Z. Jacob, J.-Y. Kim, G. V. Naik, A. Boltasseva, E. E. Narimanov, and V. M. Shalaev, *Engineering photonic density of states using metamaterials,* Applied physics B **100**, 215 (2010).

[30] K. V. Sreekanth, K. H. Krishna, A. De Luca, and G. Strangi, *Large spontaneous emission rate enhancement in grating coupled hyperbolic metamaterials,* Scientific reports **4**, 6340 (2014).

[31] Y. Wang, H. Sugimoto, S. Inampudi, A. Capretti, M. Fujii, and L. Dal Negro, *Broadband enhancement of local density of states using silicon-compatible hyperbolic metamaterials,* Applied Physics Letters **106**, 241105 (2015).

[32] T. U. Tumkur, J. K. Kitur, C. E. Bonner, A. N. Poddubny, E. E. Narimanov, and M. A. Noginov, *Control of förster energy transfer in the vicinity of metallic surfaces and hyperbolic metamaterials,* Faraday discussions **178**, 395 (2015).

[33] C. Cortes, W. Newman, S. Molesky, and Z. Jacob, *Quantum nanophotonics using hyperbolic metamaterials,* Journal of Optics **14**, 063001 (2012).

[34] X. Ni, S. Ishii, M. D. Thoreson, V. M. Shalaev, S. Han, S. Lee, and A. V. Kildishev, *Loss-compensated and active hyperbolic metamaterials,* Optics express **19**, 25242 (2011).

[35] D. Ji, H. Song, X. Zeng, H. Hu, K. Liu, N. Zhang, and Q. Gan, *Broadband absorption engineering of hyperbolic metafilm patterns,* Scientific reports **4**, 4498 (2014).

[36] P. Lebedev, *Experimental examination of light pressure,* Nuovo Cimento **15**, 195 (1883).

[37] A. Ashkin, J. M. Dziedzic, J. Bjorkholm, and S. Chu, *Observation of a single-beam gradient force optical trap for dielectric particles,* Optics letters **11**, 288 (1986).

[38] A. Ashkin and J. M. Dziedzic, *Optical trapping and manipulation of viruses and bacteria,* Science **235**, 1517 (1987).

[39] J. R. Moffitt, Y. R. Chemla, S. B. Smith, and C. Bustamante, *Recent advances in optical tweezers,* Annu. Rev. Biochem. **77**, 205 (2008).

[40] W. Wright, G. Sonek, and M. Berns, *Radiation trapping forces on microspheres with optical tweezers,* Applied Physics Letters **63**, 715 (1993).

[41] Y. Harada and T. Asakura, *Radiation forces on a dielectric sphere in the rayleigh scattering regime,* Optics communications **124**, 529 (1996).

[42] C. Rockstuhl and H. P. Herzig, *Rigorous diffraction theory applied to the analysis of the optical force on elliptical nano-and micro-cylinders,* Journal of Optics A: Pure and Applied Optics **6**, 921 (2004).

[43] P. H. Jones, O. M. Maragò, and G. Volpe, *Optical tweezers: Principles and applications* (Cambridge University Press, 2015).

[44] J. Li and X. Wu, *Fdtd simulation of trapping nanowires with linearly polarized and radially polarized optical tweezers,* Optics express **19**, 20736 (2011).

[45] T. Fujioka, *A new anisotropic correction to the formula of force and torque on materials,* International Journal of Applied Electromagnetics and Mechanics **14**, 23 (2002).

[46] L. Novotny and B. Hecht, *Principles of nano-optics* (Cambridge university press, 2012).

[47] D. Marcuse, *Light transmission optics* (Van Nostrand Reinhold New York, 1972).

[48] H. Zang, J. P. Jue, B. Mukherjee, *et al.*, *A review of routing and wavelength assignment approaches for wavelength-routed optical wdm networks,* Optical networks magazine **1**, 47 (2000).

[49] T. Rozzi, *Rigorous analysis of the step discontinuity in a planar dielectric waveguide,* IEEE Transactions on Microwave Theory and Techniques **26**, 738 (1978).

[50] *Scalar diffraction theory,* in *Electromagnetic Theory for Microwaves and Optoelectronics* (Springer Berlin Heidelberg, Berlin, Heidelberg, 2008) pp. 621–672.

[51] J. J. Braat, S. van Haver, A. J. Janssen, and P. Dirksen, *Assessment of optical systems by means of point-spread functions,* Progress in optics **51**, 349 (2008).

[52] H. Chen, R. van Uden, C. Okonkwo, and T. Koonen, *Compact spatial multiplexers for mode division multiplexing,* Optics express **22**, 31582 (2014).

2

Enhanced linear and angular optical trapping using single-crystal rutile TiO_2 nanocylinders

Optical trapping of (sub)micron-sized particles is broadly employed in nanoscience and engineering. The materials commonly employed for these particles, however, have physical properties that limit the transfer of linear or angular momentum (or both). This reduces the magnitude of forces and torques, and the spatiotemporal resolution, achievable in linear and angular traps. Here, we overcome these limitations through the use of single-crystal rutile TiO_2, which has an exceptionally large optical birefringence, a high index of refraction, good chemical stability, and is amenable to geometric control at the nanoscale. We show that rutile TiO_2 nanocylinders form powerful joint force and torque transducers in aqueous environments by using only moderate laser powers to apply $nN \cdot nm$ torques at kHz rotational frequencies to tightly trapped particles. In doing so, we demonstrate how rutile TiO_2 nanocylinders outperform other materials and offer unprecedented opportunities to expand the control of optical force and torque at the nanoscale.

Parts of this chapter have been published in: Seungkyu Ha*, **Ying Tang***, Maarten M. van Oene, Richard Janissen, Roland M. Dries, Belen Solano, Aurèle J. L. Adam, and Nynke H. Dekker, "Single-Crystal Rutile TiO_2 Nanocylinders are Highly Effective Transducers of Optical Force and Torque", ACS Photonics, **6**, 1255 (2019) [1]. (*equal contribution)

2.1. Introduction

The ability of optical tweezers to apply torque to, and thereby control the rotation of, micron-scale (or smaller) particles [2, 3] complements their well-known control of force and position and provides the opportunities for diverse novel applications at the nanoscale. For example, in biological physics, angular optical tweezers have been utilized in single-molecule torque spectroscopy [4, 5], rotational microrheology [6], and in the manipulation of cellular growth dynamics [7]. In quantum physics, rotational optomechanical effects within angular optical traps [8] are under active investigation. And in engineering applications, angular optical tweezers enable optically-driven microfluidic actuators such as micro-gears [9] and fluidic pumps [10].

Linear optical tweezers achieve stable 3D-trapping of either dielectric or metal particles using Gaussian (TEM_{00}) beams, and have been extensively described [11]. To achieve additional angular optical control, specialized forms of laser beams or trapping particles (or both) are required [5]. One of the most practical implementations for angular optical tweezers makes use of a linearly polarized Gaussian beam together with optically anisotropic (i.e., birefringent) dielectric particles [12–16]. This choice of beam enables straightforward control of torque and angle [13, 16] while obviating mode changes (e.g., into the Laguerre-Gaussian mode) [17] or modulation of the laser beam power [18]. While metal particles have been successfully trapped and rotated [19, 20], the use of dielectric particles presents several advantages. Firstly, torque detection is direct because only dielectric materials have transmitted light components that are proportional to the transfer of angular momentum [15]. Secondly, highly transparent dielectric materials do not suffer from the extreme heating of absorptive metals [21]. Thirdly, the reduced light scattering from dielectric materials relative to metals is more favorable for three-dimensional (3D) trapping. Extensive scattering from metals destabilizes axial trapping, and hence metal particles with dimensions exceeding a few hundred nanometers support only two-dimensional (2D) trapping [19, 20]. Finally, unlike inherently isotropic metals, optically anisotropic dielectric crystals make it possible to simultaneously confine all three rotational degrees of freedom (RDOF), which is advantageous for high-accuracy sensing applications. Among the wide range of dielectric materials, uniaxial crystals such as quartz SiO_2 have been popular choices due to their well-defined refractive index (n), birefringence (Δn), and optic axis [5].

Nonetheless, the full potential of combined linear and angular optical manipulation using dielectric force and torque transducers has not been achieved due to the limited performance offered by conventional dielectric materials. For example, quartz SiO_2 has a relatively low index of refraction ($n = 1.54$) that limits the efficient transfer of linear momentum (and hence the achievable maximum force [22, 23]), as well as a low birefringence ($\Delta n = 0.009$) that prohibits the efficient transfer of angular momentum (limiting the achievable maximum torque). Other materials, e.g., vaterite or calcite $CaCO_3$, have higher birefringence ($\Delta n = 0.1$ or $|\Delta n| = 0.16$, respectively), but a similarly low refractive index ($n = 1.6$ or $n = 1.56$, respectively) [3, 24]. Attempts to overcome these material limitations have come with adverse side effects. For example, one may compensate for inefficient momentum

transfer by increasing the power (and hence the momentum) in the input beam, but this enhances the risk of photodamage in biological applications[25]. Alternatively, one may employ larger particles to achieve higher force and torque, but the increased frictional drag will decrease the achievable spatiotemporal resolution in these parameters (and their conjugate variables, position and angle) [26].

Rutile TiO_2 has several key features that make it a highly propitious candidate for overcoming these drawbacks. To start, rutile TiO_2 exhibits the highest birefringence ($\Delta n = 0.26$) [27] of all known naturally occurring dielectric crystals, ~29-fold larger than that of quartz SiO_2. Next, its refractive index ($n = 2.6$) [27] is one of the largest among dielectric crystals, comparable to that of anatase TiO2 ($n = 2.5$) [27], previously selected to demonstrate the generation of very large optical forces [23], and again much larger than that of quartz SiO_2. Furthermore, rutile TiO_2 in its pure single-crystalline form can be maintained at the nanoscale level via top-down fabrication [28]. This makes it possible to harness its full nominal birefringence and optical index, without any of the reduction observed in porous poly-crystalline structures prepared by bottom-up processes [29, 30]. Lastly, rutile TiO_2 has demonstrated bio-compatibility and bio-functionalizability and is chemically, mechanically, and thermally stable [28]. This means that it may be employed under tougher conditions (e.g., high pressure, high temperature, or prolonged exposure to aqueous and biological environments) relative to other birefringent materials such as $CaCO_3$ (which dissolves in aqueous environments [24]).

Here, we demonstrate how these favorable properties collectively render rutile TiO_2, when shaped into nanocylinders, into an ideal, joint transducer of optical force and torque. To do so, we show that single-crystal rutile TiO_2 nanocylinders, even those with larger volumes, can be trapped in 3D using moderate laser powers, with no need for secondary antireflection coatings [23] or modified optics [22, 31]. We then perform measurements of differently sized nanocylinders in an optical torque wrench (OTW) [14] to quantify the applied forces and torques, which show excellent agreement with numerical calculations based on finite element methods (FEM). This allows us to show that tightly trapped rutile TiO_2 nanocylinders outperform other available dielectric materials by sustaining $\mathrm{pN \cdot nm}$ torques at kHz rotational frequencies in aqueous environments. This, together with the excellent joint resolution in force, torque and their conjugate variables (exceeding 1 pN and 1 nm; $1\ \mathrm{pN \cdot nm}$ and 1 degree) achieved, expands our control of forces and torques at the nanoscale.

2.2. Methods

2.2.1. Fabrication and surface functionalization of rutile TiO_2 nanocylinders.

To produce rutile TiO_2 nanocylinders (Fig. 2.1d), we use our developed top-down fabrication protocol (more details can be found in Ref. [28]). We use a high-quality (100) single-crystal rutile TiO_2 substrate (1 cm×1 cm, ~500 μm thickness, MTI Corp.). The optic axis is precisely aligned in every produced nanocylinder, using the (100) crystal orientation in which the optic axis is perpendicular to the substrate

surface normal. This configuration allows the precise angular manipulation around z-axis, with a trapping beam linearly polarized in xy-plane (as depicted in Fig. 2.1e). Compared to our previously reported fabrication protocol [28], we further optimized the chromium mask shape and thickness to obtain more circular cross sections and smaller taper angles (see details in Supplementary Fig. 2.14). The steps in the nanofabrication protocol that control nanocylinder diameter and height are electron-beam lithography (EBPG 5000 or EBPG 5200, Vistec) and plasma etching (Fluor Z401S, Leybold Heraeus or Plasmalab System 100, Oxford Instr.), respectively. As shown in Supplementary Table 2.1, this optimization leads to excellent structural uniformity among the fabricated TiO_2 nanocylinders (relative standard deviation 2–8% for diameters and 0.1–1.5% for heights, measured for 5–15 particles per batch), as deduced from the SEM images (S4800 FESEM, Hitachi) (Supplementary Fig. 2.8). As a result, our nanoparticles more closely resemble ideal cylinders and display more reproducible behavior. Otherwise, for example, deviations in the taper angle can lead to a substantial change in the trap stiffness (Supplementary Fig. 2.10).

To increase the probability of trapping single isolated nanocylinders in OTW measurements, it is crucial to prolong the monodispersed status of the nanocylinders in aqueous solution. For this purpose, the nanocylinders are coated with amino-terminated monofunctional polyethylene glycol (NH2-PEG) molecules (MW 5000, PEG1154, Iris Biotech) via epoxysilane linkers (3-Glycidoxypropyldimethylethoxysilane, 539260, Sigma-Aldrich) using our previously developed TiO_2 surface functionalization protocol [28]. The PEGylated nanocylinders are mechanically cleaved in phosphate buffered saline (PBS) buffer (pH 7, Sigma-Aldrich) droplets by scratching the substrate surface with a sharpened home-made plastic blade. The plastic blade is softer than the TiO_2 substrate and minimizes the production of TiO_2 dust particles. We note that the presence of short PEG molecules does not affect the trapping and rotational dynamics of our nanocylinders [21], and have observed that the monodispersity of PEGylated TiO_2 particles is maintained upon sonication and vortexing, even after year-long storage (in plastic tubes at 4 °C).

2.2.2. OTW setup and measurements.

We conducted OTW experiments with our home-built setup (1064 nm wavelength single-beam optical trap with polarization control; more details can be found in Refs. [14, 15, 28]). We use a custom-made flow cell assembled with two borosilicate glass coverslips (No. 1.5H, Marienfeld) separated by a single-layer Parafilm® spacer of ∼100 µm thickness. The use of coverslips with high-precision thickness (170 µm±5 µm for No. 1.5H) reduces possible variations in optical trap quality that might occur when the conventional coverslips with large thickness variation (e.g., 160–190 µm for No. 1.5) are used [32]. The PBS buffer containing the nanocylinders are injected into the flow cell channel and both input and output of the channel are sealed by vacuum grease (18405, Sigma-Aldrich). After $\sim$ 1 h, most of the nanocylinders in the solution are sedimented to the bottom of the flow cell. Among these nanocylinders, only a chosen nanocylinder can be lifted from the bottom by focusing the laser beam on the particle to generate a pushing force via light scattering. Using rutile TiO_2 is beneficial in this lifting process because its large

refractive index induces stronger scattering for a given laser power. Afterwards, we can trap and measure the freed nanocylinder without any hydrodynamic coupling effect that can occur if the particle concentration is too high [33]. Also, it is possible to measure for extended times (tested up to ~3 h) without losing the particle by collision with other particles entering the optical trap. The nanocylinder trapping position is kept as 18–20 μm above the bottom surface of the flow cell channel, to effectively avoid any hydrodynamic interaction with the flow cell.

We measured 14 different rutile TiO_2 nanocylinder batches (Supplementary Table 2.1), and 3–10 particles were recorded for each trappable batch (Fig. 2.3, Supplementary Fig. 2.12, Supplementary Table 2.2). For calibration of linear and angular trapping properties, we adapted the previously developed methods [15, 34]. For measurement of linear and angular fluctuations of a trapped cylinder, we employed an input beam which is linearly polarized along the x-axis. The large radial stiffness of the rutile TiO_2 particles lead to hydrodynamic effects, which contribute colored noise to the power spectrum [23, 35]. We have considered this in our analysis (Supplementary Fig. 2.14). The linear and angular fluctuation data are acquired at 250 kHz sampling frequency. We developed and employed an improved method to more precisely measure torque-speed curves (Supplementary Fig. 2.14). In our method, each curve is measured by continuously scanning the polarization rotation frequency in the range of 0–15 kHz for a few seconds using a waveform generator (33120A, Agilent), with 100 kHz sampling frequency. Compared to the conventional time-consuming method in which separate torque traces are recorded at multiple different frequency values, this high-speed recording over a wide frequency range avoids the distortion of the measured curve caused by setup drift. The downward spikes shown at high PRF in Fig. 2.3g,h are attributed to the peculiarities of the setup, such as the finite time required for the polarization reversal of electro-optic modulator (EOM) voltage [13, 16], and appear regardless of the chosen torque-speed measurement method.

In addition, we measured linear trapping properties of PS microspheres (Polybead® Microspheres, Polysciences) (Fig. 2.3c, Supplementary Fig. 2.12, Supplementary Table 2.3) since they are one of the de facto standards among optical trapping community. In general, the characteristics of optical traps are not identical among different optical tweezers due to the difference in the specifications of the laser beam, objective lens, immersion medium, and flow cell design. Therefore, comparing the results from the standard commercial PS beads with high compositional and geometrical uniformity provides a means with which experimentalists can estimate the expected trapping properties of rutile TiO_2 nanocylinders in their own instruments.

2.2.3. Numerical calculation of optical momentum transfer and hydrodynamic drag.

The cylindrical geometry and anisotropic optical property of our rutile TiO_2 particles require a numerical approach to precisely estimate their viscous drag coefficients and optical trapping force and torque. It is because the exact analytical solutions do not exist for anisotropic cylinders with arbitrary aspect ratios, unlike the commonly

used isotropic spherical probes. We utilize FEM [36] with one of its commercial implementations (COMSOL Multiphysics v5.2a, COMSOL Inc.). In general, FEM is more computationally demanding than other approaches such as T-matrix formulations [37]. However, it is more flexible and versatile in the aspect of modeling anisotropic material and irregular geometry. Using FEM is straightforward even with cylinders of small aspect ratio and exotic shapes such as tapered cylinders (Supplementary Fig. 2.10), cones, and hour-glass shapes. The validations of our numerical models are shown in Supplementary Fig. 2.14. We note that the properties (size, density, quality, etc.) of geometry meshing in FEM models should be optimized properly to obtain precise results.

To calculate linear and angular optical trapping properties, we locate a rutile TiO_2 nanocylinder at the center of the calculation domain. The cylinder is enclosed by a uniform medium (water, $n = 1.33$) of spherical shape, and the medium is terminated with a perfect matching layer to treat the size of the medium as infinite by coordinate transformation. We use the exact focus beam equation without any approximations to calculate the input background field [38]. The beam shape is defined by the vacuum wavelength ($\lambda = 1064$ nm), objective lens numerical aperture (NA=1.2), filling ratio ($\alpha = \infty$ or 1.7), linear polarization direction (along x-axis), and index of medium ($n = 1.33$). Here, the filling ratio α (=w_0/r_0) is defined as the ratio of the $1/e^2$ radius of input beam w_0 and effective input aperture radius of objective lens r_0 (= $f\ NA$, where f is the focal length of the objective lens). We use $\alpha = \infty$ as an ideal configuration in which input beam is a plane wave, and $\alpha = 1.7$ as the measured value in our OTW setup. The time-averaged optical force and torque on the cylinder is obtained by integrating the Maxwell stress tensor over the surface of a virtual sphere enclosing the cylinder [39]. We first obtain the axial force (Fz) curves, from which the axial equilibrium trapping positions (z_{eq}) are derived (Supplementary Fig. 2.9). Then we calculate radial force (F_x, F_y) and maximal torque (τ_0) at z_{eq}. The optical force is calculated at the zero-torque condition ($\theta = 0°$ in Eq. 2.1), while the torque is calculated at the maximum torque transfer condition ($\theta = 45°$ in Eq. 2.1).

To calculate hydrodynamic drag coefficients, the surrounding medium (water at 23 °C, dynamic viscosity of 0.933 mPa · s) is set to flow translationally (rotationally), inducing viscous drag force (torque) on the nanocylinder. The solutions of Navier-Stokes equations [40] result in force and torque as a function of the speed of medium flow, from which the drag coefficients can be extracted. We calculated two translational (axial, radial) and one rotational (around z-axis) drag coefficients: i) for each ideal cylinder (Supplementary Fig. 2.11) to use in calculations of angular speeds (Fig. 2.2d, Supplementary Fig. 2.13) and AD values (Supplementary Fig. 2.13), ii) for each fabricated nanocylinder batch (Supplementary Fig. 2.12) to compare with our experimentally obtained values. For the case of ideal cylinders, like ideal spheres [41], analytical expressions for the translational [42] and rotational [43] viscous drag exist. However, these are valid for only a limited range of aspect ratios and hence we used our numerical approach.

2.3. Results and discussion

2.3.1. Optimization of rutile TiO_2 particle geometry

In this section, we describe the optimization of rutile TiO_2 nanoparticle geometry for optical trapping. First, we describe how particle selection based on height can maximize the efficiency of birefringence-based torque transfer, for which the exceptionally high birefringence of rutile TiO_2 is advantageous. Then we discuss how the high refractive index of rutile TiO_2 enhances the applied force compared to other commonly-used dielectric materials. Finally, we show that a cylindrical geometry permits improved 3D trapping and full RDOF confinement.

Large birefringence for optimal angular momentum transfer.

The optical torque τ that a linearly polarized beam can apply to a birefringent particle with uniform thickness is given by:

$$\tau = -A \sin(hk_0\Delta n) \sin(2\theta), \tag{2.1}$$

where $A = S\epsilon_0 nc(E_0)^2/(2\omega)$ and S is the particle cross-sectional area, ϵ_0 is the vacuum permittivity, $n = (n_e + n_o)/2$ is mean of the particle's optical indices along the extraordinary (n_e) and ordinary (n_o) axes, c is the speed of light in vacuum, E_0 is the electric field amplitude of light in the particle, and ω is the angular frequency of the input beam. In the first sine term, h is the particle height along the direction of beam propagation, k_0 is the wavenumber of the input laser beam in vacuum, and $\Delta n = n_e - n_o$ is the particle's birefringence. The torque is modulated according to the offset angle θ between the input beam linear polarization direction and the particle optic axis as described by the second sine term, and thus the maximal torque $\tau_0 = A \sin(hk_0\Delta n)$ appears at $\theta = \pm 45°$. **Note that Eq. 2.1 does not precisely describe the torque experienced by nanoparticles trapped at a beam focus (Supplementary Fig. 2.5), as it is derived in the context of a plane wave that imparts angular momentum to an infinitely wide plate (Appendix A).** Nonetheless, Eq. 2.1 provides a reasonable starting point for torque transducer design.

As Eq. 2.1 shows, for a given particle material, the particle height h can be optimized to maximize the torque transfer efficiency. For materials with low birefringence, the optimal particle height is excessively large (e.g., ~30 μm for quartz SiO_2). This size scale not only presents a challenge to fabrication but also far exceeds the favorable particle size range for stable 3D trapping in typical single-beam optical tweezers, i.e., <~1 μm, below the size of a tightly focused beam. The conventional torque transducers of heights ~1μm [12, 14, 24] are made of low birefringence materials and cannot transfer the full angular momentum carried by the laser beam (Fig. 2.1a). However, in the case of rutile TiO2 with its exceptionally large birefringence, a torque transfer efficiency of 100 % should be achievable for 1-micron particles (Fig. 2.1a).

The ability to reach larger maximal torques (τ_0) for smaller particles (i.e., particles with lower rotational drag γ_θ) has several implications for optical torque transducers. (i) The faster maximal rotation speed ($f_0 = \tau_0/(2\pi\gamma_\theta)$) allows access to a

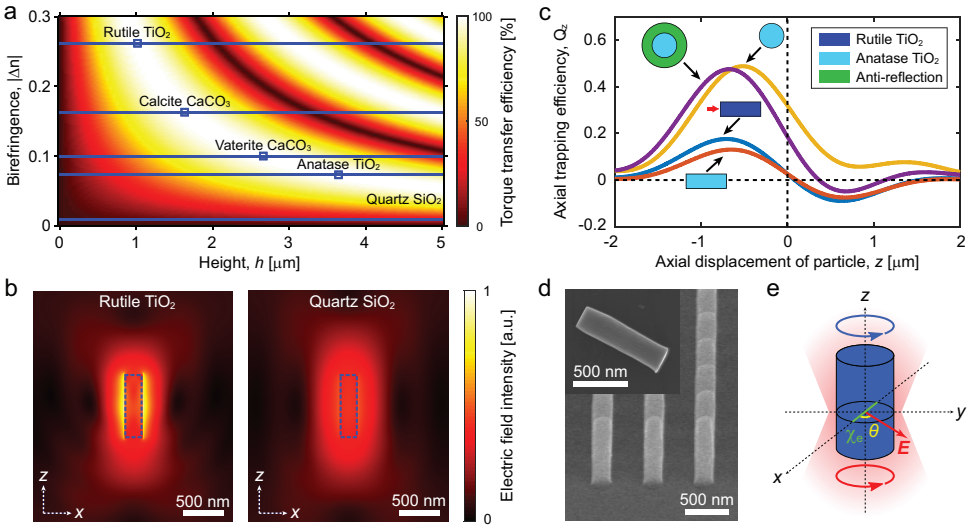

Figure 2.1: Design principles for force and torque transducers in optical tweezers. (a) Map of the torque transfer efficiency ($|\sin(hk_0\Delta n)| \times 100$; derived from Eq. 2.1) as a function of particle height (h) and birefringence ($|\Delta n|$) of different dielectric materials. The blue squares indicate the smallest particle heights at which 100 % torque transfer efficiency can be achieved (~30 μm for quartz SiO_2). (b) FEM-calculated electric field intensity around nanocylinders (blue dashed line) made of different materials, located at the laser beam focus ($z = 0$) in water. (c) FEM-calculated axial trapping efficiency (Q_z) curves for various TiO_2 nanoparticle geometries at fixed volumes. An anatase TiO_2 ($n = 2.3$; light blue) sphere ($d = 430\ nm$) cannot be trapped in 3D, but it becomes trappable upon the addition of an anti-reflection coating (green), or when reshaped (at constant volume) into a cylinder ($d = 220\ nm$, AR = 5). A rutile TiO_2 ($n = 2.6$; dark blue) cylinder with the same dimensions is also trappable. The trapping orientation of each cylinder with respect to the beam propagation direction (red arrow) is as drawn. (d) SEM micrograph (60° tilted view) of a fabricated rutile TiO_2 nanocylinder batch prior to mechanical cleaving. The inset shows a cleaved single nanocylinder. (e) Experimental scheme of the OTW. The x, y, and z axes are in the reference frame of the nanocylinder, which has the optic axis along the x-axis (as indicated by the extraordinary electric susceptibility χ_e). The laser beam propagates along the z-axis and the optical gradient force traps the nanocylinder in 3D. When a nonzero offset angle θ exists between the optic axis and the direction of the input beam linear polarization (electric field vector E in the xy-plane), the optical torque is applied on the nanocylinder.

larger torque-speed space. (ii) The increased angular trap stiffness ($\kappa_\theta = 2\tau_0$) and low drag improve measurement precision for both torque and angle, as they are proportional to $(\gamma_\theta)^{1/2}$ and $(\gamma_\theta)^{1/2}/\kappa_\theta$, respectively [26]. (iii) The shorter angular trap relaxation time ($t_{c,\theta} = \gamma_\theta/\kappa_\theta$) results in enhanced temporal resolution [26].

Large refractive index results in enhanced linear momentum transfer.

Compared to conventional dielectric materials employed in angular trapping such as quartz SiO_2, vaterite $CaCO_3$, and calcite $CaCO_3$ ($n = 1.5$–1.6), rutile TiO_2 possesses a substantially larger optical index ($n = 2.6$ on average) [27]. This implies a larger index difference with the surrounding medium (e.g., water, $n = 1.33$) and correspondingly stiffer linear trapping [22, 23]. This can be visualized through FEM calculations (Fig. 2.1b), which show more intense scattering at the interface be-

tween the particle and the medium that leads to a higher field gradient and hence an enhanced trapping force. Thus, the use of rutile TiO_2 enhances the transfer of not only angular but also linear momentum. This simultaneous enhancement is unique to rutile TiO_2, as other materials that have high birefringence possess only low refractive indices (e.g., calcite $CaCO_3$).

Cylindrical shape for stable 3D trapping.

The advantage of being able to generate high forces comes at a cost, as a higher index mismatch leads to increased scattering. This implies that radiation pressure from the incident laser beam is more likely to perturb axial trapping. Therefore, 3D trapping of high-index particles in single-beam optical traps is limited to those smaller than a certain threshold size, which is determined by the material and the particle geometry. To compensate for the adverse effect of scattering on trapping, diverse solutions have been developed. One solution is to alter the optical configuration by implementing counter-propagating beams [22] or a donut-shaped beam [31] for trapping. Another solution is to modify the particle by introducing an anti-reflection coating [23]. However, this increased sophistication in optical configuration or fabrication prevents its straightforward wide-spread implementation.

Instead, we can overcome the adverse effects of scattering by using a cylindrical shape for rutile TiO2 nanoparticles, as shown for previously described dielectric torque transducers [12–16]. This geometry decreases light scattering for a fixed volume of a particle by reducing the surface area encountered by the input laser beam. This effect is explicitly demonstrated by our numerically calculated trapping force curves comparing differently shaped high-index particles (Fig. 2.1c). Our FEM calculations show that rutile TiO2 spheres cannot be trapped in 3D if their diameter exceeds ~346 nm (Supplementary Fig. 2.6), in agreement with previously reported calculations [37]. However, as we describe in detail below, we use an OTW to demonstrate stable 3D trapping of fabricated rutile TiO2 nanocylinders (Fig. 2.1d,e) with volumes that exceed the volume threshold for the trappability of spheres. Having an increased range of trappable particle volumes available allows the application of increased force or torque. Furthermore, the omission of antireflection coatings reduces drag and thus improves the achievable maximum angular speed, temporal resolution, and measurement precision.

The use of cylindrically shaped rutile TiO_2 nanoparticles includes another important advantage, namely the full confinement of the three RDOF. For a positive or negative uniaxial birefringent sphere, the birefringence-originated torque constrains only two or one RDOF. This has the drawback that unconstrained RDOF may introduce unexpected angular fluctuations into torque and angle signals. The geometrical anisotropy provided by a non-spherical particle shape such as a cylinder can avoid these complications (Supplementary Fig. 2.7) and is hence a requirement for certain applications, e.g., high-precision single-molecule torque spectroscopy.

2.3.2. Linear and angular trapping of TiO_2 nanoparticles

Dimensions of rutile TiO_2 nanocylinders trappable in 3D.

We fabricated multiple rutile TiO_2 nanocylinder batches (Methods) with different diameters d=150–400 nm and heights h=0.5–1.5 μm, with resulting aspect ratios (AR=h/d) ranging from 2.5 to 6.5 (Supplementary Fig. 2.8; precise dimensions measured by scanning electron microscopy (SEM) are shown in Fig. 2.2 and Supplementary Table 2.1). We first tested whether these particles could be optically trapped in 3D in an aqueous environment (Methods), because stable 3D trapping is a prerequisite for the application of force and torque. We experimentally observed that rutile TiO_2 cylinders with small diameters (160–230 nm) could be stably trapped (T1–T7 in Fig. 2.2), even though their volumes are similar to or larger than that of the largest rutile TiO_2 sphere predicted to be trappable. In contrast, cylinders with diameters exceeding ~260 nm (U1–U6 in Fig. 2.2) were not trappable in 3D, but rather scattered away from the trap. Therefore, we defined an experimental threshold diameter d^*_{exp} for the trappability of the rutile TiO_2 cylinders as a function of their AR. For each AR, d^*_{exp} falls within the range 230–260 nm.

The behaviour of individual particles within cylinder batches is consistent with this transition. For example, the mean diameter of cylinder batch T8 (AR = 4.4) is 256 nm±10 nm (Fig. 2.2a). While most cylinders from this batch were not trappable or could be trapped only temporarily (with particles exiting the trap within seconds or minutes), a few were stably trapped for hours. Such behavior is expected if a small fraction of the batch has diameters that fall below d^*_{exp}.

We compare these and subsequent findings with FEM calculations (Methods). The calculated axial stiffness (κ_z) map (Fig. 2.2a; other calculated linear trapping parameters are described in Supplementary Fig. 2.9), where black pixels indicate untrappable cylinder dimensions, reveals a higher threshold range for trappability, $d^*_{cal} \approx 255\text{–}315\ nm$, defined as the minimum diameter which results in a black pixel for each aspect ratio. A few experimental factors that have not been considered in the calculations could explain the mismatch between the trappable cylinder dimensions found by experimental and numerical approaches. For example, cylinder batch U1 lies in a trappable regime of the calculated map but is experimentally untrappable. The calculations for the maps shown in Fig. 2.2 incorporate the objective lens aperture filling ratio ($\alpha = 1.7$, Methods; Supplementary Fig. 2.10). However, they do not account for optical aberrations (see also section 2.2.2.) and, for a given cylinder geometry, they assume zero taper angle, whereas trapping behaviors are largely dependent on taper angle (Supplementary Fig. 2.10).

We have also calculated maps of the radial stiffness (κ_y; Fig. 2.2b), the angular stiffness (κ_θ; Fig. 2.2c), and the maximal rotation rate ($f_0 = (\kappa_\theta/2)/(2\pi\gamma_\theta)$; Fig.2.2d, obtained using FEM-calculated drag coefficients (γ_θ; Supplementary Fig. 2.11) and angular stiffnesses (κ_θ; Fig. 2.2c), which we compare to our experimental results in the next subsections.

Rutile TiO_2 nanocylinders optimized for high stiffness, low drag, and rapid response time.

The stiffness and drag are the two primary physical parameters that describe the behavior of optically trapped particles [26]. Therefore, we experimentally determined the trap stiffness (linear and angular) and the corresponding drag coefficient

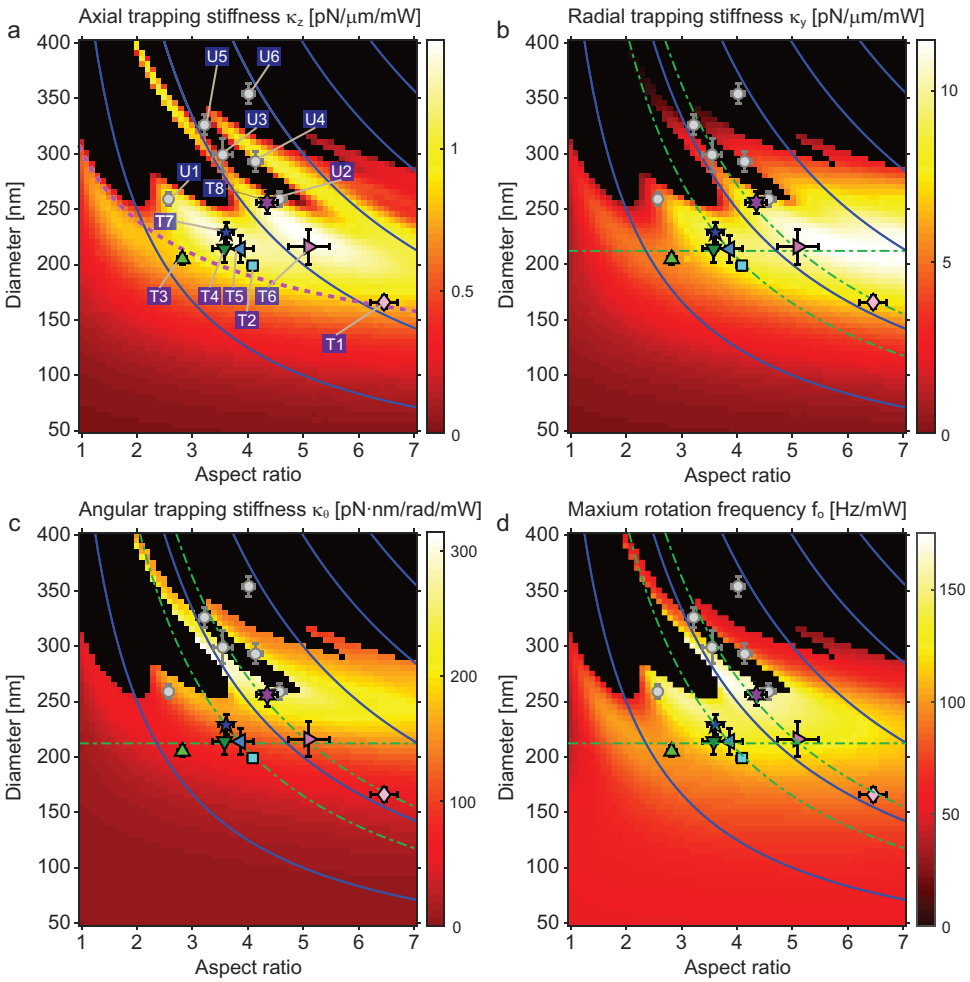

Figure 2.2: Calculated maps of linear and angular stiffness for rutile TiO_2 nanocylinders of varying dimensions, with experimentally assessed trappability per cylinder batch superimposed. (a-c) FEM-calculated (a) axial (κ_z), (b) radial (κ_y), and (c) angular (κ_θ) stiffness maps of rutile TiO_2 nanocylinders. The stiffness values are calculated with the zero-taper angle for each cylinder dimension and the measured aperture filling ratio ($\alpha = 1.7$) from our OTW setup, and normalized by the input beam power. (d) Maximum rotation frequency ($f_0 = \tau_0/(2\pi\gamma_\theta)$) map of rutile TiO_2 nanocylinders obtained from FEM-calculated maximum torque ($\tau_0 = \kappa_\theta/2$; derived from data in panel (c)) and drag (γ_θ; Supplementary Fig. 2.11). In panel (a), the region above the dashed magenta curve includes nanocylinders with volumes exceeding that of the largest trappable rutile TiO_2 sphere with $d \approx 346$ nm. In panels (b-d), dimensions relevant for the analysis in Fig. 2.3 are displayed: the horizontal dash-dotted green line represents $d \approx 213$ nm; the leftmost dash-dotted green curve represents $h \approx 825$ nm; and the rightmost dash-dotted green curve represents $h \approx 1096$ nm. In all panels, the maps are plotted as a function of the cylinder aspect ratio ($AR = 1$–7, with step size 0.1) and the cylinder diameter ($d = 100$–400 nm, with step size 5 nm). The black pixels indicate cylinders with untrappable dimensions (for which axial stiffnesses cannot be calculated). The solid blue curves are iso-height contours (500–2500 nm from left to right, with a step size of 500 nm). Trappable fabricated cylinder batches (labeled as T1–T8) are indicated by distinct symbols and colors. Untrappable fabricated cylinder batches (labeled as U1–U6) are shown as gray filled circles. Symbols and error bars denote the averages and standard deviations of the SEM-measured cylinder dimensions, respectively (N=5–10; Supplementary Table 2.1).

for each trappable rutile TiO_2 cylinder batch, with the results summarized in Fig. 2.3. We used laser powers less than 100 mW to demonstrate the high performance of rutile TiO_2 cylinders even in the low-power regime. However, we present the trapping stiffness normalized by laser power for comparison with other studies. To highlight the effect of geometrical parameters, the experimental stiffness values are plotted as a function of diameter or height at a fixed height or diameter in Fig. 2.3a,b,d,e. In Fig. 2.2b-d, the dash-dotted green lines represent the fixed heights $h \approx 1096$ nm and $h \approx 825$ nm, and the fixed diameter $d \approx 213$ nm. The results of FEM calculations based on mean particle geometries (with actual sidewall profiles as quantified by SEM and displayed in Supplementary Fig. 2.8) are co-plotted in Fig. 2.3a,b,d,e for comparison. In the case of linear trapping, we display the trapping parameters as measured in the y-dimension. Because the input beam is polarized along the x-dimension (Methods), trapping is strongest along the y-dimension (twofold and tenfold stronger than trapping in the $x-$ and z-dimensions, respectively; Supplementary Fig. 2.9). Overall, increases in either cylinder diameter (Fig.2.3a,d) or height (Fig.2.3b,e) that enhance the light-matter interaction volume tend to result in greater linear and angular trap stiffnesses. Particularly, for angular trapping, an increased cylinder diameter at a fixed height corresponds to a wider cross-sectional area S in Eq. 2.1, and hence also a higher value of the angular stiffness (Fig. 2.3d). For a fixed diameter, taller cylinders yield increased angular stiffness, until saturation occurs close to the height h in Eq. 2.1 for optimal torque transfer (Fig. 2.3e). These trends agree very well with the FEM-based predictions. Exact quantitative agreement between the experimental observations and FEM predictions is achieved upon scaling the calculated stiffnesses by $42\% \pm 14\%$ (Supplementary Fig. 2.12), which we attribute to optical aberrations that distort the electric field distribution at the beam focus [44], an experimental limitation that is challenging to include in calculations. The measured drag coefficients, which are not similarly influenced by aberrations, equal $104\% \pm 17\%$ of the values calculated by FEM (Supplementary Fig. 2.12), implying high accuracy of our calibrated measurements.

The ratio of the measured drag (Methods) and stiffness reports on the response times of trapped rutile TiO_2 cylinders. When the measured translational or rotational drag is plotted against the corresponding trap stiffness, a linear relationship is observed (Fig. 2.3c,f). Within the range of cylinder dimensions tested, this reflects the above-mentioned trend of increased stiffness with increased diameter or height (corresponding to increased drag). The slope of the fitted lines yields the overall trap relaxation time ($t_{c,y} = \gamma_y/\kappa_y$ or $t_{c,\theta} = \gamma_\theta/\kappa_\theta$), with a shorter tc reflecting a more rapid response time and increased temporal resolution.

For linear trapping, we compare the results obtained with rutile TiO_2 cylinders to those obtained with standard polystyrene (PS) spheres (representative of low-index force transducers). The linear trap stiffness of rutile TiO_2 nanocylinders is approximately two-fold higher than that of PS spheres of comparable drag, a direct consequence of the higher refractive index of rutile TiO_2 ($n = 2.6$) compared to PS ($n = 1.57$). Correspondingly, rutile TiO_2 nanocylinders enable a nearly two-fold increase in temporal response ($t_{c,y} = 11$ µs for rutile TiO_2 , versus $t_{c,y} = 26$ µs for PS at 100 mW; Fig.2.3c). These effects can be appreciated by comparing the rutile TiO_2

cylinder batch T2 with the PS sphere batch P2 ($d = 505$ nm), which both have drag coefficients of ~ 4 pN · s/mm (Fig. 2.3c). For angular trapping, the trap relaxation time of rutile TiO_2 nanocylinders ($t_{c,y} = 15$ µs at 100 mW; Fig. 2.3f) is again considerably shorter due to the high angular trap stiffness (Fig. 2.2c, deriving from the large birefringence) achievable with such low rotational drag (Supplementary Fig. 2.11). As the trap relaxation time is inversely proportional to the laser beam power, it can be further tuned using this parameter.

Rutile TiO_2 nanocylinder particles transmit nN forces and nN · nm torques with excellent measurement precision.

To deduce the range of applicable forces using trapped rutile TiO_2 nanocylinders, we examine their measured linear stiffnesses and estimate the range of their harmonic regime. The high radial trapping stiffness of rutile TiO_2 nanocylinders should permit the application of large forces up to ~nN, as demonstrated for anti-reflection coated anatase TiO_2 spheres [23]. For example, a rutile TiO_2 nanocylinder with radial trap stiffness κ_Y = 7 pN/µm/mW (cylinder batch T8) should experience a 1 nN restoring force at ~1.4 W laser power (not measured due to the limitation of available power in our setup) upon displacement of ~100 nm from the trap center, well within the estimated harmonic potential regime (Supplementary Fig. 2.9). This represents an order of magnitude improvement over the typical ~100 pN limit of optical tweezers [45].

The exceptionally large birefringence of rutile TiO_2 makes it possible to simultaneously achieve very high torques (1–10 nN · nm) and rotational speeds (1–10 kHz) at only moderate laser powers (<100 mW) in aqueous solution (Fig. 2.3g,h). Such an expansive torque-speed range is not achievable in similar measurement conditions using other dielectric particles with much lower birefringence [12, 14]. To provide a guideline for selecting cylinder dimensions, we compare the torque-speed curves of differently sized nanocylinders (Fig. 2.3g,h). We first compare cylinders with similar diameters ($d \approx 213$ nm, batches T3–T6) but different heights (Fig. 2.3g). Here, the rotational drag coefficients are similar, as observable from the slopes ($\gamma_\theta = \tau_0/\omega_0$) in the linear part of the torque-speed curves. Using a cylinder with an optimal height for torque transfer efficiency (within this dataset, batch T5) results in a higher maximum torque and increased rotational frequency. Differently stated, for a fixed cylinder diameter, the height provides a means to tune the torque transfer efficiency. We next compare two groups of cylinders with similar heights ($h \approx 1096$ nm, batches T1 and T8; $h \approx 825$ nm, batches T2 and T7) but different diameters (Fig. 2.3h). Within each group of cylinders, the torque transfer efficiencies are similar, but the drag coefficients differ substantially. A smaller drag coefficient is preferable in general for a higher rotation frequency (e.g., compare batches T1 and T8 in Fig. 2.3h). However, a reduction in drag does not always guarantee an increased rotation frequency even if torque transfer efficiency is maintained (e.g., compare batches T2 and T7 in Fig. 2.3h). This is because the resulting rotation frequency ($f_0 \propto \kappa_\theta/\gamma_\theta$) is dependent on the relative rates of change between stiffness κ_θ and drag γ_θ, which are distinct functions of particle dimensions. Hence, for a fixed cylinder height, one should select the suitable cylinder diameter to access the desired torque-speed regime.

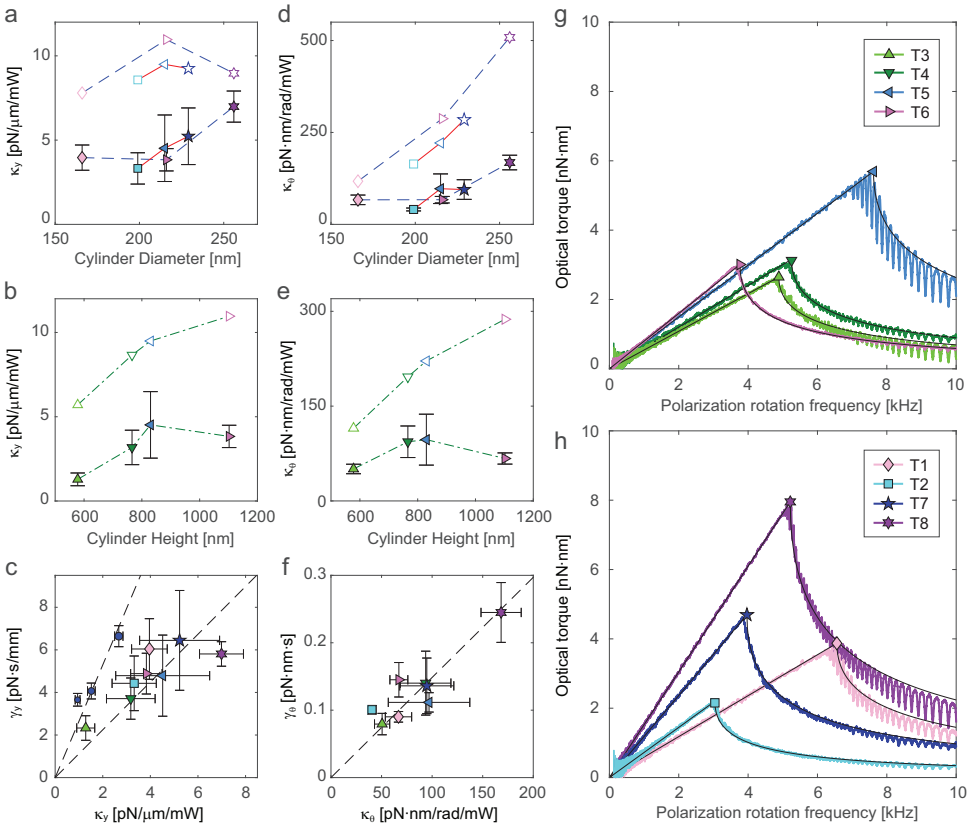

Figure 2.3: Experimentally measured linear and angular trapping performances of rutile TiO_2 nanocylinders. (a,b,d,e) Measured stiffness (κ_y, κ_θ) values plotted versus cylinder diameter or height, together with calculated values for comparison. The OTW-measured values are represented by filled symbols and associated error bars. The FEM-calculated values (which make use of SEM-measured cylinder geometries with actual sidewall profiles) are represented by empty symbols. For ease of visualization, in panel (a,d), data points from the cylinders of similar height $h \approx 1096$ nm (825 nm) are connected with dashed blue lines (solid red lines), and in panel (b,e), data points from the cylinders of similar diameter $d \approx 213$ nm are connected with dash-dotted green lines. (c,f) Measured drag coefficients (γ_y, γ_θ) plotted versus measured stiffness values (κ_y, κ_θ). The slope of a linear fit (dashed black line, forced through the origin) reports on the trap relaxation time ($t_{c,y} = 11\ s$ at 100 mW, $t_{c,\theta} = 15\ s$ at 100 mW). The measurement results from PS spheres are overlaid in panel (c) for comparison (filled blue circles; the mean diameters of batches P1, P2, and P3 are 370 nm, 505 nm, and 746 nm, respectively). A linear fit to PS data results in $t_{c,y} = 26\ s$ at 100 mW. (g,h) Moving-averaged optical torque as a function of input beam polarization rotation frequency (PRF), measured at 92 mW. Each curve represents the data obtained from a single cylinder, and its fit to the theory [16] is overlaid (black line). When the PRF exceeds the maximum rotation frequency of a cylinder (denoted by the corresponding colored symbol), the particle begins to slip and thus exhibits a decreased torque [16]. The cylinders with similar diameters ($d \approx 213\ nm$, T3–T6) are compared in panel (g), and those with similar heights ($h \approx 1096\ nm$, T1 and T8; $h \approx 825\ nm$, T2 and T7) are compared in panel (h). For the symbols employed in panels (a-h), the shape and color coding are as in Fig. 2.2.

Utilizing the high linear and angular stiffnesses achievable with low-drag rutile TiO_2 nanocylinders, we employ Allan deviation (AD) analysis [26] to demonstrate the ensuing improvements in measurement precision. For the primary quantities of physical interest – force, torque, position, and angle – we demonstrate in Fig. 2.4 that one can achieve excellent precisions below 1 pN, 1 pN · nm, 1 nm, and 1 degree, respectively, on short timescales between (sub)milliseconds and seconds. To quantify trapping, signal averaging times longer than the time at which the AD peak (colored vertical lines in Fig. 2.4) occurs are appropriate. This regime corresponds to the thermal limit, i.e., the harmonic trapping regime. AD values within this region determine the measurement precision as a function of the averaging time. Theoretically, longer averaging times increase the measurement precision, but there is a practical lower bound on the measurement precision because of long-term drift or other measurement noise [26]. In our setup, this lower bound occurs at an averaging time between ∼0.1 s and ∼10 s.

We illustrate here how the main trapping parameters affect the magnitude of the AD curve, in turn increasing or decreasing the achievable measurement precision. As an example, we selected a subset of the cylinder batches, i.e., T3–T5, that exhibits the order of increasing linear and angular stiffnesses. The force AD (Fig.2.4a) and torque AD (Fig.2.4c) are functions of drag only ($\propto (\gamma)^{1/2}$). Therefore, the best force and torque precisions are obtained from the cylinder with the smallest linear and angular drag coefficients (batch T3). However, the position AD (Fig. 2.4b) and angle AD (Fig. 2.4d) are functions of both drag and stiffness ($\propto (\gamma)^{1/2}/\kappa$). As differences in stiffness values are more significant in the chosen dataset, the best position and angle precisions are achieved with the highest linear and angular stiffnesses (batch T5).

Finally, we compare the stiffness, torque-speed regime, measurement precision, and temporal resolution between rutile TiO_2 and other common dielectric crystals, i.e., quartz SiO_2 and calcite $CaCO_3$. We chose to compare only calculated results because of the difficulty of fabricating different materials into an identical geometry. As experimentally demonstrated here (Fig. 2.3, Supplementary Fig. 2.12), we can reliably predict the overall trends in both linear and angular trapping parameters by numerical modeling. This comparison shows that rutile TiO_2 is indeed the most competent material as a combined force and torque transducer (Supplementary Fig. 2.13).

2.4. Conclusions

In this work, we have employed experimental measurements and numerical calculations based on finite-element methods to demonstrate how the collective optical properties of single-crystalline rutile TiO_2 (including high refractive index and exceptionally large birefringence), together with its shaping into nanocylinders of appropriate dimensions, make it possible to develop joint optical force and torque transducers with outstanding properties. We show that rutile TiO_2 nanocylinders exhibit high stiffness in both linear and angular domains, allowing for the application of ∼nN-scale forces and unprecedentedly high 1–10 nN · nm torques. Given their low drag coefficients, our fabricated rutile TiO_2 nanocylinders should exhibit excel-

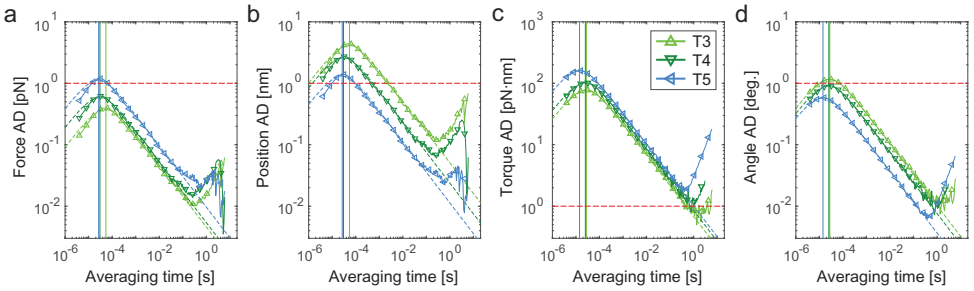

Figure 2.4: Temporal resolution and measurement precision in force, position, torque, and angle, achieved with rutile TiO_2 nanocylinders. (a-d) Allan deviation (AD) as a function of averaging time for three selected rutile TiO_2 cylinder batches (T3–T5, in order of increasing linear and angular stiffness; the same symbols and colors as in Fig. 2.2). AD plots for four different physical quantities are shown: (a) force, (b) position, (c) torque, and (d) angle. Each colored solid curve represents the normal AD obtained from a single cylinder measured at 92 mW. Colored symbols reflect the octave-sampled overlapping AD, and their fit to the theory [26] is overlaid as a dashed curve. The AD values report on the achievable measurement precision for a given averaging time, and the horizontal dashed red lines indicate the typical precisions required for measurements of individual biomolecules. For each cylinder, the trap relaxation time (t_c) can be deduced from the timescale at which the AD curve peaks ($1.8926t_c$; designated by the colored vertical lines) [26]. This relaxation time forms the lower bound of the achievable temporal resolution.

lent time response, which we have verified experimentally and exploited to highlight how rutile TiO_2 torque transducers can sustain high 1–10 kHz rotation frequencies in aqueous solution, even at a moderate trapping laser power not exceeding 100 mW. Furthermore, we show how optically trapped rutile TiO_2 nanocylinders enable high measurement precision in the key physical parameters of force, torque, position, and angle.

We expect that this coalescence of exceptional trapping properties into single rutile TiO_2 particles will open up opportunities for micro- and nanoscale applications. For example, the ability to transmit $\sim$nN $\cdot$ nm torques at $\sim$kHz rotation frequency will render measurements on systems with a wide torque-speed regime, e.g., the bacterial flagellar motor [46], accessible. Similarly, the high temporal resolution and excellent measurement precision will permit investigations of fast dynamics in other bio-molecules [4, 47]. Moreover, the small size, bio-compatibility, and chemical inertness of rutile TiO_2 nanocylinders, together with their low laser power requirements compared to other materials, will facilitate their usage in in-vivo microrheology [48] or cellular manipulation [7, 49]. Alternatively, these force and torque transducers could provide an enhanced platform for studies of quantum phenomena such as cavity cooling [6] and Casimir effects [50]. Finally, we foresee potential applications for rutile TiO_2 nanocylinders in engineering applications such as optically-driven nanomachines [9, 10], excitability-based sensors [14], or photonic force microscopy [51].

2.5. Supplementary Materials

Additional explanation of the linear trapping parameters

In addition to the axial trap stiffness κz, various other axial trapping parameters should be considered when choosing appropriate cylinder dimensions for specific practical applications. For example, the axial trap strength $F_{z,min}$ can be used as a criterion to assess stable 3D trapping. If the axial trap strength of a cylinder is very weak, despite the trap itself having high axial stiffness (e.g., the nanocylinder with $d = 300$ nm and $AR = 3.5$), then such a particle is difficult to exploit since it will escape from the trap at the slightest external perturbation. Also, the extent of the linear axial force regime z_{hp}, combined with κ_z, provides information about the maximum applicable axial force under the assumption that the axial trap is a harmonic potential well (i.e., a linear Hookean spring). This information is valuable as proper trap calibration is easiest in this regime. The above definitions and reasoning apply similarly to radial trapping in x- and y-dimensions.

Effects of nanocylinder taper angle on axial trapping properties

The dry etching process can result in nanocylinders with small taper angle (0–5°; T1–T8 and U1–U6 shown in Supplementary Fig. 2.8 and Supplementary Table 2.1), and such geometrical asymmetry can alter the optical trapping characteristics [31, 52]. To investigate this effect in rutile TiO_2 nanocylinders, we calculated axial trapping force F_z and then extracted axial stiffness κ_z for cylinders with taper angle σ of ±2° and ±4° while keeping the cylinder height and average diameter constant (thus, both the surface area and volume of the tapered cylinders are nearly the same as those of straight cylinders, allowing an unbiased comparison). For a tapered cylinder, two trapping orientations are possible with respect to the beam propagation direction. When the larger facet of a tapered cylinder is facing the source of the laser beam, the trappable regime shrinks and overall the trap stiffness decreases. This might be due to the increased light scattering at the larger entering surface of the particle, which destabilizes the trap. In contrast, when the tapered cylinder is flipped, and the smaller facet faces the beam source, the trappable regime expands and overall the trap stiffness increases. However, for each individual cylinder dimension, these changes are not proportional but nonlinearly correlated with the taper angle. For example, in the case of $d = 250$ nm and $AR = 5$ cylinder (Supplementary Fig. 2.10h), changing taper angle from 0° to –2° enhances trap stiffness, but –4° taper renders the cylinder untrappable. Importantly, this result also advises us about what are the fabrication error-tolerant cylinder sizes, with which the particles can be always 3D-trapped even with small variations in taper angles. For example, $d = 200$ nm and $AR = 4–6$ cylinders can be 3D-trapped regardless of the taper angle variations of ±4°. For the fabricated and optically trappable rutile TiO_2 nanocylinder batches (T1–T8), taper angles are rather small (0.1–1.6°) and hence their trapping behaviors are expected to be similar to those of perfectly straight cylinders.

Advantages of improved Cr etch mask fabrication protocols

The previous Cr etch mask made by one-step Cr deposition by evaporation [28] is limited in the achievable maximum thickness of each mask, and the thickness at its edge is much smaller than that at its center. As a consequence, the edge of a mask erodes much faster than the center, resulting in a more tapered cylinder with longer etch time. The eroded edge also tends to be rough, so the cross section of etched cylinder is prone to be less circular. However, the improved Cr etch mask, with its reinforced edge and high base, ensures less tapered angles and a more perfect circular cross section even for extended etch times. Therefore, it is possible to fabricate tall, high aspect ratio, and small-taper-angle rutile TiO_2 cylinders that function as optimal force and torque transducers (e.g., cylinder batch T6, $h = 1102$ nm, $AR = 5.1$, taper angle 0.2°; Supplementary Fig. 2.8, Supplementary Table 2.1).

We also improved the design pattern for writing circular disks with e-beam lithography. The new pattern consists of a single writing sequence and requires much less time compared to the conventional pattern, which approximates a disk shape with multiple trapezoidal writing sequences. As a finite overhead time exists for each writing sequence, the gain in writing time becomes more evident when patterning larger areas. The previous method also used single-sequence of writing per disk, consists of a single-pixel exposure with a defocused e-beam. The defocused e-beam is faster over large arrays of disks (~0.5 h to pattern a circular area with a 4 mm radius). However, e-beam fluctuations can decrease the circularity of these disks. Our new method produces more circular disks and can cover the same area in ~1 h.

Advantages of improved torque-speed measurement method

Using the conventional multi-frequency (MF) method, it is preferable to have a large number of data points (e.g., 50 Hz step size) for a better fit to the theory and a more precise detection of the peak position (for demonstration purpose, much less number of data points are taken than usual in the data set shown in Supplementary Fig. 2.14g). However, for fast torque transducers like rutile TiO_2 nanocylinders, a smaller step size requires excessively long measurement times to switch between PRF values. The resulting torque-speed curves are prone to distortion by the long-term drift in the setup. Also, switching between many different frequencies is not practical, especially for setups with hardware that does not support automated PRF control. For example, in our setup, measurement of each torque signal costs ~1 min of overhead time due to the time required to manually switch the PRF and write the data to the hard disk. Hence, it requires at least ~1 h to acquire the data shown in Supplementary Fig. 2.14g using the MF method with 100 Hz steps. As our frequency-sweep (FS) method allows torque measurement over a wide range of PRF values in just a few seconds, it is effectively free from the long-term drift in the setup. Hence, this method offers enhanced reliability and flexibility in torque spectroscopy.

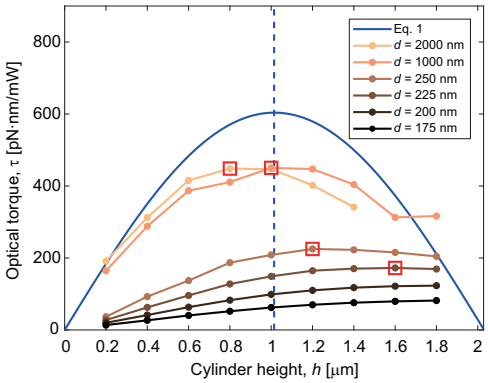

Figure 2.5: FEM-calculated rutile TiO_2 nanocylinder height for maximal torque transfer efficiency at different fixed diameters. The maximal optical torque (circles) of rutile TiO_2 nanocylinders as a function of their height (h = 0.2–1.8 m) for different diameters (d = 175–2000 nm), FEM-calculated at z_{eq} = 0 nm and $\theta = 45°$ (for the largest diameter d = 2000 nm, calculation is performed up to h = 1.4 μm due to the limitation of computing memory). Calculations are performed assuming a focus beam with the vacuum wavelength λ = 1064 nm, objective lens NA = 1.2, an objective lens filling ratio $\alpha = \infty$, and a surrounding medium index n = 1.33. For comparison, the analytical prediction (blue curve, using Eq. 2.1 from the main text) assuming a plane wave interacting with a rutile TiO_2 plate of 300 nm×300 nm surface area is co-plotted. The vertical dashed blue line ($h \approx 1$ μm) indicates the analytical prediction of optimal cylinder height for the maximal torque transfer efficiency, while the numerical predictions are designated by red squares if they exist within the calculated range. Note that nanoparticles with diameters smaller than the beam wavelength (d = 175–250 nm) deviate most from the analytical prediction. Cylinders with diameters comparable to or larger than the beam wavelength (d = 1000–2000 nm) show optical torque that more closely approximates the analytical prediction, as their geometry is closer to that of a rutile TiO_2 plate.

Parameter	Unit	Trappable cylinders								Untrappable cylinders					
		T1	T2	T3	T4	T5	T6	T7	T8	U1	U2	U3	U4	U5	U6
H (mean)	nm	1071	816	578	766	830	1102	828	1115	664	1184	1062	1214	1048	1425
H (SD)	nm	6	4	7	10	10	14	4	15	10	13	1	3	3	6
H (RSD)	%	0.6	0.4	1.1	1.4	1.2	1.3	0.5	1.3	1.5	1.1	0.1	0.3	0.3	0.5
D_{av} (mean)	nm	166	199	205	214	215	216	229	256	259	259	299	293	326	354
D_{av} (SD)	nm	6	4	5	12	12	16	9	10	6	7	15	9	9	9
D_{av} (RSD)	%	3.6	2.1	2.5	5.7	5.7	7.2	4	4.1	2.4	2.6	4.9	3	2.7	2.6
AR (mean)		6.5	4.1	2.8	3.6	3.9	5.1	3.6	4.4	2.6	4.6	3.6	4.1	3.2	4
AR (SD)		0.2	0.1	0.1	0.2	0.2	0.4	0.1	0.2	0.1	0.1	0.2	0.1	0.1	0.1
AR (RSD)	%	3.9	2.3	2.9	6	5.8	7.2	3.8	4.8	3.1	2.4	4.9	2.9	2.6	2.5
σ (mean)	deg.	0.5	0.7	–1.6	0.2	–0.1	0.2	1	–0.2	4.8	0.4	0.5	2.7	0.6	3.9
N		6	6	15	8	10	6	8	5	5	5	5	5	5	6

Table 2.1: SEM-measured dimensions of rutile TiO_2 nanocylinders. The SEM-measured dimensions of rutile TiO_2 nanocylinder batches (T1–T8, U1–U6) are listed. The parameters describing the cylinder geometry include the height (H), the averaged diameter (D_{av}), aspect ratio ($AR = H/D_{av}$), and the taper angle (σ). The parameter D_{av} is obtained by averaging the SEM-measured sidewall profile as can be seen in Supplementary Fig. 2.8c, because the fabricated nanocylinder batches exhibit slight deviations from a perfectly straight sidewall. For the same reason, the taper angle is calculated from the slope of the linear fit to the averaged sidewall profile of each nanocylinder batch. Here, a positive (negative) taper angle means that the top flat surface (i.e., the surface protected by a Cr mask during plasma etching; designated by the yellow lines in Supplementary Fig. 2.8a,b) is smaller (larger) than the bottom flat surface (i.e., mechanically cleaved position) of a cylinder. The values are obtained by measuring N = 5–15 different individual cylinders per batch. For each parameter, the displayed statistical values are the mean, the standard deviation (SD), and the relative standard deviation ($RSD = SD/mean \times 100$).

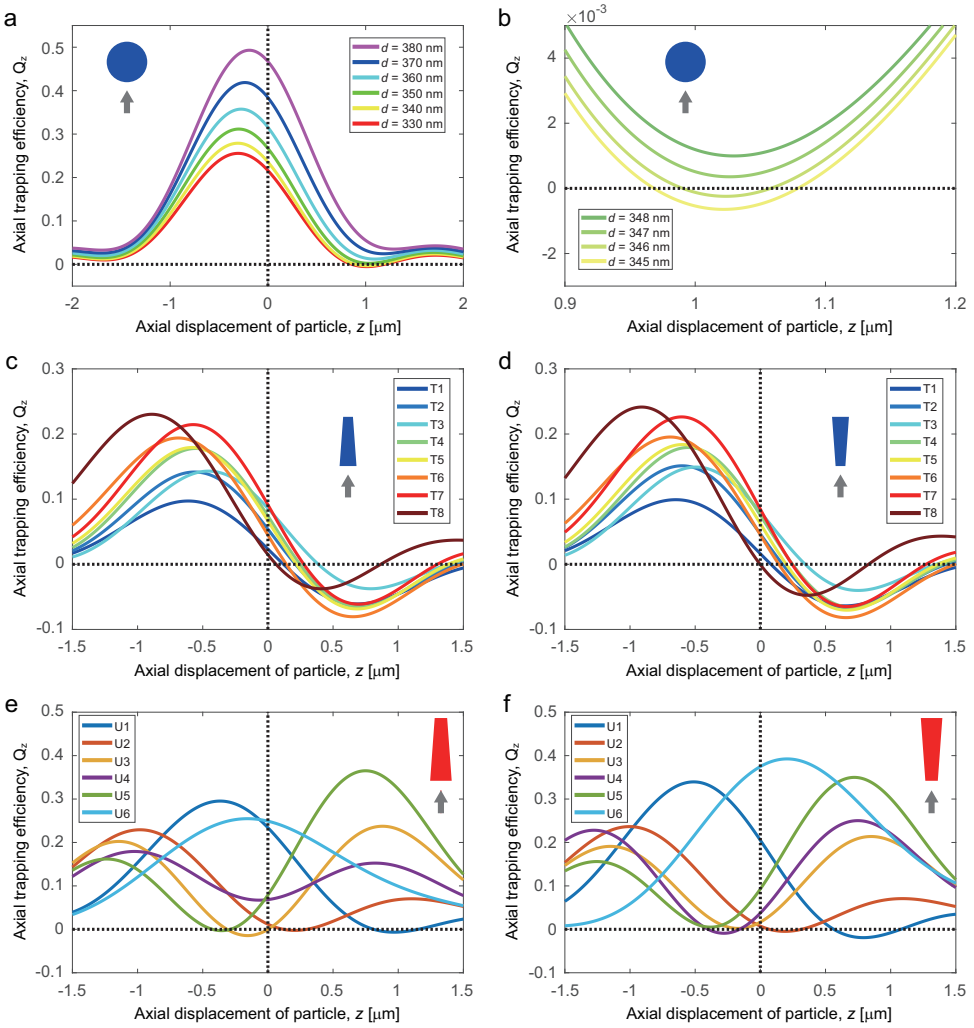

Figure 2.6: FEM-calculated optical trappability of rutile TiO_2 spheres and cylinders. (a) The FEM-calculated axial trapping efficiency (Q_z) curves (i.e., normalized axial force (F_z) curves; $Q_z = F_z/(nP/c)$, where n is the refractive index of the surrounding medium, P is the trapping laser beam power, and c is the speed of light in vacuum) for rutile TiO_2 spheres with diameters of 330–380 nm, demonstrating that spheres with large volume (≥~350 nm) are not trappable. (b) FEM-calculations of Q_z with 1 nm-step in sphere diameter (345–348 nm) reveal that the diameter of the largest trappable rutile TiO_2 sphere is 346 nm. (c–f) The FEM-calculated axial trapping efficiency (Q_z) curves for all fabricated rutile TiO_2 nanocylinder batches, using average SEM-measured dimensions with actual sidewall profiles as input parameters. The trap strengths (as defined in Supplementary Fig. 2.9) of trappable cylinders (T1–T8; (c,d)) are much larger than those of non-trappable cylinders (U1–U6; (e,f)). As the cylinders are not symmetric in the z-dimension, two different trapping orientations exist for each cylinder (with the positive (c,e) or negative (d,f) taper angle with respect to the input beam as shown in the inset diagram). For trappable cylinders (T1–T8; (c,d)), as their taper angles are small (0.1–1.6°, Supplementary Table 2.1), the trapping orientation does not significantly contribute to trapping behavior (Supplementary Fig. 2.10). All calculations in (a-f) are performed assuming a focus beam with objective lens $NA = 1.2$, an objective lens filling ratio $\alpha = 1.7$, and a surrounding medium index $n = 1.33$.

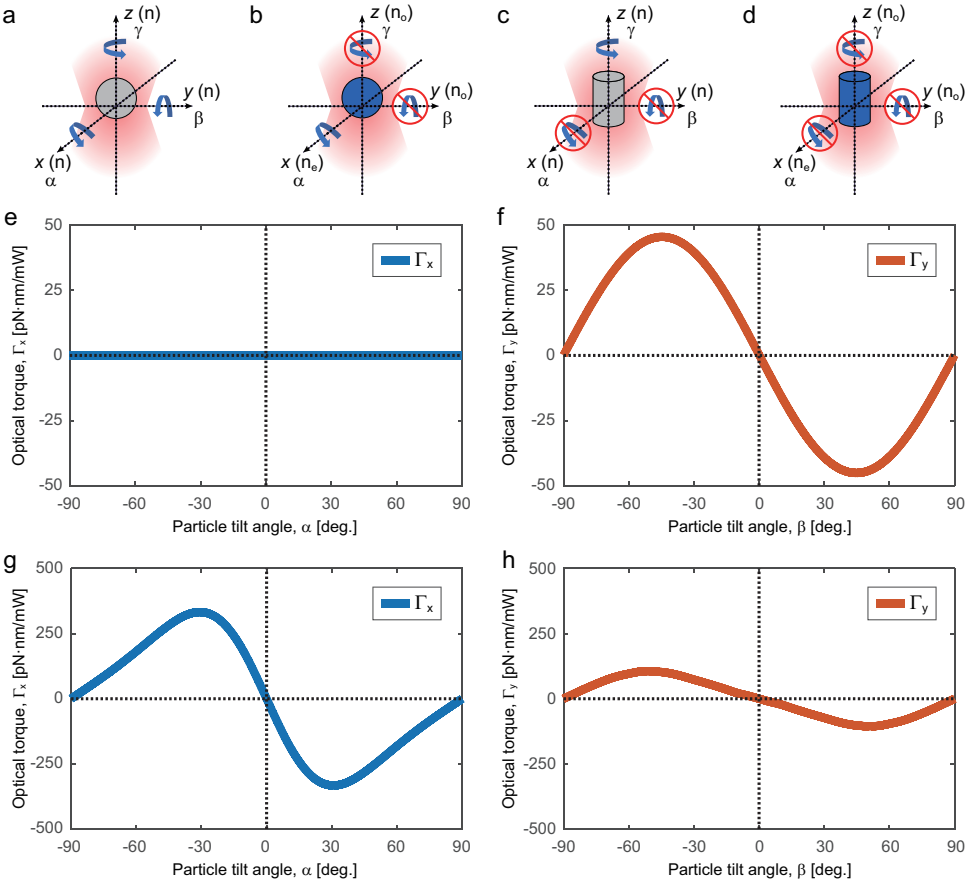

Figure 2.7: FEM-calculated RDOF confinement torque of rutile TiO_2 spheres and cylinders. Visual representation of the mechanism of RDOF confinement, supported by numerical calculations. (a-d) Illustrations of achievable confinement of the RDOF depending on the degree of geometrical or optical anisotropy. An optically isotropic particle (gray, e.g., polystyrene) has a constant refractive index (n) along its principal axes (x, y, and z), while a birefringent particle (blue, e.g., rutile TiO_2) includes an extraordinary index (n_e) that differs from the other two ordinary indices (n_o). Here, a positively birefringent crystal (e.g., rutile TiO_2) is assumed, and thus $n_e > n_o$. A blue curved arrow indicates free rotation in the absence of confinement, while an overlaid prohibitory traffic sign indicates the restriction in rotation due to confined RDOF. The incident trapping beam is assumed to be linearly polarized in the x-dimension. (a) A non-birefringent sphere, which is fully isotropic, has no confined RDOF. (b) A positively birefringent sphere that has optical anisotropy only, has two confined RDOF. (c) A non-birefringent cylinder that has geometrical anisotropy only, has two confined RDOF. (d) A positively birefringent cylinder, which is fully anisotropic, has fully confined RDOF. (e,f) FEM-calculated optical torque components for a positively birefringent sphere (rutile TiO_2, $d = 150$ nm), i.e., configuration in panel (b). The result shows that indeed the angle α is not confined, as (e) Γ_x remains zero at any angle, while the angle β is confined by the restoring torque (f) Γy from the optical birefringence. (g,h) FEM-calculated optical torque components for a positively birefringent cylinder (rutile TiO_2, $d = 200$ nm and $AR = 5$), i.e., configuration in panel (d). The confinement in the angle α results from the restoring torque (g) Γ_x generated by the uneven radiation pressure distribution on a tilted cylinder (no such geometrical effect would occur in the case of a tilted sphere). The angle β is doubly confined by the restoring torque (h) Γ_y from both geometrical and optical anisotropy. The confinement of the RDOF in the angle γ by the restoring torque Γ_z that results from particle birefringence is common to both sphere and cylinder. All calculations in (e-h) are performed assuming the vacuum wavelength of input beam $\lambda = 1064$ nm, an equilibrium axial trapping position $z_{eq} = 0$, a focus beam with objective lens $NA = 1.2$, an objective lens filling ratio $\alpha = \infty$, and a surrounding medium index $n = 1.33$.

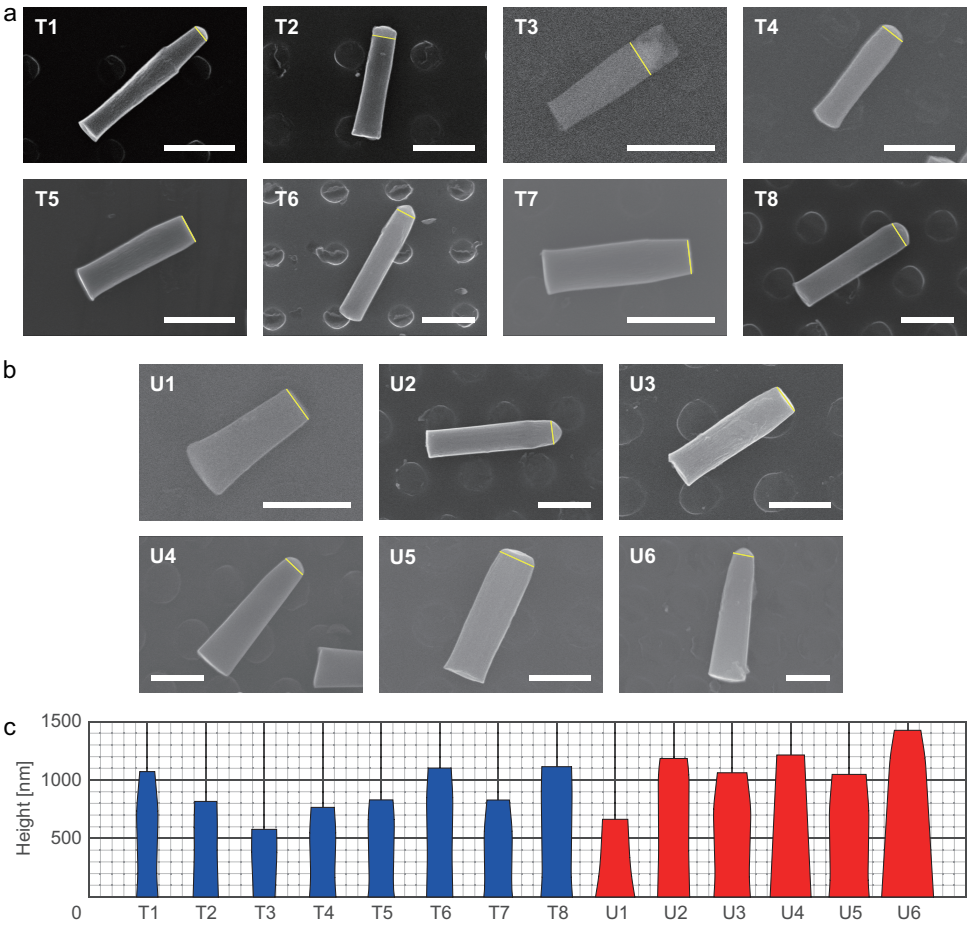

Figure 2.8: SEM micrographs of top-down fabricated single-crystal rutile TiO_2 nanocylinder batches. (a,b) A representative SEM micrograph of each cylinder batch is shown: (a) trappable nanocylinder batches (T1–T8); (b) untrappable nanocylinder batches (U1–U6). All scale bars are 500 nm. The yellow lines indicate the top surfaces of cylinders, and the structures just above them are Cr masks that remain when SEM images are taken prior to Cr removal by wet etching. (c) Geometries of trappable (blue) and untrappable (red) nanocylinders drawn up on the same scale with the mean dimensions obtained from multiple SEM images (Supplementary Table 2.1). Both vertical and horizontal grid lines have the same spacing (100 nm-step for thin lines and 500 nm-step for thick lines).

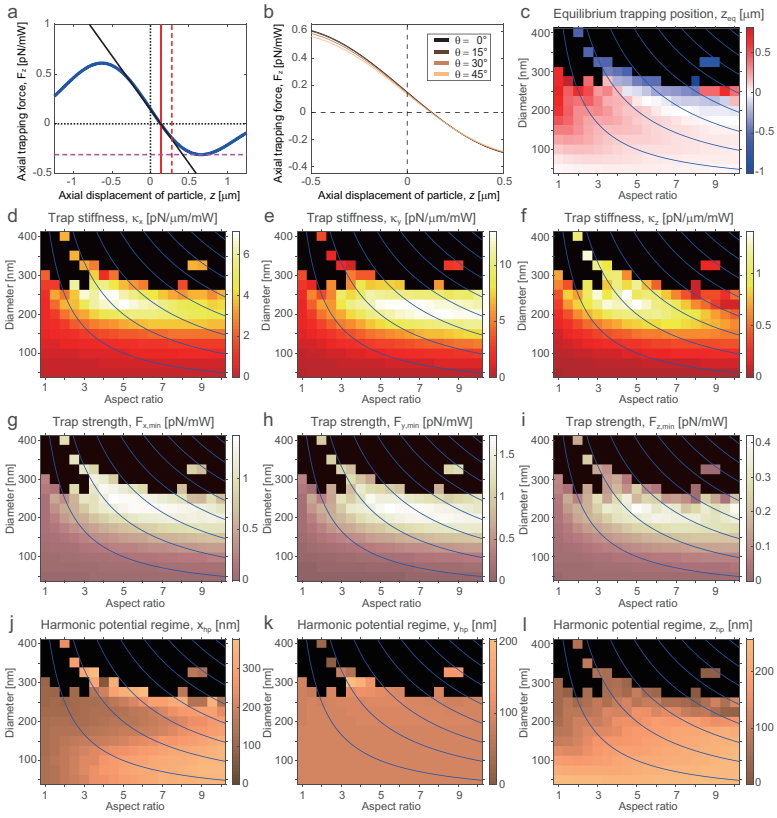

Figure 2.9: FEM-calculated parameters describing the linear optical trapping behavior of rutile TiO_2 nanocylinders. Linear trapping parameters deduced from FEM-calculated force curves, plotted as a function of cylinder diameter and aspect ratio. (a) The definitions of these parameters are graphically summarized with an axial force curve (the blue curve, for a nanocylinder with $d = 200$ nm and $AR = 5$ as an example): the axial equilibrium trapping position z_{eq} (the vertical red line which is the x-intercept of the force curve), the axial trap stiffness κ_z (the gradient of force at zeq designated by the solid black tangential line which approximates the harmonic potential well), the axial trap strength $F_{z,min}$ (the horizontal magenta dashed line over which the particle will escape from the trap), and the axial harmonic potential regime z_{hp} (the distance from z_{eq} to the nearest position at which the deviation of the actual force from the ideal harmonic approximation starts to exceed 10 % which is the conventional cutoff threshold [23, 53], represented by the vertical red dashed line). (b) The changing axial force curve shape upon rotation of the same rutile TiO_2 cylinder in (a) from $\theta = 0°$ to $\theta = 45°$ (with the rotation angle θ as defined in Eq. 2.1 from the main text). In this range, the deviation of z_{eq} is almost negligible (~6 nm) compared to the cylinder height (1 μm). As this behavior is similar to other cylinder dimensions as well, it is still valid to calculate the maximum optical torque (which occurs at $\theta = 45°$) with z_{eq} obtained at $\theta = 0°$ (Fig. 2.3c, Supplementary Fig. 2.13). (c) The map of z_{eq}. For each black colored pixel, z_{eq} does not exist (i.e., the axial force curve has no x-intercept) and hence 3D-trapping is not possible for cylinders of the corresponding dimensions. We do not calculate radial trapping parameters at these positions, since we are interested in 3D-trappable cylinder dimensions only. For 3D-trappable cylinder dimensions, the radial trapping parameters are calculated at z_{eq}. (d-f) The linear trap stiffness maps (κ_x, κ_y, κ_z). (g-i) The linear trap strength maps ($F_{x,min}$, $F_{y,min}$, $F_{z,min}$). (j-l) The linear harmonic potential regime maps (x_{hp}, y_{hp}, z_{hp}). The blue curves are iso-height contours (500–4000 nm from left to right, with a step size of 500 nm). The resolution of the maps is $\Delta AR = 0.5$ and $\Delta d = 25$ nm. All calculations in (a-l) are performed assuming the vacuum wavelength of input beam $\lambda = 1064$ nm, a focus beam with objective lens $NA = 1.2$, an objective lens filling ratio $\alpha = \infty$, and a surrounding medium index $n = 1.33$.

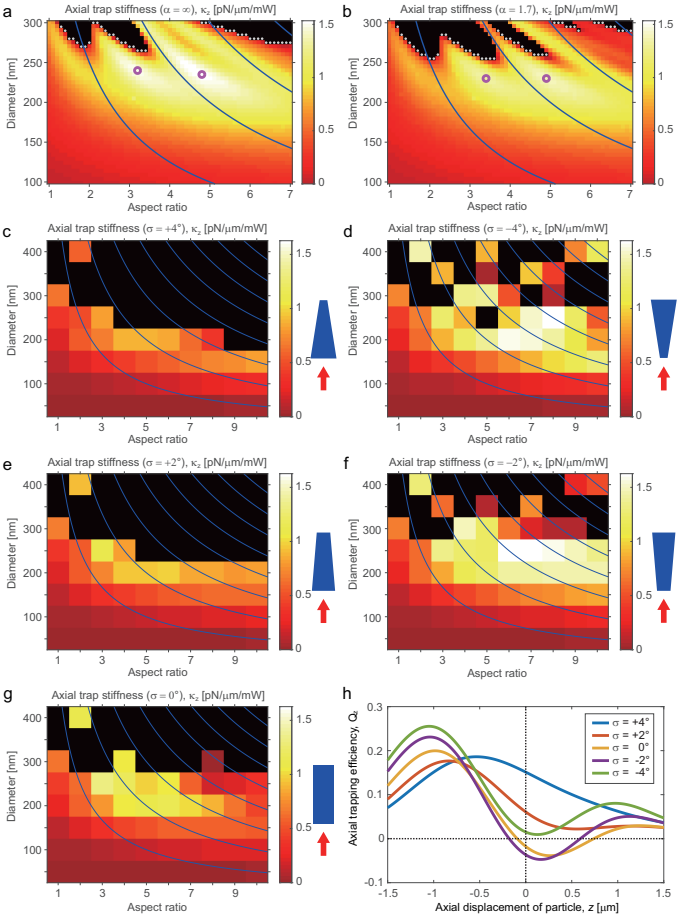

Figure 2.10: FEM-calculated maps of axial stiffness and curves of axial trapping efficiency for rutile TiO_2 nanocylinders with different objective lens aperture filling ratios and taper angles. (a,b) The FEM-calculated high-resolution maps of axial stiffness κ_z for rutile TiO_2 nanocylinders with (a) ideal ($\alpha = \infty$) and (b) measured ($\alpha = 1.7$; the same data as Fig. 2.2a) aperture filling ratios. The calculated threshold diameter d^*_{cal} for each aspect ratio is displayed as a gray dot, and the magenta circles indicate the local maxima of stiffness. Calculations based on the measured filling ratio (b) result in a narrower range of 3D-trappable cylinder diameters for aspect ratios between 1 and 5. The stiffness values at the local maxima are also reduced by ~10 %, due to the less tight beam focusing for a smaller filling ratio. The blue curves are iso-height contours (500–2000 nm from left to right, with a step size of 500 nm). The resolution of the maps is $\Delta AR = 0.1$ and $\Delta d = 5$ nm. (c-f) κ_z maps of nanocylinders with a taper angle σ of (c) +4°, (d) –4°, (e) +2°, and (f) –2°, as a function of the aspect ratio and average diameter d_{av} (with ideal aperture filling ratio $\alpha = \infty$). The schematics to the right of the maps illustrate the taper angle (not to scale) and orientation of the cylinder body with respect to the laser beam propagation direction (red arrow). (g) κ_z map of perfectly straight nanocylinders (the same data as shown in panel (a) and Supplementary Fig. 2.13), displayed for straightforward comparison with the maps of tapered cylinders. The blue curves are iso-height contours (500–4000 nm from left to right, with a step size of 500 nm). The resolution of the maps is $\Delta AR = 1$ and $\Delta d = 50$ nm. (h) Axial trapping efficiency Q_z as a function of taper angle for a representative cylinder batch with $d_{av} = 250$ nm and $AR = 5$. All calculations in (a-h) are performed assuming the vacuum wavelength of input beam $\lambda = 1064$ nm, a focus beam with objective lens $NA = 1.2$, and a surrounding medium index $n = 1.33$.

Parameter	Unit	T1	T2	T3	T4	T5	T6	T7	T8
γ_y (mean)	pN · s/mm	6	4.4	2.3	3.7	4.8	4.9	6.4	5.8
γ_y (SD)	pN · s/mm	1.4	1.3	0.6	1	1.9	1	2.3	0.6
γ_y (cal.)	pN · s/mm	4.7	4.3	3.5	4.2	4.5	5.3	4.6	5.7
κ_y (mean)	pN/µm/mW	4	3.3	1.3	3.2	4.5	3.8	5.2	7
κ_y (SD)	pN/µm/mW	0.7	0.9	0.4	1	2	0.7	1.7	0.9
κ_y (cal.)	pN/µm/mW	7.8	8.6	5.7	8.7	9.5	11	9.2	9
$t_{c,y}$ (mean)	µs (at 100 mW)	15	13	18	12	11	13	12	8
$t_{c,y}$ (SD)	µs (at 100 mW)	5	5	7	5	6	3	6	1
$t_{c,y}$ (cal.)	µs (at 100 mW)	6	5	6	5	5	5	5	6
N (linear)		4	7	8	9	9	3	10	3
γ_θ (mean)	pN · nm · s	0.09	0.1	0.08	0.14	0.11	0.15	0.14	0.24
γ_θ (SD)	pN · nm · s	0.01	0.01	0.02	0.05	0.01	0.03	0.04	0.04
γ_θ (cal.)	pN · nm · s	0.09	0.1	0.08	0.11	0.12	0.16	0.13	0.23
κ_θ (mean)	pN · nm/rad/mW	67	41	51	94	97	67	95	168
κ_θ (SD)	pN · nm/rad/mW	13	4	8	25	40	9	27	20
κ_θ (cal.)	pN · nm/rad/mW	117	164	115	196	221	287	285	508
$t_{c,\theta}$ (mean)	µs (at 100 mW)	14	25	16	15	12	22	14	15
$t_{c,\theta}$ (SD)	µs (at 100 mW)	3	3	4	6	5	5	6	3
$t_{c,\theta}$ (cal.)	µs (at 100 mW)	7	6	7	6	5	5	5	4
τ_o	nN · nm (at 100 mW)	3.3	2	2.5	4.7	4.8	3.4	4.7	8.4
f_o	kHz (at 100 mW)	5.9	3.2	5.1	5.3	6.9	3.7	5.5	5.5
N (angular)		4	7	7	9	8	3	7	3

Table 2.2: OTW-measured and FEM-calculated optical trapping parameters of the 3D-trappable rutile TiO_2 nanocylinders. The linear and angular optical trapping parameter values for all 3D-trappable rutile TiO_2 nanocylinder batches (T1–T8) are listed. Both experimental (mean, standard deviation (SD)) and numerically calculated (cal.) results are displayed. The linear trapping properties include the radial drag coefficient (γ_y), the radial trap stiffness (κ_y), and the radial trap relaxation time ($t_{c,y}$). Similarly, the angular trapping properties include the angular drag coefficient (γ_θ), the angular trap stiffness (κ_θ), and the angular trap relaxation time ($t_{c,\theta}$). Note that the drag coefficients are independent of trapping beam power, while trap stiffnesses and trap relaxation times are not. Also, the calculated stiffnesses (linear or angular) represent the mean of those that result from the two possible trapping orientations. Regarding the angular trapping, the averaged maximal torque (τ_o) and angular speed (f_o) at 100 mW beam power (scaled from the actually used ~92 mW for rapid interpretation) are also shown. The experimental values are obtained by measuring $N = 3$–10 cylinders per batch.

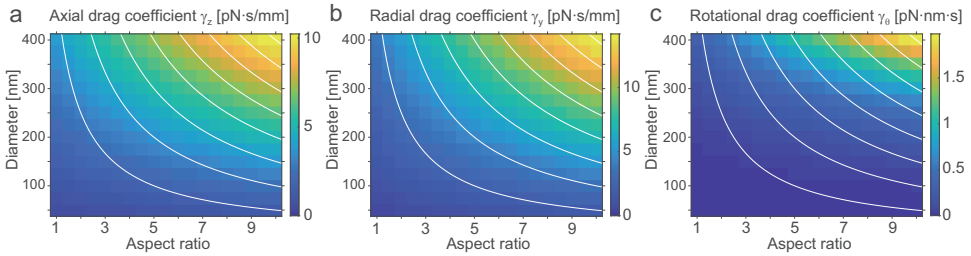

Figure 2.11: FEM-Calculated translational and rotational hydrodynamic drag coefficients of nanocylinders. (a,b) The drag coefficients for translational movements of nanocylinders in water are FEM-calculated as a function of cylinder diameter and aspect ratio: (a) the axial linear drag coefficients (movement along the z-axis), (b) the radial linear drag coefficients (movement along either the x-axis or the y-axis). (c) The drag coefficients for rotational motion of nanocylinders (rotation about the z-axis). These rotational drag coefficients are used to calculate the maps of the maximum rotation frequency (Fig. 2.2d and Supplementary Fig. 2.13). The resolution of the maps in (a-c) is $\Delta AR = 0.5$ and $\Delta d = 25$ nm. For Fig.2.2d in the main text, we used a drag map with higher resolution, $\Delta AR = 0.1$ and $\Delta d = 5$ nm. The white curves are iso-height contours (500–4000 nm from left to right, with a step size of 500 nm).

Parameter	Unit	P1	P2	P3
D (mean)	nm	370	505	746
D (SD)	nm	15	8	2
D (RSD)	%	4.1	1.6	0.3
γ_y (mean)	pN · nm · s	3.7	4.1	6.6
γ_y (SD)	pN · nm · s	0.3	0.4	0.5
γ_y (cal.)	pN · nm · s	3.3	4.4	6.6
κ_y (mean)	pN/μm/mW	0.9	1.5	2.7
κ_y (SD)	pN/μm/mW	0.1	0.2	0.2
κ_y (cal.)	pN/μm/mW	1.5	3.1	4.2
$t_{c,y}$ (mean)	μs (at 100 mW)	39	27	25
$t_{c,y}$ (SD)	μs (at 100 mW)	5	4	2
$t_{c,y}$ (cal.)	μs (at 100 mW)	22	14	15
N		5	6	7

Table 2.3: Dimensions and linear optical trapping parameters of the PS spheres. The dimensions and linear optical trapping parameter values for all measured PS sphere batches (P1–P3) are listed. For sphere diameter, the displayed statistical values are the mean, the standard deviation (SD), and the relative standard deviation (RSD = SD/mean×100). These values are provided by the supplier of the spheres. For linear optical trapping parameters, both experimental (mean, standard deviation (SD)) and numerically calculated (cal.) results are displayed. The trapping properties include the radial drag coefficient (γ_y), the radial trap stiffness (κ_y), and the radial trap relaxation time ($t_{c,y}$). Note that the drag coefficients are independent of trapping beam power, while trap stiffnesses and trap relaxation times are not. The experimental values are obtained by measuring $N = 5$–7 different individual spheres per batch.

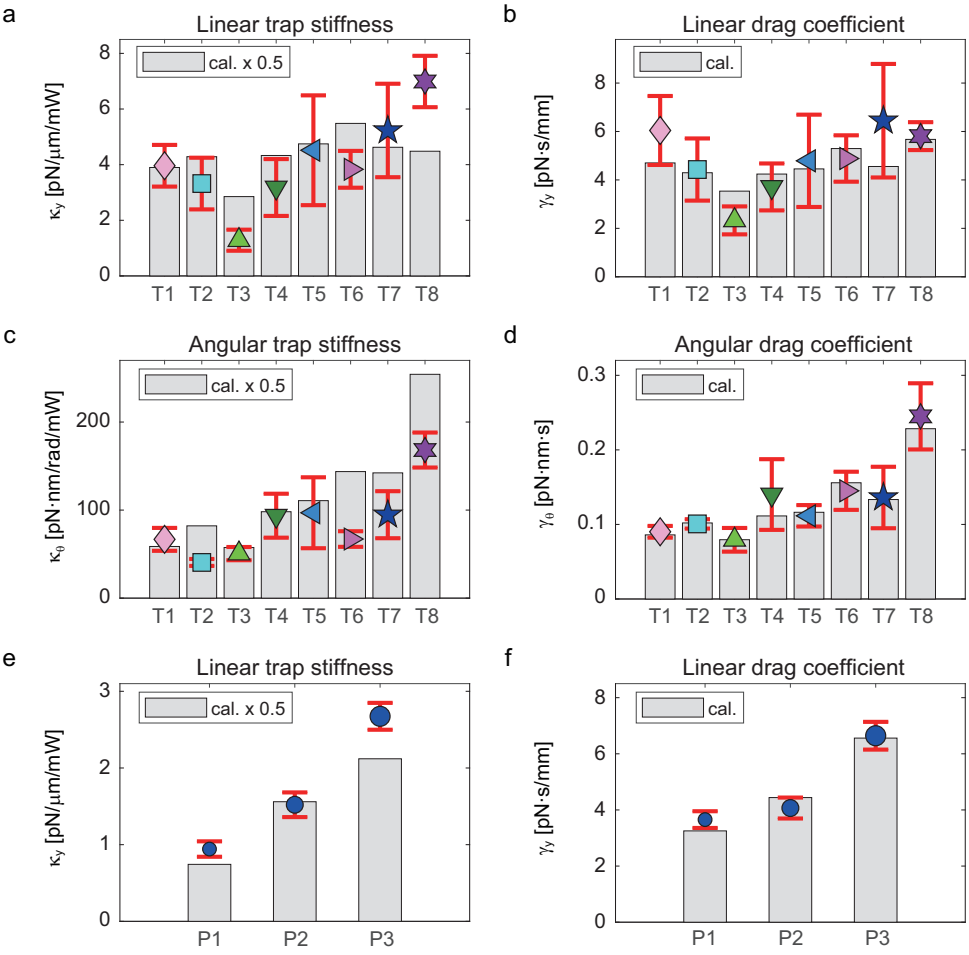

Figure 2.12: Comparison of experimentally and theoretically obtained stiffnesses and drag coefficients for trapping of rutile TiO_2 cylinders and PS spheres. For all trappable nanocylinder batches (T1–T8) and measured PS sphere batches (P1-P3), the trapping parameters obtained by both FEM calculations and OTW measurements are shown. The FEM calculations used the SEM-measured average dimensions for the cylinders and the average diameter provided by the supplier for the spheres. (a) The linear trap stiffness (κ_y), (b) linear drag coefficient (γ_y), (c) angular trap stiffness (κ_θ), and (d) angular drag coefficient (γ_θ) of the rutile TiO_2 nanocylinders (summarized in Supplementary Table 2.2). (e) The linear trap stiffness (κ_y) and (f) linear drag coefficient (γ_y) of the PS spheres (summarized in Supplementary Table 2.3). In all panels, the gray bars indicate the FEM-calculated values, while the colored symbols (mean) and red error bars (SD) indicate the experimental values obtained by OTW-measurements of multiple particles per batch ($N = 3$–10). The FEM-calculated stiffness values (a,c,e) are scaled down by 50 % for a direct comparison with experimental values (designated as cal.$\times 0.5$). The mean ratios between FEM-calculated and measured values averaged over all batches are (a) for κ_y: 46 % ± 16 %, (b) for γ_y: 104 % ± 22 %, (c) for κ_θ: 38 % ± 11 %, and (d) for γ_θ: 103 % ± 9 % in case of rutile TiO_2, and (e) for κ_y: 58 % ± 7 % and (f) for γ_y: 102 % ± 8 % (mean ± SD) in case of PS. By averaging the linear values (a) and (c) and the angular values (b) and (d) of rutile TiO_2, we arrived at the values quoted in the main text, for κ: 42 % ± 14 % and for γ: 104 % ± 17 %, respectively. Overall, the calculations properly predict all observed trends in drag and stiffness.

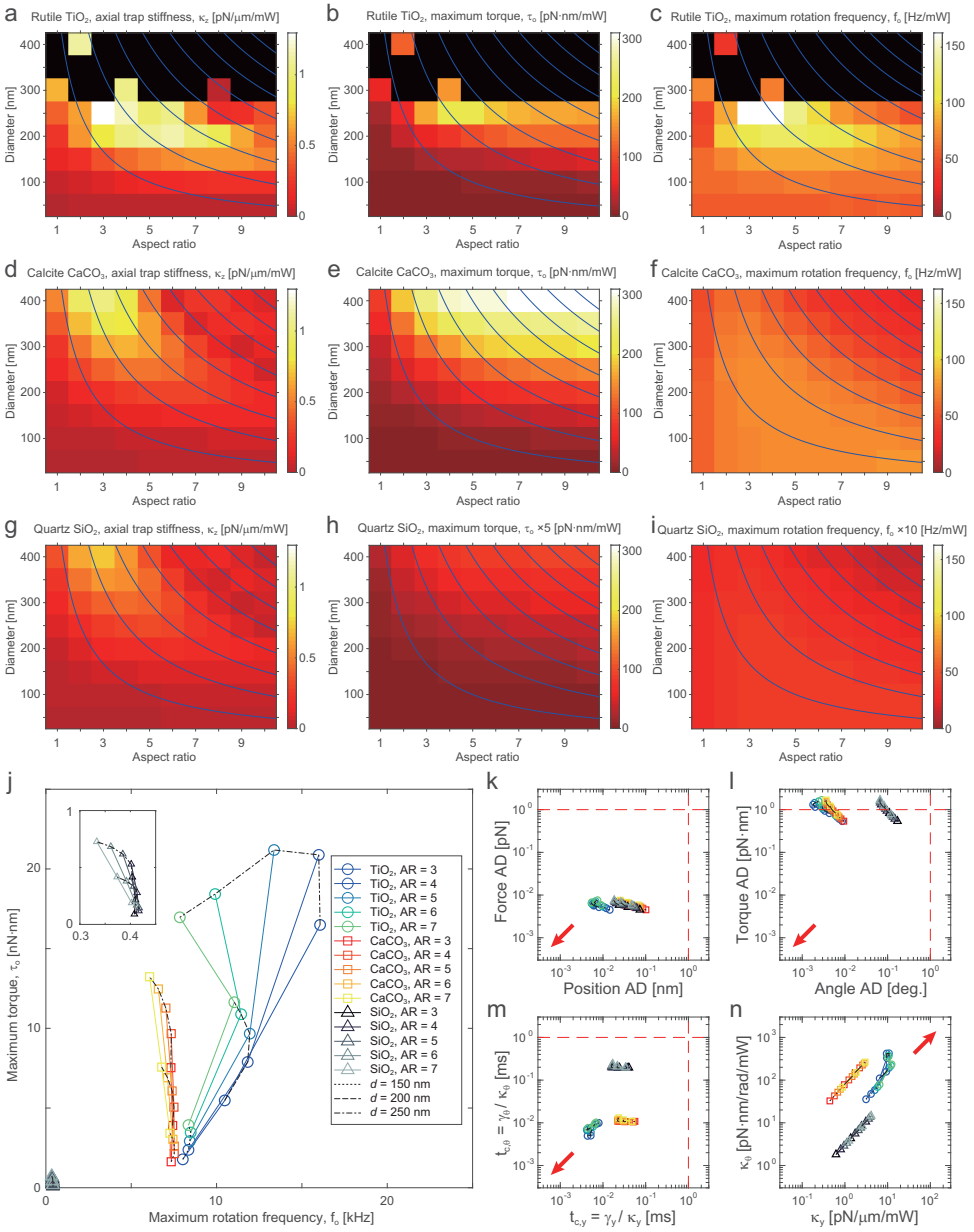

Figure 2.13: FEM-calculated linear and angular trapping parameters for different birefringent crystals. (a-i) For an unbiased comparison with the trapping parameters of (a-c) rutile TiO_2 nanocylinders, we performed similar FEM calculations for nanocylinders made of other birefringent crystals that are frequently used for OTW applications, including (d-f) calcite $CaCO_3$ and (g-i) quartz SiO_2. The calculated parameters are (a,d,g) the axial trapping stiffness κ_z, (b,e,h) the maximum torque τ_0, and (c,f,i) the maximum rotation frequency f_o. The maximum rotation frequency ($f_o = \tau_o/(2\pi\gamma\theta)$) maps are obtained using the FEM-calculated angular drag coefficients γ_θ (Supplementary Fig. 2.11). Within the calculated range of cylinder dimensions (d = 50–400 nm, AR = 1–10), only rutile TiO_2 has dimensions that are not 3D-trappable (black pixels) due to its highest refractive index. Each parameter is displayed with the same color scale across the maps of different materials. Quartz SiO_2 has the smallest birefringence, and its angular parameters (τ_o and f_o) are very small (peak values are only 18.7 pN · nm/mW and 4.3 Hz/mW,

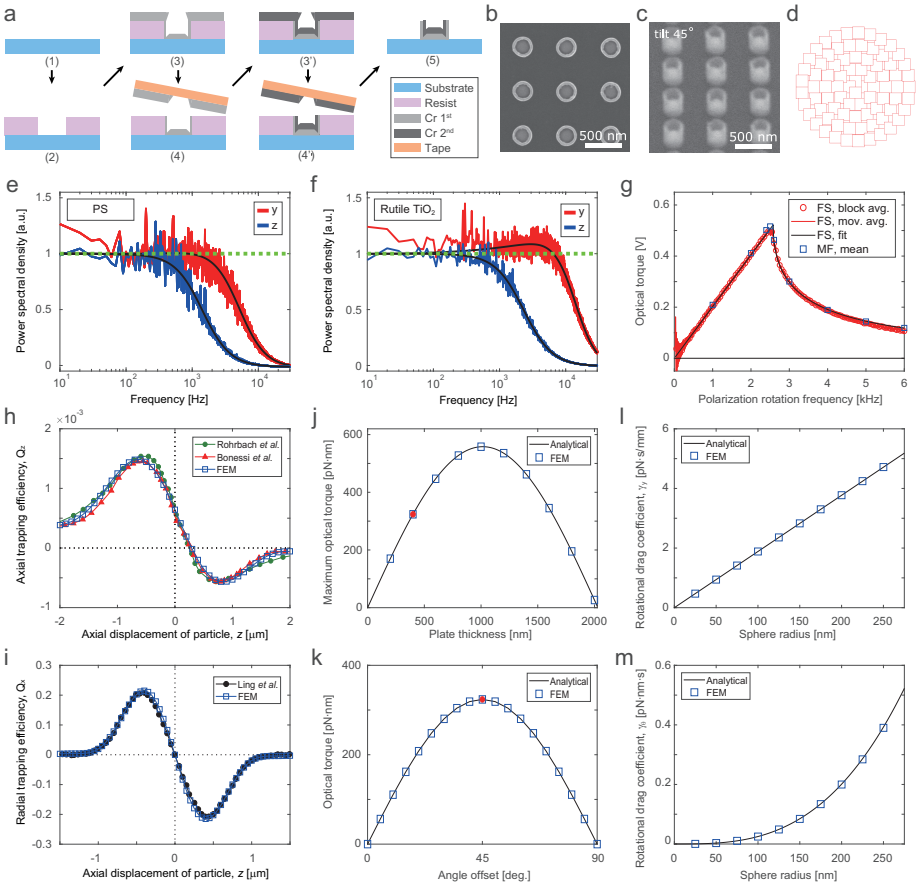

Figure 2.14: Improved methods for nanocylinder fabrication and trap calibration, and validation of FEM numerical models. (a-d) Our improvements in fabrication protocol. (a) The fabrication steps for chromium (Cr) mask for rutile TiO_2 etching: (1) A rutile TiO_2 substrate; (2) patterning of an e-beam resist layer (CSAR 62, ALLRESIST) by e-beam lithography; (3) sputtering deposition (AC450, Alliance Concept) of the first Cr layer; (4) top Cr layer lift-off by attachment and subsequent removal of adhesive tape; (3'-4') sputtering and lift-off of the second Cr layer; (5) removal of e-beam resist by solvent (N-Methyl-2-pyrrolidone (NMP), VWR Chemicals). The resulting Cr mask has a high base (~240 nm) and a tall, thick surrounding wall (~350 nm tall and ~40 nm thick). (b,c) The SEM image of the Cr mask before etching of top-view (b) and 45° tilted view (c). (d) The e-beam writing pattern for disk-shaped Cr masks. Each red square represents a position for an e-beam exposure. (e,f) The OTW-measured (solid colored lines) and fitted (solid black lines) power spectral density (PSD) plots for linear trapping of (e) a PS sphere ($d = 746$ nm) and (f) a rutile TiO_2 nanocylinder (batch T6, $d_{av} = 216$ nm, $h = 1102$ nm). For the rutile TiO_2 cylinder in (f), the PSD plot of the radial trapping (along the y-axis) is fitted by the hydrodynamically corrected PSD function [23, 54], exhibiting the hydrodynamic memory effect. The PSD plots of the axial trapping of the rutile TiO_2 cylinder in (f) and all trapping of the PS bead in (e) are fitted by the conventional Lorentzian PSD function [54], which do not show any hydrodynamic memory effect. (g) Our frequency-sweep (FS) method for torque-speed curve measurements in angular trap calibration. In this example, we swept from 25 Hz to 7525 Hz in 6 s, and acquired the signal at a sampling frequency of 100 kHz. The results agree well with the MF method [12–14, 55] (blue squares). (h-m) We validated our FEM models by comparing them with analytical and other numerical treatments of PS spheres. (h) Axial force ($d = 200$ nm sphere [56, 57]). (i) Radial force ($d = 1$ μm sphere [58]). (j,k) Angular momentum transfer by comparing with Eq. 2.1, assuming a birefringent plate of 300 nm×300 nm cross-sectional area (Appendix A). We obtained FEM-calculated maximum torques as a function of (j) the plate height h ($\theta = 45°$) and (k) the offset angle θ ($h = 400$ nm). The red dots in (j) and (k) are the same data point. (l,m) For hydrodynamic drag, we compare our FEM models with the well-known analytical equations of spheres for both (l) translational ($\gamma_y = 6\pi\eta r$; η is the dynamic viscosity of water and r is the radius of sphere) and (m) rotational drag coefficients ($\gamma\theta = 8\pi\eta r^3$) [41].

References

[1] S. Ha, Y. Tang, M. M. van Oene, R. Janissen, R. M. Dries, B. Solano, A. J. L. Adam, and N. H. Dekker, *Single-crystal rutile tio2 nanocylinders are highly effective transducers of optical force and torque,* ACS Photonics **6**, 1255 (2019).

[2] R. A. Beth, *Mechanical detection and measurement of the angular momentum of light,* Physical Review **50**, 115 (1936).

[3] M. Friese, T. Nieminen, N. Heckenberg, and H. Rubinsztein-Dunlop, *Optical alignment and spinning of laser-trapped microscopic particles,* Nature **394**, 348 (1998).

[4] S. Forth, M. Y. Sheinin, J. Inman, and M. D. Wang, *Torque measurement at the single-molecule level,* Annual review of biophysics **42**, 583 (2013).

[5] J. Lipfert, M. M. van Oene, M. Lee, F. Pedaci, and N. H. Dekker, *Torque spectroscopy for the study of rotary motion in biological systems,* Chemical reviews **115**, 1449 (2014).

[6] Y. Arita, A. W. McKinley, M. Mazilu, H. Rubinsztein-Dunlop, and K. Dholakia, *Picoliter rheology of gaseous media using a rotating optically trapped birefringent microparticle,* Analytical chemistry **83**, 8855 (2011).

[7] T. Wu, T. A. Nieminen, S. Mohanty, J. Miotke, R. L. Meyer, H. Rubinsztein-Dunlop, and M. W. Berns, *A photon-driven micromotor can direct nerve fibre growth,* nature photonics **6**, 62 (2012).

[8] Y. Arita, M. Mazilu, and K. Dholakia, *Laser-induced rotation and cooling of a trapped microgyroscope in vacuum,* Nature communications **4**, 2374 (2013).

[9] S. L. Neale, M. P. MacDonald, K. Dholakia, and T. F. Krauss, *All-optical control of microfluidic components using form birefringence,* Nature materials **4**, 530 (2005).

[10] J. Leach, H. Mushfique, R. di Leonardo, M. Padgett, and J. Cooper, *An optically driven pump for microfluidics,* Lab on a Chip **6**, 735 (2006).

[11] P. H. Jones, O. M. Maragò, and G. Volpe, *Optical tweezers: Principles and applications* (Cambridge University Press, 2015).

[12] A. La Porta and M. D. Wang, *Optical torque wrench: angular trapping, rotation, and torque detection of quartz microparticles,* Physical review letters **92**, 190801 (2004).

[13] B. Gutiérrez-Medina, J. O. Andreasson, W. J. Greenleaf, A. LaPorta, and S. M. Block, *An optical apparatus for rotation and trapping,* in *Methods in enzymology*, Vol. 475 (Elsevier, 2010) pp. 377–404.

[14] F. Pedaci, Z. Huang, M. Van Oene, S. Barland, and N. H. Dekker, *Excitable particles in an optical torque wrench,* Nature Physics **7**, 259 (2011).

[15] F. Pedaci, Z. Huang, M. van Oene, and N. H. Dekker, *Calibration of the optical torque wrench,* Optics express **20**, 3787 (2012).

[16] Z. Santybayeva and F. Pedaci, *Optical torque wrench design and calibration,* in *Optical Tweezers* (Springer, 2017) pp. 157–181.

[17] L. Allen, M. W. Beijersbergen, R. Spreeuw, and J. Woerdman, *Orbital angular momentum of light and the transformation of laguerre-gaussian laser modes,* Physical Review A **45**, 8185 (1992).

[18] M. Funk, S. J. Parkin, A. B. Stilgoe, T. A. Nieminen, N. R. Heckenberg, and H. Rubinsztein-Dunlop, *Constant power optical tweezers with controllable torque,* Optics letters **34**, 139 (2009).

[19] A. Lehmuskero, R. Ogier, T. Gschneidtner, P. Johansson, and M. Käll, *Ultrafast spinning of gold nanoparticles in water using circularly polarized light,* Nano letters **13**, 3129 (2013).

[20] L. Shao, Z.-J. Yang, D. Andren, P. Johansson, and M. Kall, *Gold nanorod rotary motors driven by resonant light scattering,* ACS nano **9**, 12542 (2015).

[21] L. Jauffred, S. M.-R. Taheri, R. Schmitt, H. Linke, and L. B. Oddershede, *Optical trapping of gold nanoparticles in air,* Nano letters **15**, 4713 (2015).

[22] A. van der Horst, P. D. van Oostrum, A. Moroz, A. van Blaaderen, and M. Dogterom, *High trapping forces for high-refractive index particles trapped in dynamic arrays of counterpropagating optical tweezers,* Applied optics **47**, 3196 (2008).

[23] A. Jannasch, A. F. Demirörs, P. D. Van Oostrum, A. Van Blaaderen, and E. Schäffer, *Nanonewton optical force trap employing anti-reflection coated, high-refractive-index titania microspheres,* Nature Photonics **6**, 469 (2012).

[24] Y. Arita, J. M. Richards, M. Mazilu, G. C. Spalding, S. E. Skelton Spesyvtseva, D. Craig, and K. Dholakia, *Rotational dynamics and heating of trapped nanovaterite particles,* ACS nano **10**, 11505 (2016).

[25] K. C. Neuman, E. H. Chadd, G. F. Liou, K. Bergman, and S. M. Block, *Characterization of photodamage to escherichia coli in optical traps,* Biophysical journal **77**, 2856 (1999).

[26] M. M. van Oene, S. Ha, T. Jager, M. Lee, F. Pedaci, J. Lipfert, and N. H. Dekker, *Quantifying the precision of single-molecule torque and twist measurements using allan variance,* Biophysical journal **114**, 1970 (2018).

[27] J. R. DeVore, *Refractive indices of rutile and sphalerite,* JOSA **41**, 416 (1951).

[28] S. Ha, R. Janissen, Y. Y. Ussembayev, M. M. van Oene, B. Solano, and N. H. Dekker, *Tunable top-down fabrication and functional surface coating of single-crystal titanium dioxide nanostructures and nanoparticles,* Nanoscale **8**, 10739 (2016).

[29] S. J. Parkin, R. Vogel, M. Persson, M. Funk, V. L. Loke, T. A. Nieminen, N. R. Heckenberg, and H. Rubinsztein-Dunlop, *Highly birefringent vaterite microspheres: production, characterization and applications for optical micromanipulation,* Optics express **17**, 21944 (2009).

[30] A. F. Demirörs, A. Jannasch, P. D. van Oostrum, E. Schäffer, A. Imhof, and A. van Blaaderen, *Seeded growth of titania colloids with refractive index tunability and fluorophore-free luminescence,* Langmuir **27**, 1626 (2011).

[31] N. Simpson, D. McGloin, K. Dholakia, L. Allen, and M. Padgett, *Optical tweezers with increased axial trapping efficiency,* Journal of Modern Optics **45**, 1943 (1998).

[32] S. N. S. Reihani, S. A. Mir, A. C. Richardson, and L. B. Oddershede, *Significant improvement of optical traps by tuning standard water immersion objectives,* Journal of Optics **13**, 105301 (2011).

[33] J.-C. Meiners and S. R. Quake, *Direct measurement of hydrodynamic cross correlations between two particles in an external potential,* Physical review letters **82**, 2211 (1999).

[34] S. F. Tolić-Nørrelykke, E. Schäffer, J. Howard, F. S. Pavone, F. Jülicher, and H. Flyvbjerg, *Calibration of optical tweezers with positional detection in the back focal plane,* Review of scientific instruments **77**, 103101 (2006).

[35] T. Franosch, M. Grimm, M. Belushkin, F. M. Mor, G. Foffi, L. Forró, and S. Jeney, *Resonances arising from hydrodynamic memory in brownian motion,* Nature **478**, 85 (2011).

[36] X. Wei, A. J. Wachters, and H. P. Urbach, *Finite-element model for three-dimensional optical scattering problems,* JOSA A **24**, 866 (2007).

[37] T. A. Nieminen, V. L. Loke, A. B. Stilgoe, G. Knöner, A. M. Brańczyk, N. R. Heckenberg, and H. Rubinsztein-Dunlop, *Optical tweezers computational toolbox,* Journal of Optics A: Pure and Applied Optics **9**, S196 (2007).

[38] L. Novotny and B. Hecht, *Principles of nano-optics* (Cambridge university press, 2012).

[39] J. Chen, J. Ng, Z. Lin, and C. Chan, *Optical pulling force,* Nature photonics **5**, 531 (2011).

[40] F. M. White, *Fluid Mechanics* (McGraw-Hill Education, 2015).

[41] J. Leach, H. Mushfique, S. Keen, R. Di Leonardo, G. Ruocco, J. Cooper, and M. Padgett, *Comparison of faxén's correction for a microsphere translating or rotating near a surface,* Physical Review E **79**, 026301 (2009).

[42] N. Khatibzadeh, A. B. Stilgoe, A. A. Bui, Y. Rocha, G. M. Cruz, V. Loke, L. Z. Shi, T. A. Nieminen, H. Rubinsztein-Dunlop, and M. W. Berns, *Determination of motility forces on isolated chromosomes with laser tweezers,* Scientific reports **4**, 6866 (2014).

[43] A. Ortega and J. Garcıa de la Torre, *Hydrodynamic properties of rodlike and disklike particles in dilute solution,* The Journal of chemical physics **119**, 9914 (2003).

[44] A. Rohrbach and E. H. Stelzer, *Trapping forces, force constants, and potential depths for dielectric spheres in the presence of spherical aberrations,* Applied optics **41**, 2494 (2002).

[45] K. C. Neuman and A. Nagy, *Single-molecule force spectroscopy: optical tweezers, magnetic tweezers and atomic force microscopy,* Nature methods **5**, 491 (2008).

[46] M. Beeby, D. A. Ribardo, C. A. Brennan, E. G. Ruby, G. J. Jensen, and D. R. Hendrixson, *Diverse high-torque bacterial flagellar motors assemble wider stator rings using a conserved protein scaffold,* Proceedings of the National Academy of Sciences , 201518952 (2016).

[47] M. Capitanio and F. S. Pavone, *Interrogating biology with force: single molecule high-resolution measurements with optical tweezers,* Biophysical journal **105**, 1293 (2013).

[48] B. R. Daniels, B. C. Masi, and D. Wirtz, *Probing single-cell micromechanics in vivo: the microrheology of c. elegans developing embryos,* Biophysical journal **90**, 4712 (2006).

[49] D. Craig, A. McDonald, M. Mazilu, H. Rendall, F. Gunn-Moore, and K. Dholakia, *Enhanced optical manipulation of cells using antireflection coated microparticles,* ACS Photonics **2**, 1403 (2015).

[50] Z. Xu and T. Li, *Detecting casimir torque with an optically levitated nanorod,* Physical Review A **96**, 033843 (2017).

[51] D. B. Phillips, J. A. Grieve, S. Olof, S. Kocher, R. Bowman, M. J. Padgett, M. Miles, and D. M. Carberry, *Surface imaging using holographic optical tweezers,* Nanotechnology **22**, 285503 (2011).

[52] D. Phillips, M. Padgett, S. Hanna, Y.-L. Ho, D. Carberry, M. Miles, and S. Simpson, *Shape-induced force fields in optical trapping,* Nature Photonics **8**, 400 (2014).

[53] M. Jahnel, M. Behrndt, A. Jannasch, E. Schäffer, and S. W. Grill, *Measuring the complete force field of an optical trap,* Optics letters **36**, 1260 (2011).

[54] K. Berg-Sørensen and H. Flyvbjerg, *Power spectrum analysis for optical tweezers,* Review of Scientific Instruments **75**, 594 (2004).

[55] Z. Huang, F. Pedaci, M. van Oene, M. J. Wiggin, and N. H. Dekker, *Electron beam fabrication of birefringent microcylinders,* ACS nano **5**, 1418 (2011).

[56] A. Rohrbach and E. H. Stelzer, *Optical trapping of dielectric particles in arbitrary fields,* JOSA A **18**, 839 (2001).

[57] D. Bonessi, K. Bonin, and T. Walker, *Optical forces on particles of arbitrary shape and size,* Journal of Optics A: Pure and Applied Optics **9**, S228 (2007).

[58] L. Ling, F. Zhou, L. Huang, and Z.-Y. Li, *Optical forces on arbitrary shaped particles in optical tweezers,* Journal of Applied Physics **108**, 073110 (2010).

3

Tunable high-birefringence meta-material probes for optical torque wrench application

The optical torque wrench (OTW) allows the direct application and measurement of both torque and angle on single molecules or rotary nanomotors. To maximize the applicable torque in an OTW, it is preferable to use probe material with large birefringence. However, naturally available highly-birefringent materials also tend to exhibit large refractive index, which severely limits the trappable probe dimension due to the large scattering. To overcome this disadvantage, we here employ dielectric multilayer meta-material (MM) as probe material. We have designed the MM probe using effective medium theory and finite element methods. The MM probes are etched and released from a sputtered multilayer film. The results in the OTW show that our MM probe can achieve a large birefringence at only moderate refractive index, displaying its superiority over existing probes. Moreover, the MM probe comes with tunability in its optical properties through changing the composite material filling ratio.

3.1. Introduction

The optical torque wrench (OTW) [1–3] enables the rotational control in optical tweezers, providing the true ability to three-dimensional manipulation of micron-scale particles, which opens up new opportunities for many applications in the micron and nano-scale, such as biological physics [4–7], optomechanics [8–10], quantum physics [11–13].

A variety of methods for optical rotation have been proposed and realized [14–18]. The fundamental principle behind is altering the angular momentum (AM) of a trapping focus beam, where the difference is transfered to the trapped particle [1]. The simplest and most sophisticated method is to use linearly polarized beam[7, 17, 19] or circularly polarized beam [20–23] in combination with birefringent probe particles [3, 24–26]. On one hand, using orbital angular momentum (OAM) for torque transfer requires extra apparatus for beam generation and AM detection [16, 27–29]. Also, the beam waist at the focus is broaden due to its donut shape intensity profile [30], which decreases linear gradient force and makes it unsuitable for small particle rotation. On the other hand, changing and detecting the spin angular momentum (SAM) of TEM_{00} Gaussian beam is trivial [31], which makes in-vivo rotation and measurement available [2, 3]. The rotation of the particle can be done either at a controlled speed with the rotation of linear-polarized light [2, 31] or at a constant torque with a circular polarized light [14].

The AM of the light is transfered to the particle through absorption [16] or scattering [32]. Absorption is essential for homogeneous isotropic particles to receive torque, which has been broadly applied in rotating metallic particles [16, 28, 33–35]. However, absorption is a detriment in most of the biological applications as the heat generated by this process can severely damage the biological cells and tissues [36]. The asymmetric shape of the particle can have different dielectric polarizabilities along different directions, and hence induces an aligning torque which aligns itself with respect to the direction of polarization of the beam [7, 13, 21]. However, this asymmetric torque transfer is inefficient [7, 8, 37] and the particle's irregular shape bring unwanted large viscous drag to many torque applications. Birefringent particles simply act as a wave plate, which alter the AM carried by the focus field, where the difference of AM is converted to the optical torque on the particle with negligible thermal effects [38]. Moreover, the shape of the birefringent particle can be tailored into cylindrical shape by nano-fabrication [24, 39, 40], which makes its position very stable in the focus and it is rotation controllable. These unique properties make it the ideal probe for biological applications [41].

The amount of transferable AM to the particle is mainly limited by the birefringence and the volume of the probe [38]. In literatures, many different birefringent probes are used to achieve the OTW functionality. Main materials are as quartz [1–3], calcite[19], vaterite[26, 42] and rutile [43]. The refractive indexes of these materials are shown in Fig. 3.1a. Nevertheless, each of these materials have their own limitation. Quartz SiO_2 particle is readily accessible in spherical shape or cylindrical shape by nano-fabrication [24, 39, 40], and possess stable chemical property in aqueous environment. However, its low birefringence (Δn=0.0087 at λ=1064 nm) severely limits the transferable torque to the material. Although the

amount of torque can be increased by enlarging the size of the probe, this will not only makes it unsuitable for single molecular torque application, but also tremendously reduces the rotational speed induced by the larger viscous drag from the surrounding medium. Both calcite and vaterite $CaCO_3$ probes have much higher birefringence (Δn= 0.1629 at λ=1064 nm) and are being used in many optical torque applications especially in vacuum [44]. However, they are solvable in water, which makes them unsuitable for biological applications. Recently we have proposed to use nanofabricated rutile TiO_2 cylinder [43, 45] as OTW probe, which has the highest birefringence (Δn= 0.26 at λ=1064 nm) among all the natural crystalline materials. Although the achievable torque and force are further increased, it suffers from large scattering due to the extraordinary high refractive index ($\bar{n} = 2.623$ at λ=1064 nm), and hence reduces the trappable size down to only around 300 nm in diameter. As far as we know, a suitable birefringent probe particle with moderate refractive index and large birefringence is still missing.

The nano-fabrication techniques have enabled the realization of nano-structures where the feature size is much smaller than the wavelength of light, and hence leads to new electromagnetic properties unseen in nature [46–48]. This new form of materials are called meta-materials (MMs). Amount all the MMs, the laminated MMs [49] draw tremendous attentions, and have been widely applied in photonic density of states engineering [50], super-resolution imaging [51, 52], waveguide engineering [53–55] and optical sensing [56–58]. The fabrication of laminated MMs can be achieved simply by sequentially depositing alternating materials on a wafer by such as sputtering [59], electron beam evaporation [60], atomic layer deposition [61]. The large number of available materials makes it a versatile tool for achieving exotic material properties.

In this chapter, we demonstrate, by using nano-fabrication technology, a realization of laminated MM OTW probe with SiO_2 and Nb_2O_5 materials. Unlike conventional OTW probes, this MM probe can have large birefringence with a moderate refractive index suitable for stable 3D trapping. Moreover, by simply changing the filling ratio of the composed materials, the property of the OTW probe can be customized by will, which makes the probe more adaptive to specific applications. The fabricated probe is chemically stable and the shape is highly controllable, which makes it ready for volume production.

3.2. Methods

3.2.1. Design

The effective medium theory (EMT) [62] is used to calculate the optical response of the multilayer structure. According to EMT, when the thickness of each layer is much smaller than the wavelength of the light, the effective optical permittivity of the structure can be approximated by a tensor

$$\underline{\underline{\epsilon}} = \begin{bmatrix} \epsilon_{\parallel} & 0 & 0 \\ 0 & \epsilon_{\parallel} & 0 \\ 0 & 0 & \epsilon_{\perp} \end{bmatrix}, \tag{3.1}$$

where $\epsilon_{\parallel}$ and $\epsilon_{\perp}$ are the permittivity component parallel and perpendicular to the interface of the multilayer stack, respectively. The values of them are given by

$$\epsilon_{\parallel} = f\epsilon_1 + (1-f)\epsilon_2, \tag{3.2}$$

$$\epsilon_{\perp} = \frac{1}{f\epsilon_1^{-1} + (1-f)\epsilon_2^{-1}}, \tag{3.3}$$

where f is the material filling ratio of material 1 in a unit cell and ϵ_1 and ϵ_2 are the permittivity values of the two consisting materials, respectively.

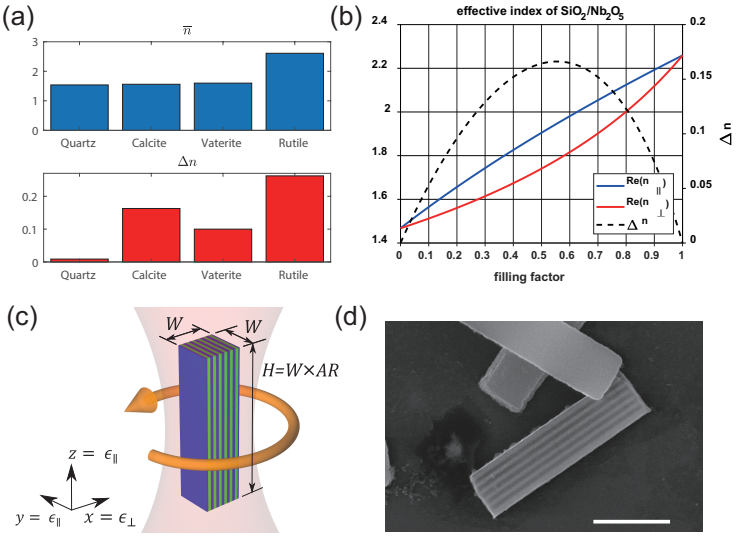

Figure 3.1: (a) The average refractive index (top) of the most common birefringent crystals materials in nature and their index difference (bottom); (b) The effective index and index difference of SiO_2 and Nb_2O_5 multilayer structure as a function of material filling factor. (c) Schematic of how is the nano-cylinder being trapped in the focus of the beam. (d) Scanning electron microscopy (SEM) image of fabricated multilayer particles with $f = 0.5$, $W = 300$ nm and $AR = 4$.

The consisting material of the MM chosen here are Nb_2O_5 (material 1) and SiO_2 (material 2), which can be deposited by sputtering [63]. In Fig. 3.1b the effective refractive index of Nb_2O_5 and SiO_2 multilayer stack versus filling ratio are shown. It can be seen that the refractive index component $n_{\parallel}$ is a straight line as a function of filling ratio f, while the refractive index component $n_{\perp}$ is a concave curve, being always smaller than $n_{\parallel}$. The difference induces a birefringent effect. Since $n_{\perp}$ is the only unique component in the tensor, one can conclude that effectively the multilayer MM behaves as a negative birefringent material with $n_{\parallel}$ $(n_e) < n_{\perp}$ (n_o). As shown in Fig. 3.1c, in order to achieve rotation along the axis of the beam (z-axis), the designed particle requires an elongated-cube shape with its multilayer interface parallel to the beam axis. This allows the longer side (H) to align with the beam axis and maintain the birefringence in the $x-y$ plane. The cross-section of the particle is designed to be a square of width W, which can eliminate the influence of the torque induced by the shape asymmetry.

Fig. 3.1b also shows that the two effective indexes both vary as filling ratio varies, which is a result of increasing the higher index Nb_2O_5 material. For smaller filing ratio, the MM can have a overall smaller refractive index, hence the MM is easier to trap due to the small scattering force. On the other hand, for MMs with higher filling ratio, the MM may experiences a higher gradient force due to the higher index contrast. However, this is at the risk of being untrappable while scattering force is also enhanced. The dashed line of Fig. 3.1b also shows the index difference. We can see that the maximum $\Delta n = 0.1662$ is achieved at around $f = 0.55$, which provides a birefringence slightly larger than Calcite. We may interpret that for the same material dimension, the maximum torque transfer can be achieved for this filling ratio. If we further increase the filling ratio, the linear trapping stiffness can be further increased due to the larger index contrast, while the torque transfer efficiency can be reduced. Hence, depending on the required application, the material filling ratio can be chosen for best suitability.

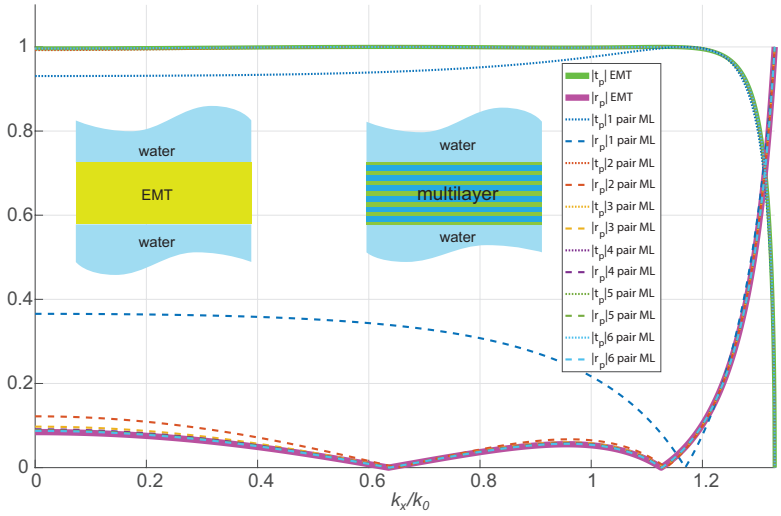

Figure 3.2: The absolute value of Fresnel coefficient t_p and r_p of effective medium theory (EMT) and SiO_2/Nb_2O_5 multilayer (ML) structures as function of transversal wavenumber. The incident and exit material are both water, the total thickness are both 300 nm for EMT and ML, and the wavelength is 1064 nm. For n pair of ML, in order to have a symmetric structure, we always keep the starting/ending layer SiO_2. The inserts show the schematics of EMT model and 5 pair ML model.

In order to understand the accuracy of the EMT approximation, the Fresnel coefficients of the real multilayer are calculated and being compared to the effective birefringent medium. In the calculation, the incident and the transmission materials are both water, and the middle layer is either the multilayer stack or the effective birefringent MM, with a fix total thickness of 300 nm. The number of layer-pairs varies from 1 to 6. As shown in Fig. 3.2, the Fresnel coefficients of the real multilayer structure get closer to the one of the effective birefringent medium as the number of layer-pairs increases. For the five layer-pair case, the maximum difference in the coefficients is smaller than 0.4%. This result confirms that the EMT is a good

description for our multilayer structure.

3.2.2. Modeling

Finite element method (FEM) software COMSOL Multiphysics 5.2a is used to calculate the optical response of our MM probes. The cube-shape probe particle is surrounded by a uniform medium (water $n = 1.33$) of spherical shape with the perfect match layer (PML) shell. The scattering of the particle is calculated under the background illumination of a highly focus Gaussian beam incident from the negative z-direction. The x-polarized highly focus field is described by Richards & Wolf's integral [64, 65]. The numerical aperture (NA) used is 1.2 and the aperture filling factor is 1.7, which are identical to our experimental setup. The optical force and the torque are retrieved by integrating Maxwell stress tensor on a virtual sphere surrounding the particle [66].

First, in order to determine the trappability and equilibrium position of the probe, the optical force F_z in the z-direction is calculated. In the simulation, the particle is fixed in the center of the domain and the focus beam is moved up and down to calculate the force on the particle at different z-position. The equilibrium position Z_{eq} is found when the particle experiences zero F_z. Second, after knowing the equilibrium position Z_{eq} of the particle, the particle is fixed on this z-position and F_x, F_y and T_z are calculated, which are the force in the x and y-direction and the torque in the z-direction, respectively. For F_x (F_y) calculation, the focus beam is moved in the x (y)-direction. For the T_z calculation, the particle is rotated 45 ° along the z-axis respecting to the polarization direction of the focus beam. The heights of the particle H modeled are between 250 nm and 450 nm with an incremental step of 5 nm, and the aspect ratio (AR = H/W, where W is the side length of the cube particle) is from 1 to 7, with an incremental step of 0.1. In order to reduce the computational time, the symmetric condition is utilized in the F_z, F_x, F_y simulation. One quarter of the computational domain is simulated in F_z and half of the computational domain is simulated in F_x and F_y.

The viscous drag coefficients are also simulated using the Computational Fluid Dynamics (CFD) module in COMSOL. The surrounding medium (H_2O) is set to flow translationally (or rotationally), inducing viscous drag force (or torque) on the nanocube. The solutions of Navier-Stokes equations result in force and torque as a function of the speed of the medium flow, from which the linear (rotational) drag coefficients can be extracted.

3.2.3. Fabrication

The multilayer MM particles are fabricated using a top-down fabrication process (Fig. 3.3), which is adapted from our previous work [43, 45]. First, a four-inch silicon (Si) wafer is cleaned with fuming (99.5%) HNO_3 (10 min), followed by thoroughly washing with DI and spin dry (Fig. 3.3a). Next, a 100 nm-thick sacrificial chromium (Cr) layer is deposited on the Si wafer by electron-beam evaporation (FC-2000, Temescal) with the film deposition rate of 0.5 Å/s at the chamber pressure of $\sim 3\times10^{-7}$ Torr (Fig. 3.3b). This slow deposition allows to obtain a high-quality Cr-coating with small surface roughness. Then, the Nb_2O_5/SiO_2 multilayer is deposited using plasma-assisted

reactive magnetron sputtering (HELIOS, Bühler) (Fig. 3.3c), with which the layer thicknesses are precisely monitored and controlled with the aid of in-situ ellipsometry). The whole multilayer stack is designed to be symmetric by starting and finishing with SiO_2 layers. The detailed multilayer composition of the fabricated samples are described in Supplementary Table 3.1. The particles of square cuboid

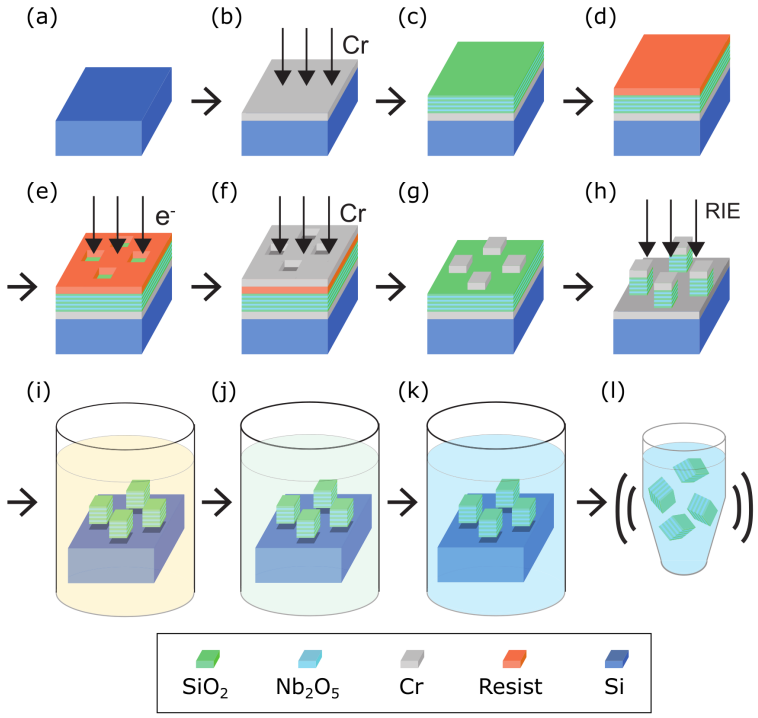

Figure 3.3: The fabrication process of meta-material probe particles.(a) Sequencial deposition of the Cr sub-layer and the multilayer, followed by the spin-coating of a positive electron beam resist. (b) Patterning of the resist layer with electron beam lithography. (c) Sputter deposition of a layer of Cr hard mask. (d) Removal of the unwanted Cr mask and the residual resist by firstly using Kapton tape and then heated resist stripper. (e) Etching into the multilayer structure vertically by reactive ion etching. (f) Removal of the top Cr hard mask layer and the bottom sacrificial Cr layer by using a chromium wet etchant. The sample is submerged into the etchant solution vertically and gently without any agitation.(g) Washing off the chromium etchant by dipping the sample into ample amount of DI water, again without any agitation. (h) Harvesting the fabricated particles by submerging the sample into DI water-filled plastic tube and vortexing for 1 min. Then the substrate is removed from the tube.

geometry are shaped by lithography and etching with Cr hard mask. The substrate is first machine-diced to 1 cm × 1 cm sizes, which are then cleaned with HNO_3 and DI as like the Si wafer preparation step. Then, the samples are further cleaned in an ultrasonic bath with acetone (5 min) and isopropyl alcohol (IPA, 5 min), and spin-dried. A layer of ~250 nm-thick positive-tone electron-beam resist (AR-P 6200.9, Allresist) is spin-coated (Fig. 3.3d) and patterned by electron-beam lithog-

raphy (EBPG 5000+,Vistec) with an exposure dose of 240 μC/cm^2 (Fig. 3.3e). The particles are patterned in a hexagonal array (Fig. 3.4), with a large enough gap size (1 μm) between adjacent particles for a better wetting in the later Cr wet etching step. The development of the patterned resist layer is performed with ultrasonication, sequentially dipping the sample in pentyl acetate (2 min), 1:1 mixture of methyl isobutyl ketone (MIBK) and IPA (1 min), and then IPA (1 min), followed by spin dry. A hard etch mask layer (∼70 nm-thick Cr) is deposited by argon (Ar)-plasma sputtering (AC450, Alliance Concept), with radio frequency (RF) power of 100 W, Ar supply of 20 sccm, and chamber pressure of 100 μbar (Fig. 3.3f). This sputtering condition is optimized for conformal deposition of Cr, allowing the enhanced etch mask shape which results in more vertical sidewalls after etching [45]. For lift-off, adhesive tape (Kapton) is initially used to remove most of the top Cr layer, and then the remaining resist layer is removed by dipping the sample in PRS-3000 (J.T.Baker) resist stripper at 80 °C for 30 min (Fig. 3.3g). After rinsing the sample thoroughly with DI and spin-drying, a reactive ion etcher (RIE; Fluor Z401S, Leybold Hereaus) is used for etching the multilayer vertically (Fig. 3.3h). The mixture of CHF_3 (50 sccm) and O_2 (3 sccm) is used for this dry etching [43], in which the chamber pressure and the RF power are 50 μbar and 200 W, respectively (resulting the multilayer etch rate of ∼50 nm/min). For ensuring the complete removal of the multilayer film within the unmasked region, ∼15 s of additional etching is done after observing the endpoint by a laser interferometer (LEM, HORIBA Scientific). In the same RIE machine, an Ar-plasma sputter cleaning process (20 sccm Ar flow, 10 μbar chamber pressure, and 100 W RF power) is performed for 5 min to remove the oxidized Cr layer on the surface of the hard mask and the sacrificial layer, which is probably induced during the previous etching step. This additional step substantially enhances the wet etching process of the remnant Cr layers in the later step as such oxidized Cr is much less dissoluble in Cr etchant solution.

To retrieve the particles, the samples are manually cleaved into 5 mm × 5 mm chips. Each chip is firstly soaked in a Cr etchant solution (dark yellow; TechniEtch Cr01, MicroChemicals) for 10 min, where the top Cr mask and the bottom sacrificial Cr layer are dissolved altogether (Fig. 3.3i). Then, the chip is gently immersed into ample amount of DI water for 30 s for the initial washing of Cr etchant droplets (the color of DI water turns into light yellow after washing) (Fig. 3.3j, followed by the second immersion into another beaker of ample DI water for 1 min without any agitation, which completely removes all etchant from its surface (the DI water after washing remains as transparent as the fresh DI water) (Fig. 3.3k. Until this second immersion into the DI beaker, the most MM particles are still staying on the surface. However, they become visibly released from the surface when the chip is very slowly taken out from the second DI beaker and passing through the water-air interface while keeping its surface facing upward, presumably due to the surface tension of the water. The taken out chip and the water droplet (which is already containing many released particles) on its surface are then transferred together into a 2 mL-volume plastic tube containing fresh DI of 200 μL, followed by vortexing of the tube for 30 s (Fig. 3.3l). The chip, whose surface is only clean Si after the vortexing, is removed from the tube and the remaining particle solution has concentration of

$\sim 2\times10^4$ particles per µL, considering the pitches of the particle array (Fig. 3.4). As the particles are directly dispersible into the water, the fraction of actually collected particles is much higher than what we have observed from our another top-down protocol without using a sacrificial layer, in which some fraction of particles are lost by contacting a sharp blade and a pipette tip [45]. By SEM inspection of the randomly dispersed MM particles on a Si substrate, the complete removal of both top Cr layer as a hard mask and bottom Cr layer as a sacrificial layer has been observed (Fig. 3.4). This observation is further confirmed by the stable 3D optical trapping of MM particles, as such trapping would not be possible due to the high scattering force if there remains any Cr layer on MM particle surface.

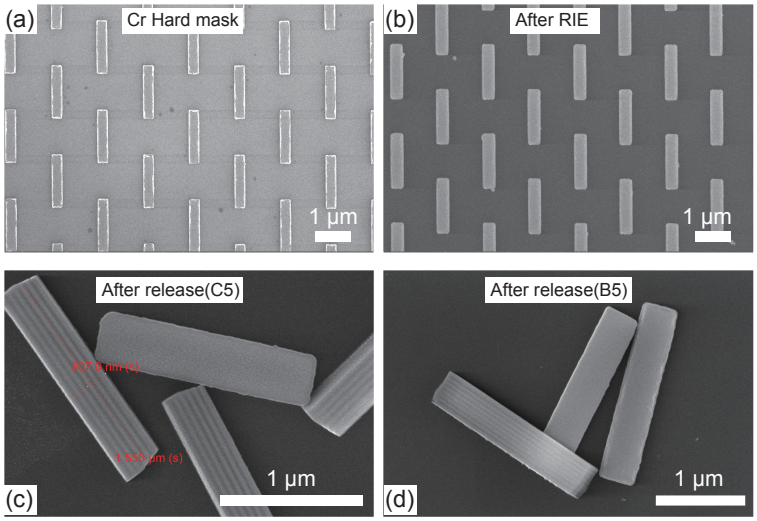

Figure 3.4: Scanning electron microscopy (SEM) image of (a) top view of multilayer particles with Cr hard mask after lift-off process; (b) top view of multilayer sample with Cr hard mask after reactive ion etching (RIE); (c) Square cuboid particle C5 after release from the substrate; (d) Square cuboid particle B5 after release from the substrate.

3.2.4. Experiment

The OTW experiments are conducted on our home-built setup shown in Fig. 3.5. The optical isolator (OI) and acoustic-optic modulator (AOM) together provide a stable laser output at a wavelength of 1064 nm. The electro-optic modulator (EOM) is used for active control of the polarization state of the laser beam and the beam is expanded to the required diameter. A reference branch is used to monitor the output polarization state of the beam after the EOM, which consist of two quarter wave-plate (QWP), polarized beam splitter (QBS) and two photo-diodes (PDs). After sending the light through the objective, another identical objective is used to collect the light. The position sensitive detector (PSD) is used to measure the linear displacement of the probe, and the two PDs in the detection branch are used to measure the torque transfered to the probe particle. The detailed measurement

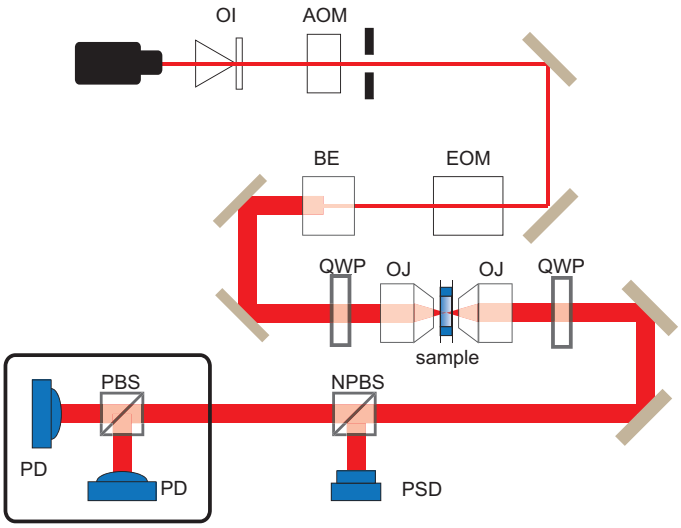

Figure 3.5: Schematic of the experimental setup. OI: optical isolator; AOM: acoustic-optic modulator; BE: beam expander; EOM: electro-optic modulator; NPBS: non-polarizing beam splitter; QWP: quarter wave-plate; PBS: polarizing beam splitter; PD: photo-detector; PSD: position sensitive detector; OJ: microscope objective.

principle can be found in [31]. For the sample holder, we use a custom-made flow cell assembled with two borosilicate glass coverslips (No. 1.5H, Marienfeld) separated by a single-layer Parafilm spacer of ~100 μm thickness. The use of coverslips with high-precision thickness (170±5 μm for No. 1.5H) reduces possible variations in optical trap quality that might occur when the conventional coverslips with large thickness variation (e.g., 160–190 μm for No. 1.5) are used 61. The PBS buffer containing the nano-cylinders are injected into the flow cell channel and both input and output of the channel are sealed by vacuum grease (18405, Sigma-Aldrich). After more than an hour, most of the nano-cylinders in the solution are still floating in the flow cell. Afterwards, we can trap and measure the freed nano-cylinders without any hydrodynamic coupling effect that can occur if the particle concentration is too high. Also, it is possible to measure for extended times (tested up to ~3 hours) without losing the particle by collision with other particles entering the optical trap. The nano-cylinder trapping position is kept as ~20 μm above the bottom surface of the flow cell channel, to effectively avoid any hydrodynamic interaction with the flow cell.

We measured on all 10 different MM nano-cylinder batches, and 3–9 particles were recorded for each batch. For calibration of linear and angular trapping properties, we have adapted the previously developed methods [31]. Also, in power spectrum analysis, we properly considered the hydrodynamic effect arising from the large stiffnesses of MM probes. The linear and angular fluctuation data are acquired at a 250 kHz sampling frequency. A frequency sweep method is used for the torque measurement. In this method, each curve is measured by continu-

ously scanning the polarization rotation frequency in the range of 0–15 kHz for a few seconds using a waveform generator (33120A, Agilent) at 100 kHz sampling frequency. Compared to the conventional time-consuming method in which many number of data traces are recorded at each different constant frequency, this high-speed recording over a wide frequency range avoids the distortion of the measured curve caused by setup drift.

3.3. Results

3.3.1. Modeling results

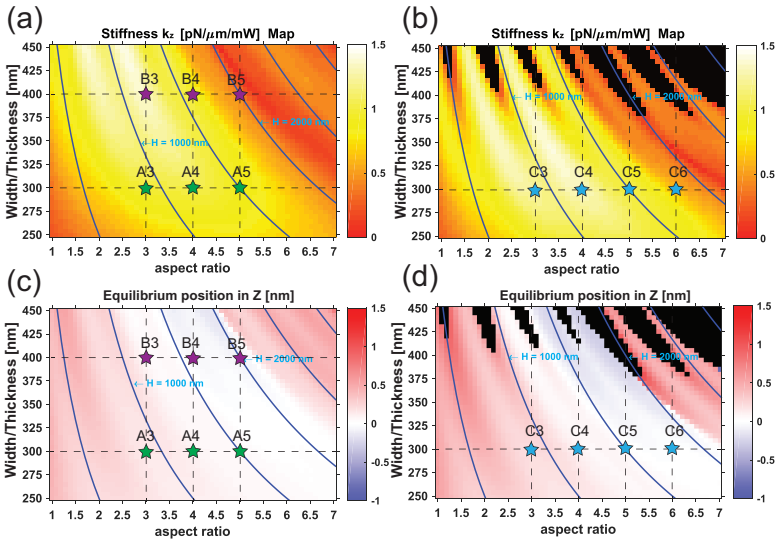

Figure 3.6: The stiffness map and equilibrium position map for different aspect ratio and width/thickness of the nano-cylinders. (a) (b): The stiffness map of the trapping in the z-direction; (c) (d): the equilibrium position of the particle along the z-direction. (a),(c) is for material filling ratio $f = 0.3$ and (b),(d) is for $f = 0.5$. The solid blue lines represent the equal height of the nano-cylinder with an interval of 500 nm

We have calculated the linear stiffness k_z for $f = 0.3$ and $f = 0.5$, which are shown in Fig.3.6a and Fig.3.6b, respectively. For our modeling, it can be seen from the figure that the nano-cylinders of $f = 0.3$ are trappable for all width and aspect ratio. And there are two peak stiffness lobes which are at around $W = 425$ nm, $AR = 2.7$ and $W = 425$ nm, $AR = 1.3$, with values around 1.39 pN/μm/mW. For the nano-cylinders of $f = 0.5$, the peak stiffness values are also around 1.39 pN/μm/mW, which are achieved at the particle dimension of $W = 340$ nm, $AR = 3.4$ and $W = 360$ nm, $AR = 1.3$. It can be seen from Fig. 3.6c,d that, for both filling ratios, these stiffness peaks are achieved at a plane close to the focus center (Zeq = 0 nm), where the maximum gradient takes place. In Fig. 3.6b, the trappable and non-trappable boundary of the $f = 0.5$ particles is clearly seen, which is around 375-400 nm. This is caused by the large scattering force due to

the large effective refractive index of the materials. On the other hand, the $f = 0.3$ particles are all trappable for all dimensions in the map, and the maximum trappable width is around 525-550 nm (see Supplementary Fig. 3.11). This clearly indicates that for the force in the z-direction, the $f = 0.3$ and $f = 0.5$ particle has their own optimum performance region. And depending on the specific application, we can fabricate particles with a different filling ratio.

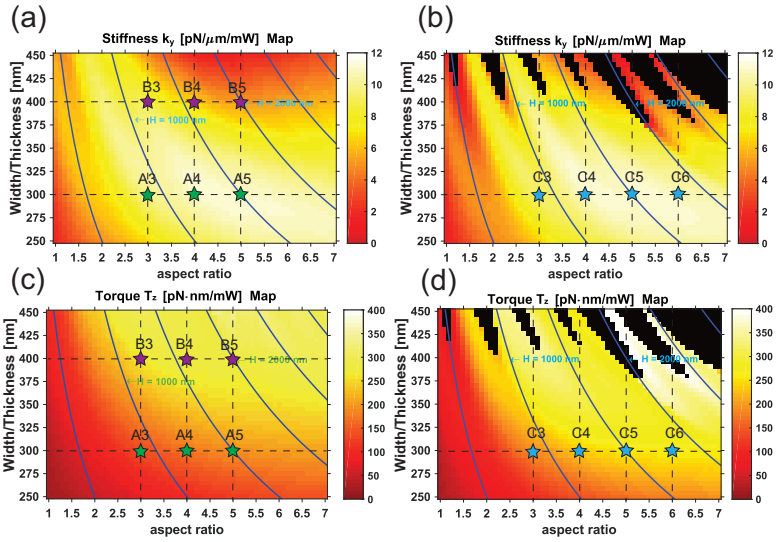

Figure 3.7: The stiffness k_y map (a) (b) and the maximum torque T_z map (c) (d) for different aspect ratio and width/thickness of the nano-cylinders. (a),(c) is for material filling ratio $f = 0.3$ and (b),(d) is for $f = 0.5$. The solid blue lines represent the equal height of the nano-cylinder with an interval of 500 nm.

When it comes to the lateral stiffness k_y in Fig. 3.7a and Fig. 3.7b, the performance becomes quite similar for both filling ratios. The maximum k_y are achieved at $W = 300$ nm, AR around 4~5. The result shows that the maximum transversal stiffness does not increase as the particle dimension increases, but is limited to an optimal width (around 300 nm).

The maximum torque results are shown in Fig. 3.7c and Fig. 3.7d. One can see that the maximum torque of the particles increases as the particle size grows. This is due to the fact that the torque transfer efficiency does not depend on the gradient of the focus field, but on the interaction volume with the focus light [38]. Hence, while the size of the particle is comparable to the shape of the focus field, the transfer of torque is proportional to the size of the particle. For the $f = 0.5$ nano-cylinders, the maximum torque of the same geometry is larger than the one of the $f = 0.3$ nano-cylinders due to its higher birefringence. Although the maximum torque is around 400 pN $\cdot$ nm/mW, it is very difficult to utilize as those particle dimension is located at the finger area [67], which requires both high fabrication precision and good optical system alignments. On the other hand, the $f = 0.3$ nano-cylinders only have a moderate torque value. But due to their low refractive

index, they can be trapped and rotated for every dimension shown in the map.

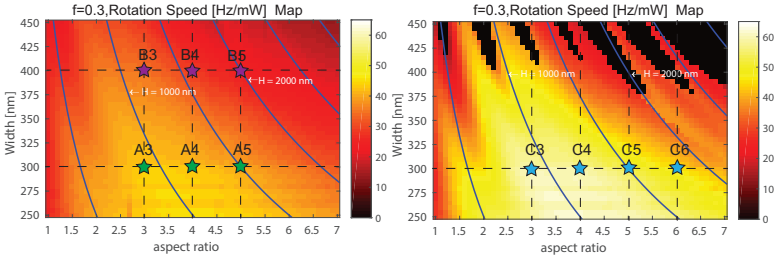

Figure 3.8: The rotational speed map for different aspect ratio and width/thickness of the nano-cylinders with material filling ratio $f = 0.3$ (a) and $f = 0.5$ (b). The solid blue lines represent the equal height of the nano-cylinder with an interval of 500 nm

In Fig. 3.8, we show the calculated rotational speed map for the nano-cylinders with a 1 mW input power. It can be seen that for both the material filling ratio particles, the maximum rotational speed are achieved at smaller dimensions. To be precise, the maximum rotational speed are achieved at width around 300 nm and aspect ratio around 3 to 4. This is due to the fact that the larger particles severely suffer from the drag force from the surrounding water medium and cannot rotate at a higher speed compared to smaller ones.

3.3.2. Experiment results

The linear trapping measurements of the nano-cylinders are shown in Fig. 3.9a. It can be seen that they behave very consistently, with a relative standard deviation (RSD=SD/mean×100) smaller than 10 percent. This confirms that our particles are very uniform and have controllable optical properties. For the linear stiffness, the measured linear stiffness are about 50 percent of the simulated ones. This result is expected as no optical aberration is considered in the simulation, which can play an important role for the stiffness measurement. In Fig. 3.9a, the measured linear drags along all directions are about 70 percent of the simulated ones. This can be explained that: in the simulation, the nano-cylinders are considered to be perfect with sharp edges, while in reality the particles always have rounded corners, which can have a reduced drag from the water.

The experimental results of the angular properties of the nano-cylinders are shown in Fig. 3.9b and Fig. 3.9c. It can been seen in Fig. 3.9c that again the rotational drag coefficients are smaller than the simulation ones. The explanation is similar to the linear drag, where the edges of the cylinders are smoother than the simulation and hence reduce the rotational drag as well. The measured rotational drags are about 60 percent of the simulated ones. For the angular stiffness in Fig. 3.9b, the measured values are about 55 percent of the simulated ones. And it can be seen that although A4 and C4 have the same geometry, because the filling ratios are different, the measured angular stiffness are different as well. The angular stiffness of C4 is about 65 pN · nm/rad/mW larger than A4. This matches with our theory that larger birefringence is more desirable for optical torque application.

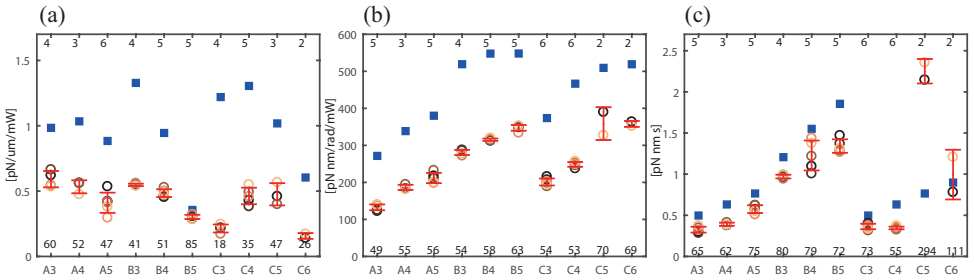

Figure 3.9: **Experimental results for all fabricated samples.** In all plots: the blue square denotes simulation value; the circles denote the measured value in experiment; the red bar denotes the standard deviation of the measurement; the x label denotes the name of the sample; the number at the bottom denotes the difference of measurement and simulation (measurement/simulation×100); the number on the top denotes the number of measured sample. (a) The linear stiffness k_z per milliwatt. (b) The angular stiffness k_r per milliwatt. (c) The angular drag γ_r in water. The data values shown in all panels are summarized in Supplementary Table 3.2

In Fig. 3.10, the maximum rotational frequency is also shown. The experimental values are almost equal to the simulated ones, which is a consequence of both the reduced rotational stiffness and the reduced rotational drag. For C4 particles, the rotation speed can go up to 5381 Hz at 92 mW input laser power with a maximum applicable torque of 11.436 nN·nm. On the other hand, A4 particles with the same size can only rotate at 3409 Hz with a maximum applicable torque of 8.578 nN·nm. This result shows that we are able to design and tune to optical property of the nano-cylinders by simply changing its material filling ratio, which opens up new opportunity in many applications. Again the statistic analysis shows that the fabricated samples have superior uniformity, where the RSD is only around 2 to 5 percent. This result means our fabrication process is stable and reproducible.

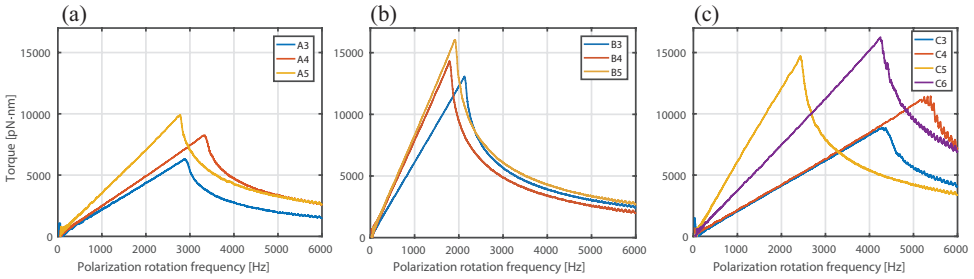

Figure 3.10: A typical frequency sweep trace measurement for (a) Sample A, (a) Sample B and (c) Sample C.

In Fig. 3.10, typical traces of transfer torque versus polarization rotation frequency are shown. It can be clearly seen that as the polarization rotation frequency increases, the amount of transferred torque also increases linearly. In this process, the angle between the in-plane electric-field and the n_o refractive index direction increases in order to maintain the proper amount of AM transfer. When the po-

larization rotation speed is further increased, the angular displacement gets larger and finally reach 45 degree where the maximum transferable torque can take place. After this point the particles can no longer follow the rotation of the polarization and hence the amount of transferred torque drops dramatically.

3.4. Conclusion

In this chapter, we have demonstrated a robust way to fabricate free-floating meta-material nano-particles. The nano-particles are fabricated by top-down method, using etching into a multilayer stack of sub-wavelength SiO_2 and Nb_2O_5 layers. The particles are released from the substrate by dissolving the Cr sacrificing layer in the Cr etchant. The meta-material particles are indissoluble in water and hence are compatible with biological applications. We are able to control the particle geometry precisely, where high geometrical uniformity is shown. Moreover, the density of the nano-particles dispensed in water can reach 22000/uL, which is more than enough for many applications.

The fabricated nano-particles have unique optical birefringence and index combination that are not seen in nature. By changing the ratio of composited materials, we are able to tune the optical property of the nano-particles. Our calculation shows that the particles are able to exhibit a birefringence that is comparable to the calcite $CaCO_3$ crystal.

We have both theoretically calculated and experimentally demonstrated the application of our fabricated nano-particles as optical torque wrench probes. The results show that our probes have moderate refractive index and very high birefringence. The probes are highly efficient in torque transfer, which can generate a torque value at $nN \cdot nm$ level. This is by far the highest torque that can be achieved in the micro scale. Overall, the potential of meta-material nano-particles are demonstrated, and it is expected to expand the library of materials for optical torque transducers.

3.5. Supplementary Materials

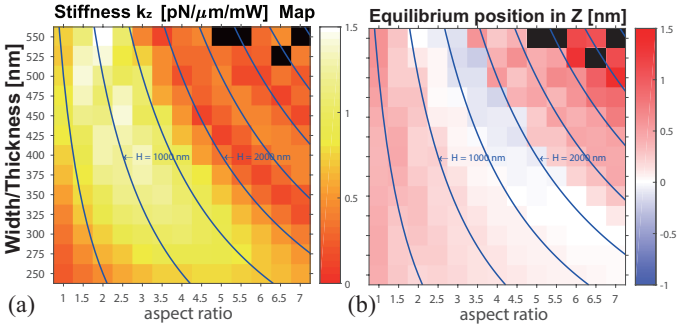

Figure 3.11: Extended linear stiffness k_z map (a) and equilibrium position map (b) for material filling ratio $f = 0.3$. The solid blue lines represent the equal height of the nano-cylinder with an interval of 500 nm. The black pixels indicates that the particle is not trappable in this geometry.

Table 3.1: The thickness of each consisting layer in fabrication for sample A, B and C. The layer 0 is the sacrificing chromium layer.

		Sample A	**Sample B**	**Sample C**
Layer no.	**material**	**thickness / nm**	**thickness / nm**	**thickness / nm**
0	**Cr**	100	100	100
1	SiO_2	17.5	17.5	12.5
2	Nb_2O_5	15	15	25
3	SiO_2	35	35	25
4	Nb_2O_5	15	15	25
5	SiO_2	35	35	25
6	Nb_2O_5	15	15	25
7	SiO_2	35	35	25
8	Nb_2O_5	15	15	25
9	SiO_2	35	35	25
10	Nb_2O_5	15	15	25
11	SiO_2	35	35	25
12	Nb_2O_5	15	15	25
13	SiO_2	17.5	35	12.5
14	Nb_2O_5		15	
15	SiO_2		35	
16	Nb_2O_5		15	
17	SiO_2		17.5	
	total	300	400	300

Table 3.2: The FEM-cacluated and OTW-measured linear and angular stiffness and drag values.

Parameter	Unit	A3	A4	A5	B3	B4	B5	C3	C4	C5	C6
γ_y (mean)	pN·s/mm	**3.9**	**5.1**	**6.6**	**7.5**	**9.4**	**10.6**	**4.1**	**4.8**	**8.0**	**8.9**
γ_y (SD)	pN·s/mm	0.3	0.2	0.1	1.0	0.4	0.3	0.2	0.5	0.8	0.5
γ_y (cal.)	pN·s/mm	6.1	7.1	8.1	8.1	9.5	10.9	6.1	7.1	8.1	0.0
κ_y (mean)	pN/μm/mW	**2.6**	**4.4**	**5.2**	**5.9**	**7.1**	**6.7**	**3.2**	**5.5**	**7.3**	**6.8**
κ_y (SD)	pN/μm/mW	0.1	0.1	0.0	0.8	0.3	0.4	0.1	0.8	0.6	0.5
κ_y (cal.)	pN/μm/mW	9.8	10.8	10.9	8.8	6.5	5.2	9.3	10.9	11.0	10.7
$\tau_{c,y}$ (mean)	μs (at 100 mW)	**14.7**	**11.7**	**12.9**	**12.6**	**13.2**	**15.8**	**13.0**	**8.7**	**11.0**	**13.0**
$\tau_{c,y}$ (SD)	μs (at 100 mW)	1.3	0.4	0.3	2.4	0.8	1.1	0.6	1.5	1.5	1.1
$\tau_{c,y}$ (cal.)	μs (at 100 mW)	6.2	6.6	7.4	9.2	14.7	20.9	6.6	6.5	7.4	0.0
N_y		6	3	6	4	4	5	5	5	6	7
γ_θ (mean)	pN·nm·s	**0.32**	**0.39**	**0.58**	**0.98**	**1.23**	**1.35**	**0.37**	**0.35**	**0.53**	**0.58**
γ_θ (SD)	pN·nm·s	0.03	0.02	0.04	0.02	0.16	0.06	0.03	0.02	0.03	0.02
γ_θ (cal.)	pN·nm·s	0.50	0.63	0.76	1.21	1.55	1.85	0.50	0.63	0.76	0.90
κ_θ (mean)	pN·nm/rad/mW	**133**	**186**	**213**	**282**	**317**	**350**	**203**	**249**	**283**	**288**
κ_θ (SD)	pN·nm/rad/mW	6	7	13	6	4	6	6	6	5	5
κ_θ (cal.)	pN·nm/rad/mW	271	338	380	519	548	548	374	467	509	519
$\tau_{c,\theta}$ (mean)	μs (at 100 mW)	**24.3**	**21.2**	**27.1**	**34.9**	**38.9**	**38.6**	**18.1**	**13.9**	**18.8**	**19.9**
$\tau_{c,\theta}$ (SD)	μs (at 100 mW)	2.4	1.4	2.6	1.0	5.2	2.0	1.5	0.7	1.1	0.7
$\tau_{c,\theta}$ (cal.)	μs (at 100 mW)	18.3	18.7	20.1	23.2	28.3	33.8	13.3	13.5	15.0	17.3
τ_o	nN·nm (at 100 mW)	**6.6**	**9.3**	**10.6**	**14.1**	**15.9**	**17.5**	**10.2**	**12.4**	**14.2**	**14.4**
f_o	kHz (at 100 mW)	**3.3**	**3.8**	**2.9**	**2.3**	**2.0**	**2.1**	**4.4**	**5.7**	**4.2**	**4.0**
N_θ		5	3	5	4	5	5	6	6	4	7

References

[1] A. La Porta and M. D. Wang, *Optical torque wrench: angular trapping, rotation, and torque detection of quartz microparticles,* Physical review letters **92**, 190801 (2004).

[2] J. Inman, S. Forth, and M. D. Wang, *Passive torque wrench and angular position detection using a single-beam optical trap,* Optics letters **35**, 2949 (2010).

[3] F. Pedaci, Z. Huang, M. Van Oene, S. Barland, and N. H. Dekker, *Excitable particles in an optical torque wrench,* Nature Physics **7**, 259 (2011).

[4] S. Forth, M. Y. Sheinin, J. Inman, and M. D. Wang, *Torque measurement at the single-molecule level,* Annual review of biophysics **42**, 583 (2013).

[5] J. Ma, L. Bai, and M. D. Wang, *Transcription under torsion,* Science **340**, 1580 (2013).

[6] X. Liu, J. Huang, Y. Li, Y. Zhang, and B. Li, *Rotation and deformation of human red blood cells with light from tapered fiber probes,* Nanophotonics **6**, 309 (2017).

[7] G. Garab, P. Galajda, I. Pomozi, L. Finzi, T. Praznovszky, P. Ormos, and H. Van Amerongen, *Alignment of biological microparticles by a polarized laser beam,* European Biophysics Journal **34**, 335 (2005).

[8] X.-F. Lin, G.-Q. Hu, Q.-D. Chen, L.-G. Niu, Q.-S. Li, A. Ostendorf, and H.-B. Sun, *A light-driven turbine-like micro-rotor and study on its light-to-mechanical power conversion efficiency,* Applied Physics Letters **101**, 113901 (2012).

[9] T. Asavei, T. A. Nieminen, V. L. Y. Loke, A. B. Stilgoe, R. Bowman, D. Preece, M. J. Padgett, N. R. Heckenberg, and H. Rubinsztein-Dunlop, *Optically trapped and driven paddle-wheel,* New Journal of Physics **15**, 063016 (2013).

[10] I. Williams, E. C. Oğuz, T. Speck, P. Bartlett, H. Löwen, and C. P. Royall, *Transmission of torque at the nanoscale,* Nature Physics **12**, 98 (2016).

[11] L. Magrini, R. A. Norte, R. Riedinger, I. Marinković, D. Grass, U. Delić, S. Gröblacher, S. Hong, and M. Aspelmeyer, *Near-field coupling of a levitated nanoparticle to a photonic crystal cavity,* Optica **5**, 1597 (2018).

[12] R. Reimann, M. Doderer, E. Hebestreit, R. Diehl, M. Frimmer, D. Windey, F. Tebbenjohanns, and L. Novotny, *Ghz rotation of an optically trapped nanoparticle in vacuum,* Physical Review Letters **121**, 033602 (2018).

[13] J. Ahn, Z. Xu, J. Bang, Y.-H. Deng, T. M. Hoang, Q. Han, R.-M. Ma, and T. Li, *Optically Levitated Nanodumbbell Torsion Balance and GHz Nanomechanical Rotor,* Physical Review Letters **121** (2018).

[14] K. D. Wulff, D. G. Cole, and R. L. Clark, *Controlled rotation of birefringent particles in an optical trap,* Applied Optics **47**, 6428 (2008).

[15] R. Diekmann, D. L. Wolfson, C. Spahn, M. Heilemann, M. Schüttpelz, and T. Huser, *Nanoscopy of bacterial cells immobilized by holographic optical tweezers,* Nature Communications **7**, 13711 (2016).

[16] L. Shao and M. Käll, *Light-Driven Rotation of Plasmonic Nanomotors,* Advanced Functional Materials **28**, 1706272 (2018).

[17] M. S. Aporvari, F. Kheirandish, and G. Volpe, *Optical Trapping and Control of a Dielectric Nanowire by a Nanoaperture,* Optics Letters **40**, 1 (2015).

[18] A. Ivinskaya, M. I. Petrov, A. A. Bogdanov, I. Shishkin, P. Ginzburg, and A. S. Shalin, *Plasmon-assisted optical trapping and anti-trapping,* Light: Science & Applications **6**, e16258 (2016).

[19] M. E. J. Friese, T. A. Nieminen, N. R. Heckenberg, and H. Rubinsztein-Dunlop, *Optical alignment and spinning of laser-trapped microscopic particles,* Nature **394**, 348 (1998).

[20] F. Hajizadeh, L. Shao, D. Andrén, P. Johansson, H. Rubinsztein-Dunlop, and M. Käll, *Brownian fluctuations of an optically rotated nanorod,* Optica **4**, 746 (2017).

[21] N. Sule, Y. Yifat, S. K. Gray, and N. F. Scherer, *Rotation and Negative Torque in Electrodynamically Bound Nanoparticle Dimers,* Nano Letters **17**, 29 (2017).

[22] S. Kuhn, B. A. Stickler, A. Kosloff, F. Patolsky, K. Hornberger, M. Arndt, and J. Millen, *Optically driven ultra-stable nanomechanical rotor,* Nature Communications **8**, 1670 (2017).

[23] S. Kuhn, A. Kosloff, B. A. Stickler, F. Patolsky, K. Hornberger, M. Arndt, and J. Millen, *Full rotational control of levitated silicon nanorods,* Optica **4**, 356 (2017).

[24] Z. Huang, F. Pedaci, M. Van Oene, M. J. Wiggin, and N. H. Dekker, *Electron Beam Fabrication of Birefringent Microcylinders,* ACS Nano (2011).

[25] P. B. Bareil and Y. Sheng, *Optical trapping of the anisotropic crystal nanorod,* Optics Express **23**, 13130 (2015).

[26] A. I. Bishop, T. A. Nieminen, N. R. Heckenberg, and H. Rubinsztein-Dunlop, *Optical Microrheology Using Rotating Laser-Trapped Particles,* Physical Review Letters **92** (2004).

[27] D. Gao, W. Ding, M. Nieto-Vesperinas, X. Ding, M. Rahman, T. Zhang, C. Lim, and C.-W. Qiu, *Optical manipulation from the microscale to the nanoscale: fundamentals, advances and prospects,* Light: Science & Applications **6**, e17039 (2017).

[28] Z. Yan and N. F. Scherer, *Optical vortex induced rotation of silver nanowires,* The Journal of Physical Chemistry Letters **4**, 2937 (2013).

[29] A. Lehmuskero, Y. Li, P. Johansson, and M. Käll, *Plasmonic particles set into fast orbital motion by an optical vortex beam,* Optics express **22**, 4349 (2014).

[30] A. Lehmuskero, P. Johansson, H. Rubinsztein-Dunlop, L. Tong, M. Käll, and M. Kä, *Laser Trapping of Colloidal Metal Nanoparticles,* ACS Nano **9**, 3453 (2015).

[31] F. Pedaci, Z. Huang, M. van Oene, and N. H. Dekker, *Calibration of the optical torque wrench,* Optics Express **20**, 3787 (2012).

[32] Y. Harada and T. Asakura, *Radiation forces on a dielectric sphere in the Rayleigh scattering regime,* Optics Communications **124**, 529 (1996).

[33] J.-W. Liaw, W.-J. Lo, and M.-K. Kuo, *Wavelength-dependent longitudinal polarizability of gold nanorod on optical torques,* Optics Express **22**, 10858 (2014).

[34] J.-W. Liaw, Y.-S. Chen, and M.-K. Kuo, *Maxwell stress induced optical torque upon gold prolate nanospheroid,* Applied Physics A **122**, 182 (2016).

[35] A. Lehmuskero, P. Johansson, H. Rubinsztein-Dunlop, L. Tong, and M. Kall, *Laser trapping of colloidal metal nanoparticles,* ACS nano **9**, 3453 (2015).

[36] D. Andrén, L. Shao, N. O. Länk, S. S. Aćimović, P. Johansson, and M. Käll, *Probing Photothermal Effects on Optically Trapped Gold Nanorods by Simultaneous Plasmon Spectroscopy and Brownian Dynamics Analysis,* ACS Nano **11**, 10053 (2017).

[37] C. Bradac, *Nanoscale Optical Trapping: A Review,* Advanced Optical Materials **6**, 1800005 (2018).

[38] J. Lipfert, M. M. van Oene, M. Lee, F. Pedaci, and N. H. Dekker, *Torque spectroscopy for the study of rotary motion in biological systems,* Chemical reviews **115**, 1449 (2014).

[39] C. Deufel, S. Forth, C. R. Simmons, S. Dejgosha, and M. D. Wang, *Nanofabricated quartz cylinders for angular trapping: Dna supercoiling torque detection,* Nature methods **4**, 223 (2007).

[40] P.-C. Li, J.-C. Chang, A. La Porta, and T. Y. Edward, *Fabrication of birefringent nanocylinders for single-molecule force and torque measurement,* Nanotechnology **25**, 235304 (2014).

[41] P. Polimeno, A. Magazzù, M. A. Iatì, F. Patti, R. Saija, C. D. Esposti Boschi, M. G. Donato, P. G. Gucciardi, P. H. Jones, G. Volpe, and O. M. Maragò, *Optical tweezers and their applications,* Journal of Quantitative Spectroscopy and Radiative Transfer **218**, 131 (2018).

[42] S. Zhang, L. J. Gibson, A. B. Stilgoe, I. A. Favre-Bulle, T. A. Nieminen, and H. Rubinsztein-Dunlop, *Ultrasensitive rotating photonic probes for complex biological systems,* Optica **4**, 1103 (2017).

[43] S. Ha, R. Janissen, Y. Y. Ussembayev, M. M. van Oene, B. Solano, and N. H. Dekker, *Tunable top-down fabrication and functional surface coating of single-crystal titanium dioxide nanostructures and nanoparticles,* Nanoscale **8**, 10739 (2016).

[44] F. Monteiro, S. Ghosh, E. C. Van Assendelft, and D. C. Moore, *Optical rotation of levitated spheres in high vacuum,* Physical Review A **97**, 051802 (2018), arXiv:1803.04297 .

[45] S. Ha, Y. Tang, M. M. van Oene, R. Janissen, R. M. Dries, B. Solano, A. J. Adam, and N. H. Dekker, *Single-crystal rutile tio2 nanocylinders are highly effective transducers of optical force and torque,* ACS photonics (2019).

[46] J. Sun, M. I. Shalaev, and N. M. Litchinitser, *Experimental demonstration of a non-resonant hyperlens in the visible spectral range,* Nature Communications **6**, 7201 (2015).

[47] Z. Liu, S. Durant, H. Lee, Y. Pikus, Y. Xiong, C. Sun, and X. Zhang, *Experimental studies of far-field superlens for sub-diffractional optical imaging,* Optics express **15**, 6947 (2007).

[48] X. Yang, J. Yao, J. Rho, X. Yin, and X. Zhang, *Experimental realization of three-dimensional indefinite cavities at the nanoscale with anomalous scaling laws,* Nature Photonics **6**, 450 (2012).

[49] Y. Guo, W. Newman, C. L. Cortes, and Z. Jacob, *Applications of hyperbolic metamaterial substrates,* Advances in OptoElectronics **2012**, 1 (2012).

[50] Z. Jacob, J.-y. Y. Kim, G. V. Naik, E. E. Narimanov, A. E. Boltasseva, E. E. Narimanov, and V. M. Shalaev, *Engineering photonic density of states using metamaterials,* Applied Physics B: Lasers and Optics **100**, 215 (2010).

[51] D. Lee, Y. D. Kim, M. Kim, S. So, H.-J. Choi, J. Mun, D. M. Nguyen, T. Badloe, J. G. Ok, K. Kim, *et al.*, *Realization of wafer-scale hyperlens device for sub-diffractional biomolecular imaging,* ACS Photonics (2017).

[52] J. Sun and N. M. Litchinitser, *Toward practical, subwavelength, visible-light photolithography with hyperlens,* ACS nano **12**, 542 (2018).

[53] S. Ishii, M. Y. Shalaginov, V. E. Babicheva, A. Boltasseva, and A. V. Kildishev, *Plasmonic waveguides cladded by hyperbolic metamaterials,* Optics letters **39**, 4663 (2014).

[54] Y. Tang, Z. Xi, M. Xu, S. Bäumer, A. Adam, and H. Urbach, *Spatial mode-selective waveguide with hyperbolic cladding,* Optics letters **41**, 4285 (2016).

[55] V. E. Babicheva, M. Y. Shalaginov, S. Ishii, A. Boltasseva, and A. V. Kildishev, *Finite-width plasmonic waveguides with hyperbolic multilayer cladding,* Optics express **23**, 9681 (2015).

[56] K. V. Sreekanth, Y. Alapan, M. ElKabbash, E. Ilker, M. Hinczewski, U. A. Gurkan, A. De Luca, and G. Strangi, *Extreme sensitivity biosensing platform based on hyperbolic metamaterials,* Nature materials **15**, 621 (2016).

[57] N. Vasilantonakis, G. Wurtz, V. Podolskiy, and A. Zayats, *Refractive index sensing with hyperbolic metamaterials: strategies for biosensing and nonlinearity enhancement,* Optics express **23**, 14329 (2015).

[58] A. Kabashin, P. Evans, S. Pastkovsky, W. Hendren, G. Wurtz, R. Atkinson, R. Pollard, V. Podolskiy, and A. Zayats, *Plasmonic nanorod metamaterials for biosensing,* Nature materials **8**, 867 (2009).

[59] S. Lang, H. S. Lee, A. Y. Petrov, M. Störmer, M. Ritter, and M. Eich, *Gold-silicon metamaterial with hyperbolic transition in near infrared,* Applied Physics Letters **103**, 1 (2013).

[60] S. S. Kruk, Z. J. Wong, E. Pshenay-Severin, K. O'Brien, D. N. Neshev, Y. S. Kivshar, and X. Zhang, *Magnetic hyperbolic optical metamaterials,* Nature Communications **7**, 11329 (2016).

[61] A. A. High, R. C. Devlin, A. Dibos, M. Polking, D. S. Wild, J. Perczel, N. P. de Leon, M. D. Lukin, and H. Park, *Visible-frequency hyperbolic metasurface,* Nature **522**, 192 (2015).

[62] W. Cai and V. M. Shalaev, *Optical metamaterials*, Vol. 10 (Springer, 2010).

[63] T. Begou and J. Lumeau, *Accurate analysis of mechanical stress in dielectric multilayers,* Optics letters **42**, 3217 (2017).

[64] B. Richards and E. Wolf, *Electromagnetic diffraction in optical systems, ii. structure of the image field in an aplanatic system,* Proc. R. Soc. Lond. A **253**, 358 (1959).

[65] E. Wolf, *Electromagnetic diffraction in optical systems-i. an integral representation of the image field,* Proc. R. Soc. Lond. A **253**, 349 (1959).

[66] L. Novotny and B. Hecht, *Principles of nano-optics* (Cambridge university press, 2012).

[67] M. Muradoglu and T. W. Ng, *Optical trapping map of dielectric spheres,* Applied optics **52**, 3500 (2013).

4

Spatial mode filter with hyperbolic-cladded waveguide

Hyperbolic Meta-Materials (HMMs) are anisotropic materials with permittivity tensor that has both positive and negative eigenvalues. Here we report that by using a type II HMM as cladding material, a waveguide which only supports higher order modes can be achieved, while the lower order modes become leaky and are absorbed in the HMM cladding. This counter-intuitive property can lead to novel application in optical communication and photonic integrated circuit. The loss in our HMM-Insulator-HMM (HIH) waveguide is smaller than that of similar guided mode in a Metal-Insulator-Metal (MIM) waveguide.

Parts of this chapter have been published in: **Y. Tang**, Z. Xi, M. Xu, S. Bäumer, A. J. L. Adam, and H. P. Urbach, "Spatial mode-selective waveguide with hyperbolic cladding," Opt. Lett. **41**, 4285-4288 (2016) [1]

4.1. Introduction

Meta-materials are structures engineered at the sub-wavelength scale to exhibit specific electromagnetic properties. The development of nano-fabrication techniques allows to make these structures and to realize new properties that are unobtainable with conventional media. Among the varieties of meta-materials, Hyperbolic Meta-Materials (HMMs) have gained tremendous attention. Their exotic hyperbolic dispersion property is the key to numerous emerging nano-photonics applications, including sub-diffraction-limit imaging [2–6], Purcell factor enhancement [7–12], sensing [13–15], and plasmonic waveguide [16–20]. Here we report a new application of HMM for waveguide spatial mode engineering, which brings up new possibility in Spatial-Division Multiplexing (SDM).

SDM utilizes the last unexplored physical dimension, space, to further increase the data carrying capacity in optical communication [21]. The excitation and separation of spatial modes is essential in SDM [22]. In this letter, we propose a mode selective slab waveguide design by using a HMM as a cladding material. With a cladding consisting of HMM, the lower order modes with larger propagation constant become propagating wave in the HMM cladding material, such that they are turned into leaky modes. At the same time, higher order modes with smaller propagation constant are evanescent wave in the HMM cladding and remain guided in the core. Therefore, a waveguide with HMM cladding can be designed to excite and separate spatial modes in SDM.

4.2. Planar waveguide

4.2.1. Theory

We only consider transverse magnetic (TM) wave ($E_y = 0$) because the hyperbolic cladding only has the desired property for this state of polarization. The TM wave is propagating in a slab waveguide core towards the positive z direction (Fig. 4.1a). The core thickness is $2a$. The magnetic field of the mode is independent of the y-coordinate, and has the form $H_y = H(x)\exp(i\beta_m z)$, where $\beta_m = k_{z,m}$ is the propagation constant of the m^{th} order mode along the z-direction, which satisfies the equation $\beta_m^2 + k_{x,m}^2 = n_c k_0^2$, where $k_{x,m}$ is the transverse wavenumber of the m^{th} order mode in the x direction, n_c is the refractive index of the core, and k_0 is the wavenumber in vacuum. The mode numbering convention in this chapter is corresponding to the number of zeros of the magnetic field amplitude in transverse direction. The fundamental mode TM_0 has the smallest transverse wavenumber and thus corresponds to the largest propagation constant β_0. Higher order modes like TM_1, TM_2 with larger transverse wavenumber correspond to smaller propagation constant β_1, β_2, with $\beta_0 > \beta_1 > \beta_2$. For a conventional slab waveguide with sufficiently large index contrast or core thickness, such that the m^{th} higher order mode is guided, all the lower order modes TM_0, ..., TM_{m-1} are also guided. When the core thickness or the index contrast is reduced, the number of guided modes decreases in sequence of m. Therefore by decreasing the core thickness or index contrast one can select the lower order modes. However the selection of higher order modes can not be easily achieved through conventional method.

Now assume that the cladding material is replaced by a HMM, with its optical axis parallel to the x-axis. With respect to our Cartesian coordinate system, the permittivity tensor of the HMM is diagonal and given by:

$$\bar{\epsilon} = \begin{bmatrix} \epsilon_x & 0 & 0 \\ 0 & \epsilon_y & 0 \\ 0 & 0 & \epsilon_z \end{bmatrix}. \tag{4.1}$$

If $\mathrm{Re}(\epsilon_y) = \mathrm{Re}(\epsilon_z) < 0$ and $\mathrm{Re}(\epsilon_x) > 0$, the HMM is of type II [23]. For transverse electric (TE) wave, the electric field only experiences the ϵ_y component and hence the HMM cladding behaves as a normal metallic material and the waveguide has the properties of a conventional waveguide described above. However, for TM waves, the projection of isofrequency contour on k_x-k_z plane is a hyperbola, as indicated by the red curve in Fig. 4.1c (note k_z is the tangential component of wave vector along the core/cladding interface). The intersection point of the hyperbola and the k_z-axis is given by $k_0\epsilon_x^{1/2}$. This number is the minimum value of k_z for which waves are propagating in the HMM. For k_z below this value, the wave is evanescent in the x-direction inside the cladding and hence for a guided mode there must hold: $\beta = k_z < k_0\epsilon_x^{1/2}$. If a lower order mode has a large propagation constant (e.g. β_0 in Fig. 4.1c), a propagating wave solution can be found in the HMM cladding, with transverse wavenumber $k_{x,h}$. Therefore the field becomes leaky. However, for a higher order mode with a smaller propagation constant (e.g. $\beta_1 < k_0\epsilon_x^{1/2}$ in Fig. 4.1c), no solution for propagating wave can be found in the HMM cladding and therefore it is a guided mode. Hence a waveguide with HMM cladding can act as a mode selector that only allows higher order modes to propagate within the core.

4.2.2. Calculation results

By writing down the waveguide field equations and match the boundary condition at the interface, we can find out the waveguide mode dispersion equation. The detail derivation can be found in the Appendix B.1. For a symmetric structure, the result solution is described by two sets of equation:

$$\text{odd modes} \quad : \tan(k_x a) = -\frac{k_x \epsilon_z}{\gamma_h \epsilon_c}, \tag{4.2}$$

$$\text{even modes} \quad : \cot(k_x a) = \frac{k_x \epsilon_z}{\gamma_h \epsilon_c}, \tag{4.3}$$

where $k_x = (n_c^2 k_0^2 - \beta^2)^{1/2}$ is the transverse wavenumber in the core, and γ_h is the attenuation coefficient in the HMM cladding defined by $\gamma_h = [(\epsilon_z/\epsilon_x)\beta^2 - \epsilon_z k_0^2]^{1/2}$.

In our study, the waveguide core is made of silicon with refractive index 3.5 for all wavelengths we considered in this chapter. Though no natural hyperbolic material around 1550 nm wavelength is found so far [24], the HMM cladding can be approximated by a multilayer structure consisting of periodically alternating metal and dielectric layers, of which the interfaces are parallel to the $y-z$ plane. According to the effective medium theory (EMT) [25], when the thickness of each layer is much

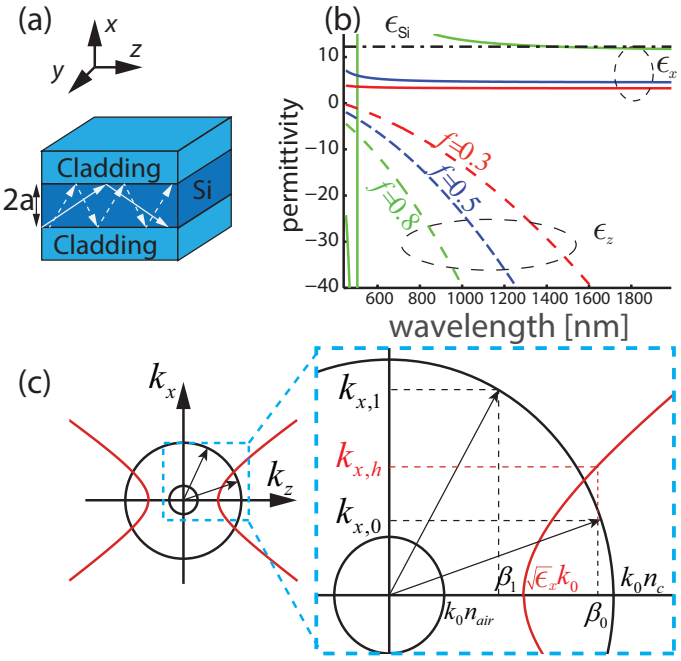

Figure 4.1: (a) Schematic diagram of the multimode slab waveguide structure; (b) Real part of the effective permittivity versus wavelength with filling factor f=0.3, 0.5 and 0.8. The horizontal black dash-dotted line indicates the permittivity of the silicon core; (c) 2D isofrequency contour of the isotropic core and the air (in black) and the HMM cladding (in red) in the k_x-k_z plane.

smaller than the wavelength, the eigenvalues of the effective optical permittivity tensor are given by $\epsilon_x^{-1} = f\epsilon_m^{-1} + (1-f)\epsilon_d^{-1}$, $\epsilon_y = \epsilon_z = f\epsilon_m + (1-f)\epsilon_d$, where f is the filling factor of metal in a unit cell, ϵ_m and ϵ_d are the permittivity of the metal and the dielectric, respectively. We use Ag and Al_2O_3 as the constituent materials, with refractive index of Al_2O_3 equals to 1.5 for all wavelengths, and the permittivity of Ag taken from [26]. The thickness of the core is chosen as $2a$ = 1000 nm. Because the metal is lossy, the propagation constant β is complex. We define the effective mode index n_{eff} and the propagation length L as:

$$n_{\text{eff}} = \text{Re}(\beta)k_0^{-1}, \tag{4.4}$$

$$L = [\text{Im}(2\beta)]^{-1}. \tag{4.5}$$

In Fig. 4.1b, the real parts of the effective ϵ_x and ϵ_z are shown as a function of wavelength. In a broad wavelength range, ϵ_x is positive while ϵ_z is negative, giving a type II hyperbolic behavior. By changing the filing factor f, the wavelength range of the hyperbolic dispersion and the permittivity values can be tuned. The value of ϵ_x increases as the filling factor increases. In order to fulfil the requirement ${\epsilon_x}^{1/2} < n_c$, the filling factor must have a moderate value. We choose a filling factor

of 0.5, leading to $\mathrm{Re}(\epsilon_x^{1/2}) \approx 2.3 < n_{\mathrm{Si}}$.

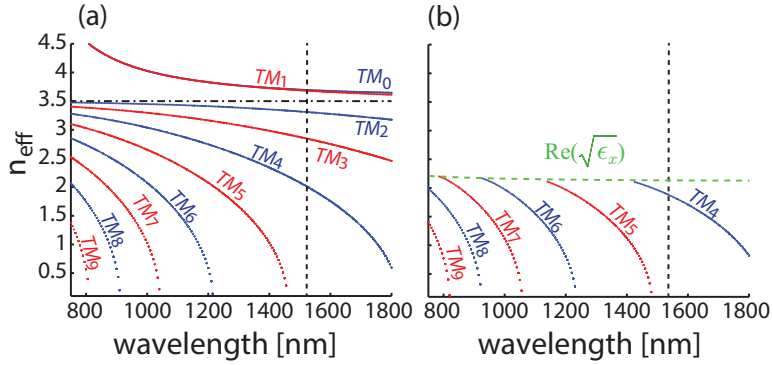

Figure 4.2: Effective indices of guided modes for different filing factors: (a) f=1 (MIM); (b)f=0.5. The waveguide thicknesses are both $2a = 1000$ nm. The horizontal dash-dotted line indicates the refractive index of the core and the vertical black dashed line indicates the wavelength of interest (1550 nm).

For these values of the parameters, the solutions of the dispersion relations (2) and (3) of the guided TM modes are shown in Fig. 4.2b. For comparison, the MIM (metal-insulator-metal) case is shown in Fig 4.2a, obtained by setting the filling factor equal to 1. The red curves and the blue curves represent the odd and even modes, respectively. As can be seen in Fig. 4.2a, when $f = 1$ (MIM), all the guided modes are found. At the wavelength 800 nm, 10 guided modes are supported by the waveguide. The TM_0 and TM_1 are the symmetric and anti-symmetric plasmonic mode, respectively, and the other higher order modes are oscillatory modes [27]. The TM_0 mode always exists for all wavelength. But for other orders of modes, as the wavelength increases (frequency decreases), higher order modes reach their cut-off frequency first and disappear. Eventually for λ=1600 nm, only the first five order modes remain (TM_0 to TM_4). However, in the case of HIH waveguide ($f = 0.5$) in Fig. 4.2b, the first four order modes from TM_0 to TM_3 do not exist at the wavelengths shown in the plot. The lowest guided mode varies from TM_4 to TM_9 when the wavelength is decreased. The modes with $n_{\mathrm{neff}} > Re({\epsilon_x}^{1/2})$ above the green dashed line disappear, because they propagate in the HMM cladding. If the filling factor is further decreased, the lowest order of the guided modes increases.

The mode selection property is further studied as a function of the filling factor for the hyperbolic cladding at 1550 nm wavelength. Both the effective mode index and the propagation length are shown in Fig. 4.3. For all effective indices shown in Fig. 4.3a, five modes exist for f=1 (MIM). As the filling factor decreases, the plasmonic mode TM_0 and TM_1 are cut-off first at around $f = 0.8$. The TM_2 mode only exists for f >0.77, the TM_3 exists for f >0.67, and the TM_4 mode disappears only when f <0.22. The TM_5 emerges for f <0.12. This is because the cut-off frequency of the TM_5 mode red-shifts when the filling factor decreases. Again, the effective index can not exceed $\mathrm{Re}({\epsilon_x}^{1/2})$, which is indicated by the green dashed line. It should be pointed out that for $f < 0.67$, the waveguide becomes a single mode waveguide which only guides either the TM_4 mode or the TM_5 mode. Such

phenomenon can not be achieved with conventional waveguides. It is seen in Fig. 4.3b that the propagation length of all modes are longer for smaller filling factor. The reason is that with a smaller filling factor, less metal is used in the HMM cladding, and thus the modes experience less metallic loss. For the TM_4 mode, the maximum propagation length can exceed 400 μm, which is an order of magnitude longer than the propagation length of this mode in a metallic waveguide with Ag cladding (i.e. with fill factor of 1). However, in the HIH case, the field confinement becomes relatively weak. As shown in Fig. 4.3c the field has the longest decay tail in the transverse direction for f=0.3. This is because the field decay rate in the cladding is determined by γ_h, and when β approaches $\epsilon_x^{1/2} k_0$, the value of γ_h becomes smaller, and hence the field distribution is broadened.

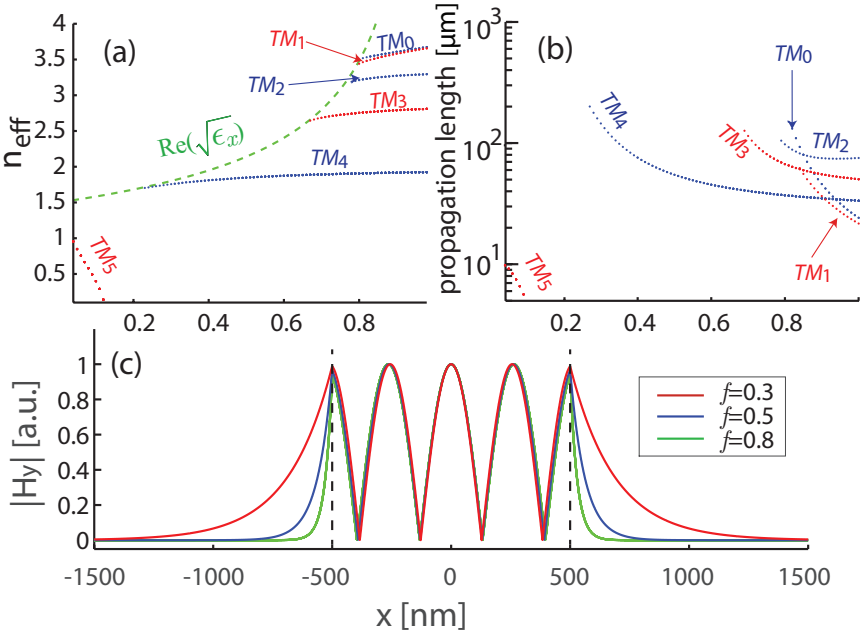

Figure 4.3: Effective indices (a) and propagation length (b) of guided modes as a function of the filling factor f at λ=1550 nm and waveguide thickness $2a = 1000$ nm. (c) Magnetic field amplitude distribution of the TM_4 mode with different filling factors. Vertical dashed line indicates the waveguide boundary.

4.2.3. Simulation results

To confirm the validity of this particular mode selection property, both the HMM with effective medium model and the real multilayer HMM cladded waveguide are simulated for the wavelength of 1550 nm using the finite element method (FEM) software COMSOL 4.4 . In the effective medium situation, the HMM cladding is modeled as a semi-infinite half-space. In the real multilayer case, the layers are

made of 20 pairs of Ag and Al_2O_3 on each side, of which Ag is next to the core. The thicknesses of the dielectric and the metal layers are both 20 nm, hence the filling factor is 0.5. The material outside the cladding is air (n=1). In both simulations, a MIM waveguide with Ag as metal (on the left) is connected to a HIH waveguide (on the right) with identical silicon core (2a = 1000 nm, $n_c = n_{Si} = 3.5$), as shown in Fig. 4.4. The TM_2, TM_3 and TM_4 modes are excited separately in the MIM waveguide and enter from the left end. If the mode is also supported by the HIH waveguide on the right, the energy will be coupled at the interface and continues to be confined in the core of the HIH waveguide, otherwise it will leak out into the cladding layer.

The results are shown in Fig. 4.4. From the top to the bottom, the magnetic field amplitude of the TM_2, TM_3 and TM_4 modes are shown. In Fig. 4.4a, where the effective medium is used, the field of the TM_2 and the TM_3 mode leak quickly into the cladding after entering the HIH region, and the field amplitude decreases fast. However for the TM_4 mode most of the field is still confined in the HIH waveguide, because it is a guided mode in HIH waveguide. A small leakage and reflection is observed due to a small mode mismatch between the MIM and the HIH waveguide. For the multilayer cladding shown in Fig. 4.4b, the field of the TM_2 mode spreads out after entering the HIH region, but not as quickly as in the EMT case. The propagation length of TM_2 is only 3 μm. The field of the TM_3 mode immediately starts to leak into the cladding, and reflects back at the outer interface between the cladding and the air because of mode mismatch, and dissipates in the cladding. The field of the TM_4 mode is well confined to the core of the HIH waveguide and only a small portion of energy leaks into the cladding. The simulation result confirms that this HIH waveguide possesses high-pass mode selection property.

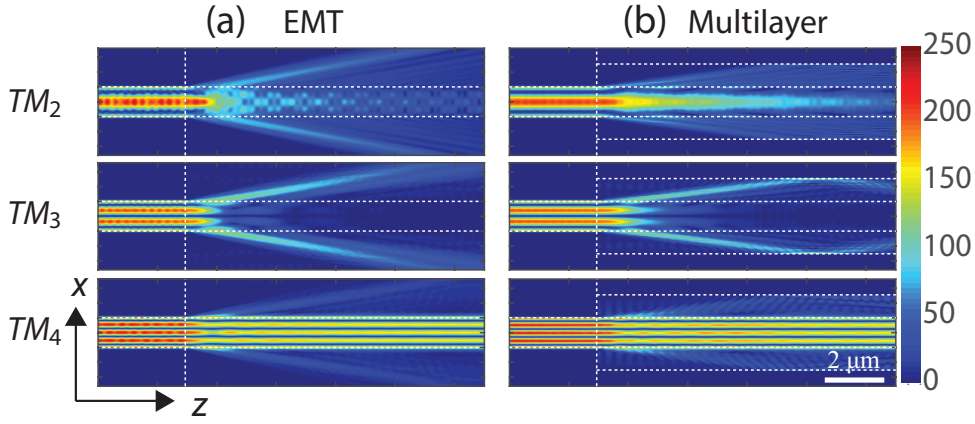

Figure 4.4: Simulated magnetic field amplitude of three guided modes in a MIM waveguide coupled to a HIH waveguide. The filling factor of the multilayer is 0.5. The white dashed line indicates the boundary. (a) Hyperbolic cladding modelled using the effective medium theory ; (b) Multilayer cladding.

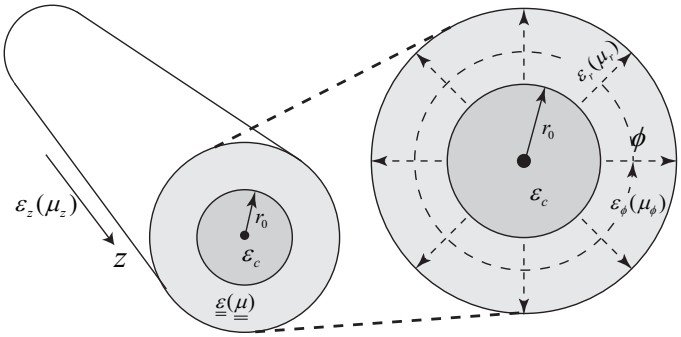

Figure 4.5: Schematic of cylindrical waveguide with anisotropic cladding. The core area is isotropic with permittivity of ϵ_c and radius of r_0. The cladding area is cylindrically anisotropic with the three eigen permittivity (permeability) component along r, ϕ and z direction, respectively.

4.2.4. Conclusion

It can be seen that by choosing the right filling factor for the cladding one can design a 'single mode' waveguide only guiding one specific higher order mode, which can be applied as mode launcher or mode receiver in a SDM system. Compared to conventional spatial multiplexing techniques based on interference [28] or holography [29], our approach merely modifies the waveguide property and requires no extra optical component, which is more compact and efficient.

To summarize, we propose a novel mode selective waveguide by using a HMM as cladding material. By choosing the right dielectric and metal and the proper filling factor for HMM, we can achieve a waveguide structure which only allows certain higher order modes to be guided. Moreover, the propagation length of HIH waveguide can be much longer than that of a MIM waveguide. Our design combining meta-material with conventional waveguide design, opens up new possibilities for waveguide engineering.

4.3. Cylindrical waveguide

The case of planar waveguide is relatively simple as the electric field and the magnetic field can be uncoupled. Here we also present the study of cylindrical waveguide with hyperbolic anisotropic cladding, as shown in Fig. 4.5. The hyperbolic cladding is circularly symmetric, hence the three permittivity eigenvalues are along the radial, azimuthal and z-axis. The radial axis is the optical axis, hence $\epsilon_z = \epsilon_\phi$.

Nevertheless, we start with the most general case in which both permittivity and permeability are both tensors given by:

$$\underline{\underline{\epsilon}} = \begin{pmatrix} \epsilon_r & 0 & 0 \\ 0 & \epsilon_\phi & 0 \\ 0 & 0 & \epsilon_z \end{pmatrix}, \tag{4.6}$$

and

$$\underline{\underline{\mu}} = \begin{pmatrix} \mu_r & 0 & 0 \\ 0 & \mu_\phi & 0 \\ 0 & 0 & \mu_z \end{pmatrix}, \tag{4.7}$$

where r, ϕ and z are the three coordinate of cylindrical system.

4.3.1. Maxwell's equations in the cladding

The fields in the cladding derives from the Maxwell's equations.

$$\nabla \times \vec{H} = \frac{\partial \vec{D}}{\partial t} = \frac{\partial}{\partial t}\epsilon_0 \underline{\underline{\epsilon}} \vec{E} = -i\omega\epsilon_0 \underline{\underline{\epsilon}} \vec{E}, \tag{4.8}$$

$$\nabla \times \vec{E} = -\frac{\partial \vec{B}}{\partial t} = -\mu_0 \frac{\partial \vec{H}}{\partial t} = i\omega\mu_0 \underline{\underline{\mu}} \vec{H}. \tag{4.9}$$

We assume the time dependence of the field to be given by the factor $\exp(-i\omega t)$, with $\omega > 0$. Using cylindrical coordinates we get

$$(\nabla \times \vec{H})_r = \frac{1}{r}\frac{\partial H_z}{\partial \phi} - \frac{\partial H_\phi}{\partial z} = -i\omega\epsilon_0\epsilon_r E_r, \tag{4.10}$$

$$(\nabla \times \vec{H})_\phi = \frac{\partial H_r}{\partial z} - \frac{\partial H_z}{\partial r} = -i\omega\epsilon_0\epsilon_\phi E_\phi, \tag{4.11}$$

$$(\nabla \times \vec{H})_z = \frac{1}{r}\left(\frac{\partial r H_\phi}{\partial r} - \frac{\partial H_r}{\partial \phi}\right) = -i\omega\epsilon_0\epsilon_z E_z, \tag{4.12}$$

and

$$(\nabla \times \vec{E})_r = \frac{1}{r}\frac{\partial E_z}{\partial \phi} - \frac{\partial E_\phi}{\partial z} = i\omega\mu_0\mu_r H_r, \tag{4.13}$$

$$(\nabla \times \vec{E})_\phi = \frac{\partial E_r}{\partial z} - \frac{\partial E_z}{\partial r} = i\omega\mu_0\mu_\phi H_\phi, \tag{4.14}$$

$$(\nabla \times \vec{E})_z = \frac{1}{r}\left(\frac{\partial r E_\phi}{\partial r} - \frac{\partial E_r}{\partial \phi}\right) = i\omega\mu_0\mu_z H_z. \tag{4.15}$$

We assume the field has the form:

$$\vec{E}(r,\phi,z) = \vec{E}(r)\exp(iv\phi)\exp[i(\beta z - \omega t)] \tag{4.16}$$

$$\vec{H}(r,\phi,z) = \vec{H}(r)\exp(iv\phi)\exp[i(\beta z - \omega t)] \tag{4.17}$$

Therefore we can rewrite the above equation 4.10-4.15 as

$$\frac{\nu}{r}H_z - \beta H_\phi = -\omega\epsilon_0\epsilon_r E_r \tag{4.18}$$

$$\beta H_r + iH_z' = \omega\epsilon_0\epsilon_\phi E_\phi \tag{4.19}$$

$$\frac{H_\phi}{r} + H_\phi' - \frac{i\nu}{r}H_r = -i\omega\epsilon_0\epsilon_z E_z \tag{4.20}$$

$$\frac{\nu}{r}E_z - \beta E_\phi = \omega\mu_0\mu_r H_r \tag{4.21}$$

$$\beta E_r + iE_z' = \omega\mu_0\mu_\phi H_\phi \tag{4.22}$$

$$\frac{E_\phi}{r} + E_\phi' - \frac{i\nu}{r}E_r = i\omega\mu_0\mu_z H_z \tag{4.23}$$

Equations 4.18 and 4.22 imply:

$$E_r = \frac{1}{\kappa_{r,\phi}^2}\left(i\beta E_z' - \frac{\omega\nu\mu_0\mu_\phi}{r}H_z\right), \tag{4.24}$$

$$H_\phi = \frac{1}{\kappa_{r,\phi}^2}\left(i\omega\epsilon_0\epsilon_r E_z' - \frac{\beta\nu}{r}H_z\right), \tag{4.25}$$

where $\kappa_{r,\phi}^2 = \omega^2\epsilon_0\mu_0\epsilon_r\mu_\phi - \beta^2$.

Similarly, equations 4.19 and 4.21 imply:

$$E_\phi = -\frac{1}{\kappa_{\phi,r}^2}\left(\frac{\beta\nu}{r}E_z + i\omega\mu_0\mu_r H_z'\right), \tag{4.26}$$

$$H_r = \frac{1}{\kappa_{\phi,r}^2}\left(\frac{\omega\epsilon_0\epsilon_\phi\nu}{r}E_z + i\beta H_z'\right), \tag{4.27}$$

where $\kappa_{\phi,r}^2 = \omega^2\epsilon_0\mu_0\epsilon_\phi\mu_r - \beta^2$.

Then, by substituting equation 4.27 and 4.25 into equation 4.20 and by substituting equation 4.24 and 4.26 into equation 4.23, we get:

$$r^2E_z''(r) + rE_z'(r) + \left(\frac{\kappa_{r,\phi}^2\epsilon_z}{\epsilon_r}r^2 - \frac{\kappa_{r,\phi}^2\epsilon_\phi}{\kappa_{\phi,r}^2\epsilon_r}\nu^2\right)E_z(r) - i\frac{\mu_0\omega\beta\nu(\epsilon_r\mu_\phi - \epsilon_\phi\mu_r)}{\epsilon_r\kappa_{\phi,r}^2}rH_z'(r) = 0, \tag{4.28}$$

$$r^2H_z''(r) + rH_z'(r) + \left(\frac{\kappa_{\phi,r}^2\mu_z}{\mu_r}r^2 - \frac{\kappa_{\phi,r}^2\mu_\phi}{\kappa_{r,\phi}^2\mu_r}\nu^2\right)H_z(r) - i\frac{\epsilon_0\omega\beta\nu(\epsilon_r\mu_\phi - \epsilon_\phi\mu_r)}{\mu_r\kappa_{r,\phi}^2}rE_z'(r) = 0. \tag{4.29}$$

The above equations represent a second order coupled differential equations system, which is very difficult to be solved.

However, if we have $\epsilon_r = \epsilon_\phi, \mu_r = \mu_\phi$, then the above equation will be simplified to

$$r^2 E_z''(r) + r E_z'(r) + \left(\frac{\kappa^2 \epsilon_z}{\epsilon_r} r^2 - \nu^2\right) E_z(r) = 0, \tag{4.30}$$

$$r^2 H_z''(r) + r H_z'(r) + \left(\frac{\kappa^2 \mu_z}{\mu_r} r^2 - \nu^2\right) H_z(r) = 0. \tag{4.31}$$

In this equation the E_z and H_z are decoupled, hence become relatively easy to solve.

if we loss the condition to $\epsilon_r \mu_\phi = \epsilon_\phi \mu_r$, then we can also have

$$r^2 E_z''(r) + r E_z'(r) + \left(\frac{\kappa^2 \epsilon_z}{\epsilon_r} r^2 - \frac{\epsilon_\phi}{\epsilon_r} \nu^2\right) E_z(r) = 0, \tag{4.32}$$

$$r^2 H_z''(r) + r H_z'(r) + \left(\frac{\kappa^2 \mu_z}{\mu_r} r^2 - \frac{\mu_\phi}{\mu_r} \nu^2\right) H_z(r) = 0. \tag{4.33}$$

4.3.2. Poynting Vector

Before we solve the above equations 4.30 and 4.31, we need to know if the solution is physically correct. For a waveguide, the energy is confined and being propagated along z axis, hence there should be no energy flowing outwards (r axis). The The time average Poynting vector is defined as:

$$\begin{aligned} \vec{S} &= \frac{1}{2} \vec{E} \times \vec{H}^* \\ &= \frac{1}{2} \left[(E_\phi H_z^* - E_z H_\phi^*) \hat{r} + (E_z H_r^* - E_r H_z^*) \hat{\phi} + (E_r H_\phi^* - E_\phi H_z^*) \hat{z} \right]. \end{aligned} \tag{4.34}$$

In the cladding, we should have the r component of Poynting vector being zero. Hence

$$\begin{aligned} S_r &= \frac{1}{2} (E_\phi H_z^* - E_z H_\phi^*) \\ &= \frac{\beta \nu E_z H_z^*}{r} \left(\frac{1}{\kappa_{r,\phi}^2} - \frac{1}{\kappa_{\phi,r}^2} \right) + i\omega \left(\frac{\epsilon_0 \epsilon_r E_z'^* E_z}{\kappa_{r,\phi}^2} - \frac{\mu_0 \mu_r H_z' H_z^*}{\kappa_{r,\phi}^2} \right) \\ &= 0. \end{aligned} \tag{4.35}$$

In the cladding area, the field has to exponentially decay away from the core-cladding interface, hence the solution of E_z and H_z should have a constant phase, hence we assume

$$E_z = C f(r) \tag{4.36}$$

$$H_z = D g(r) \tag{4.37}$$

where C and D are both complex number, $f(r)$ and $g(r)$ are two unknown real functions. hence we have

$$S_r = \frac{\beta\nu CD^* f(r)g(r)}{r}\left(\frac{1}{\kappa_{r,\phi}^2}-\frac{1}{\kappa_{\phi,r}^2}\right)+i\omega\left(\frac{\epsilon_0\epsilon_r CC^* f(r)f(r)'}{\kappa_{r,\phi}^2}-\frac{\mu_0\mu_r DD^* g(r)g(r)'}{\kappa_{r,\phi}^2}\right)$$
$$= \frac{\beta\nu CD^* f(r)g(r)}{r}\left(\frac{1}{\kappa_{r,\phi}^2}-\frac{1}{\kappa_{\phi,r}^2}\right)+i\omega\left(\frac{\epsilon_0\epsilon_r |C|^2 f(r)f(r)'}{\kappa_{r,\phi}^2}-\frac{\mu_0\mu_r |D|^2 g(r)g(r)'}{\kappa_{r,\phi}^2}\right). \quad (4.38)$$

So in order to have a confined mode (means $Re(S_r) = 0$), one of the below condition has to be fulfill:

$$Re(CD^*) = 0 \quad (4.39)$$
$$\kappa_{r,\phi}^2 = \kappa_{\phi,r}^2 \quad (4.40)$$

where

$$\kappa_{r,\phi}^2 = \omega^2\epsilon_0\mu_0\epsilon_r\mu_\phi - \beta^2 = k_0^2\epsilon_r\mu_\phi - \beta^2, \quad (4.41)$$
$$\kappa_{\phi,r}^2 = \omega^2\epsilon_0\mu_0\epsilon_\phi\mu_r - \beta^2 = k_0^2\epsilon_\phi\mu_r - \beta^2. \quad (4.42)$$

The first condition implies that the E_z and H_z needs to have phase shift of $\pi/2$, and second condition implies that

$$\epsilon_r\mu_\phi = \epsilon_\phi\mu_r \quad (4.43)$$

4.3.3. Boundary condition

For field at this boundary r_0, we have continuous relation for E_z, H_z, E_ϕ and H_ϕ. For the field in the core, it is trivial to find the solution of the below form

$$E_z^{(in)}(r_0) = AJ_\nu(\kappa_c r_0), \quad (4.44)$$
$$H_z^{(in)}(r_0) = BJ_\nu(\kappa_c r_0), \quad (4.45)$$
$$E_\phi^{(in)}(r_0) = -\frac{1}{\kappa_c^2}\left[\frac{\beta\nu}{r_0}Aj_\nu(\kappa_c r_0) + i\omega\mu_0\kappa_c BJ_\nu'(\kappa_c r_0)\right], \quad (4.46)$$
$$H_\phi^{(in)}(r_0) = \frac{1}{\kappa_c^2}\left[i\omega\epsilon_0\epsilon_c\kappa_c AJ_\nu'(\kappa_c r_0) - \frac{\beta\nu}{r_0}BJ_\nu(\kappa_c r_0)\right]. \quad (4.47)$$

For the field in the cladding area, we take the form of E_z and H_z from Eq. 4.36 and Eq. 4.37, and from the Eq. 4.26 and 4.25 we also know the E_ϕ and H_ϕ

$$E_z^{(out)}(r_0) = Cf(r_0), \tag{4.48}$$

$$H_z^{(out)}(r_0) = Dg(r_0), \tag{4.49}$$

$$\begin{aligned} E_\phi^{(out)}(r_0) &= -\frac{1}{\kappa_{\phi,r}^2}\left[\frac{\beta\nu}{r_0}E_z^{(out)}(r_0) + i\omega\mu_0\mu_r H_z'^{(out)}(r_0)\right] \\ &= -\frac{1}{\kappa_{\phi,r}^2}\left[\frac{\beta\nu}{r_0}Cf(r_0) + i\omega\mu_0\mu_r Dg(r_0)'\right], \end{aligned} \tag{4.50}$$

$$\begin{aligned} H_\phi^{(out)}(r_0) &= \frac{1}{\kappa_{r,\phi}^2}\left[i\omega\epsilon_0\epsilon_r E_z'^{(out)}(r_0) - \frac{\beta\nu}{r_0}H_z^{(out)}(r_0)\right] \\ &= \frac{1}{\kappa_{r,\phi}^2}\left[i\omega\epsilon_0\epsilon_r Cf(r_0)' - \frac{\beta\nu}{r_0}Dg(r_0)\right]. \end{aligned} \tag{4.51}$$

Therefore, we have a system of equations

$$AJ_\nu(\kappa_c r_0) - Cf(r_0) = 0, \tag{4.52}$$

$$BJ_\nu(\kappa_c r_0) - Dg(r_0) = 0, \tag{4.53}$$

$$\beta\nu\kappa_{\phi,r}^2 AJ_\nu(\kappa_c r_0) + i\omega\mu_0 r_0\kappa_{\phi,r}^2\kappa_c BJ_\nu'(\kappa_c r_0) - \beta\nu\kappa_c^2 Cf(r_0) - i\omega\mu_0\mu_r r_0\kappa_c^2 Dg(r_0)' = 0, \tag{4.54}$$

$$i\omega\epsilon_0\epsilon_c r_0\kappa_{r,\phi}^2\kappa_c AJ_\nu'(\kappa_c r_0) - \beta\nu\kappa_{r,\phi}^2 BJ_\nu(\kappa_c r_0) - i\omega\epsilon_0\epsilon_r r_0\kappa_c^2 Cf(r_0)' + \beta\nu\kappa_c^2 Dg(r_0) = 0. \tag{4.55}$$

To have a non-zeros solutions, the determinant of the system needs to be zero. And then we are able to have the dispersion relation for anisotropic cladding waveguide

$$\begin{aligned} &\left[\frac{\kappa_c}{\kappa_c^2}\frac{J_\nu'(\kappa_c r_0)}{J_\nu(\kappa_c r_0)} - \frac{\mu_r}{\kappa_{\phi,r}^2}\frac{g'(r_0)}{g(r_0)}\right]\left[\frac{\epsilon_c\kappa_c}{\kappa_c^2}\frac{J_\nu'(\kappa_c r_0)}{J_\nu(\kappa_c r_0)} - \frac{\epsilon_r}{\kappa_{r,\phi}^2}\frac{f'(r_0)}{f(r_0)}\right] \\ =&\frac{\beta^2\nu^2 k_0^2}{r_0^2\kappa_c^4\kappa_{r,\phi}^2\kappa_{\phi,r}^2}\left(\epsilon_c - \epsilon_r\mu_\phi\right)\left(\epsilon_c - \epsilon_\phi\mu_r\right). \end{aligned} \tag{4.56}$$

The above equation is the dispersion relation for anisotropic cladding and isotropic nonmagnetic core. The details of the derivation can be found in Appendix B.2.

In the case of isotropic nonmagnetic cladding, the above equation degenerates to

$$\left[\frac{\kappa_c}{\kappa_c^2}\frac{J_\nu'(\kappa_c r_0)}{J_\nu(\kappa_c r_0)} - \frac{1}{\kappa_2^2}\frac{g'(r_0)}{g(r_0)}\right]\left[\frac{\epsilon_c\kappa_c}{\kappa_c^2}\frac{J_\nu'(\kappa_c r_0)}{J_\nu(\kappa_c r_0)} - \frac{\epsilon_2}{\kappa_2^2}\frac{f'(r_0)}{f(r_0)}\right] = \frac{\beta^2\nu^2 k_0^2}{r_0^2\kappa_c^4\kappa_2^4}\left(\epsilon_c - \epsilon_2\right)^2. \tag{4.57}$$

4.3.4. Field solution in the cladding for type II hyperbolic material

The rest of the task is to find a solution of differiential equation system 4.28 and 4.29. In the case of nonmagnetic ($\mu_* = 1$) and $\epsilon_\phi = \epsilon_z < 0$ and $\epsilon_r > 0$, The equation system become

$$r^2 E_z''(r) + rE_z'(r) + \left(\frac{\kappa_r^2 \epsilon_z}{\epsilon_r} r^2 - \frac{\kappa_r^2 \epsilon_\phi}{\kappa_\phi^2 \epsilon_r} \nu^2\right) E_z(r) - i \frac{\mu_0 \omega \beta \nu (\epsilon_r - \epsilon_\phi)}{\epsilon_r \kappa_\phi^2} rH_z'(r) = 0, \tag{4.58}$$

$$r^2 H_z''(r) + rH_z'(r) + \left(\kappa_\phi^2 r^2 - \frac{\kappa_\phi^2}{\kappa_r^2} \nu^2\right) H_z(r) - i \frac{\epsilon_0 \omega \beta \nu (\epsilon_r - \epsilon_\phi)}{\kappa_r^2} rE_z'(r) = 0 \tag{4.59}$$

4

To make the system more symmetric, we write

$$G_z(r) = \frac{-\kappa_r}{\kappa_\phi} \sqrt{\frac{\mu_0}{\epsilon_0 \epsilon_r}} H_z(r), \tag{4.60}$$

$$H_z(r) = \frac{-\kappa_\phi}{\kappa_r} \sqrt{\frac{\epsilon_0 \epsilon_r}{\mu_0}} G_z(r), \tag{4.61}$$

where the square roots $\kappa_r = \sqrt{k_0^2 \epsilon_r - \beta^2}$ and $\kappa_\phi = \sqrt{k_0^2 \epsilon_\phi - \beta^2}$ are defined such that the square root of a positive real number is positive real and that of a negative number is positive imaginary. Then

$$r^2 E_z''(r) + rE_z'(r) + \left(\frac{\kappa_r^2 \epsilon_z}{\epsilon_r} r^2 - \frac{\kappa_r^2 \epsilon_\phi}{\kappa_\phi^2 \epsilon_r} \nu^2\right) E_z(r) + i \frac{k_0 \beta (\epsilon_r - \epsilon_\phi) \nu}{\sqrt{\epsilon_r} \kappa_r \kappa_\phi} rG_z'(r) = 0, \tag{4.62}$$

$$r^2 G_z''(r) + rG_z'(r) + \left(\kappa_\phi^2 r^2 - \frac{\kappa_\phi^2}{\kappa_r^2} \nu^2\right) G_z(r) + i \frac{k_0 \beta (\epsilon_r - \epsilon_\phi) \nu}{\sqrt{\epsilon_r} \kappa_r \kappa_\phi} rE_z'(r) = 0 \tag{4.63}$$

Where $k_0 = \omega/c = \omega\sqrt{\mu_0 \epsilon_0}$.
We define

$$p_0 = \frac{\kappa_r^2 \epsilon_\phi}{\kappa_\phi^2 \epsilon_r}, \tag{4.64}$$

$$p_2 = -\frac{\kappa_r^2 \epsilon_z}{\epsilon_r}, \tag{4.65}$$

$$q_0 = -\frac{\kappa_\phi^2}{\kappa_r^2} \tag{4.66}$$

$$q_2 = -\kappa_\phi^2 \tag{4.67}$$

$$s = i \frac{k_0 \beta (\epsilon_r - \epsilon_\phi)}{\sqrt{\epsilon_r} \kappa_r \kappa_\phi}. \tag{4.68}$$

Then the above equation is simplified as:

$$r^2 E_z''(r) + r E_z'(r) - \left(p_2 r^2 + p_0\, \nu^2\right) E_z(r) + s\, \nu\, r G_z'(r) = 0, \tag{4.69}$$
$$r^2 G_z''(r) + r G_z'(r) - \left(q_2 r^2 - q_0\, \nu^2\right) G_z(r) + s\, \nu\, r E_z'(r) = 0. \tag{4.70}$$

When the medium is hyperbolic of type II with the r-axis as optical axis, $\epsilon_r > 0$, $\epsilon_\phi = \epsilon_z < 0$. In order that the wave is evanescent in the r-direction, we must have $\beta^2 < k_0^2 \epsilon_r$, hence

$$\kappa_r^2 = k_0^2 \epsilon_r - \beta^2 > 0, \quad \kappa_\phi^2 = \kappa_z^2 = k_0^2 \epsilon_\phi - \beta^2 < 0, \tag{4.71}$$
$$\kappa_r > 0, \quad \kappa_\phi = +i|\kappa_\phi|. \tag{4.72}$$

Hence all coefficents p_0, p_2, q_0, q_2, s are positive in this case.

4

Case of $\nu = 0$

In this case, Eq. 4.69 and Eq. 4.70 are simplified to

$$r^2 E_z''(r) + r E_z'(r) - p_2 r^2 E_z(r) = 0, \tag{4.73}$$
$$r^2 G_z''(r) + r G_z'(r) - q_2 r^2 G_z(r) = 0, \tag{4.74}$$

in which there is one physical solution

$$E_z(r) = C_1\, K_0(\sqrt{p_2} r), \tag{4.75}$$
$$H_z(r) = C_2\, K_0(\sqrt{q_2} r). \tag{4.76}$$

By substituting them into the dispersion relationship Eq. 4.56, we are able to find the $\nu = 0$ waveguide modes in the cylinderical waveguide with hyperbolic cladding.

The results are shown in Fig. 4.6. In this plot, multilayer type hyperbolic material is used, in which Ag and Al_2O_3 are used as the composing materials with filling rato $f = 0.5$. For simplicity, only the real part of the effective permittivites are considered, which gives $\epsilon_r < 0 < \epsilon_\phi = \epsilon_z$. The waveguide core material is silicon ($n_{Si} = 3.5$) with a radius of 600 nm. The calculated TE photonic modes are only bonded by the index of the Si core, while the TM modes are bonded by the dashed green line, which is given by $\sqrt{\epsilon_r}$ of the hyperbolic cladding. The field distribution of the TM mode at wavelength of 1550 nm is shown in Fig. 4.7a, which is a TM_3 mode. It is seen that both E_r and E_z component exist in this mode, indicating that both ϵ_r and ϵ_z play a role in defining the mode. However the TE modes has only E_ϕ electric field component as shown Fig. 4.7b, in which only the azimuthal component ϵ_ϕ of the cladding permittivity tensor plays a role. Hence normal waveguide with metallic cladding behavior is expected.

This result confirms that waveguides with type II hyperbolic cladding can only support higher order TM modes with $n_{eff} < \sqrt{\epsilon_r}$, while the lower order TM modes with $n_{eff} > \sqrt{\epsilon_r}$ are filtered out, which leak into the hyperbolic cladding area.

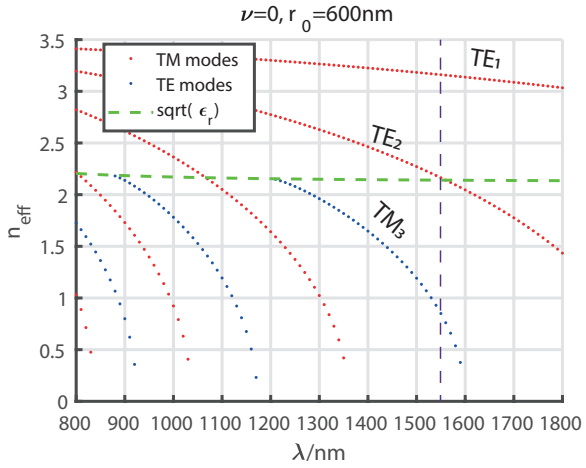

Figure 4.6: Photonic waveguide modes of cylinderical waveguide with hyperbolic cladding. Multilayer type hyperbolic material is used, in which Ag and Al_2O_3 are the composing materials with filling rato $f = 0.5$. For simplicity, only the real part of the effective permittivites are considered, which gives $\epsilon_r < 0 < \epsilon_\phi = \epsilon_z$. The waveguide core material is silicon ($n_{Si} = 3.5$) with a radius of 600 nm. The vertical dashed line is at the wavelength of 1550 nm.

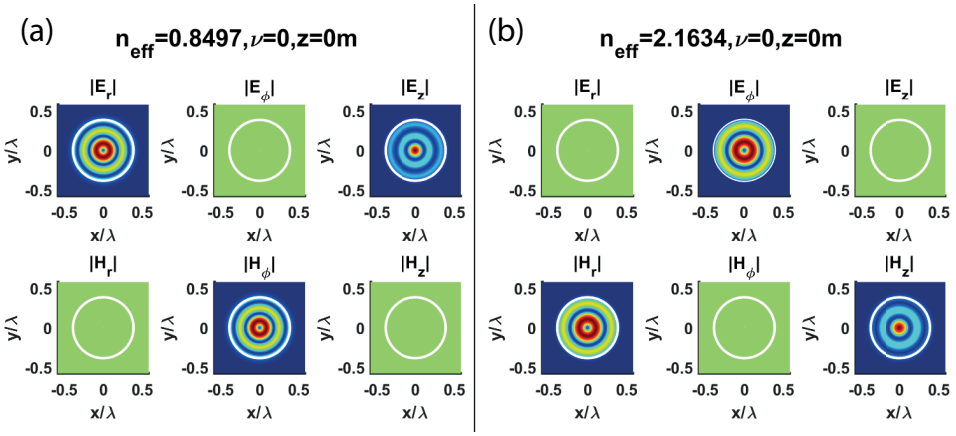

Figure 4.7: Field distribution for the waveguide modes at the wavelength of 1550 nm. The waveguide is the the same as in Fig. 4.6 with a radius of 600 nm (marked by white circles). (a) TM_3 mode field distributions. In this mode, only E_r, E_z, H_ϕ are non-zero. (b) TE_2 mode field distributions. In this mode, only H_r, H_z, E_ϕ are non-zero.

Case of $\nu \neq 0$

In this case the Eq. 4.69 and Eq. 4.70 together form a second order coupled differential equation system. The difficulty lies in the fact that they are both Bessel-like differential equations. Although we strongly believe that there is a real solution towards the differential equation system Eq. 4.69 and Eq. 4.70, we have not yet found the exact form of the physical solution (monotonically decay as $r > r_0$ increases). Nevertheless, we present our attempt for solving it by using asymptotic approximation, which will hopefully provide a potential good starting point.

we assume the asymptotic solution of the equation system will have the form

$$E(r) = (\alpha r)^{\sigma_1} \exp(-\alpha r^{\rho}) \sum_{n=0}^{\infty} a_n \left(\frac{1}{\alpha r}\right)^n = \exp(-\alpha r^{\rho}) \sum_{n=0}^{\infty} a_n (\alpha r)^{-n+\sigma_1}, \quad (4.77)$$

$$G(r) = (\alpha r)^{\sigma_2} \exp(-\alpha r^{\rho}) \sum_{n=0}^{\infty} b_n \left(\frac{1}{\alpha r}\right)^n = \exp(-\alpha r^{\rho}) \sum_{n=0}^{\infty} a_n (\alpha r)^{-n+\sigma_1}. \quad (4.78)$$

where $\sigma_1, \sigma_2 \neq 0, \alpha, \rho > 0$. This assumption will make sure that when $r \to \infty$, the solutions will approach zero, which has a physical meaning.

After a cumbersome derivation (see Appendix B.1), the resulting asymptotic solution of Eq. 4.69 and 4.70 is given by

$$\begin{bmatrix} E(r) \\ G(r) \end{bmatrix} \sim \begin{bmatrix} (\sqrt{p_2}r)^{-\frac{1}{2}} \exp(-\sqrt{p_2}r) \sum_{n=0}^{\infty} a_n \left(\sqrt{p_2}r\right)^{-n} & (\sqrt{q_2}r)^{-\frac{3}{2}} \exp(-\sqrt{q_2}r) \sum_{n=0}^{\infty} c_n \left(\sqrt{q_2}r\right)^{-n} \\ (\sqrt{p_2}r)^{-\frac{3}{2}} \exp(-\sqrt{p_2}r) \sum_{n=0}^{\infty} b_n \left(\sqrt{p_2}r\right)^{-n} & (\sqrt{q_2}r)^{-\frac{1}{2}} \exp(-\sqrt{q_2}r) \sum_{n=0}^{\infty} d_n \left(\sqrt{q_2}r\right)^{-n} \end{bmatrix} \begin{bmatrix} C_1 \\ C_2 \end{bmatrix}, \quad (4.79)$$

where a_n, b_n, c_n and d_n has the recursive relation:

$$a_0 = 1, \tag{4.80}$$

$$b_0 = \frac{p_2 s\nu}{p_2 - q_2} a_0, \tag{4.81}$$

$$a_1 = \frac{4p_0\nu^2 - 1}{8} a_0 + \frac{s\nu}{2} b_0, \tag{4.82}$$

$$b_1 = \frac{p_2}{p_2 - q_2}\left(\frac{s\nu}{2} a_0 + s\nu a_1 - 2b_0\right), \tag{4.83}$$

$$a_n = \frac{4p_0\nu^2 - (2n-1)^2}{8n} a_{n-1} + \frac{s\nu}{2n} b_{n-1} + \frac{s\nu(2n-1)}{4n} b_{n-2}, \tag{4.84}$$

$$b_n = \frac{p_2}{p_2 - q_2}\left(\frac{s\nu(2n-1)}{2} a_{n-1} + s\nu a_n - \frac{4q_0\nu^2 + (2n-1)^2}{4} b_{n-2} - 2nb_{n-1}\right), \tag{4.85}$$

$$d_0 = 1, \tag{4.86}$$

$$c_0 = \frac{q_2 s\nu}{q_2 - p_2} d_0, \tag{4.87}$$

$$d_1 = -\frac{4q_0\nu^2 + 1}{8} d_0 + \frac{s\nu}{2} c_0, \tag{4.88}$$

$$c_1 = \frac{q_2}{q_2 - p_2}\left(\frac{s\nu}{2} d_0 + s\nu d_1 - 2c_0\right), \tag{4.89}$$

$$d_n = -\frac{4q_0\nu^2 + (2n-1)^2}{8n} d_{n-1} + \frac{s\nu}{2n} c_{n-1} + \frac{s\nu(2n-1)}{4n} c_{n-2}, \tag{4.90}$$

$$c_n = \frac{q_2}{q_2 - p_2}\left(\frac{s\nu(2n-1)}{2} d_{n-1} + s\nu d_n - \frac{(2n-1)^2 - 4p_0\nu^2}{4} c_{n-2} - 2nc_{n-1}\right). \tag{4.91}$$

4.3.5. Conclusion

In Sec. 4.3, the modes solution for waveguide with anisotropic cladding is discussed. Here a general case is considered, where both permittivity and permeability are anisotropic and diagonalized with respect to cylindrical coordinate system. The derivation of general dispersion relation is presented without knowing the exact solution formula in the cladding area. When applying type II hyperbolic materials as cladding material with $\epsilon_r < 0 < \epsilon_\phi = \epsilon_z$, the description of the electromagnetic field in the cladding become a coupled second order differential equation system. The special case $\nu = 0$ is discussed and it is confirmed that the low order TM modes with larger effective index can be filtered out by using hyperbolic cladding in cylindrical waveguide. For more general case with $\nu \neq 0$, the analytical solution is not found yet. However, we present our attempt for solving this problem by using asymptotic approximation.

References

[1] Y. Tang, Z. Xi, M. Xu, S. Bäumer, A. J. L. Adam, and H. P. Urbach, *Spatial mode-selective waveguide with hyperbolic cladding,* Opt. Lett. **41**, 4285 (2016).

[2] Z. Jacob, L. V. Alekseyev, and E. Narimanov, *Optical hyperlens: far-field imaging beyond the diffraction limit,* Opt. Express **14**, 8247 (2006).

[3] Z. Liu, H. Lee, Y. Xiong, C. Sun, and X. Zhang, *Far-field optical hyperlens magnifying sub-diffraction-limited objects,* Science **315**, 1686 (2007).

[4] E. Forati, G. W. Hanson, A. B. Yakovlev, and A. Alu, *Planar hyperlens based on a modulated graphene monolayer,* Phys. Rev. B **89**, 081410 (2014).

[5] J. Sun, M. I. Shalaev, and N. M. Litchinitser, *Experimental demonstration of a non-resonant hyperlens in the visible spectral range,* Nat. Commun. **6** (2015).

[6] T. Repän, A. V. Lavrinenko, and S. V. Zhukovsky, *Dark-field hyperlens: Super-resolution imaging of weakly scattering objects,* Opt. Express **23**, 25350 (2015).

[7] T. Galfsky, H. Krishnamoorthy, W. Newman, E. Narimanov, Z. Jacob, and V. Menon, *Active hyperbolic metamaterials: enhanced spontaneous emission and light extraction,* Optica **2**, 62 (2015).

[8] A. N. Poddubny, P. A. Belov, and Y. S. Kivshar, *Purcell effect in wire metamaterials,* Phys. Rev. B **87**, 035136 (2013).

[9] A. Chebykin, A. Orlov, A. Shalin, A. Poddubny, and P. Belov, *Strong purcell effect in anisotropic ε-near-zero metamaterials,* Phys. Rev. B **91**, 205126 (2015).

[10] K. V. Sreekanth, K. H. Krishna, A. De Luca, and G. Strangi, *Large spontaneous emission rate enhancement in grating coupled hyperbolic metamaterials,* Sci. Rep. **4** (2014).

[11] D. Lu, J. J. Kan, E. E. Fullerton, and Z. Liu, *Enhancing spontaneous emission rates of molecules using nanopatterned multilayer hyperbolic metamaterials,* Nat. Nanotechnol. **9**, 48 (2014).

[12] C. Guclu, T. S. Luk, G. T. Wang, and F. Capolino, *Radiative emission enhancement using nano-antennas made of hyperbolic metamaterial resonators,* Appl. Phys. Lett. **105**, 123101 (2014).

[13] N. Vasilantonakis, G. Wurtz, V. Podolskiy, and A. Zayats, *Refractive index sensing with hyperbolic metamaterials: strategies for biosensing and nonlinearity enhancement,* Opt. Express **23**, 14329 (2015).

[14] T. G. Mackay, *Toward optical sensing with hyperbolic metamaterials,* Opt. Eng. **54**, 067102 (2015).

[15] S. Tang, Y. Fang, Z. Liu, L. Zhou, and Y. Mei, *Tubular optical microcavities of indefinite medium for sensitive liquid refractometers,* Lab Chip **16**, 182 (2016).

[16] Y. He, S. He, J. Gao, and X. Yang, *Nanoscale metamaterial optical waveguides with ultrahigh refractive indices,* J. Opt. Soc. Am. B **29**, 2559 (2012).

[17] S. Ishii, M. Y. Shalaginov, V. E. Babicheva, A. Boltasseva, and A. V. Kildishev, *Plasmonic waveguides cladded by hyperbolic metamaterials,* Opt. Lett. **39**, 4663 (2014).

[18] V. E. Babicheva, M. Y. Shalaginov, S. Ishii, A. Boltasseva, and A. V. Kildishev, *Finite-width plasmonic waveguides with hyperbolic multilayer cladding,* Opt. Express **23**, 9681 (2015).

[19] V. E. Babicheva, M. Y. Shalaginov, S. Ishii, A. Boltasseva, and A. V. Kildishev, *Long-range plasmonic waveguides with hyperbolic cladding,* Opt. Express **23**, 31109 (2015).

[20] N. Vasilantonakis, M. E. Nasir, W. Dickson, G. A. Wurtz, and A. V. Zayats, *Bulk plasmon-polaritons in hyperbolic nanorod metamaterial waveguides,* Laser Photon. Rev. **9**, 345 (2015).

[21] D. Richardson, J. Fini, and L. Nelson, *Space-division multiplexing in optical fibres,* Nature Photon. **7**, 354 (2013).

[22] H. Chen, R. van Uden, C. Okonkwo, and T. Koonen, *Compact spatial multiplexers for mode division multiplexing,* Opt. Express **22**, 31582 (2014).

[23] J. D. Caldwell, A. V. Kretinin, Y. Chen, V. Giannini, M. M. Fogler, Y. Francescato, C. T. Ellis, J. G. Tischler, C. R. Woods, A. J. Giles, M. Hong, K. Watanable, T. Taniguchi, S. A. Maier, and K. S. Novoselov, *Sub-diffractional volume-confined polaritons in the natural hyperbolic material hexagonal boron nitride,* Nat. Commun. **5** (2014).

[24] K. Korzeb, M. Gajc, and D. A. Pawlak, *Compendium of natural hyperbolic materials,* Opt. Express **23**, 25406 (2015).

[25] W. Cai and V. M. Shalaev, *Optical Metamaterials*, Vol. 10 (Springer, 2010).

[26] P. B. Johnson and R.-W. Christy, *Optical constants of the noble metals,* Phys. Rev. B **6**, 4370 (1972).

[27] C.-I. Lin and T. K. Gaylord, *Multimode metal-insulator-metal waveguides: Analysis and experimental characterization,* Phys. Rev. B **85**, 085405 (2012).

[28] N. Riesen and J. D. Love, *Ultra-broadband tapered mode-selective couplers for few-mode optical fiber networks,* IEEE Photon. Technol. Lett. **25**, 2501 (2013).

[29] K. Aoki, A. Okamoto, Y. Wakayama, A. Tomita, and S. Honma, *Selective multimode excitation using volume holographic mode multiplexer,* Opt. Lett. **38**, 769 (2013).

5

Hyperlens design and performance evaluation under the lossy condition

Hyperbolic materials are capable of supporting high-spatial frequency propagating waves. This property offers them a high potential in the super-resolution imaging applications, such as hyperlens. However, all of the current hyperbolic materials and hyperbolic meta-materials have intrinsic absorption, which influence the resolution performance of the hyperlens. In this chapter, a theoretical study on the refraction of light incident from an isotropic medium to a lossy hyperbolic medium is presented. The results show that the absorption in the medium plays an essential role in the refraction property and the design of the hyperlens. Based on the lossy condition, the hyperlens is designed using geometrical optics. By using the Rayleigh diffraction integral, we investigate the resolution of the hyperlens as function of the size of the lens.

5.1. Introduction

Super-resolution technologies have drawn broad interests as a powerful tool to overcome the Abbe's diffraction limit in conventional optical system. Ever since the invention of the perfect lens [1], the developments of the hyperlens have been extensively explored both theoretically [2–15] and experimentally [16–21]. Hyperlens is a super-resolution technique that make use of hyperbolic materials (HMs), which is an anisotropic material with both positive and negative permittivity components in the permittivity tensor. HMs present hyperbolic dispersion which can allow high spatial-frequency propagation modes. The underlying physics behind the hyperlens is the conversion of evanescent waves, which carry the subwavelength detailed information of an object, to propagation waves. HMs also have been widely applied in Purcell factor engineering [22–26], waveguide [27–33], and in sensing applications [34–36]. The HM property has been achieved by using nano-fabricated meta-materials (MMs) [18, 37, 38]. Most recently natural HMs have also been found [39–43].

The hyperlens has been demonstrated using cylindrically or spherically anisotropic HMs, where the permittivity tensor of the HM is diagonal in cylindrical or spherical coordinate [2–10, 16–20, 44, 45]. These designs are difficult to fabricate because the interface of multilayer meta-material hyperlens are curved surfaces, and they can not be realized with natural HMs. Recently a simpler type of hyperlens has been proposed, which only requires HMs of Cartesian anisotropic where the permittivity tensor of the HM is diagonal in Cartesian coordinate [7, 11–15, 21, 45]. The surface profile of the hyperlens is carefully designed, such that a collimated beam can be coupled to the high-spatial frequency modes of the HM and can be focused to a subwavelength spot. The HMs of this hyperlens can be achieved with meta-materials based on multilayer or nanowires, and are compatible with natural HMs. This design is also called metalens [46, 47] or meta-material immersion lens [14].

Ideally, the resolution of a hyperlens is unlimited as it can propagate arbitrarily high-spatial frequency wave. Nevertheless, to the best of our knowledge, the HMs found or fabricated so far all come with intrinsic material absorption, which leads to attenuation of the ray propagating from the interface and hence severely reduces the resolution. Because the light attenuates more over longer propagation distances, the size of hyperlens has to be small. Moreover, the absorption in the material does not only influence the propagation decay of the wave inside, but also changes the refraction of light, which leads to aberrations. As a consequence, the designed surface profile has to be optimized to reduce the aberrations caused by this refraction.

In this work, a comprehensive analysis of the influence of absorption on the HMs refraction and on the resolution power of the hyperlens is presented, offering guidelines for the hyperlens design. The HMs or the effective hyperbolic meta-materials (HMMs) considered here are of complex permittivity tensors. We study the refraction and transmission of the light incident at the interface for arbitrary orientation between an isotropic medium and a HM. It is shown that the refraction angle is reduced as well as the phase of the wave is shifted due to the absorption

of the material. By including the absorption coefficient in the hyperlens design, the adapted hyperlens profile deviates from the lossless hyperlens. Furthermore, the Rayleigh diffraction integral is used to evaluate the deterioration of the resolution power of hyperlens, and numerical simulations agree well with the Rayleigh diffraction integral.

5.2. Refraction of light at a given interface

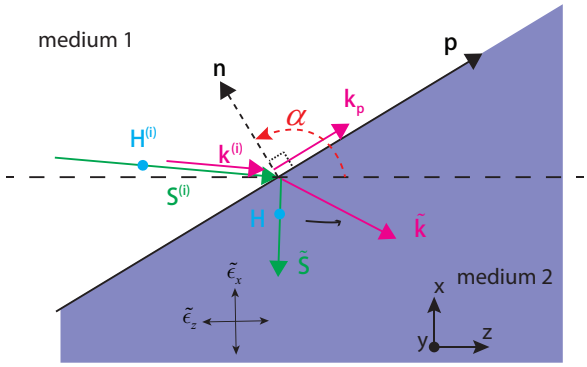

Figure 5.1: The schematic of the studied refraction situation. The p-polarized light ($E_y = 0$) is incident from the lossless isotropic medium 1 (white region, e.g. air) to the lossy hyperbolic anisotropic medium 2 (blue region). The permittivity tensor of the HM is a complex diagonal in the Cartesian coordinate system. The orientation of the interface is denoted by the normal vector $\mathbf{n}$, which angle is given by α respecting to the z-axis.

In this chapter, only the two-dimensional (2D) situation and the p-polarized light is discussed. As shown in Fig. 5.1, in a Cartesian coordinate system, the geometry is invariant along the y-axis and the electric field along y is zero ($E_y = 0$). The tangential and the normal vector of the interface are denoted by $\mathbf{p}$ and $\mathbf{n}$ (pointing towards the incident medium), respectively, where the angle between $\mathbf{n}$ and the z-axis is defined as α (from $\hat{z}$ to $\mathbf{n}$, $-\pi < \alpha \leq \pi$). The incident medium on the left (white area) is isotropic and lossless. Therefore, for the incident field, the wavevector $\mathbf{k}^{(\mathbf{i})}$ is parallel to the energy flow $\mathbf{S}^{(\mathbf{i})}$. The medium on the right (blue shade area) is a lossy HM with its optical axis along the z-axis, such that the permittivity tensor is given by

$$\underline{\underline{\tilde{\epsilon}}} = \begin{bmatrix} \tilde{\epsilon}_x & 0 & 0 \\ 0 & \tilde{\epsilon}_y & 0 \\ 0 & 0 & \tilde{\epsilon}_z \end{bmatrix} = \begin{bmatrix} \epsilon_{x,r} + i\epsilon_{x,i} & 0 & 0 \\ 0 & \epsilon_{x,r} + i\epsilon_{x,i} & 0 \\ 0 & 0 & \epsilon_{z,r} + i\epsilon_{z,i} \end{bmatrix}, \tag{5.1}$$

where $\tilde{\epsilon}_x$ and $\tilde{\epsilon}_y$ are equal. For p-polarized light with E_y=0, the wavevector $\tilde{\mathbf{k}}$ inside the medium 2 is not always parallel to the energy flow $\tilde{\mathbf{S}}$ in the anisotropic medium. Assuming the HM is obtained using silver (Ag) [48] nanowires embedded in the air domain, with the nanowire parallel to the z-axis, the effective permittivity of the

HM is given by [49]

$$\tilde{\epsilon}_z = f\epsilon_{\mathrm{Ag}} + (1-f)\epsilon_{\mathrm{air}}, \tag{5.2}$$

$$\tilde{\epsilon}_x = \tilde{\epsilon}_y = \frac{[(1+f)\epsilon_{\mathrm{Ag}} + (1-f)\epsilon_{\mathrm{air}}]\epsilon_{\mathrm{air}}}{(1-f)\epsilon_{\mathrm{Ag}} + (1+f)\epsilon_{\mathrm{air}}}, \tag{5.3}$$

where f is the filling factor given by the area ratio of Ag versus air in the cross-section plane. ϵ_{Ag} and ϵ_{air} are the permittivities of the Ag and the air, respectively. At the wavelength of 633 nm, the effective permittivity values as functions of filling factor are shown in Fig. 5.2. It can be seen that besides the anisotropic behavior of the real part of the permittivities (Fig. 5.2a), the imaginary part of the permittivities (Fig. 5.2b) are also anisotropic. Consequently, the wavevector component perpendicular to the interface of the refracted light in this lossy medium will also become complex. It leads to a complex total wavevector $\tilde{\mathbf{k}} = \mathbf{k_r} + i\,\mathbf{k_i}$, where $\mathbf{k_r}$ and $\mathbf{k_i}$ are the real part and the imaginary part of the complex wavevector in the HM, representing propagation and attenuation of the light, respectively.

In Fig. 5.2a, the maximum achievable NA of the lossless hyperlens is also plotted as black dotted line. In the HMs as well as in the conventional anisotropic media, the maximum achievable NA is not given by the geometrical incident angle of the light, but is given by the maximum excitable transversal wavenumber $k_x^{(\max)}$ in the media. The optical axis is along z, hence $\mathrm{NA}^{(\max)} = k_x^{(\max)}/k_0$, where k_0 is the wavenumber of the light in vacuum. The detailed derivation of $\mathrm{NA}^{(\max)}$ can be found in Supplementary Material Sec. 5.7.3. It can be seen that if the absorption is not considered, the maximum achievable NA of the hyperlens depends on the consisting materials, and can be even infinite.

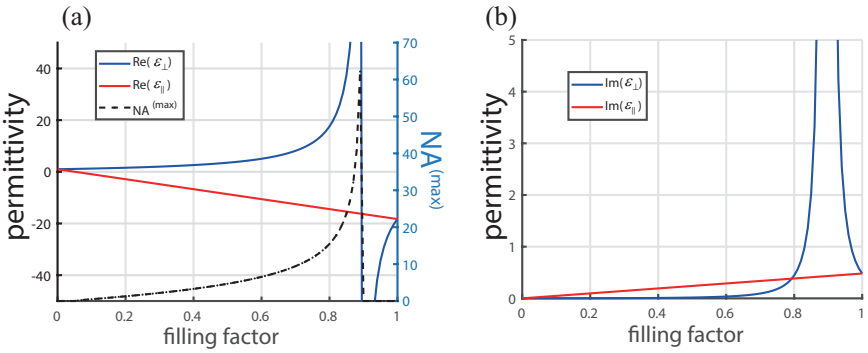

Figure 5.2: The effective permittivity of an effective HMM, made of silver nanowire embedded in the air domain at the wavelength of 633 nm. (a) The real part of the permittivity components parallel to the nanowire $\epsilon_\parallel$ and perpendicular to the nanowire $\epsilon_\perp$. The dot line indicates the maximum achievable NA of a hyperlens made from the HM, as given by Eq. 5.46. (b) The imaginary part of the permittivity components parallel to the nanowire and perpendicular to the nanowire.

In order to extract the complex $\tilde{\mathbf{k}}$ in the lossy HM, we begin with the boundary conditions at the interface. Using the continuity of tangential component of the wavevector along the interface, the tangential component of the wavevector in the

HM can be calculated. In the $x-z$ plane, the normal unit vector of the interface is $\hat{\mathbf{n}} = \langle \sin(\alpha), \cos(\alpha) \rangle$, and the tangential unit vector of the interface is $\hat{\mathbf{p}} = \langle \cos(\alpha), -\sin(\alpha) \rangle$. Here the y component of the coordinate is ignored for simplicity. Therefore, the tangential component of the wavevector is given by

$$\mathbf{k_p} = \left(\mathbf{k^{(i)}} \cdot \hat{\mathbf{p}}\right) \hat{\mathbf{p}} = \left(k_x^{(i)} \cos^2(\alpha) - k_z^{(i)} \sin(\alpha)\cos(\alpha), k_x^{(i)} \sin(\alpha)\cos(\alpha) - k_z^{(i)} \sin^2(\alpha)\right), \tag{5.4}$$

where $\mathbf{k^{(i)}} = (k_x^{(i)}, k_z^{(i)})$.

Inside the HM, the wavevector becomes complex due to the absorption. However, it is clear that the tangential wavevector component $\mathbf{k_p}$ is preserved to be real. The complex part of this wavevector originates only from the orthogonal wavevector (perpendicular to the interface). Hence the total wavevector $\tilde{\mathbf{k}} = \left(\tilde{k}_x, \tilde{k}_z\right)$ in the HM can be written as

$$\begin{aligned} \tilde{\mathbf{k}} =& \mathbf{k_p} + \tilde{\beta}\hat{\mathbf{n}} = (\tilde{k}_x, \tilde{k}_z) \\ =& \left(k_x^{(i)} \cos^2(\alpha) - k_z^{(i)} \sin(\alpha)\cos(\alpha) + \tilde{\beta}\sin(\alpha), \right. \\ & \left. k_x^{(i)} \sin(\alpha)\cos(\alpha) - k_z^{(i)} \sin^2(\alpha) + \tilde{\beta}\cos(\alpha)\right), \end{aligned} \tag{5.5}$$

where $\tilde{\beta}$ is a complex number. Since the wavevector $\tilde{\mathbf{k}}$ also needs to fulfill the dispersion relation of the HM

$$\frac{(\tilde{k}_x^2 + \tilde{k}_y^2)}{\tilde{\epsilon}_z} + \frac{\tilde{k}_z^2}{\tilde{\epsilon}_x} = 1, \tag{5.6}$$

where $\tilde{k}_y = 0$, one can derive that

$$\begin{aligned} &\frac{\left(k_x^{(i)} \cos^2(\alpha) - k_z^{(i)} \sin(\alpha)\cos(\alpha) + \tilde{\beta}\sin(\alpha)\right)^2}{\tilde{\epsilon}_z} \\ &+ \frac{\left(k_x^{(i)} \sin(\alpha)\cos(\alpha) - k_z^{(i)} \sin^2(\alpha) + \tilde{\beta}\cos(\alpha)\right)^2}{\tilde{\epsilon}_x} = 1. \end{aligned} \tag{5.7}$$

Solving Eq. 5.7 leads to a complex $\tilde{\beta}$ and hence a complex $\tilde{\mathbf{k}}$ can be obtained. Please note that Eq. 5.7 is a quadratic equation, hence two solutions of $\tilde{\beta}$ can be found. One should choose the solution of which the Poynting vector $\tilde{\mathbf{S}}$ (the energy flow) points away from the interface. The time-averaged Poynting vector in the lossy anisotropic medium is given by

$$\begin{aligned} \langle \mathbf{S} \rangle \equiv& \frac{1}{2} \mathrm{Re}\left(\mathbf{E} \times \mathbf{H}^*\right), \\ =& \frac{|H_y|^2}{2\omega\epsilon_0} \mathrm{Re}\left(\begin{bmatrix} \frac{\tilde{k}_x}{\tilde{\epsilon}_z} \\ 0 \\ \frac{\tilde{k}_z}{\tilde{\epsilon}_x} \end{bmatrix}\right) \exp\left(-2\,\mathrm{Im}(\tilde{\mathbf{k}})\mathbf{r}\right), \end{aligned} \tag{5.8}$$

where H_y is the amplitude of the magnetic field. The detailed derivation can be found in the Supplementary Material Sec. 5.7.1.

One can see in Eq. 5.8 that the direction of the energy flow depends on the **real** part of the ratio between $\tilde{k}_x/\tilde{\epsilon}_z$ and $\tilde{k}_z/\tilde{\epsilon}_x$. The last term of Eq. 5.8 represents the exponential decay of the energy flow due to the absorption of the material, which is fully determined by the **imaginary** part of the wavevector.

To understand the influence of the absorption of the HM on the refraction angle, the refraction of light on HM with real and complex permittivity tensor are compared. The HM used here is the same as in Fig. 5.2, with a filling ratio $f = 0.8$. The effective permittivities are $\epsilon_x = \epsilon_y = 17.58 + 0.44i$ and $\epsilon_z = -14.44 + 0.38i$. The results are shown in Fig. 5.3. In all Fig. 5.3a-c, the arrow lines of the incident rays $\mathbf{M_{air}}$ and the refraction rays $\mathbf{M_{HM}}$ are defined as

$$\mathbf{M_{air}} = (1 - |r|^2)\,\mathrm{Re}\left(\begin{bmatrix} k_x^{(i)} \\ 0 \\ k_z^{(i)} \end{bmatrix}\right),\quad \mathbf{M_{HM}} = |t|^2\,\mathrm{Re}\left(\begin{bmatrix} \frac{\tilde{k}_x}{\tilde{\epsilon}_z} \\ 0 \\ \frac{\tilde{k}_z}{\tilde{\epsilon}_x} \end{bmatrix}\right), \tag{5.9}$$

which are proportional to the real part of the Poynting vector. It can be interpreted that the projection of $\mathbf{M}$ along the normal of the interface ($\mathbf{M} \cdot \hat{\mathbf{n}}$) indicates the coupling efficiency of light to the HM.

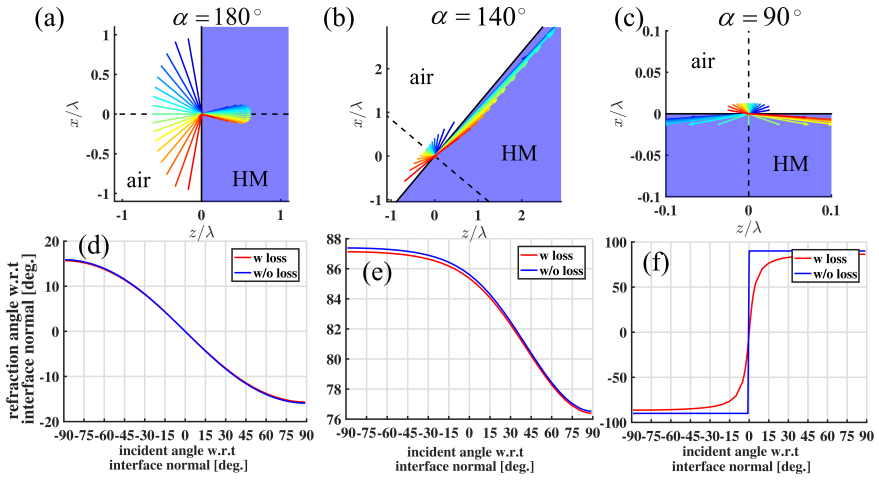

Figure 5.3: **The planewave refraction from the air (white region) to the HM (blue region) of different interface orientations.** The effective HM considered here is given by silver nanowires (parallel to the optical axis z) embedded in the air domain. With a filling factor of 0.80, the effective permittivities are $\epsilon_x = 17.58 + 0.44i$ and $\epsilon_z = -14.44 + 0.38i$, respectively. The three columns represent the interfaces of different angles, respectively. In the first row (a),(b),(c) show planewave refraction at the interface, where different colors represent different incident angles. In the second row (d),(e),(f) show the refraction angles as functions of incident angles, where the blue curve and the red curve are the cases of HM without and with absorption, respectively.

Fig. 5.3a illustrates the light refracted from the air ($\epsilon_{\text{air}} = 1$) (on the left) to the HM (on the right). In this case, the normal of the interface is perpendicular to the

optical axis (z) and the colored rays indicate different incident angles. It can be seen that as expected, for all incident angles, the light experiences negative refraction. The refraction angle versus incident angle is plotted in Fig. 5.3d. Compared to the lossless case, the refraction angles are slightly smaller when the absorption (imaginary part of $\underline{\underline{\epsilon}}$) is included. The discrepancy deviates further as the incident angle increases. In Fig. 5.3b the refraction at the interface with $\alpha = 140°$ is shown. In this case, the negative refraction only occurs for negative incident angles, while for positive incident angles, the refraction are positive. This is the phenomenon of directional light emission inside HMs, where the Poynting vector direction is always confined to a cone [50]. In Fig. 5.3e the comparison between the lossy and the lossless refraction angles are shown. Similarly, the refraction angles are reduced in the lossy HM. This deviation of the refraction angle is severer when the light is coupled to the high-k modes in the HM. Fig. 5.3c and Fig. 5.3f show similar results for the interface parallel to the optical axis. In this case, only positive refraction takes place at the interface. For the lossless situation, the refraction angle is maintained at $\pm 90°$, indicating zero transmission of light. This is due to the existence of the bandgap of the HM and hence no light can be coupled through. However, for the lossy HM, a small fraction of the light is still able to be coupled to the HM, indicating that the bandgap is no longer perfect.

5.3. Fresnel coefficients

Once the complex wavevector $\tilde{\mathbf{k}}$ and the orientation of the interface α are known, the Fresnel coefficients can be calculated. The Fresnel coefficients are derived using the continuity condition of the magnetic field (H_y) and the projection of the electric field along the tangential of the interface (along $\mathbf{p}$). The detailed derivation can be found in the Supplementary Material Sec. 5.7.2. The Fresnel coefficients are given by

$$\begin{bmatrix} r \\ t \end{bmatrix} = \begin{bmatrix} -\frac{\cos(\alpha)k_z^{(r)} + \sin(\alpha)k_x^{(r)}}{\epsilon^{(i)}} & \left(\frac{\cos(\alpha)k_z^{(t)}}{\tilde{\epsilon}_x} + \frac{\sin(\alpha)k_x^{(t)}}{\tilde{\epsilon}_z} \right) \\ -1 & 1 \end{bmatrix}^{-1} \begin{bmatrix} \frac{\cos(\alpha)k_z^{(i)} + \sin(\alpha)k_x^{(i)}}{\epsilon^{(i)}} \\ 1 \end{bmatrix} \tag{5.10}$$

where $\epsilon^{(i)}$ is the permittivity constant of the incident medium; r and t are the reflection and transmission coefficients, respectively. $k_x^{(r)}$ and $k_z^{(r)}$ are the wavevector components of the reflection light along the x-axis and the z-axis, respectively.

From Eq. 5.10, one can see that for a lossless HM ($\underline{\underline{\epsilon}}$ is real), the wavevector $\mathbf{k}$ becomes real. Therefore, the Fresnel coefficients are real, and there is no phase jump for the field at the interface.

However, once the material become lossy, the matrix in Eq. 5.10 will become complex as well as the Fresnel coefficients. One can rewrite the Fresnel coefficients

$$\begin{bmatrix} \tilde{r} \\ \tilde{t} \end{bmatrix} = \begin{bmatrix} |\tilde{r}| \exp(i\phi_r) \\ |\tilde{t}| \exp(i\phi_t) \end{bmatrix}, \tag{5.11}$$

where ϕ_r and ϕ_t denote the phase jump for Fresnel coefficients of the reflected and the transmitted light, respectively.

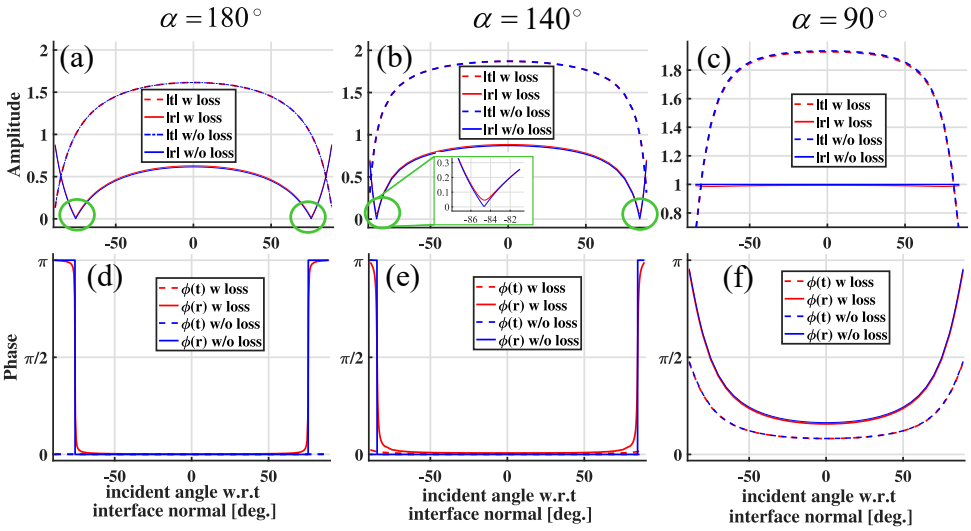

Figure 5.4: The Fresnel transmission/reflection coefficients for a planewave incident from the air to the HM for different orientation of the interface. (a),(b),(c): the absolute values of the Fresnel coefficients. The green circles indicate the Brewster angle. Insert in (b) shows the Brewster angle does not reach 0 for HM with loss. (d),(e),(f): the phase of the Fresnel coefficients.

In Fig. 5.4, the Fresnel coefficients versus incident angles for different interface orientations are plotted. Fig. 5.4a and Fig. 5.4b show that, similar to conventional medium, the p-polarized incident light also experiences a Brewster angle where the reflectance ($R = |r|^2$) reaches zero. However, when the absorption is taken into account, the dip at the Brewster angle does not reach completely zero as shown in the insert of the Fig. 5.4b. This result shows that it is possible to couple light to HM with high efficiency (close to unity). In Fig. 5.4d and Fig. 5.4e, the phase of the Fresnel coefficients are shown. It can be seen that the transmission t and the reflection r have zero phase shift for lossless case, while the phase changes smoothly with the incident angle in the lossy case.

In Fig. 5.4c and Fig. 5.4f, the Fresnel coefficients for $\alpha = 90°$ are plotted. It can be seen that the reflection r is unity for lossless case, indicating a pure metallic behavior for the HM. However, in the case of lossy HM, the reflection r is not unity anymore, showing the light can still be partially coupled to the HM.

In the three interface orientations shown here, although it is symmetric as expected for α equals to $180°$ and $90°$, it is surprising to see that the Fresnel coefficients are still symmetric even for the interface oriented at $140°$, while the refraction angle is not symmetric at all as shown in Fig. 5.3.

5.4. Influence on the hyperlens profile

From the above discussion, it is clear that the absorption of the HM influences the refraction angle, and hence it is necessary to take the absorption into account when designing a hyperlens. The change of the hyperlens profile is demonstrated at the wavelength of 633 nm. The incident medium is air, and the HM considered here is an effective HMM, given by silver nanowires (parallel to the optical axis z) embedded in the air domain. With a filling factor of 0.85, the effective permittivities of the HM are ϵ_x=37.52 + 2.03i and ϵ_z=-15.40 + 0.41i, respectively.

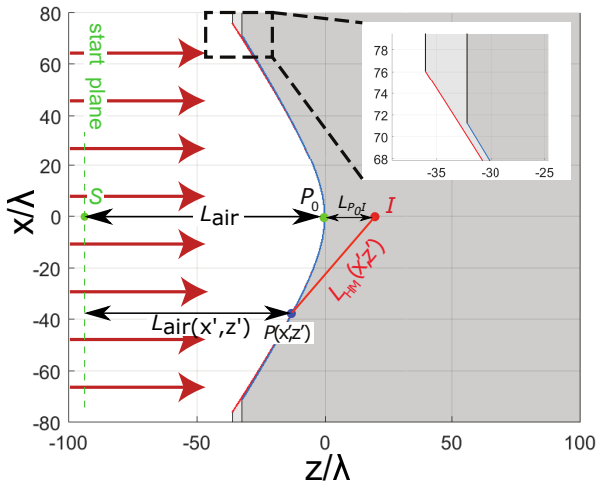

Figure 5.5: The hyperlens profile for wavelength of 633 nm and NA=7.0. The incident beam is a collimated planewave incident from the air side, the effective HM is silver (ϵ_{Ag}=-18.30+0.48i) nanowires (along z) embedded in the air domain with a filling factor of 0.85. The effective permittivity of the material is ϵ_x=37.52 + 2.03i and ϵ_z=-15.40 + 0.41i, respectively. The red curved interface denotes the hyperlens profile with absorption and the blue curved interface denotes the hyperlens profile without absorption. For all hyperlens profiles, the straighted-lines parts parallel to the x-axis are considered as the infinite thin nontransparent aperture. The inset is a zoom in of the edge area, showing the profile difference clearly. The red dot at $Z = 20\lambda$ is the focal center of the lens.

The curvature of the lens is constructed using geometrical optics. The apex of the lens P_0 (Fig. 5.5) is at the origin of the coordinate and the focal center I is at $(0,\ 20\lambda)$, where λ is the wavelength of the light. The optical path length (OPD) is calculated by $\mathrm{OPD}_0 = L_{\mathrm{air}} n_{\mathrm{air}} + \phi_t/2\pi + L_{P_0 I} n_{\mathrm{eff}}$, where L_{air} is the physical path length starting from an arbitrary start point S on the z-axis to P_0, ϕ_t is the phase jump of the Fresnel transmission coefficient, $L_{P_0 I}$ is the physical path length from the apex of the hyperlens to the focal center and n_{eff} is the effective index of the HM along this direction. With the OPD_0 one can search for all the other intersection points $P(x', z')$ for all the off-axis parallel beams, of which the OPDs should be equal to OPD_0.

$$L_{\mathrm{air}}(x', z') n_{\mathrm{air}} + \phi_t(x', z')/2\pi + L_{\mathrm{HM}}(x', z') n_{\mathrm{eff}}(x', z') = \mathrm{OPD}_0, \tag{5.12}$$

Where the x' and z' are the coordinate of the points P of the interface.

In Fig. 5.5, two hyperlenses with NA of 7.0 are shown. The red interface is the designed hyperlens profile for the lossy HM, while the blue one is the designed hyperlens for the lossless HM. It is clearly seen that the hyperlens of the lossy HM bends inwards with a smaller radius of curvature. For achieving the same NA, the aperture width of the lossy HM hyperlens needs to be larger compared to the lossless HM hyperlens. This can be explained by the fact that the absorption reduces the refraction angle. Hence the surface of the lens needs to move towards the negative z direction in order to focus the light to the same focal center. It can be calculated that the maximum achievable NA of the lossless hyperlens is ≈23 (see Fig. 5.2). If the NA is further increased, the discrepancy between the lossy and lossless hyperlens profile will be even larger.

5.5. Influence on the resolution power of hyperlens

Once the hyperlens is designed using the geometrical optical approach, the field distribution at the focus needs to be evaluated using wave optics. The Rayleigh diffraction integral [51] is used to evaluate the resolution of the hyperlens, which is defined as the full width half maximum (FWHM) of the magnetic-field amplitude ($|H_y|$). Only a 2D situation is considered, therefore the scalar diffraction theory is used with only the magnetic field component H_y.

We start from the Maxwell equation in medium 2

$$\nabla \times \mathbf{E} = i\omega\mu_0\mathbf{H}, \tag{5.13}$$

$$\nabla \times \mathbf{H} = -i\omega\epsilon_0\underline{\underline{\tilde{\epsilon}}}\mathbf{E}. \tag{5.14}$$

By substituting Eq. 5.14 into Eq. 5.13, the vectorial Helmholtz equation for the magnetic field is given by

$$\nabla \times \left(\underline{\underline{\tilde{\epsilon}}}\nabla \times \mathbf{H}\right) = k_0^2\mathbf{H}, \tag{5.15}$$

where $k_0^2 = \omega^2\epsilon_0\mu_0$. By setting $\mathbf{H} = (0, H_y, 0)$, the above vectorial equation can be simplified to a scalar case

$$\tilde{\epsilon}_x\frac{\partial^2 H_y}{\partial x^2} + \tilde{\epsilon}_z\frac{\partial^2 H_y}{\partial z^2} + \tilde{\epsilon}_x\tilde{\epsilon}_z k_0^2 H_y = 0. \tag{5.16}$$

In order to solve Eq. 5.16, one can introduce $u = \sqrt{\tilde{\epsilon}_z}x, v = \sqrt{\tilde{\epsilon}_x}z$. Eq. 5.16 can hence be simplified to a scalar Helmholtz equation

$$\frac{\partial^2 H_y}{\partial u^2} + \frac{\partial^2 H_y}{\partial v^2} + k_0^2 H_y = 0, \tag{5.17}$$

with a typical solution being

$$U(u, v) = \frac{\exp(ik_0\rho)}{\rho}, \tag{5.18}$$

where $\rho = \sqrt{u^2 + v^2}$. This solution is a spherical wave originated from the center of the coordinate system. Hence by substituting the original variables x and y back, Eq. 5.16 has a solution

$$U(x,y) = \frac{\exp(ik_0\tilde{R}(x,z))}{\tilde{R}(x,z)}, \tag{5.19}$$

where $\tilde{R}(x,z) = \sqrt{\tilde{\epsilon}_z x^2 + \tilde{\epsilon}_x z^2}$, representing a complex distance from the origin.

The field amplitude and phase of Eq. 5.19 are shown in Fig. 5.6. The HM used here is an effective HMM made of silver nanowires (parallel to the optical axis z) embedded in air. At the wavelength of 633 nm and $f = 0.70$, the permittivities are ϵ_x=9.44+0.09i and ϵ_z=-12.51+0.34i. The solution represents a decaying directional-emission point source originating from the center. The emission is confined inside the upwards (downwards) cone area [50]. The phase plot in Fig. 5.6b reveals that the phase follows a hyperbolic shape, where the high-spatial frequency components are located close to the border of the cone.

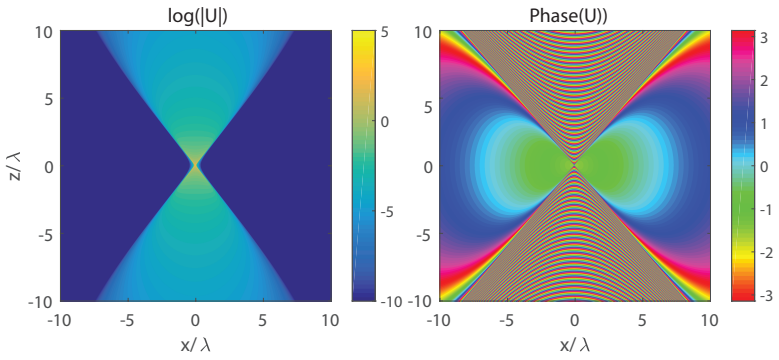

Figure 5.6: The 2D plotting of the function $U(x,y)$ in Eq. 5.19. It is a decaying hyperbolic wave originating from the center. The field is directionally distributed inside a cone area. The phase of the field modulate faster close the border of the cone.

Using the Rayleigh diffraction integral, the field distribution at the focal region can be evaluated by integrating the field at the surface of the hyperlens

$$H_y(x,z) = \frac{1}{2\pi}\int_S H_y(x',z')\frac{\partial U(x',z')}{\partial n}ds, \tag{5.20}$$

where x and z denote the coordinates in the focal area; S denotes the hyperlens surface; n denotes the normal of the surface; x' and z' denote the coordinates on the hyperlens; $H_y(x',z')$ denotes the field distribution at the surface of the hyperlens. This equation indicates that the field distribution in the focal region depends on the field distribution on the integral boundary and the first derivative of the solution of the Helmholtz equation Eq. 5.16.

In Fig. 5.7, the calculated field distributions of the hyperlenses with a constant focal length $L = 15\lambda$ (the distance from the apex P_0 of the lens to the focal center

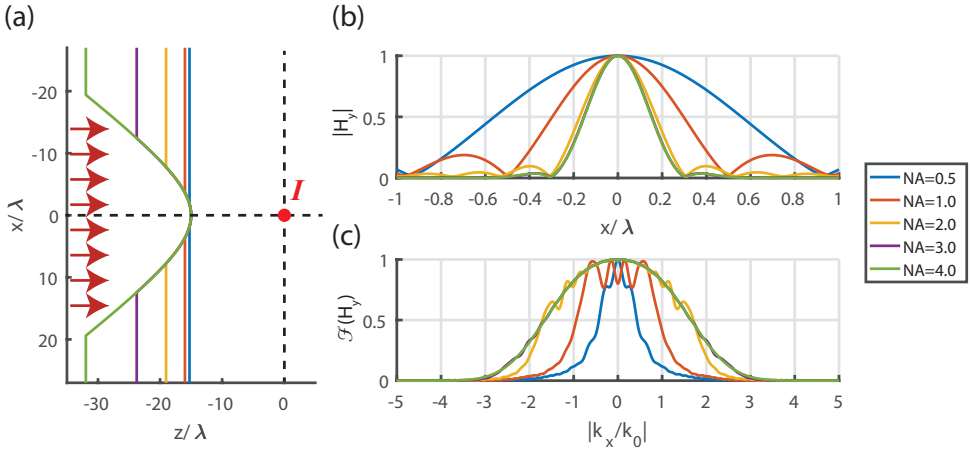

Figure 5.7: The comparison of hyperlens performance of different designed NA with a constant focal distance $L = 15\lambda$. The HM is made of silver (Ag) nanowires embedded in the air domain with $f = 0.70$, where the nanowire is parallel to the optical axis (z). The wavelength is 633 nm. The effective permittivities are ϵ_x=9.44+0.09i and ϵ_z=-12.51+0.34i. (a) Schematics of the hyperlenses. For all hyperlens profiles, the straighted-lines parts parallel to the x-axis are considered as the infinite thin nontransparent aperture. The red dot I denotes the focal center. The red arrows denote the incident planewaves from the air side. (b) The normalized amplitude of the magnetic field at the focal plane. (c) The normalized amplitude of Fourier transform of the corresponding magnetic field in (b).

I) and different NA are shown. It can be seen that the size of the hyperlens gets larger as the NA increases. Also, the width of the spot reduces for increasing NA. However, for NA=3.0 and NA=4.0, there is almost no reduction of the spot width. The minimum spot width in this situation is about 0.34λ. The Fourier spectrum in Fig. 5.7c shows that the spatial frequency of these two lenses are almost identical. This is because the high-spatial frequency components ($k_x/k_0 > 3$) of the field decay to a negligible value before reaching the focal plane, and hence can not contribute to the resolution enhancement. This result shows that if this focal length is chosen, it is impossible to increase the resolution by increasing the NA of the designed hyperlens (NA>3 in this case). The aperture width of the hyperlens of NA=3.0 is about $24.8\lambda = 15.7$ um.

In Fig. 5.8, the calculated field distributions of hyperlenses for different focal lengths are shown. In this situation, the designed NA of the hyperlenses are all 4.0, and the focal length varies from $L = 5\lambda$ to $L = 35\lambda$. One can see that the profiles of the hyperlenses grow proportionally as the focal length increases, and the profiles are confined to a cone region with the same asymptotic behavior. In Fig. 5.8b, the different spot widths at the focal plane are shown. The minimum spot width of 0.172λ is achieved for $L = 5\lambda$. Its Fourier spectrum in Fig. 5.8c shows that the spatial frequency reaches up to $5k_0$. As the focal length increases, the spot width at the focal plane increases, with the maximum spot width of 0.494λ for $L = 35\lambda$.

The Rayleigh diffraction integral is a semi-analytical method, and becomes less

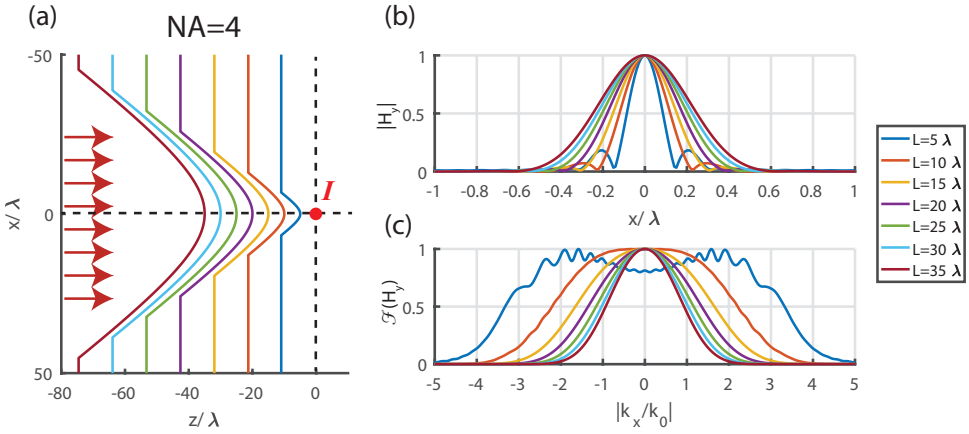

Figure 5.8: The comparison of the hyperlens performance for different sizes with a fixed NA=4.0. The HM considered here is the same as in Fig. 5.7. (a) Schematics of the hyperlenses. For all hyperlens profiles, the straighted-lines parts parallel to the x-axis are considered as the infinite thin non-transparent aperture. The red dot denotes the focal center I. The red arrows denote the incident planewaves from the air side. (b) The normalized amplitude of the magnetic field at the focal plane. (c) The normalized amplitude of Fourier transform of the corresponding magnetic field in (b).

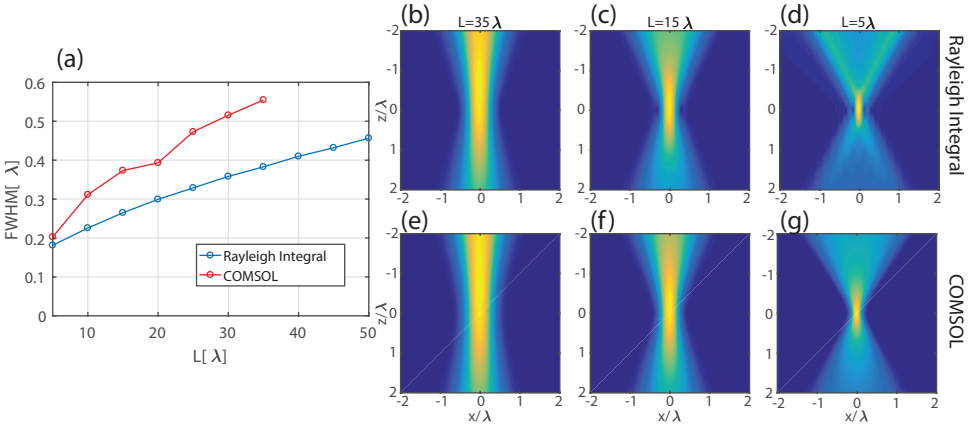

Figure 5.9: Comparison between the Rayleigh diffraction integral and the FEM simulation for the optimized hyperlens. (a) The spot widths (FWHM) at the focal plane as functions of the focal length of the hyperlens with a fixed designed NA=4.0. (b)-(d) The calculated normalized focal spot using the Rayleigh diffraction integral for a focal length of 35λ, 15λ and 5λ, respectively. (e)-(g) The simulated normalized focal spot using FEM simulation for a focal length of 35λ, 15λ and 5λ, respectively.

accurate for smaller focal length. Here the results are compared with a finite element method (FEM) simulation using a commercial package (COMSOL 5.2a). In COMSOL, the boundary condition is defined on the hyperlens surface, which profile and the complex field distribution on it are calculated using geometrical optics as described in Sec. 5.4. In order to resolve the high-k propagation modes, the maximum mesh size is set to be $\lambda/60$. The field distributions at the focal region are shown in Fig. 5.9b-g. It can be seen that both the Rayleigh diffraction integral and the numerical method have similar focal field distributions. The spot widths get larger for larger focal length L. Also, the depth of focus becomes larger as L increases. It is interesting to see that in both Fig. 5.9b and Fig. 5.9e, although the beam waists are located at the focal plane $z = 0$, the maximum amplitudes are located at $z < 0$. The FWHM of the H_y amplitude at the focal plane are shown in Fig. 5.9a. The results of COMSOL simulation are only calculated up to $L = 35\ \lambda$ due to the limited memory of the server. It can be seen that the spot widths calculated by the Rayleigh diffraction integral show a similar trend as the COMSOL simulation, but smaller compared to the COMSOL simulation. However, in our analysis, the main goal is to understand the resolution of hyperlens of all sizes; for smaller geometries, alternative methods such as numerical simulation can have a better performance. But it is not suitable to use pure numerical method for larger geometries as it requires heavy computation. This result shows that in order to maintain the performance of the hyperlens, the size of the lens has to be limited.

5.6. Conclusion

In this chapter, the refraction from lossless isotropic material to lossy anisotropic HM has been studied. The results show that the absorption of the HM reduces the refraction angle of the transmitted beam. Also the bandgap of the HM becomes non-ideal due to the absorption and hence the coupling of light to the HM bandgap becomes possible. It is also shown that the Brewster angle exists at the interface between air and the HM, indicating that the coupling efficiency can be maximized.

Based on the above analysis, we show that the designed hyperlens profile of the lossy HM is changed compared to lossless case. In the design, the directional phase jump at the interface of the lossy HM should be considered. The Rayleigh diffraction integral is used to evaluate the field distribution at the hyperlens focal region. It is shown that the resolution reduces as the size of the lens increases. In the example, a maximum NA of 3 can be achieved for a hyperlens with focal length $L = 15\ \lambda$ and width of $24.8\ \lambda$. The limited NA is caused by the fact that the high-spatial frequency components decay to a negligible value before reaching the focal plane. These high-spatial frequency components have a higher propagation attenuation and also needs to travel longer physical distance before reaching the focus. We have shown that, for a large hyperlens, it is impossible to achieve better resolution by increasing the NA of the hyperlens. In the example a designed NA=4.0 hyperlens can only achieve the desired resolution when the focal length L is smaller than $10\ \lambda$. The accuracy of the Rayleigh diffraction integral is compared with numerical method and good agreement is shown.

Although the hyperlens studied here is 2D, it can also be extended to a three

dimensional (3D) case, which is rotational symmetric along the z-axis. In this case, the illumination can be a collimated radial polarized light [6], where on all locations on the interface the p-polarized incidence can be maintained.

5.7. Supplementary Materials

5.7.1. Derivation of Poynting vector in lossy hyperbolic medium.

The HM has a permittivity tensor of the form

$$\underline{\underline{\tilde{\epsilon}}} = \begin{bmatrix} \tilde{\epsilon_x} & 0 & 0 \\ 0 & \tilde{\epsilon_y} & 0 \\ 0 & 0 & \tilde{\epsilon_z} \end{bmatrix}, \tag{5.21}$$

where $\mathrm{Re}(\tilde{\epsilon_z}) < 0 < \mathrm{Re}(\tilde{\epsilon_x}) = \mathrm{Re}(\tilde{\epsilon_y})$.

For p-polarized light, the H_y, E_x and E_z components are considered. Hence the magnetic field is given by

$$\mathbf{H} = \begin{bmatrix} 0 \\ \tilde{H}_y \\ 0 \end{bmatrix} = \begin{bmatrix} 0 \\ \tilde{A}_H \exp(i\tilde{\mathbf{k}}\mathbf{r}) \\ 0 \end{bmatrix}, \tag{5.22}$$

where $\tilde{A}_H$ is the complex amplitude of the magnetic field, $\tilde{\mathbf{k}} = (\tilde{k}_x, 0, \tilde{k}_z)$ is the complex wavevector of the electromagnetic field, $\mathbf{r}$ is the spatial coordinate. The Maxwell's equations leads to

$$\nabla \times \mathbf{H} = -i\omega\epsilon_0 \underline{\underline{\tilde{\epsilon}}} \mathbf{E}, \tag{5.23}$$

$$\begin{aligned} \mathbf{E} &= \frac{i}{\omega\epsilon_0} \underline{\underline{\tilde{\epsilon}}}^{-1} \nabla \times \mathbf{H}, \\ &= \frac{i}{\omega\epsilon_0} \underline{\underline{\tilde{\epsilon}}}^{-1} \begin{bmatrix} -\frac{\partial}{\partial z} H_y \\ 0 \\ \frac{\partial}{\partial x} H_y \end{bmatrix}, \\ &= \frac{i}{\omega\epsilon_0} \begin{bmatrix} -\tilde{\epsilon_x}^{-1} \frac{\partial}{\partial z} H_y \\ 0 \\ \tilde{\epsilon_z}^{-1} \frac{\partial}{\partial x} H_y \end{bmatrix}, \\ &= \begin{bmatrix} \frac{1}{\omega\epsilon_0 \tilde{\epsilon}_x} \tilde{k}_z H_y \\ 0 \\ -\frac{1}{\omega\epsilon_0 \tilde{\epsilon}_z} \tilde{k}_x H_y \end{bmatrix}. \end{aligned} \tag{5.24}$$

Hence the time-averaged Poynting vector can be calculated as

$$\begin{aligned} \langle \mathbf{S} \rangle &\equiv \frac{1}{2} \mathrm{Re}\left(\mathbf{E} \times \mathbf{H}^*\right), \\ &= \frac{|H_y|^2}{2\omega\epsilon_0} \mathrm{Re}\left(\begin{bmatrix} \frac{\tilde{k}_x}{\tilde{\epsilon}_z} \\ 0 \\ \frac{\tilde{k}_z}{\tilde{\epsilon}_x} \end{bmatrix} \right) \exp\left(-2\,\mathrm{Im}(\tilde{\mathbf{k}})\mathbf{r}\right). \end{aligned} \tag{5.25}$$

It is very important that the energy-flow should be decaying along the energy propagation direction. Hence the below condition should be valid

$$\mathrm{Re}\left(\begin{bmatrix} \frac{\tilde{k}_x}{\tilde{\epsilon}_z} \\ 0 \\ \frac{\tilde{k}_z}{\tilde{\epsilon}_x} \end{bmatrix}\right) \cdot \mathrm{Im}(\tilde{\mathbf{k}}) > 0. \tag{5.26}$$

5.7.2. Derivation of the Fresnel coefficients for anisotropic medium

Here a simple case is discussed, in which the permittivity tensors of both the incident medium and the transmission medium are diagonal with respect to the Cartesian coordinate system. In this case, the complex wavevector of the incident light $\tilde{\mathbf{k}}^{(i)}$, the reflection light $\tilde{\mathbf{k}}^{(r)}$, the transmission light $\tilde{\mathbf{k}}^{(t)}$, and the direction of the interface $\mathbf{n}$ are known, the Fresnel coefficients at the interface needs to be determined.

The optical properties of the input/output materials are given by the permittivity tensors

$$\underline{\underline{\tilde{\epsilon}_1}} = \begin{bmatrix} \epsilon_x^{(1)} & 0 & 0 \\ 0 & \epsilon_y^{(1)} & 0 \\ 0 & 0 & \epsilon_z^{(1)} \end{bmatrix}, \underline{\underline{\tilde{\epsilon}_2}} = \begin{bmatrix} \epsilon_x^{(2)} & 0 & 0 \\ 0 & \epsilon_y^{(2)} & 0 \\ 0 & 0 & \epsilon_z^{(2)} \end{bmatrix}. \tag{5.27}$$

It is not difficult to derive from the Maxwell's equation that

$$\mathbf{D} \equiv \epsilon_0 \underline{\underline{\tilde{\epsilon}}} \mathbf{E} = \mathbf{H} \times \frac{\mathbf{k}}{\omega}. \tag{5.28}$$

Since only the p-polarized light is considered, it is easy to write down the magnetic field components for the incident, reflected and transmitted waves. Assuming the incident wave amplitude is 1 ($|H^{(i)}| = 1$), one can have

$$\mathbf{H^{(i)}} = \begin{bmatrix} 0 \\ 1 \\ 0 \end{bmatrix}, \mathbf{H^{(r)}} = \begin{bmatrix} 0 \\ r \\ 0 \end{bmatrix}, \mathbf{H^{(t)}} = \begin{bmatrix} 0 \\ t \\ 0 \end{bmatrix}. \tag{5.29}$$

Assuming the wavevectors for the incident, reflected and transmitted waves are given by

$$\mathbf{k^{(i)}} = \begin{bmatrix} k_x^{(i)} \\ 0 \\ k_z^{(i)} \end{bmatrix}, \mathbf{k^{(r)}} = \begin{bmatrix} k_x^{(r)} \\ 0 \\ k_z^{(r)} \end{bmatrix}, \mathbf{k^{(t)}} = \begin{bmatrix} k_x^{(t)} \\ 0 \\ k_z^{(t)} \end{bmatrix}. \tag{5.30}$$

the displacement vector can be calculated

$$\mathbf{D^{(i)}} = \begin{bmatrix} \frac{k_z^{(i)}}{\omega} \\ 0 \\ -\frac{k_x^{(i)}}{\omega} \end{bmatrix}, \mathbf{D^{(r)}} = \begin{bmatrix} \frac{rk_z^{(r)}}{\omega} \\ 0 \\ -\frac{rk_x^{(r)}}{\omega} \end{bmatrix}, \mathbf{D^{(t)}} = \begin{bmatrix} \frac{tk_z^{(t)}}{\omega} \\ 0 \\ -\frac{tk_x^{(t)}}{\omega} \end{bmatrix}. \tag{5.31}$$

In the Cartesian coordinate system, the permittivity tensor is diagonal. Hence it is easy to get the electric field at the interface

$$\mathbf{E^{(i)}} = \begin{bmatrix} \frac{k_z^{(i)}}{\epsilon_0 \epsilon_x^{(1)} \omega} \\ 0 \\ -\frac{k_x^{(i)}}{\epsilon_0 \epsilon_z^{(1)} \omega} \end{bmatrix}, \mathbf{E^{(r)}} = \begin{bmatrix} \frac{r k_z^{(r)}}{\epsilon_0 \epsilon_x^{(1)} \omega} \\ 0 \\ -\frac{r k_x^{(r)}}{\epsilon_0 \epsilon_z^{(1)} \omega} \end{bmatrix}, \mathbf{E^{(t)}} = \begin{bmatrix} \frac{t k_z^{(t)}}{\epsilon_0 \epsilon_x^{(2)} \omega} \\ 0 \\ -\frac{t k_x^{(t)}}{\epsilon_0 \epsilon_z^{(2)} \omega} \end{bmatrix}. \tag{5.32}$$

The boundary condition impose that the tangential component of electric field is continuous. Hence, assuming the tangent direction is given by $\hat{\mathbf{p}} = \langle \cos(\alpha), 0, -\sin(\alpha) \rangle$, the tangential components of the electric field are

$$E_t^{(i)} = \hat{\mathbf{p}} \cdot \mathbf{E^{(i)}} = \frac{\cos(\alpha) k_z^{(i)}}{\epsilon_0 \epsilon_x^{(1)} \omega} + \frac{\sin(\alpha) k_x^{(i)}}{\epsilon_0 \epsilon_z^{(1)} \omega}, \tag{5.33}$$

$$E_t^{(r)} = \hat{\mathbf{p}} \cdot \mathbf{E^{(r)}} = \frac{\cos(\alpha) r k_z^{(r)}}{\epsilon_0 \epsilon_x^{(1)} \omega} + \frac{\sin(\alpha) r k_x^{(r)}}{\epsilon_0 \epsilon_z^{(1)} \omega}, \tag{5.34}$$

$$E_t^{(t)} = \hat{\mathbf{p}} \cdot \mathbf{E^{(t)}} = \frac{\cos(\alpha) t k_z^{(t)}}{\epsilon_0 \epsilon_x^{(2)} \omega} + \frac{\sin(\alpha) t k_x^{(t)}}{\epsilon_0 \epsilon_z^{(2)} \omega}. \tag{5.35}$$

Hence one can has the following continuity condition for the electric field and the magnetic field

$$\frac{\cos(\alpha) k_z^{(i)}}{\epsilon_x^{(1)}} + \frac{\sin(\alpha) k_x^{(i)}}{\epsilon_z^{(1)}} + \frac{\cos(\alpha) r k_z^{(r)}}{\epsilon_x^{(1)}} + \frac{\sin(\alpha) r k_x^{(r)}}{\epsilon_z^{(1)}} = \frac{\cos(\alpha) t k_z^{(t)}}{\epsilon_x^{(2)}} + \frac{\sin(\alpha) t k_x^{(t)}}{\epsilon_z^{(2)}}, \tag{5.36}$$

$$1 + r = t, \tag{5.37}$$

which in matrix format is

$$\begin{bmatrix} -\left(\frac{\cos(\alpha) k_z^{(r)}}{\epsilon_x^{(1)}} + \frac{\sin(\alpha) k_x^{(r)}}{\epsilon_z^{(1)}}\right) & \left(\frac{\cos(\alpha) k_z^{(t)}}{\epsilon_x^{(2)}} + \frac{\sin(\alpha) k_x^{(t)}}{\epsilon_z^{(2)}}\right) \\ -1 & 1 \end{bmatrix} \begin{bmatrix} r \\ t \end{bmatrix} = \begin{bmatrix} \left(\frac{\cos(\alpha) k_z^{(i)}}{\epsilon_x^{(1)}} + \frac{\sin(\alpha) k_x^{(i)}}{\epsilon_z^{(1)}}\right) \\ 1 \end{bmatrix}. \tag{5.38}$$

Hence, the Fresnel coefficients are

$$\begin{bmatrix} r \\ t \end{bmatrix} = \begin{bmatrix} -\left(\frac{\cos(\alpha) k_z^{(r)}}{\epsilon_x^{(1)}} + \frac{\sin(\alpha) k_x^{(r)}}{\epsilon_z^{(1)}}\right) & \left(\frac{\cos(\alpha) k_z^{(t)}}{\epsilon_x^{(2)}} + \frac{\sin(\alpha) k_x^{(t)}}{\epsilon_z^{(2)}}\right) \\ -1 & 1 \end{bmatrix}^{-1} \begin{bmatrix} \left(\frac{\cos(\alpha) k_z^{(i)}}{\epsilon_x^{(1)}} + \frac{\sin(\alpha) k_x^{(i)}}{\epsilon_z^{(1)}}\right) \\ 1 \end{bmatrix}. \tag{5.39}$$

5.7.3. Maximum NA of a hyperlens

Here the maximum achievable NA for a lossless HM is derived. The maximum achievable NA of a hyperlens is equivalent to the maximum achievable transversal

wavevector $k_x^{(\max)}$ inside the HM that is coupled from a planewave from an isotropic medium. The nominal dispersion curve ($k_0 = 1$) is shown in Fig. 5.10. Assuming the incident beam propagates in the z direction, the wavevector for the incident light in the isotropic medium is parallel to the z-axis and being $k_i = n_i$, where n_i is the refractive index of the incident medium. The wavevector in the HM should be the intersection point of the dispersion curve of the HM and a line passing through the point $(n_i, 0)$ and parallel to $\mathbf{n}$, where $\mathbf{n}$ is the normal direction of the interface. The maximum NA (maximum k_x) is achieved only when the line becomes the tangent line of the hyperbolic dispersion curve.

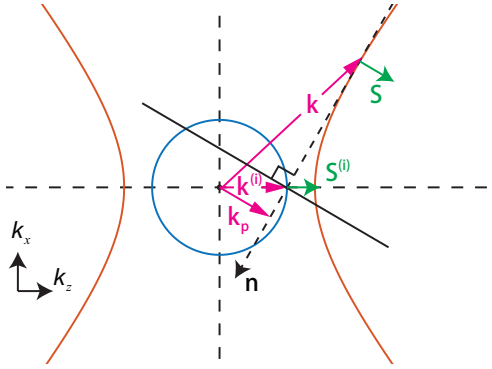

Figure 5.10: Illustration of the achievable maximum NA condition for planewave incident in k-space. The solid blue and red curve are the isofrequency curve for the dielectric material (incident side) and the HM (output side). The magenta solid arrows denote the incident wavevector $\mathbf{k_i}$, the tangential wavevector $\mathbf{k_p}$ and the transmission wavevector $\mathbf{k_{HM}}$, respectively. The projection of $\mathbf{k_i}$ and $\mathbf{k_{HM}}$ on the interface should be identical and equal to $\mathbf{k_p}$. The green arrows are the Poynting vectors of the incident beam $\mathbf{S_i}$ and the transmission beam $\mathbf{S_{HM}}$. The solid black line is the line parallel to the interface while the dark blue arrow denotes the direction of the interface normal.

Assuming the line is represented by $k_x = \gamma(k_z - n_i k_0)$, one can substitute it into the dispersion relation of the HM, which gives

$$\frac{\gamma^2(k_z - n_i k_0)^2}{\epsilon_z} + \frac{k_z^2}{\epsilon_x} = 1. \tag{5.40}$$

By collecting the terms of k_z, one can has

$$\left(\frac{1}{\epsilon_x} + \frac{\gamma^2}{\epsilon_z}\right)k_z^2 - \left(\frac{2\gamma^2 n_i k_0}{\epsilon_z}\right)k_z + \frac{\gamma^2 n_i^2 k_0^2}{\epsilon_z} - 1 = 0. \tag{5.41}$$

In order to have the line tangent to the dispersion curve of the HM, the discriminant of the quadratic equation Eq. 5.41 should be zero. Hence one has

$$\left(\frac{2\gamma^2 n_i k_0}{\epsilon_z}\right)^2 - 4\left(\frac{1}{\epsilon_x} + \frac{\gamma^2}{\epsilon_z}\right)\left(\frac{\gamma^2 n_i^2 k_0^2}{\epsilon_z} - 1\right) = 0. \tag{5.42}$$

The solutions are

$$\gamma = \pm\sqrt{\frac{\epsilon_z}{n_i^2 k_0^2 - \epsilon_x}}. \tag{5.43}$$

By substituting γ back to Eq. 5.41, one can find the corresponding maximum k_z, k_x, and the corresponding NA

$$k_z^{(\max)} = \pm\frac{\epsilon_x}{n_i}k_0, \tag{5.44}$$

$$k_x^{(\max)} = \pm\frac{\sqrt{\epsilon_z(n_i^2 - \epsilon_x)}}{n_i}k_0, \tag{5.45}$$

$$NA^{(\max)} = \left|\frac{k_x^{(\max)}}{k_0}\right| = \frac{\sqrt{\epsilon_z(n_i^2 - \epsilon_x)}}{n_i}. \tag{5.46}$$

5

References

[1] J. B. Pendry, *Negative refraction makes a perfect lens,* Physical review letters **85**, 3966 (2000).

[2] L. Shen, L. J. Prokopeva, H. Chen, and A. V. Kildishev, *Designing optimal nanofocusing with a gradient hyperlens,* Nanophotonics **7**, 479 (2017).

[3] M. Otomori, T. Yamada, K. Izui, S. Nishiwaki, and J. Andkjær, *Topology optimization of hyperbolic metamaterials for an optical hyperlens,* Structural and Multidisciplinary Optimization **55**, 913 (2017).

[4] M. Kim, S. So, K. Yao, Y. Liu, and J. Rho, *Deep sub-wavelength nanofocusing of UV-visible light by hyperbolic metamaterials,* Scientific Reports **6**, 38645 (2016).

[5] T. Repän, A. V. Lavrinenko, and S. V. Zhukovsky, *Dark-field hyperlens: Super-resolution imaging of weakly scattering objects,* Optics express **23**, 25350 (2015).

[6] B. H. Cheng, Y.-C. Lan, and D. P. Tsai, *Breaking optical diffraction limitation using optical Hybrid-Super-Hyperlens with radially polarized light,* Optics express **21**, 14898 (2013).

[7] T. Zhang, L. Chen, and X. Li, *Graphene-based tunable broadband hyperlens for far-field subdiffraction imaging at mid-infrared frequencies,* Optics Express **21**, 20888 (2013).

[8] Y. Xiong, Z. Liu, and X. Zhang, *A simple design of flat hyperlens for lithography and imaging with half-pitch resolution down to 20 nm,* Applied Physics Letters **94**, 1 (2009).

[9] Z. Jacob, L. V. Alekseyev, and E. Narimanov, *Semiclassical theory of the Hyperlens,* J. Opt. Soc. Am. A **1**, 2 (2007).

[10] I. I. Smolyaninov, Y.-J. Hung, and C. C. Davis, *Magnifying superlens in the visible frequency range,* science **315**, 1699 (2007).

[11] E. Narimanov, *Hyperstructured illumination,* ACS Photonics **3**, 1090 (2016), https://doi.org/10.1021/acsphotonics.6b00157 .

[12] Z. H. Narimanov and E. E, *Optical imaging with photonic hyper-crystals: Veselago lens and beyond,* Journal of Optics **16**, 114009 (2014).

[13] C. Ma and Z. Liu, *Designing super-resolution metalenses by the combination of metamaterials and nanoscale plasmonic waveguide couplers,* Journal of Nanophotonics **5**, 051604 (2011).

[14] C. Ma and Z. Liu, *Focusing light into deep subwavelength using metamaterial immersion lenses.* Optics express **18**, 4838 (2010).

[15] A. Salandrino and N. Engheta, *Far-field subdiffraction optical microscopy using metamaterial crystals: Theory and simulations,* Physical Review B - Condensed Matter and Materials Physics **74**, 1 (2006).

[16] D. Lee, Y. D. Kim, M. Kim, S. So, H.-J. Choi, J. Mun, D. M. Nguyen, T. Badloe, J. G. Ok, K. Kim, *et al.*, *Realization of wafer-scale hyperlens device for sub-diffractional biomolecular imaging,* ACS Photonics (2017).

[17] M. Byun, D. Lee, M. Kim, Y. Kim, K. Kim, J. G. Ok, J. Rho, and H. Lee, *Demonstration of nanoimprinted hyperlens array for high-throughput sub-diffraction imaging,* Scientific Reports **7**, 46314 (2017).

[18] J. Sun, M. I. Shalaev, and N. M. Litchinitser, *Experimental demonstration of a non-resonant hyperlens in the visible spectral range,* Nature Communications **6**, 7201 (2015).

[19] J. Rho, Z. Ye, Y. Xiong, X. Yin, Z. Liu, H. Choi, G. Bartal, and X. Zhang, *Spherical hyperlens for two-dimensional sub-diffractional imaging at visible frequencies.* Nature Communications **1**, 143 (2010).

[20] Z. Liu, H. Lee, Y. Xiong, C. Sun, and X. Zhang, *Far-field optical hyperlens magnifying sub-diffraction-limited objects,* science **315**, 1686 (2007).

[21] M. S. Habib, A. Stefani, S. Atakaramians, S. C. Fleming, A. Argyros, and B. T. Kuhlmey, *A prism based magnifying hyperlens with broad-band imaging,* Applied Physics Letters **110**, 101106 (2017).

[22] D. Lu, H. Qian, K. Wang, H. Shen, F. Wei, Y. Jiang, E. E. Fullerton, P. K. Yu, and Z. Liu, *Nanostructuring multilayer hyperbolic metamaterials for ultrafast and bright green ingan quantum wells,* Advanced Materials **30**, 1706411 (2018).

[23] D. J. Roth, A. V. Krasavin, A. Wade, W. Dickson, A. Murphy, S. Kéna-Cohen, R. Pollard, G. A. Wurtz, D. Richards, S. A. Maier, *et al.*, *Spontaneous emission inside a hyperbolic metamaterial waveguide,* ACS Photonics **4**, 2513 (2017).

[24] O. Makarova, M. Shalaginov, S. Bogdanov, A. Kildishev, A. Boltasseva, and V. Shalaev, *Patterned multilayer metamaterial for fast and efficient photon collection from dipolar emitters,* Optics letters **42**, 3968 (2017).

[25] A. P. Slobozhanyuk, P. Ginzburg, D. A. Powell, I. Iorsh, A. S. Shalin, P. Segovia, A. V. Krasavin, G. A. Wurtz, V. A. Podolskiy, P. A. Belov, *et al.*, *Purcell effect in hyperbolic metamaterial resonators,* Physical Review B **92**, 195127 (2015).

[26] D. Lu, J. J. Kan, E. E. Fullerton, and Z. Liu, *Enhancing spontaneous emission rates of molecules using nanopatterned multilayer hyperbolic metamaterials,* Nature nanotechnology **9**, 48 (2014).

[27] H. Li, S. Atakaramians, R. Lwin, X. Tang, Z. Yu, A. Argyros, and B. T. Kuhlmey, *Flexible single-mode hollow-core terahertz fiber with metamaterial cladding,* Optica **3**, 941 (2016).

[28] S. Tang, Y. Fang, Z. Liu, L. Zhou, and Y. Mei, *Tubular optical microcavities of indefinite medium for sensitive liquid refractometers,* Lab on a Chip **16**, 182 (2016).

[29] N. Vasilantonakis, M. E. Nasir, W. Dickson, G. A. Wurtz, and A. V. Zayats, *Bulk plasmon-polaritons in hyperbolic nanorod metamaterial waveguides,* Laser & photonics reviews **9**, 345 (2015).

[30] V. E. Babicheva, M. Y. Shalaginov, S. Ishii, A. Boltasseva, and A. V. Kildishev, *Long-range plasmonic waveguides with hyperbolic cladding,* Optics express **23**, 31109 (2015).

[31] S. Ishii, M. Y. Shalaginov, V. E. Babicheva, A. Boltasseva, and A. V. Kildishev, *Plasmonic waveguides cladded by hyperbolic metamaterials,* Optics letters **39**, 4663 (2014).

[32] Y. Tang, Z. Xi, M. Xu, S. Bäumer, A. Adam, and H. Urbach, *Spatial mode-selective waveguide with hyperbolic cladding,* Optics letters **41**, 4285 (2016).

[33] V. E. Babicheva, M. Y. Shalaginov, S. Ishii, A. Boltasseva, and A. V. Kildishev, *Finite-width plasmonic waveguides with hyperbolic multilayer cladding,* Optics express **23**, 9681 (2015).

[34] K. V. Sreekanth, Y. Alapan, M. ElKabbash, E. Ilker, M. Hinczewski, U. A. Gurkan, A. De Luca, and G. Strangi, *Extreme sensitivity biosensing platform based on hyperbolic metamaterials,* Nature materials **15**, 621 (2016).

[35] N. Vasilantonakis, G. Wurtz, V. Podolskiy, and A. Zayats, *Refractive index sensing with hyperbolic metamaterials: strategies for biosensing and nonlinearity enhancement,* Optics express **23**, 14329 (2015).

[36] A. Kabashin, P. Evans, S. Pastkovsky, W. Hendren, G. Wurtz, R. Atkinson, R. Pollard, V. Podolskiy, and A. Zayats, *Plasmonic nanorod metamaterials for biosensing,* Nature materials **8**, 867 (2009).

[37] Z. Liu, S. Durant, H. Lee, Y. Pikus, Y. Xiong, C. Sun, and X. Zhang, *Experimental studies of far-field superlens for sub-diffractional optical imaging,* Optics express **15**, 6947 (2007).

[38] X. Yang, J. Yao, J. Rho, X. Yin, and X. Zhang, *Experimental realization of three-dimensional indefinite cavities at the nanoscale with anomalous scaling laws,* Nature Photonics **6**, 450 (2012).

[39] M. N. Gjerding, R. Petersen, T. G. Pedersen, N. A. Mortensen, and K. S. Thygesen, *Layered van der Waals crystals with hyperbolic light dispersion,* Nature Communications **8**, 320 (2017).

[40] K. Korzeb, M. Gajc, and D. A. Pawlak, *Compendium of natural hyperbolic materials,* Optics Express **23**, 25406 (2015).

[41] E. E. Narimanov and A. V. Kildishev, *Metamaterials: Naturally hyperbolic,* Nature Photonics **9**, 214 (2015).

[42] J. Sun, N. M. Litchinitser, and J. Zhou, *Indefinite by Nature: From Ultraviolet to Terahertz,* ACS Photonics **1**, 293 (2014).

[43] M. Esslinger, R. Vogelgesang, N. Talebi, W. Khunsin, P. Gehring, S. De Zuani, B. Gompf, and K. Kern, *Tetradymites as Natural Hyperbolic Materials for the Near-Infrared to Visible,* ACS Photonics **1**, 1285 (2014).

[44] J. Sun and N. M. Litchinitser, *Toward practical, subwavelength, visible-light photolithography with hyperlens,* ACS nano **12**, 542 (2018).

[45] D. Lu and Z. Liu, *Hyperlenses and metalenses for far-field super-resolution imaging.* Nature communications **3**, 1205 (2012).

[46] C. Ma and Z. Liu, *A super resolution metalens with phase compensation mechanism,* Applied Physics Letters **96**, 183103 (2010).

[47] C. Ma, M. A. Escobar, and Z. Liu, *Extraordinary light focusing and Fourier transform properties of gradient-index metalenses,* Physical Review B - Condensed Matter and Materials Physics **84**, 1 (2011).

[48] P. B. Johnson and R.-W. Christy, *Optical constants of the noble metals,* Physical review B **6**, 4370 (1972).

[49] R. Z. Zhang and Z. M. Zhang, *Validity of effective medium theory in multilayered hyperbolic materials,* Journal of Quantitative Spectroscopy and Radiative Transfer **197**, 132 (2017).

[50] A. S. Potemkin, A. N. Poddubny, P. A. Belov, and Y. S. Kivshar, *Green function for hyperbolic media,* Physical Review A **86**, 023848 (2012).

[51] J. J. Braat, S. van Haver, A. J. Janssen, and P. Dirksen, *Assessment of optical systems by means of point-spread functions,* Progress in optics **51**, 349 (2008).

6

Conclusion and outlook

6.1. Conclusion

In this thesis, the simulation, fabrication and experiment of both natural rutile TiO_2 crystal and multilayer meta-material (MM) nano-structures are discussed. The natural TiO_2 crystal and all-dielectric multilayer MMs have shown large birefringence and good trapperbility in optical trapping, which makes them ideal candidates for optical tweezer applications. In this thesis, we have demonstrated that our optical tweezer probes can generate both large three-dimensional linear trapping stiffness and also up to $nN \cdot nm$ rotational torque. We demonstrated the superior optical property of the probes both theoretically and experimentally. The fabrication process of the probes is mastered and the detailed procedures are discussed.

The metal-dielectric MMs show hyperbolic dispersion property, which can support either all spatial frequency propagation modes or only high spatial frequency propagation modes. The former type of the MM is called type I hyperbolic meta-material (HMMs), and the later one is called type II HMMs. The type I HMM is capable of propagating all spatial frequency information and it has been demonstrated as super-resolution lens named hyperlens. We have shown and discussed that the absorption of the HM plays an important role in the refraction property of the hyperlens. Therefore, the complex permittivity of the material needs to be considered in order to achieve the optimal focusing property. Also, we demonstrated that the absorption of the material severely reduce the optical resolution by attenuating the propagation of high spatial frequency component in the HM.

We also demonstrated the type II HM can be used as a high-pass filter in optical waveguide engineering. We demonstrated that by using type II HM as the cladding material in a planar waveguide, the fundamental mode in the waveguide can be removed and only higher order modes remain. The waveguide theory of using HMs as the cladding material of cylindrical waveguide is discussed as well.

Nevertheless, it is noticeable that there are more interesting research works related to this thesis but have not been discussed in the main chapters of this

thesis yet. here we briefly discuss the possible future following works.

6.2. Dynamics of optical trapping and rotation

In Chapter 2 and chapter 3, the 3D trapping and rotation of birefringent Rutile TiO_2 and MM are discussed. In the discussion, the trapping orientation of the nano-cylinder particle is assumed to be parallel to the focus beam axis and the optical axis of the particle is aligned with the linear polarization direction of the beam. The equilibrium position of the particle is in the center of the focus beam axis. In many cases this assumption is accurate and it is also verified in our experimental setup. In the insert of Fig. 6.1, the microscopy image of a cylindrical particle in the trapping is shown, the scattered field of the particle shows symmetric along the focus axis, which is an indirect prove that the particle is align with the beam axis. However, in literature, it is also demonstrated that nano-particle can be trapped with different orientation including oblique orientation [1]. Also, the dynamic process of how the particle is driven to the focus center is important. This requires a dynamics modeling of the particle's rotation and linear movement as functions of force (torque) and time. By using COMSOL and Matlab Livelink we are able to achieve this modeling.

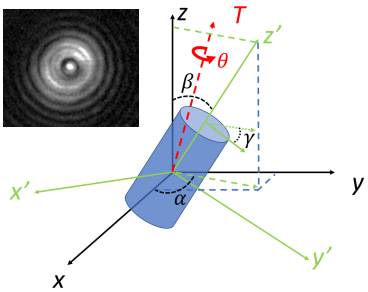

Figure 6.1: Schematic of a cylindrical particle of arbitrary orientation. The black axes x, y, z are the global Cartesian coordinate. The blue axes x', y', z' are the local Cartesian coordinate with z' being the direction of the cylinder height, x' being the direction of the extraordinary axis of birefringence. $\mathbf{T}$ is the direction of the total optical torque on the particle and the particle is rotated around $\mathbf{T}$ with a certain angle θ. α is the angle between x and the projection of z' in the $x-y$ plane. β is the angle between z and z'. γ is the angle between y' and the projection of y' in the $z-z'$ plane. The insert is the top view of a cylindrical particle being trapped in the focus, where the scattered field shows axis symmetric.

In reality, the dynamic movement of nano-particles is a process of acceleration and deceleration of the particles, which considers both the total applied optical force (or torque) and viscous drag from the surrounding medium. This process is complex and requires precise description of the particle motion. To simplify the model, we only consider the optical force and torque. We assume the position (or rotation) of the particle is perturbed by the optical force (or torque), and we update the position (or rotation) of the particle iteratively, with a discretized movement (or rotation) proportional to the applied optical force (or torque) at the previous position. This simplification is not precise but should be enough for particle position

tracing purpose as long as the delta of particle movement (or rotation) we used is small. Since calculating the linear movement of a particle is relatively easy, here we will mainly discuss the rotation behavior of the particle. We define that, for a arbitrary oriented birefringent cylinder, the particle is parallel to the z'-axis and extraordinary axis is in x', as shown in Fig. 6.1. The axes x', y' and z' are orthogonal to each other and define the unique orientation of the particle. We refer this axes as the local coordinate system.

Since the particle orientation is arbitrary, the permittivity tensor $\underline{\underline{\epsilon}}$ in the global coordinate is non-diagonal. However, in local coordinate it is still a diagonal tensor and is given by

$$\underline{\underline{\epsilon'}} = \begin{bmatrix} \epsilon_x & 0 & 0 \\ 0 & \epsilon_y & 0 \\ 0 & 0 & \epsilon_z \end{bmatrix}. \tag{6.1}$$

By using the rotation matrix $\mathbf{R} = [\hat{x}'; \hat{y}'; \hat{z}']$, where $\hat{x}'$, $\hat{y}'$ and $\hat{z}'$ are the unit vectors along the direction of x', y' and z', respectively, we are able to find the permittivity tensor in the global coordinate

$$\underline{\underline{\epsilon}} = \mathbf{R} \cdot \underline{\underline{\epsilon'}} \cdot \mathbf{R}^{-1}. \tag{6.2}$$

This tensor can be feed to the COMSOL software to describe the material property and hence the force (or torque) applied to the arbitrary positioned (or oriented) particle can be calculated.

In the model, the particle's linear movement is replaced by the linear movement of the focus beam, while the angular rotation of the beam can be described by the rotation along a main axis, where this axis is given by

$$\mathbf{T} = \mathbf{T_x} + \mathbf{T_y} + \mathbf{T_z}, \tag{6.3}$$

where $\mathbf{T_x}$, $\mathbf{T_y}$ and $\mathbf{T_z}$ are the torque applied on the particle along the x, y and z axis. Please note that while updating the rotation of the particle, not only the particle itself needs to be rotated, by also the global optical permittivity tensor needs to be update accordingly.

This torque $\mathbf{T}$ will make the particle rotate counterclockwise around the axis given by $\hat{T}$. This means that the local coordinate system needs to rotate around $\hat{T}$ as well. Assuming the rotation angle is given by θ, by using the Euler–Rodrigues formula, the new local coordinates are given by

$$\hat{x}'_{rot} = \hat{x}' \cos\theta + (\hat{T} \times \hat{x}') \sin\theta + \hat{T}(\hat{T} \cdot \hat{x}')(1 - \cos\theta), \tag{6.4}$$

$$\hat{y}'_{rot} = \hat{y}' \cos\theta + (\hat{T} \times \hat{y}') \sin\theta + \hat{T}(\hat{T} \cdot \hat{y}')(1 - \cos\theta), \tag{6.5}$$

$$\hat{z}'_{rot} = \hat{z}' \cos\theta + (\hat{T} \times \hat{z}') \sin\theta + \hat{T}(\hat{T} \cdot \hat{z}')(1 - \cos\theta), \tag{6.6}$$

where θ is the angle that the particle rotates.

In Fig. 6.2, an example is illustrated. The particle considered here is a Rutile TiO_2 particle of diameter 200 nm and aspect ratio of 4. The linear polarized (in x)

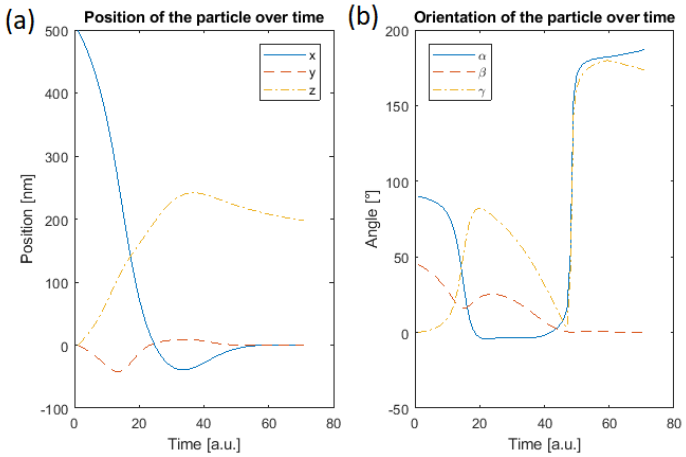

Figure 6.2: the linear position (a) and angular position (b) of the simulated cylinder as a function of simulation iterations. The particle converges to the center of the focus and being vertically aligned with the beam axis.

focus beam is of NA=1.2, and incident on the particle from the negative z-axis. The starting position of the particle is at (x, y, z)=(500,0,0) nm, with the orientation of (α, β, γ) = (90,45,0) Deg. Here α is the angle between the projection of $\hat{z}$ in the xy-plane and the positive x-axis. β is the angle between the z'-axis and the z-axis. γ is the angle between y'-axis and projection of it in the plane given by z and z'. In Fig. 6.2(a), it is clearly shown that the particle moves towards the focus center while the lateral positions x and y get close to zero in the end. It is also shown that the vertical position z of the particle get increase first and then reduce to a certain value around 200 nm, which is the z-equilibrium position of the trapping. In Fig. 6.2(b) the orientation of the particle is shown. As predicted, the cylindrical particle is aligned with optical axis z of the laser beam (β reduces to zero). Also it is shown that eventually the extraordinary axis is 180 Deg aligned with the x-axis. However, the angle of α changes dramatically in the simulation, which is not consistency as what we expected. This preliminary result should be further improved.

6.3. Simultaneous force and torque measurement

In our OTW experiment, we provide probe particles that can simultaneously achieve large linear and angular stiffness, which can be beneficial in many biological applications. However, the simultaneous measurement of large force and torque is not in the scope of the chapter and it is sometimes necessary, as shown in [2]. Nevertheless, in our optical setup we do have the potential to conduct simultaneous measurement of force and torque, as both detectors are in the setup and not blocking each other. Here we briefly discuss the possibility and the potential problems.

When one consider measure both torque and force simultaneous, the crosstalk of the signals needs to be considered and minimized. This crosstalk between the

rotational and translational degrees of freedom can be originated from both the inherent dynamics of the Rutile TiO_2 cylinders as well as the measurements performed on them. Physical correlations between rotational and translational degrees of freedom will occur because rutile TiO2 cylinders exhibit both optical and geometrical anisotropy, and this will influence their dynamics within a tightly focused beam. Additionally, there can be crosstalk due to the measurement configuration of the setup or the employed signal detectors. Highly precise calibration and in-depth calculations for simultaneous measurements are thus complex and will need to be separately addressed for specific applications.

We also expect the maximum achievable force and torque will be reduced when conducting simultaneous force and torque measurement. For instance, we modulate the movement of particle in lateral direction when measuring lateral force. if the torque measurement is also conduct during the modulation, the amount of average torque will be reduced as the particle is not always in the center of the optical axis, when the light-matter interaction is maximum. On the other hand, the difference of force in x and y will not exist as we rotate the linear polarized beam at a large frequency, the measure force along this two directions will be averaged out.

6.4. Hyperbolic material for nanoparticle detection

In Chapter 4 and chapter 5, we discuss the application of hyperbolic materials in waveguide application, and showed that the type II HM can support only high spatial-frequency propagating waves. This optical property can be utilized for nanoparticle detection. A nano-particle can scatter the incident light coming from free space and generate variants of spatial frequency information. The particle is no detectable because 1) The high spatial frequency components ($k > k_0$, where k_0 is the wavenumber in free space) of the scattered light are evanescent waves, which can not be propagated and stays in the near field; 2) the scattered field intensity is too low and being buried in the incident field background, which signal to noise ratio is too low for detection. In order to solve this problem, the type II HM can be used to filter out the incident field ($k_{in} < k_0$) and keep only the scattered field. Assuming that the nano-particle needs to be detected lays on top of a type II HM, the incident light comes from the free space with the wavenumber equals to k_0. The incident light hits the nano-particle and it is partially converted to scattered light and the majority of the light experiences specular reflection from the HM surface. This is because the transversal wavenumber of the incident light is too small and located in the bandgap of the HM. However, the nano-particle generate a spectrum of spatial frequency from zero to very large. Only those spatial frequency components that are larger than the bandgap of the HM will be coupled into the HM and become propagating waves. Therefore, inside the HM only scattered light presents and the background noise is filtered out. Hence the signal to noise ratio is highly increased.

In Fig. 6.3, a two dimensional simulation is shown. In the simulation, a cylindrical SiO_2 ($\epsilon = 2.25$) particle of radius 0.5 λ is located on top of a type II multilayer HM material. The HM meta-material consists of Au ($\epsilon = -50 + 2.08i$) and SiO_2 ($\epsilon = 2.25$), with a filling ratio of 0.3. A Gaussian beam hits the particle and

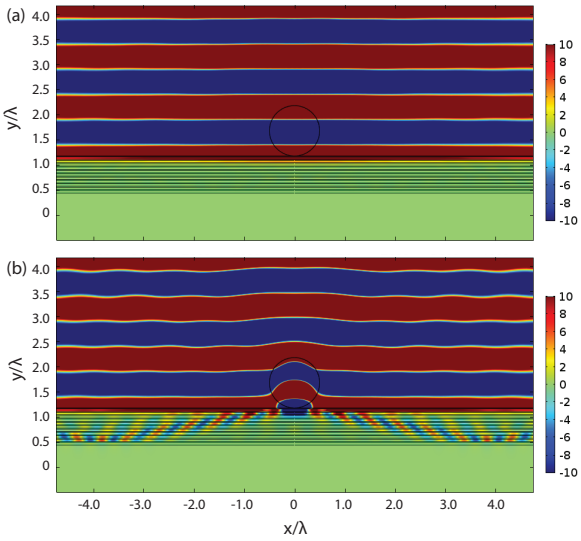

Figure 6.3: Magnetic field $|H_z|$ of a Gaussian beam incident on a type II HM material substrate with normal incident angle. The HM meta-material consists of Au ($\epsilon = -50 + 2.08i$) and SiO_2 ($\epsilon = 2.25$), with a filling ratio of 0.3. (a) The light is 100% reflected as there is no particle located on top of the HM. (b) A SiO_2 particle (diameter=$1\times\lambda$) locates on top of a type II HM material substrate. The particle scatters light and part of the scattered light enters the HM substrate.)

6

being mostly reflected. Nevertheless, the HM substrate is able to pick up the scattered light generated from the particle and convert them into propagation wave in the HM.

Now the remaining task is to detect the propagating waves inside the HM. This waves has spatial frequency larger than k_0 and can no be propagated in free-space. This means we need to convert the scattered field to lower spatial frequency again in order to detect them in the far-field. This can be achieved by either having a scattering layer (e.g. grating) on the other side of the HM or having a fluorescent layer and couple the light to incoherent propagating waves.

6.5. Hyperlens for extended object

In Chapter 5 the super-resolution focusing property of the hyperlens is discussed and it is shown that the hyperlens is capable of focusing the light into a sub-wavelength spot. In the chapter only normal incident planewave is discussed (on-axis). However, it is well known that for high-NA optical systems, the aberrations are large and need to be optimized. For instance, the imaging property of off-axis object is highly influenced by the coma aberration. Therefore, imaging of an extended object is required, which is not considered and optimized in the current hyperlens design.

In order to improve the imaging property of hyperlens, similar to modern microscopy objective assembly, multiple lens can be introduced in order to reduce

the amount of aberrations. Here we propose to use the simultaneous multiple surface (SMS) method [3] to find a multi interfaces hyperlens profile for extended object imaging. The SMS method traces a number of off-axis imaging points and construct a non-spherical lens profile in order to have minimum aberrations on this points. Although the aberration of the on-axis point is increased, the overall total aberrations is reduced in the field of view. Once the lens profile is constructed, one can use this as a good starting point for optimization algorithm (e.g. in CodeV or Zemax) and find a local minimum of the aberration.

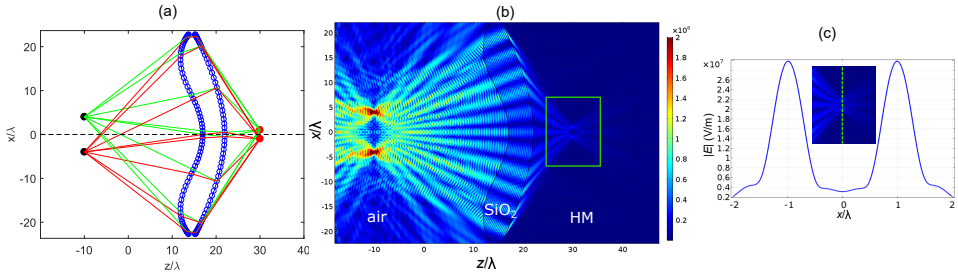

Figure 6.4: (a) The reconstructed hyperlens profile (blue) using SMS method. The object points (black dots) are located at (z,x)=(-10,±4) λ and the two image points (red dots) are located at (z,x)=(30,±1) λ. The red and green lines are the traces of the rays for the the off-axis objects. The materials used here are air (left, $\epsilon = 1$), glass (middle, $\epsilon = 2.25$) and HM (right, $\epsilon_z = -3 + 0.1i$ and $\epsilon_x = 10 + 0.1i$). (b) Numerical simulated electric field amplitude of the hyperlens in (a). The two point objects are two dipoles with dipole moment along z. (c) Cross-section of the image plane in (b). The insert is the focal region in the green box of (b).

Here we demonstrate a hyperlens profile constructed by the SMS method. As shown in Fig. 6.4 (a), an extra glass layer ($\epsilon_{glass} = 2.25$) is inserted between air (on the left) and HM (on the right) such that the hyperlens consists of two interfaces. The permittivity of the HM used here are $\epsilon_z = -3 + 0.1i$ and $\epsilon_x = 10 + 0.1i$. The two symmetric off-axis points are defined at (z,x)=(-10,±4) λ, and the two symmetric image points are defined at (z,x)=(30,±1) λ, where the lateral magnification is chosen to be 4. The two blue interfaces are constructed hyperlens profile using SMS method, where the apex of the lens are defined at (z,x)=(17,0) λ and (z,x)=(22,0) λ. The blue circles on the hyperlens are the points where SMS method is used for constructing the interfaces. The red and green lines are the traces of the rays for the the off-axis objects. The reconstructed hyperlens can support maximum $k_x = 3.23k_0$, corresponding to $NA_{max} = 3.23$. In Fig. 6.4 (b), the numerical simulation result of the electric field amplitude is shown, where the two dipole sources of dipole moment in z are used as the point objects. It can be seen that in the HM area, two images are shown at the image plane. The cross-section of this image plane is shown in Fig. 6.4 (c). The peaks of the spots are at $x = \pm 1\lambda$, which is the same as design. Moreover, the shape of the profile are symmetric, which indicates the coma aberration is small.

References

[1] Y. Cao, A. B. Stilgoe, L. Chen, T. A. Nieminen, and H. Rubinsztein-Dunlop, *Equilibrium orientations and positions of non-spherical particles in optical traps,* Optics Express **20**, 12987 (2012).

[2] A. Ramaiya, B. Roy, M. Bugiel, and E. Schäffer, *Kinesin rotates unidirectionally and generates torque while walking on microtubules,* Proceedings of the National Academy of Sciences **114**, 10894 (2017).

[3] P. Gimenez-Benitez, J. C. Miñano, J. Blen, R. M. Arroyo, J. Chaves, O. Dross, M. Hernández, and W. Falicoff, *Simultaneous multiple surface optical design method in three dimensions,* Optical Engineering **43**, 1489 (2004).

A

Derivation of the analytical equation for optical torque transfer from a linearly polarized plane wave to an infinitely wide birefringent plate with uniform thickness.

The purpose of this section is to confirm the validity of Eq. 2.1, as in the literature many different forms of this equation exist in the absence of detailed derivation [1–4]. First, we start with torque on a single dipole in a plate:

$$\vec{\tau} = \vec{p} \times \vec{E}, \tag{A.1}$$

where $\vec{p}$ is the electric dipole moment and $\vec{E}$ is the electric field in the plate [5]. We can derive the torque per unit volume of a dielectric plate of uniform thickness perpendicular to the beam propagation direction by considering multiple dipoles in a given volume:

$$N\vec{\tau} = N\vec{p} \times \vec{E} = \vec{P} \times \vec{E} = \epsilon_0 \underline{\chi} \vec{E} \times \vec{E}, \tag{A.2}$$

where N is the number of dipoles, $\vec{P}$ is the polarization per unit volume, ϵ_0 is the vacuum permittivity, and $\underline{\chi}$ is the electric susceptibility tensor in the plate. The input beam is set to be a plane wave that propagates in the z-direction, being

linearly polarized in $x-y$ plane. Thus, the electric field $\vec{E}$ has zero intensity in the z-dimension ($E_z = 0$) and hence torque is applied in the z-direction only:

$$N\vec{\tau} = \begin{bmatrix} \chi_x & 0 & 0 \\ 0 & \chi_y & 0 \\ 0 & 0 & \chi_z \end{bmatrix} \begin{bmatrix} E_x \\ E_y \\ 0 \end{bmatrix} \times \begin{bmatrix} E_x \\ E_y \\ 0 \end{bmatrix} = \epsilon_0 \begin{bmatrix} 0 \\ 0 \\ (\chi_x - \chi_y) E_x E_y \end{bmatrix}. \tag{A.3}$$

Using the known relationship $\chi = n^2 - 1$, the torque in the z direction can be described as:

$$N\tau_z = \epsilon_0(\chi_x - \chi_y)E_x E_y = \epsilon_0(n_x^2 - n_y^2)E_x E_y. \tag{A.4}$$

In Eq. A.4, the electric field vectors (E_x, E_y) in time t and space z are defined as:

$$\begin{aligned} E_x &= E_x(z,t) = E_{0,x}\cos(k_x z - \omega t), \\ E_y &= E_y(z,t) = E_{0,y}\cos(k_y z - \omega t), \end{aligned} \tag{A.5}$$

where $E_{0,x} = E_0 \cos(\theta)$, $E_{0,y} = E_0 \sin(\theta)$, and θ is the angle between the x-axis and the linear polarization direction of the electric field with amplitude E_0 in the plate. Also, $k_x = k_0 n_x$, $k_y = k_0 n_y$, while n_x, n_y are refractive indices of the plate along the x- and y-axis, k_x, k_y are wavenumbers in the plate along the x- and y-axis, and $k_0 = \omega/c$ is the wavenumber in vacuum (here, ω is the laser optical frequency and c is the speed of light in vacuum). We rewrite Eq. A.5 similarly to Beth's derivation [3]:

$$\begin{aligned} E_x(z,t) &= E_{0,x}\cos\left(\frac{(k_x + k_y)}{2}z + \frac{(k_x - k_y)}{2}z - \omega t\right) = E_{0,x}\cos(Z + D), \\ E_y(z,t) &= E_{0,y}\cos\left(\frac{(k_x + k_y)}{2}z + \frac{(k_x - k_y)}{2}z - \omega t\right) = E_{0,y}\cos(Z - D), \end{aligned} \tag{A.6}$$

where $Z = kz - \omega t$ and $D = \Delta k z/2$ (here, $k = (k_x + k_y)/2$, $\Delta k = k_x - k_y = k_0(n_x - n_y) = k_0 \Delta n$). Using trigonometric identities, we can further simplify the factor $E_x E_y$ in Eq. A.4. This allows us to express the z-component of the instantaneous torque per unit volume as:

$$N\tau_z = \epsilon_0(n_x^2 - n_y^2)E_x E_y = \frac{\epsilon_0(n_x^2 - n_y^2)E_0^2}{4}\sin(2\theta)\left(\cos(2Z) + \cos(2D)\right), \tag{A.7}$$

and its time-averaged variant as:

$$\langle N\tau_z \rangle = \frac{1}{T}\int_0^T dt N\tau_z = \frac{\epsilon_0(n_x^2 - n_y^2)E_0^2}{4}\sin(2\theta)\cos(z\Delta k). \tag{A.8}$$

To obtain the torque per unit area for a given plate thickness (i.e., height) h, we integrate along the z-axis:

$$\int_0^h dz\langle N\tau_z\rangle = hN\langle\tau_z\rangle = \frac{\epsilon_0(n_x^2-n_y^2)E_0^2}{4}\sin(2\theta)\left(\frac{1}{\Delta k}[\sin(z\Delta k)]_0^h\right) \tag{A.9}$$
$$= \frac{\epsilon_0 c(n_x^2-n_y^2)E_0^2}{4\omega\Delta n}\sin(2\theta)\sin(h\Delta k)$$
$$= \frac{\epsilon_0 ncE_0^2}{2\omega}\sin(2\theta)\sin(hk_0\Delta n),$$

where n is the mean index (i.e., $n=(n_x+n_y)/2$) of the plate. Finally, the torque per plate volume can be obtained by rewriting $N=N_d/V=N_d/hS$, where N_d is the total number of dipoles within the plate and S is the area of the plate surface with which the beam interacts:

$$\langle\tau_{z,total}\rangle = N_d\langle\tau_z\rangle = \frac{S\epsilon_0 ncE_0^2}{2\omega}\sin(hk_0\Delta n)\sin(2\theta), \tag{A.10}$$

which is identical to the amplitude of torque in Eq. 2.1 in the main text. We note that this equation is derived under the idealized condition of a plane wave interacting only with an infinitely wide plate of uniform thickness. It does not take into account the surrounding medium, and as such, the accompanying reflections at the material interfaces. When we use such idealized conditions in our FEM calculations, we obtain results identical to those predicted by Eq. 2.1 (Supplementary Fig. 2.14; although a plate of finite size, e.g., 300 nm×300 nm surface area, is required by FEM models, it is equivalent to the infinite case when light diffraction near the plate edges is ignored). Therefore, torque values acquired under non-ideal but realistic conditions deviate from the predictions of Eq. 2.1. As further detailed in Supplementary Fig. 2.5, one such example is a particle with a finite size trapped by a tightly-focused beam, e.g., rutile TiO_2 experiments in OTW as shown in Fig. 2.1e.

References

[1] M. Friese, T. Nieminen, N. Heckenberg, and H. Rubinsztein-Dunlop, *Optical alignment and spinning of laser-trapped microscopic particles,* Nature **394**, 348 (1998).

[2] D. Moothoo, J. Arlt, R. Conroy, F. Akerboom, A. Voit, and K. Dholakia, *Beth's experiment using optical tweezers,* American Journal of Physics **69**, 271 (2001).

[3] R. A. Beth, *Mechanical detection and measurement of the angular momentum of light,* Physical Review **50**, 115 (1936).

[4] F. Pedaci, Z. Huang, M. Van Oene, S. Barland, and N. H. Dekker, *Excitable particles in an optical torque wrench,* Nature Physics **7**, 259 (2011).

[5] A. La Porta and M. D. Wang, *Optical torque wrench: angular trapping, rotation, and torque detection of quartz microparticles,* Physical review letters **92**, 190801 (2004).

B

Dispersion relationship derivation for waveguides with anisotropic cladding

B.1. Planar waveguide

We start with Maxwell equations:

$$\nabla \times \vec{E} = i\omega\mu_0\vec{H}, \tag{B.1}$$

$$\nabla \times \vec{H} = -i\omega\epsilon_0\bar{\epsilon}\vec{E}. \tag{B.2}$$

Substitute equation B.2 to equation B.1, and for time harmonic field we get

$$\nabla \times \begin{bmatrix} \epsilon_x^{-1}\hat{x}\nabla \times \vec{H} \\ \epsilon_y^{-1}\hat{y}\nabla \times \vec{H} \\ \epsilon_z^{-1}\hat{z}\nabla \times \vec{H} \end{bmatrix} = \nabla \times \begin{bmatrix} \dot{X} \\ \dot{Y} \\ \dot{Z} \end{bmatrix} = k_0^2\vec{H} = k_0^2 \begin{bmatrix} H_x \\ H_y \\ H_z \end{bmatrix}. \tag{B.3}$$

For a TM polarized field, only y component of magnetic field exists and has the form $H_y = H(x)\exp(i\beta z)$. Therefore, the above equation can be simplified to:

$$\frac{\partial \dot{Z}}{\partial x} - \frac{\partial \dot{X}}{\partial z} = -k_0^2 H_y. \tag{B.4}$$

By substituting the value

$$\dot{X} = -\epsilon_x^{-1}\frac{\partial H_y}{\partial z}, \tag{B.5}$$

$$\dot{Z} = \epsilon_z^{-1}\frac{\partial H_y}{\partial x}, \tag{B.6}$$

into equation B.4, we get:

$$\frac{\partial^2 H_y}{\partial x^2} + (\frac{\epsilon_z}{\epsilon_x}\frac{\partial^2}{\partial z^2} - \epsilon_z k_0^2)H_y = 0. \tag{B.7}$$

B

Substitute $H_y = H(x)\exp(i\beta z)$ in the equation above we get:

$$\frac{\partial^2 H(x)}{\partial x^2} + (\epsilon_z k_0^2 - \frac{\epsilon_z}{\epsilon_x}\beta^2)H(x) = 0. \tag{B.8}$$

- In the core area, we have isotropic material, which $\epsilon_x = \epsilon_z = \epsilon_c$. the equation B.8 becomes:

$$\frac{\partial^2 H(x)}{\partial x^2} + (\epsilon_c k_0^2 - \beta^2)H(x) = 0. \tag{B.9}$$

The solution of this equation is:

$$H(x) = C_1 \exp(ik_x x) + C_2 \exp(-ik_x x), \tag{B.10}$$

where $k_x^2 = \epsilon_c k_0^2 - \beta^2$.

As the waveguide is axial symmetry at $x = 0$, the above result can be decomposed in two orthogonal sets:

$$\text{odd mode} \quad : H(x) = A\sin(k_x x), \tag{B.11}$$

$$\text{even mode} \quad : H(x) = A\cos(k_x x). \tag{B.12}$$

The electric field can be easily derived by taking the curl of the magnetic field:

$$\text{odd mode} : \vec{E} = \left(E_x, 0, \frac{ik_x}{\omega\epsilon_0\epsilon_c}A\cos(k_x x)\right), \tag{B.13}$$

$$\text{even mode} : \vec{E} = \left(E_x, 0, -\frac{ik_x}{\omega\epsilon_0\epsilon_c}A\sin(k_x x)\right). \tag{B.14}$$

- In the HMM cladding area, the energy must be exponentially decayed from the interface. Those force us to have the solution of the form:

$$H(x) = C_3 \exp(-\gamma_h|x|), \tag{B.15}$$

where $\gamma_h^2 = \frac{\epsilon_z}{\epsilon_x}\beta^2 - \epsilon_z k_0^2 > 0$.

By taking the curl of the magnetic field, the electric field become:

$$\vec{E} = \left(E_x, 0, -\text{sgn}(x)\frac{i\gamma_h}{\omega\epsilon_0\epsilon_z}B\exp(\gamma_h|x|)\right). \tag{B.16}$$

The boundary condition tells us that H_y and E_z are continuous at the interface $x = \pm a$. Therefore, by letting the field on both side equal, two orthogonal dispersion equations can be derived:

$$\text{odd modes} \quad : \tan(k_x a) = -\frac{k_x\epsilon_z}{\gamma_z\epsilon_c}, \tag{B.17}$$

$$\text{even modes} \quad : \cot(k_x a) = \frac{k_x\epsilon_z}{\gamma_z\epsilon_c}. \tag{B.18}$$

B.2. Cylindrical waveguide dispersion relation

From the main text in Chapter 4.3, we have the below boundary conditions

$$AJ_\nu(\kappa_c r_0) - Cf(r_0) = 0, \tag{B.19}$$

$$BJ_\nu(\kappa_c r_0) - Dg(r_0) = 0, \tag{B.20}$$

$$\beta\nu\kappa_{\phi,r}^2 AJ_\nu(\kappa_c r_0) + i\omega\mu_0 r_0 \kappa_{\phi,r}^2 \kappa_c BJ_\nu'(\kappa_c r_0) - \beta\nu\kappa_c^2 Cf(r_0) - i\omega\mu_0\mu_r r_0 \kappa_c^2 Dg(r_0)' = 0, \tag{B.21}$$

$$i\omega\epsilon_0\epsilon_c r_0 \kappa_{r,\phi}^2 \kappa_c AJ_\nu'(\kappa_c r_0) - \beta\nu\kappa_{r,\phi}^2 BJ_\nu(\kappa_c r_0) - i\omega\epsilon_0\epsilon_r r_0 \kappa_c^2 Cf(r_0)' + \beta\nu\kappa_c^2 Dg(r_0) = 0. \tag{B.22}$$

If we rewrite the above equations in matrix form, and setting the determinant to zero, we can have the dispersion formula.

for matrix of the form

$$M = \begin{bmatrix} A_1 & 0 & -A_3 & 0 \\ 0 & B_2 & 0 & -B_4 \\ C_1 & iC_2 & -C_3 & -iC_4 \\ iD_1 & -D_2 & -iD_3 & D_4 \end{bmatrix}, \tag{B.23}$$

$$\begin{aligned} det(M) = &+ A_1 B_2 (C_4 D_3 - C_3 D_4) + A_1 B_4 (C_3 D_2 - C_2 D_3) \\ &+ A_3 B_2 (C_1 D_4 - C_4 D_1) + A_3 B_4 (C_2 D_1 - C_1 D_2), \end{aligned} \tag{B.24}$$

in which

$$\begin{aligned} &A_1 B_2 (C_4 D_3 - C_3 D_4) \\ =&J_\nu^2(r_0)\left[\omega^2\mu_0\epsilon_0\epsilon_r\mu_r r_0^2\kappa_c^4 g'(r_0)f'(r_0) - \beta^2\nu^2\kappa_c^4 g(r_0)f(r_0)\right], \end{aligned} \tag{B.25}$$

$$\begin{aligned} &A_1 B_4 (C_3 D_2 - C_2 D_3) \\ =&J_\nu(\kappa_c r_0)g(r_0)\left[\beta^2\nu^2\kappa_c^2\kappa_{r,\phi}^2 f(r_0)J_\nu(r_0) - \omega^2\epsilon_0\mu_0\epsilon_r r_0^2\kappa_c^3\kappa_{\phi,r}^2 f'(r_0)J_\nu'(r_0)\right], \end{aligned} \tag{B.26}$$

$$\begin{aligned} &A_3 B_2 (C_1 D_4 - C_4 D_1) \\ =&J_\nu(\kappa_c r_0)f(r_0)\left[\beta^2\nu^2\kappa_c^2\kappa_{\phi,r}^2 g(r_0)J_\nu(\kappa_c r_0) - \omega^2\epsilon_0\mu_0\epsilon_c\mu_r r_0^2\kappa_c^3\kappa_{r,\phi}^2 g'(r_0)J_\nu'(r_0)\right], \end{aligned} \tag{B.27}$$

$$\begin{aligned} &A_3 B_4 (C_2 D_1 - C_1 D_2) \\ =&g(r_0)f(r_0)\left[\omega^2\epsilon_0\mu_0\epsilon_c r_0^2\kappa_c^2\kappa_{r,\phi}^2\kappa_{\phi,r}^2 (J_\nu'(\kappa_c r_0))^2 - \beta^2\nu^2\kappa_{r,\phi}^2\kappa_{\phi,r}^2 (J_\nu(\kappa_c r_0))^2\right]. \end{aligned} \tag{B.28}$$

Hence,

$$\begin{aligned} det(M) =& J_\nu^2(r_0)\left[\omega^2\mu_0\epsilon_0\epsilon_r\mu_r r_0^2\kappa_c^4 g'(r_0)f'(r_0) - \beta^2\nu^2\kappa_c^4 g(r_0)f(r_0)\right] \\ &+J_\nu(\kappa_c r_0)g(r_0)\left[\beta^2\nu^2\kappa_c^2\kappa_{r,\phi}^2 f(r_0)J_\nu(r_0) - \omega^2\epsilon_0\mu_0\epsilon_r r_0^2\kappa_c^3\kappa_{\phi,r}^2 f'(r_0)J_\nu'(r_0)\right] \\ &+J_\nu(\kappa_c r_0)f(r_0)\left[\beta^2\nu^2\kappa_c^2\kappa_{\phi,r}^2 g(r_0)J_\nu(\kappa_c r_0) - \omega^2\epsilon_0\mu_0\epsilon_c\mu_r r_0^2\kappa_c^3\kappa_{r,\phi}^2 g'(r_0)J_\nu'(r_0)\right] \\ &+g(r_0)f(r_0)\left[\omega^2\epsilon_0\mu_0\epsilon_c r_0^2\kappa_c^2\kappa_{r,\phi}^2\kappa_{\phi,r}^2(J_\nu'(\kappa_c r_0))^2 - \beta^2\nu^2\kappa_{r,\phi}^2\kappa_{\phi,r}^2(J_\nu(\kappa_c r_0))^2\right] \\ &=0. \end{aligned} \tag{B.29}$$

Divided by $J_\nu^2(r_0)g(r_0)f(r_0)$ we can get

$$\begin{aligned} &\left[\omega^2\mu_0\epsilon_0\epsilon_r\mu_r r_0^2\kappa_c^4\frac{g'(r_0)f'(r_0)}{g(r_0)f(r_0)} - \beta^2\nu^2\kappa_c^4\right] \\ &+\left[\beta^2\nu^2\kappa_c^2\kappa_{r,\phi}^2 - \omega^2\epsilon_0\mu_0\epsilon_r r_0^2\kappa_c^3\kappa_{\phi,r}^2\frac{f'(r_0)J_\nu'(r_0)}{f(r_0)J_\nu(r_0)}\right] \\ &+\left[\beta^2\nu^2\kappa_c^2\kappa_{\phi,r}^2 - \omega^2\epsilon_0\mu_0\epsilon_c\mu_r r_0^2\kappa_c^3\kappa_{r,\phi}^2\frac{g'(r_0)J_\nu'(r_0)}{g(r_0)J_\nu(r_0)}\right] \\ &+\left[\omega^2\epsilon_0\mu_0\epsilon_c r_0^2\kappa_c^2\kappa_{r,\phi}^2\kappa_{\phi,r}^2\left(\frac{J_\nu'(\kappa_c r_0)}{J_\nu(\kappa_c r_0)}\right)^2 - \beta^2\nu^2\kappa_{r,\phi}^2\kappa_{\phi,r}^2\right] \\ &=0, \end{aligned} \tag{B.30}$$

$$\begin{aligned} &\left[\omega^2\mu_0\epsilon_0\epsilon_r\mu_r r_0^2\kappa_c^4\frac{g'(r_0)f'(r_0)}{g(r_0)f(r_0)}\right] \\ &-\left[\omega^2\epsilon_0\mu_0\epsilon_r r_0^2\kappa_c^3\kappa_{\phi,r}^2\frac{f'(r_0)J_\nu'(r_0)}{f(r_0)J_\nu(r_0)}\right] \\ &-\left[\omega^2\epsilon_0\mu_0\epsilon_c\mu_r r_0^2\kappa_c^3\kappa_{r,\phi}^2\frac{g'(r_0)J_\nu'(r_0)}{g(r_0)J_\nu(r_0)}\right] \\ &+\left[\omega^2\epsilon_0\mu_0\epsilon_c r_0^2\kappa_c^2\kappa_{r,\phi}^2\kappa_{\phi,r}^2\left(\frac{J_\nu'(\kappa_c r_0)}{J_\nu(\kappa_c r_0)}\right)^2\right] \\ &=\beta^2\nu^2\kappa_c^4 - \beta^2\nu^2\kappa_c^2\kappa_{r,\phi}^2 - \beta^2\nu^2\kappa_c^2\kappa_{\phi,r}^2 + \beta^2\nu^2\kappa_{r,\phi}^2\kappa_{\phi,r}^2 \\ &=\beta^2\nu^2\left(\kappa_c^4 - \kappa_c^2\kappa_{r,\phi}^2 - \kappa_c^2\kappa_{\phi,r}^2 + \kappa_{r,\phi}^2\kappa_{\phi,r}^2\right) \\ &=\beta^2\nu^2\left(\kappa_c^2 - \kappa_{r,\phi}^2\right)\left(\kappa_c^2 - \kappa_{\phi,r}^2\right) \\ &=\beta^2\nu^2 k_0^4\left(\epsilon_c - \epsilon_r\mu_\phi\right)\left(\epsilon_c - \epsilon_\phi\mu_r\right). \end{aligned} \tag{B.31}$$

Since $\omega^2\epsilon_0\mu_0 = k_0^2$, one can have

$$\begin{aligned} &\frac{\epsilon_c\kappa_c^2}{\kappa_c^4}\left(\frac{J_\nu'(\kappa_c r_0)}{J_\nu(\kappa_c r_0)}\right)^2 - \frac{\epsilon_r\kappa_c}{\kappa_c^2\kappa_{r,\phi}^2}\frac{f'(r_0)J_\nu'(r_0)}{f(r_0)J_\nu(r_0)} - \frac{\epsilon_c\mu_r\kappa_c}{\kappa_c^2\kappa_{\phi,r}^2}\frac{g'(r_0)J_\nu'(r_0)}{g(r_0)J_\nu(r_0)} + \frac{\epsilon_r\mu_r}{\kappa_{r,\phi}^2\kappa_{\phi,r}^2}\frac{g'(r_0)f'(r_0)}{g(r_0)f(r_0)} \\ =&\frac{\beta^2\nu^2 k_0^2}{r_0^2\kappa_c^4\kappa_{r,\phi}^2\kappa_{\phi,r}^2}\left(\epsilon_c - \epsilon_r\mu_\phi\right)\left(\epsilon_c - \epsilon_\phi\mu_r\right). \end{aligned} \tag{B.32}$$

Combine terms and we can get

$$\left[\frac{\kappa_c}{\kappa_c^2}\frac{J_\nu'(\kappa_c r_0)}{J_\nu(\kappa_c r_0)} - \frac{\mu_r}{\kappa_{\phi,r}^2}\frac{g'(r_0)}{g(r_0)}\right]\left[\frac{\epsilon_c\kappa_c}{\kappa_c^2}\frac{J_\nu'(\kappa_c r_0)}{J_\nu(\kappa_c r_0)} - \frac{\epsilon_r}{\kappa_{r,\phi}^2}\frac{f'(r_0)}{f(r_0)}\right]$$
$$= \frac{\beta^2\nu^2 k_0^2}{r_0^2\kappa_c^4\kappa_{r,\phi}^2\kappa_{\phi,r}^2}\left(\epsilon_c - \epsilon_r\mu_\phi\right)\left(\epsilon_c - \epsilon_\phi\mu_r\right). \tag{B.33}$$

The above equation is the dispersion relation for anisotropic cladding and isotropic nonmagnetic core.

B.3. Asymptotic solution for coupled second order differential equation system

The differential equation system needed to be solved is

$$r^2E'' + rE' - (p_2r^2 + p_0\nu^2)E + s\nu rG' = 0, \tag{B.34}$$
$$r^2G'' + rG' - (q_2r^2 - q_0\nu^2)G + s\nu rE' = 0. \tag{B.35}$$

We use asymptotic theory to solve the above equation. First, we assume the asymptotic solution of the equation will have the form

$$E(r) = (\alpha r)^{\sigma_1}\exp(-\alpha r^\rho)\sum_{n=0}^{\infty} a_n\left(\frac{1}{\alpha r}\right)^n = \exp(-\alpha r^\rho)\sum_{n=0}^{\infty} a_n\,(\alpha r)^{-n+\sigma_1}, \tag{B.36}$$

$$G(r) = (\alpha r)^{\sigma_2}\exp(-\alpha r^\rho)\sum_{n=0}^{\infty} b_n\left(\frac{1}{\alpha r}\right)^n = \exp(-\alpha r^\rho)\sum_{n=0}^{\infty} a_n\,(\alpha r)^{-n+\sigma_1}, \tag{B.37}$$

where $\sigma_1, \sigma_2 \neq 0, \alpha, \rho > 0$. This assumption will make sure that when $r \to \infty$, the solutions will approach zero, which has a physical meaning.

So the first derivative of Eq. B.36 and Eq. B.37 are

$$E'(r) = -\sum_{n=0}^{\infty}\alpha^{2-\rho}\rho a_n(\alpha r)^{-n+\sigma_1+\rho-1}\exp(-\alpha r^\rho) + \sum_{n=0}^{\infty}\alpha(-n+\sigma_1)a_n(\alpha r)^{-n+\sigma_1-1}\exp(-\alpha r^\rho), \tag{B.38}$$

$$G'(r) = -\sum_{n=0}^{\infty}\alpha^{2-\rho}\rho b_n(\alpha r)^{-n+\sigma_2+\rho-1}\exp(-\alpha r^\rho) + \sum_{n=0}^{\infty}\alpha(-n+\sigma_2)b_n(\alpha r)^{-n+\sigma_2-1}\exp(-\alpha r^\rho). \tag{B.39}$$

The second derivative of Eq. B.36 and Eq. B.37 are

$$
\begin{aligned}
E''(r) = &\sum_{n=0}^{\infty} \alpha^{4-2\rho}\rho^2 a_n (\alpha r)^{-n+\sigma_1+2\rho-2} \exp(-\alpha r^{\rho}) \\
&- \sum_{n=0}^{\infty} \alpha^{3-\rho}\rho(-n+\sigma_1+\rho-1) a_n (\alpha r)^{-n+\sigma_1+\rho-2} \exp(-\alpha r^{\rho}) \\
&- \sum_{n=0}^{\infty} \alpha^{3-\rho}\rho(-n+\sigma_1) a_n (\alpha r)^{-n+\sigma_1+\rho-2} \exp(-\alpha r^{\rho}) \\
&+ \sum_{n=0}^{\infty} \alpha^{2}(-n+\sigma_1)(-n+\sigma_1-1) a_n (\alpha r)^{-n+\sigma_1-2} \exp(-\alpha r^{\rho}), \qquad \text{(B.40)} \\
G''(r) = &\sum_{n=0}^{\infty} \alpha^{4-2\rho}\rho^2 b_n (\alpha r)^{-n+\sigma_2+2\rho-2} \exp(-\alpha r^{\rho}) \\
&- \sum_{n=0}^{\infty} \alpha^{3-\rho}\rho(-n+\sigma_2+\rho-1) b_n (\alpha r)^{-n+\sigma_2+\rho-2} \exp(-\alpha r^{\rho}) \\
&- \sum_{n=0}^{\infty} \alpha^{3-\rho}\rho(-n+\sigma_2) b_n (\alpha r)^{-n+\sigma_2+\rho-2} \exp(-\alpha r^{\rho}) \\
&+ \sum_{n=0}^{\infty} \alpha^{2}(-n+\sigma_2)(-n+\sigma_2-1) b_n (\alpha r)^{-n+\sigma_2-2} \exp(-\alpha r^{\rho}). \qquad \text{(B.41)}
\end{aligned}
$$

Also we can calculate

$$-(p_2 r^2 + p_0 v^2)E = -\sum_{n=0}^{\infty} p_2 \alpha^{-2} a_n (\alpha r)^{-n+\sigma_1+2} \exp(-\alpha r^\rho) - \sum_{n=0}^{\infty} p_0 v^2 a_n (\alpha r)^{-n+\sigma_1} \exp(-\alpha r^\rho), \tag{B.42}$$

$$-(q_2 r^2 - q_0 v^2)G = -\sum_{n=0}^{\infty} q_2 \alpha^{-2} b_n (\alpha r)^{-n+\sigma_2+2} \exp(-\alpha r^\rho) + \sum_{n=0}^{\infty} q_0 v^2 b_n (\alpha r)^{-n+\sigma_2} \exp(-\alpha r^\rho), \tag{B.43}$$

$$svrE(r)' = -\sum_{n=0}^{\infty} sv\alpha^{1-\rho}\rho a_n (\alpha r)^{-n+\sigma_1+\rho} \exp(-\alpha r^\rho) + \sum_{n=0}^{\infty} sv(-n+\sigma_1) a_n (\alpha r)^{-n+\sigma_1} \exp(-\alpha r^\rho), \tag{B.44}$$

$$svrG'(r) = -\sum_{n=0}^{\infty} sv\alpha^{1-\rho}\rho b_n (\alpha r)^{-n+\sigma_2+\rho} \exp(-\alpha r^\rho) + \sum_{n=0}^{\infty} sv(-n+\sigma_2) b_n (\alpha r)^{-n+\sigma_2} \exp(-\alpha r^\rho). \tag{B.45}$$

Putting eqjuation B.40,B.38,B.42 and B.45 together, we can construct the equation B.34. Also we simplify a little bit by neglecting the common term $\exp(-\alpha r^\rho)$

$$\sum_{n=0}^{\infty} \alpha^{2-2\rho}\rho^2 a_n(\alpha r)^{-n+\sigma_1+2\rho} - \sum_{n=0}^{\infty} \alpha^{1-\rho}\rho(-n+\sigma_1+\rho-1)a_n(\alpha r)^{-n+\sigma_1+\rho}$$
$$- \sum_{n=0}^{\infty} \alpha^{1-\rho}\rho(-n+\sigma_1)a_n(\alpha r)^{-n+\sigma_1+\rho} + \sum_{n=0}^{\infty}(-n+\sigma_1)(-n+\sigma_1-1)a_n(\alpha r)^{-n+\sigma_1}$$
$$- \sum_{n=0}^{\infty} \alpha^{1-\rho}\rho a_n(\alpha r)^{-n+\sigma_1+\rho} + \sum_{n=0}^{\infty}(-n+\sigma_1)a_n(\alpha r)^{-n+\sigma_1}$$
$$- \sum_{n=0}^{\infty} p_2\alpha^{-2}a_n(\alpha r)^{-n+\sigma_1+2} - \sum_{n=0}^{\infty} p_0\nu^2 a_n(\alpha r)^{-n+\sigma_1}$$
$$- \sum_{n=0}^{\infty} s\nu\alpha^{1-\rho}\rho b_n(\alpha r)^{-n+\sigma_2+\rho} + \sum_{n=0}^{\infty} s\nu(-n+\sigma_2)b_n(\alpha r)^{-n+\sigma_2}$$
$$= 0. \tag{B.46}$$

Now we would like to analysis the leading term behavior. As $r \to \infty$, the sub-dominant terms and all $n > 0$ terms can be neglect and we get the asymptotic form

$$\alpha^{2-2\rho}\rho^2 a_0(\alpha r)^{\sigma_1+2\rho} - p_2\alpha^{-2}a_0(\alpha r)^{\sigma_1+2} \sim s\nu\alpha^{1-\rho}\rho b_0(\alpha r)^{\sigma_2+\rho}. \tag{B.47}$$

The same procedure can be apply to equation B.41, B.39, B.43 and B.44. By combining them and neglect the sub-dominant terms we can get the other asymptotic form

$$\alpha^{2-2\rho}\rho^2 b_0(\alpha r)^{\sigma_2+2\rho} - q_2\alpha^{-2}b_0(\alpha r)^{\sigma_2+2} \sim s\nu\alpha^{1-\rho}\rho a_0(\alpha r)^{\sigma_1+\rho}. \tag{B.48}$$

Each of the above equations contains three terms. Let's look at the first equation first. According to the asymptotic theory, the coefficient of the dominant term should be zero. since $\alpha, \rho, p_2, a_0, b_0 \neq 0$, we have to discuss case by case.

B.3.1. Solution discussion

Case 1: $\sigma_1 + 2 = \sigma_1 + 2\rho > \sigma_2 + \rho$

This impose that $\rho = 1$. Then the Eq. B.47 becomes

$$a_0(\alpha r)^{\sigma_1+2} \sim p_2\alpha^{-2}a_0(\alpha r)^{\sigma_1+2} \tag{B.49}$$

Therefore we can have

$$\alpha = \sqrt{p_2}. \tag{B.50}$$

We can also update Eq. B.48

$$\left(1 - q_2 p_2^{-1}\right) b_0 (\alpha r)^{\sigma_2+2} \sim s\nu a_0 (\alpha r)^{\sigma_1+1}. \tag{B.51}$$

Because $p_2 \neq q_2$, non of the above terms can be the leading term since no coefficient can be zero. therefore

$$\sigma_2 = \sigma_1 - 1, \tag{B.52}$$

$$b_0 = \frac{p_2 s\nu}{p_2 - q_2} a_0. \tag{B.53}$$

Case 2: $\sigma_1 + 2 = \sigma_2 + \rho > \sigma_1 + 2\rho$
this case impose that

$$\rho < 1. \tag{B.54}$$

Therefore, Eq. B.47 and B.48 become

$$-p_2 \alpha^{-2} a_0 (\alpha r)^{\sigma_1+2} \sim s\nu \alpha^{1-\rho} \rho b_0 (\alpha r)^{\sigma_2+\rho}, \tag{B.55}$$

$$-q_2 \alpha^{-2} b_0 (\alpha r)^{\sigma_2+2} \sim s\nu \alpha^{1-\rho} \rho a_0 (\alpha r)^{\sigma_1+\rho}. \tag{B.56}$$

Together it should satisfy

$$\begin{cases} \sigma_2 + \rho = \sigma_1 + 2, \\ \sigma_1 + \rho = \sigma_2 + 2. \end{cases} \tag{B.57}$$

Therefore, $\rho = 2$, which is contradictory. This case is invalid.

Case 3: $\sigma_1 + 2 < \sigma_1 + 2\rho = \sigma_2 + \rho$
This case impose that $\rho > 1$ Therefore, Eq. B.47 and B.48 become

$$\alpha^{2-2\rho} \rho^2 a_0 (\alpha r)^{\sigma_1+2\rho} \sim s\nu \alpha^{1-\rho} \rho b_0 (\alpha r)^{\sigma_2+\rho}, \tag{B.58}$$

$$\alpha^{2-2\rho} \rho^2 b_0 (\alpha r)^{\sigma_2+2\rho} \sim s\nu \alpha^{1-\rho} \rho a_0 (\alpha r)^{\sigma_1+\rho}. \tag{B.59}$$

Together it should satisfy

$$\begin{cases} \sigma_1 + 2\rho = \sigma_2 + \rho, \\ \sigma_2 + 2\rho = \sigma_1 + \rho. \end{cases} \tag{B.60}$$

Therefore,$\rho = 0$, which is contradictory.

Case 4: $\sigma_1 + 2 = \sigma_1 + 2\rho = \sigma_2 + \rho$
then we have $\rho = 1$, and $\sigma_1 = \sigma_2 - 1$ Therefore, Eq. B.47 and B.48 become

$$\left(1 - p_2\alpha^{-2}\right) a_0(\alpha r)^{\sigma_1+2} \sim sv b_0(\alpha r)^{\sigma_2+1}, \tag{B.61}$$

$$b_0(\alpha r)^{\sigma_2+2} \sim q_2\alpha^{-2} b_0(\alpha r)^{\sigma_2+2}. \tag{B.62}$$

Eq. B.62 tells us that

$$\alpha = \sqrt{q_2}. \tag{B.63}$$

Therefore, we can solve out Eq. B.61

$$a_0 = \frac{q_2 sv}{q_2 - p_2} b_0. \tag{B.64}$$

B.3.2. Summary 1

From the above discussion, we can know that the above Eq. B.34 and B.35 has the asymptotic solution of the form:

$$\begin{cases} E(r) & = \exp(-\sqrt{p_2}r) \sum_{n=0}^{\infty} a_n \left(\sqrt{p_2}r\right)^{-n+\sigma_1} \\ G(r) & = \exp(-\sqrt{p_2}r) \sum_{n=0}^{\infty} b_n \left(\sqrt{p_2}r\right)^{-n+\sigma_1-1} \end{cases} \tag{B.65}$$

where

$$b_0 = \frac{p_2 sv}{p_2 - q_2} a_0 \tag{B.66}$$

or

$$\begin{cases} E(r) & = \exp(-\sqrt{q_2}r) \sum_{n=0}^{\infty} a_n \left(\sqrt{q_2}r\right)^{-n+\sigma_2-1} \\ G(r) & = \exp(-\sqrt{q_2}r) \sum_{n=0}^{\infty} b_n \left(\sqrt{q_2}r\right)^{-n+\sigma_2} \end{cases} \tag{B.67}$$

where

$$a_0 = \frac{q_2 sv}{q_2 - p_2} b_0 \tag{B.68}$$

B.3.3. parameter value of the first solution

Let's first look at the solution Eq. B.65, we substitute it back to Eq. B.34 and get:

$$\begin{aligned} &-\sum_{n=0}^{\infty} (2(-n+\sigma_1)+1) a_n (\sqrt{p_2}r)^{-n+\sigma_1+1} + \sum_{n=0}^{\infty} (-n+\sigma_1)^2 a_n (\sqrt{p_2}r)^{-n+\sigma_1} \\ &\qquad - \sum_{n=0}^{\infty} p_0 v^2 a_n (\sqrt{p_2}r)^{-n+\sigma_1} \\ &- \sum_{n=0}^{\infty} sv b_n (\sqrt{p_2}r)^{-n+\sigma_1} + \sum_{n=0}^{\infty} sv(-n+\sigma_1-1) b_n (\sqrt{p_2}r)^{-n+\sigma_1-1} \\ &\qquad = 0. \end{aligned} \tag{B.69}$$

The dominant terms are When $n = 0$ and the most dominant term is the first term. Therefore, the first term tells that when $n = 0$

$$\sigma_1 = -\frac{1}{2}. \tag{B.70}$$

Then Eq. B.69 becomes

$$\sum_{n=0}^{\infty} 2na_n(\sqrt{p_2}r)^{-n+\frac{1}{2}} + \sum_{n=0}^{\infty}\left[\left((n+\frac{1}{2})^2 - p_0\nu^2\right)a_n - s\nu b_n\right](\sqrt{p_2}r)^{-n-\frac{1}{2}} + \sum_{n=0}^{\infty} s\nu(-n-\frac{3}{2})b_n(\sqrt{p_2}r)^{-n-\frac{3}{2}} = 0. \tag{B.71}$$

We shift the order of the second and the third term and get

$$\sum_{n=0}^{\infty} 2na_n(\alpha r)^{-n+\frac{1}{2}} + \sum_{n=1}^{\infty}\left[\left((n-\frac{1}{2})^2 - p_0\nu^2\right)a_{n-1} - s\nu b_{n-1}\right](\alpha r)^{-n+\frac{1}{2}} - \sum_{n=2}^{\infty} s\nu(n-\frac{1}{2})b_{n-2}(\alpha r)^{-n+\frac{1}{2}} = 0. \tag{B.72}$$

Therefore, when $n = 1$

$$a_1 = \frac{4p_0\nu^2 - 1}{8}a_0 + \frac{s\nu}{2}b_0. \tag{B.73}$$

When $n \geq 2$, we have

$$a_n = \frac{4p_0\nu^2 - (2n-1)^2}{8n}a_{n-1} + \frac{s\nu}{2n}b_{n-1} + \frac{s\nu(2n-1)}{4n}b_{n-2}. \tag{B.74}$$

Next we need to retrieve the recursion relation for b_n. Substitute the value of γ_1, α, ρ to Eq. B.41,B.39,B.43 and B.44, and combine them up in Eq. B.35, we are able to get (with the common term $(\sqrt{p_2}r)^{\sigma_1}\exp(-\sqrt{p_2}r)$ neglected)

$$\sum_{n=0}^{\infty}\left[(1-q_2p_2^{-1})b_n - s\nu\, a_n\right](\sqrt{p_2}r)^{-n+1} + \sum_{n=0}^{\infty}\left[(2n+2)b_n - s\nu(n+\frac{1}{2})a_n\right](\sqrt{p_2}r)^{-n} + \sum_{n=0}^{\infty}\left((n+\frac{3}{2})^2 + q_0\nu^2\right)b_n(\sqrt{p_2}r)^{-n-1} = 0. \tag{B.75}$$

Again, by shifting the order of second and third term by 1 and 2, respectively, we can get

$$\sum_{n=0}^{\infty}\left[(1-q_2p_2^{-1})b_n - sv\ a_n\right](\sqrt{p_2}r)^{-n+1} + \sum_{n=1}^{\infty}\left[(2nb_{n-1} - sv(n-\frac{1}{2})a_{n-1}\right](\sqrt{p_2}r)^{-n+1} + \sum_{n=2}^{\infty}\left((n-\frac{1}{2})^2 + q_0v^2\right)b_{n-2}(\sqrt{p_2}r)^{-n+1} = 0. \tag{B.76}$$

Therefore, the leading term is $n = 0$, and we find

$$b_0 = \frac{p_2 sv}{p_2 - q_2}a_0. \tag{B.77}$$

The next leading term is when $n = 1$, and we find:

$$b_1 = \frac{p_2}{p_2 - q_2}\left(\frac{sv}{2}a_0 + sva_1 - 2b_0\right). \tag{B.78}$$

The resting term ($n \geq 2$) has the following recursion relationship

$$b_n = \frac{p_2}{p_2 - q_2}\left(\frac{sv(2n-1)}{2}a_{n-1} + sva_n - \frac{4q_0v^2 + (2n-1)^2}{4}b_{n-2} - 2nb_{n-1}\right). \tag{B.79}$$

Therefore, from now on we are able to construct all the parameters in the first solution.

B.3.4. Parameter value of the second solution

Similarly, we can substitute Eq. B.67 into Eq. B.34 and B.35, and then we can get

$$\sigma_2 = -\frac{1}{2}, \tag{B.80}$$

$$b_1 = -\frac{4q_0v^2 + 1}{8}b_0 + \frac{sv}{2}a_0, \tag{B.81}$$

$$b_n = -\frac{4q_0v^2 + (2n-1)^2}{8n}b_{n-1} + \frac{sv}{2n}a_{n-1} + \frac{sv(2n-1)}{4n}a_{n-2}, \tag{B.82}$$

$$a_0 = \frac{q_2 sv}{q_2 - p_2}b_0, \tag{B.83}$$

$$a_1 = \frac{q_2}{q_2 - p_2}\left(\frac{sv}{2}b_0 + svb_1 - 2a_0\right), \tag{B.84}$$

$$a_n = \frac{q_2}{q_2 - p_2}\left(\frac{sv(2n-1)}{2}b_{n-1} + svb_n - \frac{(2n-1)^2 - 4p_0v^2}{4}a_{n-2} - 2na_{n-1}\right). \tag{B.85}$$

B.3.5. Summary 2

The general asymptotic solution to the differential equation system

$$r^2E'' + rE' - (p_2r^2 + p_0v^2)E + svrG' = 0, \tag{B.86}$$
$$r^2G'' + rG' - (q_2r^2 - q_0v^2)G + svrE' = 0, \tag{B.87}$$

is

$$C_1\begin{cases}(\sqrt{p_2}r)^{-\frac{1}{2}}\exp(-\sqrt{p_2}r)\sum_{n=0}^{\infty}a_n\left(\sqrt{p_2}r\right)^{-n}\\(\sqrt{p_2}r)^{-\frac{3}{2}}\exp(-\sqrt{p_2}r)\sum_{n=0}^{\infty}b_n\left(\sqrt{p_2}r\right)^{-n}\end{cases}+C_2\begin{cases}(\sqrt{q_2}r)^{-\frac{3}{2}}\exp(-\sqrt{q_2}r)\sum_{n=0}^{\infty}c_n\left(\sqrt{q_2}r\right)^{-n}\\(\sqrt{q_2}r)^{-\frac{1}{2}}\exp(-\sqrt{q_2}r)\sum_{n=0}^{\infty}d_n\left(\sqrt{q_2}r\right)^{-n},\end{cases} \tag{B.88}$$

where a_n, b_n, c_n and d_n has the recursive relation:

$$a_0 = 1, \tag{B.89}$$
$$b_0 = \frac{p_2sv}{p_2 - q_2}a_0, \tag{B.90}$$
$$a_1 = \frac{4p_0v^2 - 1}{8}a_0 + \frac{sv}{2}b_0, \tag{B.91}$$
$$b_1 = \frac{p_2}{p_2 - q_2}\left(\frac{sv}{2}a_0 + sva_1 - 2b_0\right), \tag{B.92}$$
$$a_n = \frac{4p_0v^2 - (2n-1)^2}{8n}a_{n-1} + \frac{sv}{2n}b_{n-1} + \frac{sv(2n-1)}{4n}b_{n-2}, \tag{B.93}$$
$$b_n = \frac{p_2}{p_2 - q_2}\left(\frac{sv(2n-1)}{2}a_{n-1} + sva_n - \frac{4q_0v^2 + (2n-1)^2}{4}b_{n-2} - 2nb_{n-1}\right), \tag{B.94}$$

$$d_0 = 1, \tag{B.95}$$
$$c_0 = \frac{q_2sv}{q_2 - p_2}d_0, \tag{B.96}$$
$$d_1 = -\frac{4q_0v^2 + 1}{8}d_0 + \frac{sv}{2}c_0, \tag{B.97}$$
$$c_1 = \frac{q_2}{q_2 - p_2}\left(\frac{sv}{2}d_0 + svd_1 - 2c_0\right), \tag{B.98}$$
$$d_n = -\frac{4q_0v^2 + (2n-1)^2}{8n}d_{n-1} + \frac{sv}{2n}c_{n-1} + \frac{sv(2n-1)}{4n}c_{n-2}, \tag{B.99}$$
$$c_n = \frac{q_2}{q_2 - p_2}\left(\frac{sv(2n-1)}{2}d_{n-1} + svd_n - \frac{(2n-1)^2 - 4p_0v^2}{4}c_{n-2} - 2nc_{n-1}\right). \tag{B.100}$$

Acknowledgment

Sometimes I still could not believe that I have left China and have come to the Netherlands for pursuing a PhD, which is really a game changer of my life.

In October 2013, I finally arrived at Schiphol airport, and joined Optics Research Group in TU Delft. I can still clearly remember the first day when I visited Optica. I tried to call Lei's office phone number when I arrived at the faculty front door, but he was at a meeting with Paul. Fortunately, Matthias picked up the phone, and very kindly welcomed me at the reception and brought me to the Optica corridor. On that day I was warmly welcomed by so many people from the group, which made me feel like talking to a bunch of old friends. Thinking back those memories now in 2019, I feel they are still as fresh as yesterday. It has been a very long journey and adventure for me, but I must say coming to the Netherlands and joining Optica is one of the best decisions that I have ever made. I have not only gained deeper knowledges in optics, but also obtained completely new understandings of the world, different cultures and also myself from a new perspective. Before I came, I had no idea about the Netherlands, but now I am happily enjoying my life living here with my wife and a baby to come!

I would like express my sincere gratitude from the bottom of my heart to everyone that I have met on this journey. The help and care that I received in the past 6 years are extremely invaluable, for which I will be eternally grateful.

First of all, I would like to thank my promoter Prof. H. Paul Urbach and co-promoter Dr. Aurèle Adam. Paul, it is really nice to learn from you how to have a mathematical mind set. It is always amazing that you can easily point out the flaws in the research by deriving complex mathematical. Aurèle, thank you for helping me in every aspect. This thesis defense could not happen without your constant help. You are an excellent presenter and I learned a lot from you. You also gave me a lot of freedom in research and provided me with your best support. I would like to also thank Man to get me started with my PhD, especially working with TNO is a valuable experience for me. Thank you for all the tips on finding a job in the Netherlands. I would also like to thank the thesis committee for reading and evaluating this thesis.

I would also like to thank all the other Optica staff members, Yvonne, Roland, Thim, Rob, Joseph, Nandini, Silvaia, Florian, Omar, Peter and Jeff. Yvonne, thank you for your kindness and willingness for helping everyone in the group including me, it is always a pleasure to chat with you. Roland, Thim and Rob, you are the golden triangle of Optica and can always come up with adequate solutions. Joseph, you are a truly honorable scientist, it is my great honor to share the office for a short period with you.

It is my best luck to have Andreas, Nishant and Daniel as my officemates. Thank you Andreas for always grabbing me to the coffee break, which helped me to im-

prove my English a lot. I will never forget your funny lame jokes. Thank you Nishant for helping me with cleanroom exercise, which was always a lot of fun. Daniel, it was always great to have beer with you, and thank you very much for being the guardian of Agora.

I would like to say thank you to all my PhD fellows: Yifeng, Zhe, Hamed, Matthias, Luca, Priya, Fellipe, Kefei, Wouter, Anna, Adonis, Zheng, Marco, Katsiaryna, Lauryna, Sander (specially thanks for helping with the samenvatting), Lei, Peiwen, Gerward, Yan, Iman, Paolo, Dmytro, Po-Ju, Po-Sheng, Xiujie, Yuxin, Boling, Jin, Min, Alessandro. Special acknowledgment to Seungkyu and Prof. Nynke Dekker. It is my great honor to work together with you. Seungkyu, I won't forget all those very long discussions with you until late night, you are a true scientist with deep understanding of nano-world. I wish you a bright future for your career.

I also thank all the cleanroom staffs who helped me in getting on board for nano-fabrication, which is a valuable experience for my professional career. I also thank all the students that I worked with: Fabian, Thomas, Julien. Their work help me shaping this thesis.

Lastly, I would like to thank all of my family members who have been always supportive from the back. I profoundly thank my wife Guoying. I am truly grateful for having your company for all these years. I never felt homesick because of your presence. This PhD thesis could never be achieved without your constant encouragement. Thank you!

Ying Tang

Curriculum Vitæ

Ying TANG

10-12-1987	Born in Shaodong, China.

Education

2003–2006	High School Shunde No. 1 Middle School, Foshan, China
2006–2010	Bachelor of Engineering in Optoelectronic Infomation Engineering Huazhong University of Science and Technology, Wuhan, China
2010–2013	Master of Engineering in Optoelectronic Infomation Engineering Huazhong University of Science and Technology, Wuhan, China
2013–2019	PhD candidate, Optics Delft University of Technology, Delft, the Netherlands
2019–	Design Engineer ASML, Veldhoven, the Netherlands

Awards

2008	School Outstanding Student Leader Award, HUST
2010	Graduate Student's Full Scholarship, HUST
2012	Excellent Graduate Student Leader Award, HUST
2017	ScienceDATE Interdisciplinary Research Grant, TU Delft

List of Publications

9. **Y. Tang**, Z. Hou, Y. Shao, A. J. L. Adam, and H. P. Urbach, *Hyperlens design and performance evaluation under the loss condition* (in preparation).

8. **Y. Tang**, S. Ha*, T. Begou, J Lumeau, H. P. Urbach, N. Dekker, and A. J. L. Adam, *Birefringent metamaterial nanocuboids with tailored optical constants for force and torque transduction* (in preparation). (*equally contributed)

7. S. Ha*, **Y. Tang***, M. van Oene, R. Janissen, R. Dries, B. Solano, A. Adam, and N. Dekker, *Single-Crystal Rutile TiO_2 Nanocylinders are Highly Effective Transducers of Optical Force and Torque*, ACS Photonics, **6**, 1255, (2019). (*equally contributed)

6. X. Lu; Y. Shao, C. Zhao, S.Konijnenberg, X. Zhu, **Y. Tang**, Y. Cai and H. P. Urbach, *Noniterative spatially partially coherent diffractive imaging using pinhole array mask*, Advanced Photonics, **1**, 016005, (2019)

5. Y. Shao, M. Loktev, **Y. Tang**, F. Bociort, and H. P. Urbach, *Spatially varying aberration calibration using a pair of matched periodic pinhole array masks*, Optics Express, **27**, 729 (2019)

4. **Y. Tang**, Z. Xi, M. Xu, A. J. L. Adam, H. P. Urbach, *Spatial mode filter with hyperbolic-cladded waveguide*, Proceeding. SPIE **10112**, 101120E, (2017)

3. **Y. Tang**, Z. Xi, M. Xu, S. Bäumer, A. J. L. Adam, and H. P. Urbach, *Spatial mode-selective waveguide with hyperbolic cladding*, Optics Letters, **41**, 4285, (2016).

2. H. He, **Y. Tang**, F. Zhou, J. Wang, Q. Luo, and P. Li, *Lateral laser speckle contrast analysis combined with line beam scanning illumination to improve the sampling depth of blood flow imaging*, Optics Letters, **37**, 3774 (2012).

1. H. Chen, Z. Xie, X. Jin, C. Luo, C. You, **Y. Tang**, D. Chen, Z. Li, and X. Fan. *TiO_2 and N-Doped TiO_2 induced photocatalytic inactivation of staphylococcus aureus under 405 nm LED blue light irradiation*, International Journal of Photoenergy, **2012**, 848401 (2012).